Ph.D. Thesis / UNIVERSITÉ DE BRETAGNE OCCIDENTALE
part of Université européenne de Bretagne
for the degree of
DOCTOR AT UNIVERSITÉ DE BRETAGNE OCCIDENTALE
Specialized in mechanics
École Doctorale des Sciences Pour l'Ingénieur

Submitted by
Nedeleg BIGI
Completed at ENSTA Bretagne, in the Dupuy de Lôme Research Institute (IRDL - CNRS FRE 3744)

Investigation of the dynamic motions and operability of a ship towed by kite

Evaluation des limites d'utilisation des navires tractés par kite par l'étude des mouvements de tenue à la mer et de manœuvrabilité

Ph. D. thesis examined on 15th December 2017

Committee members

Prof. Dominic A. Hudson
Shell Professor of Ship Safety and Efficiency at the University of Southampton / *Reviewer*

Prof. Carlos Guedes Soares
Distinguished professor at the Technical University of Lisbon / *Reviewer*

Prof. Sandrine Aubrun
Professor at Centrales Nantes, LHEEA / *Examiner*

Prof. Xavier Carton
Professor at University of Western Brittany / *Examiner*

Dr.-Ing. Richard Leloup
Research and Development Director at beyond the sea® / *Examiner*

Dr. Sime Malenica
Deputy Director of the Research Department of Bureau Veritas, France / *Examiner*

Dr. Serge Sutulo
Associate Professor at the Technical University of Lisbon / *Examiner*

Dr.-Ing. habil. Christian Jochum
Associate Professor, ENSTA Bretagne / *Primary supervisor*

Invited

Dr. Lorenzo Fagiano
Associate professor at Politecnico Di Milano

Ing. Marc Le Boulluec
Research Engineer at IFREMER

Dr. Eng. Gian Mauro Maneia
Senior researcher at Ce.S.I Centro Studi Industriali

Co-supervisors

Dr. Jean-Baptiste Leroux
Associate Professor, IRDL, ENSTA Bretagne

Dr. Alain Nême
Associate Professor, IRDL, ENSTA Bretagne

Dr. Kostia Roncin
Associate Professor, IRDL, ENSTA Bretagne

A mon père,

"La vraie générosité envers l'avenir consiste à tout donner au présent."
Albert Camus, *L'homme révolté*, 1951.

Remerciements

Sous l'apparence d'un travail individuel, l'exercice de thèse est un travail collectif à bien des égards et à ce titre, je remercie l'ensemble des personnes qui y ont contribué de près ou de loin.

Il me semble tout d'abord essentiel de remercier mon équipe de travail et notamment mon directeur de thèse et mes encadrants car ils ont été les instigateurs et les porteurs à l'ENSTA Bretagne du projet beyond the sea initié par Yves Parlier. Ainsi, je remercie Christian Jochum pour son énergie et enthousiasme. Je voudrais également souligner la bienveillance qu'il a eue à mon égard tout au long des trois ans. Je remercie Jean-Baptiste Leroux, Alain Nême et Kostia Roncin pour la pédagogie et la rigueur dont ils ont fait preuve pour m'aider à réaliser cette thèse.

Je remercie également mes collègues doctorants et ingénieurs de recherche de l'équipe beyond the sea: Morgann Behrel, Vincent Podeur, Antoine Maison, Chloé Duport et Alain de Solminihac. Leur curiosité et leur motivation ont été un véritable atout. Je peux dire que sans cette équipe de travail la tâche aurait été bien plus complexe !

Je voudrais aussi remercier tous mes autres collègues de l'ENSTA Bretagne, en particulier Antoine Morvan, Julien Le Clanche, Martin Monloubou, Guilhem Blès, Jean-Marc Laurens, Jean-Yves Pradillon et Yves-Marie Scolan.

Je remercie également les collègues de la société beyond the sea, Yves Parlier, Richard Leloup et Fabien Griffon avec qui il a été agréable d'échanger sur la thématique des navires tractés par kite.

Je souhaite remercier également mon comité de suivi de thèse Sime Malenica et Marc Le Boulluec pour leurs conseils avisés. Mes deux rapporteurs, Carlos Guedes Soares et Dominic Hudson, pour leur relecture détaillée du manuscrit. Je remercie également l'ensemble des membres du jury ainsi que les invités.

Ce manuscrit de thèse marque aussi la fin de mes études, c'est donc le moment d'exprimer ma gratitude envers tous ceux qui m'ont soutenu tout au long de mon parcours. Depuis le lycée, j'ai suivi un cursus aménagé à la pratique de la voile à haut niveau. Ce parcours m'a donnée les qualités humaines nécessaires à la réalisation d'une thèse. C'est donc un grand merci à mon coach René Baget (« faut rien lâcher ! »). C'est aussi un grand merci à Pierre Johannel proviseur du Lycée Kerichen en 2008 et Damien Coadour, enseignent

chercheur de l'ENSTA Bretagne et responsable formation au pôle Sciences Humaines et Sociales qui ont œuvrés à créer une convention inédite entre le pôle France voile de Brest, l'ENSTA Bretagne et les classes préparatoires aux grandes écoles du lycée Kerichen dont j'ai pu bénéficier et qui m'a indirectement permis de réaliser cette thèse.

Ce n'est qu'après avoir expliqué ce parcours sportif et scolaire atypique que je peux remercier pleinement Morgann Behrel ami depuis le lycée en classe sport-étude avec qui ensemble nous avons suivi le même parcours jusqu'à poursuivre un doctorat pour le même projet de recherche. Je ne saurais suffisamment remercier le soutien indéfectible qu'il m'a apporté tout au long de cette aventure.

Je tiens à remercier particulièrement ma sœur ainée qui m'a donné l'envie de suivre ses pas dans la recherche, ma mère qui m'a transmis sa curiosité et son goût de la découverte. Je veux aussi remercier mon petit frère qui m'a toujours soutenu.

Je souhaite remercier mes amis proches : ma colloc' Albane, Hugo, Yvan, mon équipage de J80, Fabrice Morin, Frédéric Hauville et Patrick Bot. Ils ont toujours été de bon conseil pour ma thèse et bien plus encore.

Enfin, je tiens également à exprimer ma gratitude à Aurélie, ma compagne, pour son soutien, sa disponibilité et sa patience en particulier lors de la période de rédaction.

Abstract

In order to reduce greenhouse gas emissions and shipping costs, the use of kites as an auxiliary propulsion device for ships is promising. In fact, compared to the use of classic sails, a kite does not reduce the pay load storage capacity and generates a greater towing force thanks to dynamic flights. Assuming that the interactions between a ship and a kite are negligible, the literature has shown by solving the mean equilibrium of the system that fuel savings are significant. These assumptions are strong since the kite induces ship motions and due to sea state the ship motion may change the kite flight. In order to estimate more accurately the performance and the operability of a kite-towed vessel, a dynamic modeling of the system is implemented.

A classical kite modeling is used. This model neglects the mass of the kite and assumes straight and inelastic tethers. These assumptions lead to a kinematic model depending on the lift coefficient and the aerodynamic lift to drag ration angle. A linear evolution of these aerodynamic coefficients as a function of the curvature of the flight path is proposed. In addition, by developing a quasi-analytical line model, it is shown that from 2 $m.s^{-1}$ of relative wind the straight tether assumption is reasonable. Based on the tether model, an analytical criterion assessing the minimum wind speed to enable a quasi-static kite flight is developed. In particular, it is shown that for a kite surfing kite, the minimum wind launch for quasi-static fly is 3.4 $m.s^{-1}$. In order to solve all the interaction terms between the kite and the ship, a time domaine seakeeping model based on the linearized ship equation of motion assuming a potential flow is developed. The convolution product of the impulse response of the ship is computed with state-space systems. This method has the advantage to run fast. However, since horizontal ship motions are not well represented by such theories, a coupling with a maneuverability model is presented. Comparisons to front sea basin tests and gyration and zigzagging tests show rather good results.

To study the interactions between the kite and the ship a monolithic coupling and a dissociated coupling are compared. The dissociated coupling neglects the influence of ship motions on the kite flight. In a calm water case, results obtained by the two types of coupling are very close. In regular waves, ship motions are dominated by the wave influence. Thus, a network of low frequency subharmonic appears in the kite excitation spectrum. The fundamental frequency of the subharmonic is given by the difference between the wave frequency and the frequency of the nearest kite excitation harmonic. When this difference is small enough, a lock-in phenomenon appears. This kite lock-in phenomenon is a benefit for the kite and the ship when the shift of the excitation harmonics corresponds to an increase. The kite towing is increased up to 34% and the kite efficiency is increased up to 4% compared to a calm water case. The roll amplitude is reduced by 20% compared to a flight configuration at the boundary of the kite lock-in phenomenon. This phenomenon as it is not visible with the dissociated approach shows the interest of a monolithic coupling. Furthermore, a course keeping stability study shows that the rudder needs to be actively controlled.

Résumé

Afin de réduire les émissions de gaz à effet de serre et le coût du transport maritime, l'utilisation des cerfs-volants comme système de propulsion auxiliaire des navires est prometteuse. Un cerf-volant réduit très peu la capacité d'emport et à surface égale permet en vol dynamique de générer une traction importante. En supposant que les interactions entre un navire et un cerf-volant sont négligeables, la littérature a montré en résolvant l'équilibre moyen du système que les économies de carburant pouvaient être significative. Ces hypothèses sont fortes car le cerf-volant impose des mouvements au navire qui lui même, en étant soumis aux vagues, peut modifier le vol du cerf-volant. Pour estimer plus précisément les performances et l'opérabilité d'un navire tracté par cerf-volant, une modélisation dynamique du système est alors mise en œuvre.

Une modélisation analytique de cerf-volant est utilisée. Ce modèle néglige la masse du cerf-volant et suppose que les lignes sont droites et indéformablee. Ces hypothèses conduisent à un modèle cinématique dépendant du coefficient de portance et de la finesse aérodynamique. Une évolution linéaire des coefficients aérodynamiques en fonction de la courbure de la trajectoire de vol est proposée. Par ailleurs, en développant un modèle quasi-analytique de ligne, il est montré qu'à partir de 2 $m.s^{-1}$ de vent relatif que l'hypothèse de ligne droite est raisonnable. En se basant sur un modèle de ligne, un critère analytique de vitesse de vent minimum permettant un vol quasi-statique est présenté. Dans le but de résoudre l'ensemble des termes d'interaction entre le cerf-volant et le navire, un modèle linéarisé de tenue à la mer temporelle est développé. Le produit de convolution de la réponse impulsionnelle du navire est calculé avec des systèmes d'états. Cette méthode à l'avantage d'être rapide à calculer. Cependant comme celle-ci représente mal les mouvements horizontaux des navires, le modèle développé est alors couplé à un modèle de manœuvrabilité.

Pour étudier les interactions entre le cerf-volant et le navire un couplage monolithique et un couplage dissocié sont comparés. Le couplage dissocié néglige l'influence des mouvements du navire sur le vol du cerf-volant. En cas de mer calme, les résultats obtenus par les deux types de couplage sont très proches. En cas de houle régulière les mouvements du navires sont principalement causés par la vague. Un réseau de sous-harmoniques basse fréquence apparait alors dans le spectre d'excitation du navire. La fréquence fondamentale des sous-harmoniques est donnée par la différence entre la fréquence de vague et la fréquence de l'harmonique la plus proche de l'excitation du kite. Quand cette différence est suffisamment petite, un phénomène d'accrochage apparait. Ce phénomène est bénéfique pour le cerf-volant et le navire quand le décalage des harmoniques d'excitation correspond à une augmentation. La traction du cerf-volant est augmentée jusqu'à 34% et l'efficacité du kite est augmenté jusqu' 4% par rapport au cas en mer calme. L'amplitude de roulis est diminuée de 20% par rapport à une configuration de vol en limite du phénomène d'accrochage. Ce phénomène n'est pas visible avec l'approche dissociée ce qui montre l'intérêt d'un couplage monolithique. Par ailleurs, une étude de la stabilité de route montre qu'il est nécessaire de contrôler activement le safran.

Contents

List of Figures

List of Tables

Nomenclature

Abbreviations

ADEME	French Environment and Energy Management Agency	[–]
CFD	Computational Fluid Dynamic	[–]
CO_2	Carbon Dioxide	[–]
dof	Degree(s) of freedom	[–]
ECA	Emission Control Area	[–]
ECMWF	European Center for Medium range Weather Forecast	[–]
EFD	Experimental Fluid Dynamic	[–]
FE	Finite Element	[–]
FEI	Fuel-Efficiency Improvement	[–]
FSI	Fluid Structure Interaction	[–]
JMUC	Japan Marine United Corporation	[–]
KCS	Kriso Container Ship	[–]
LNG	Liquefied Natural Gas	[–]
MMG	Mathematical Modeling Group	[–]
PID	Proportional Integral Derivative controller	[–]
RCP	Representative Concentration Pathways	[$W.m^{-2}$]
SSP	Shared Socioeconomic Pathway	[–]
SSPA	Swedish Ship Testing Institute	[–]
SVA	Potsdam Schiffbau-Versuchsanstalt GmbH, Germany	[–]
TEU	Twenty-foot equivalent unit	[–]

UHMWPE	Ultra-high-molecular-weight polyethylene	[–]

Reference frames

$\mathbf{c}$	Current reference frame $\left(O_c, \underline{x}_c, \underline{y}_c, \underline{z}_c\right)$	[m,–]
$\mathbf{h}$	Seakeeping reference frame $\left(O_h, \underline{x}_h, \underline{y}_h, \underline{z}_h\right)$	[m,–]
$\mathbf{k}$	Kite reference frame $\left(K, \underline{x}_k, \underline{y}_k, \underline{z}_k\right)$	[m,–]
$\mathbf{kn}$	Kite reference frame $\left(K, \underline{x}_{kn}, \underline{y}_{kn}, \underline{z}_{kn}\right)$	[m,–]
$\mathbf{n}$	Earth fixed frame $\left(O_n, \underline{x}_n, \underline{y}_n, \underline{z}_n\right)$	[m,–]
$\mathbf{rw}_{xy}$	Relative wind basis with respect to $\underline{U}_{rw,xy}$; $\left(\underline{x}_{rw,xy}, \underline{y}_{rw,xy}, \underline{z}_{rw,xy}\right)$	[–]
$\mathbf{s}$	Ship fixed frame $\left(O_s, \underline{x}_s, \underline{y}_s, \underline{z}_s\right)$	[m,–]
$\mathbf{t}$	Tether reference frame $(A, \underline{x}_t, \underline{t}_k, \underline{z}_t)$	[m,–]
$\mathbf{tw}$	True wind basis $\left(\underline{x}_{tw}, \underline{y}_{tw}, \underline{z}_{tw}\right)$	[–]

Greek symbols

α_r	Rudder inflow angle of attack	[rad]
α_t	Tether angle of attack	[rad]
β_s	Ship drift angle defined as $\beta_s = -\arctan\frac{v_s}{u_s}$	[rad]
β_w	Wave direction with respect to ship heading	[rad]
$\dot{\delta}_r$	Rudder maximum turning rate	[rad.s^{-1}]
$\Delta\phi_8$	Azimuth amplitude of the kite trajectory for $\chi_8 = 0$	[rad]
δ_r	Rudder angle	[rad]
Δ_s	Ship displacement mass	[kg]
$\Delta\theta_8$	Elevation amplitude of the kite trajectory for $\chi_8 = 0$	[rad]
ϵ_w	random initial phase of a wave	[rad]

ϵ_0	Kite lift to drag ratio angle with a zero time derivative of the heading	[rad]
ϵ_k	Kite lift to drag ratio angle	[rad]
η_k	Kite power saving ratio	[–]
η_{kf}	Kite fuel saving ratio	[–]
η_p	Kite profit ratio	[–]
η_x	Kite efficiency	[–]
γ_r	Rudder flow rectification factor	[–]
κ_ϵ	Coefficient of the linear law of the kite lift to drag ratio angle with respect to the time derivative of the heading	[–]
κ_l	Coefficient of the linear law of the kite lift coefficient with respect to the time derivative of the heading	[–]
λ_r	Rudder aspect ratio	[–]
∇_s	Ship displacement volume	[m^3]
ω	Angular frequency	[rad.s^{-1}]
ω_e	Wave frequency of encounter	[rad.s^{-1}]
ω_{ki}	Angular frequency of the principal kite excitation harmonic $i \in \mathbb{N}^{+*}$	[rad.s^{-1}]
$\omega_{ki}^{'}$	Angular frequency of the kite excitation subharmonics $i \in \mathbb{N}^{+*}$	[rad.s^{-1}]
ω_{roll}	Natural roll frequency of the ship	[rad.s^{-1}]
ϕ_8	Azimuth amplitude of the center of the kite trajectory	[rad]
ϕ_C	Azimuth of a point of the trajectory $\mathscr{C}$	[–]
ϕ_k	Azimuth of the kite position with respect to the $\mathbf{rw}_k a$ frame	[rad]
ϕ_w	reflection phase change of the Froude-Krylov and diffraction force with respect to the free surface elevation	[rad]
Ψ_s	Desired ship heading	[rad]
ψ_w	Wave direction with respect to $\underline{x}_n$	[rad]
ρ_a	Air density	[kg.m^{-3}]

ρ_w	Water density	[kg.m^{-3}]
σ_d	Kite aerodynamic pressure of design	[N.m^{-2}]
σ_k	Mean aerodynamic pressure of the kite overs its surface	[N.m^{-2}]
θ_8	Elevation amplitude of the center of the kite trajectory	[rad]
θ_C	Elevation of a point of the trajectory $\mathscr{C}$	[–]
θ_k	Elevation of the kite position with respect to the $\mathbf{rw}_k a$ frame	[rad]
$\underline{\xi}$	Generalized ship position with respect to the $\mathbf{h}$ frame expressed into $\mathbf{h}$	[m,rad]

Roman symbols

A	Tether attachment point on the ship, $\underline{O_s A} = [a_x, a_y, a_z]^T$	[m]
A_f	Frontal windage area	[m^2]
A_k	Kite area	[m^2]
A_l	Lateral windage area	[m^2]
$\underline{\underline{A}}$	Generalized added mass matrix with respect to the $\mathbf{s}$ frame	[kg,kg.m,kg.m^2]
$\underline{\underline{A}}^*$	Generalized added mass matrix with respect to the $\mathbf{h}$ frame	[kg,kg.m,kg.m^2]
$\underline{\underline{\tilde{A}}}$	Generalized added mass matrix at infinit frequency with respect to the $\mathbf{s}$ frame	[kg,kg.m,kg.m^2]
A_r	Rudder area	[m^2]
$\mathcal{A}$	Fourier transform amplitude	[–]
$\underline{\underline{B}}^*_\phi$	Additional generalized damping matrix acounting for roll motion with respect to the $\mathbf{h}$ frame	[kg.s^{-1},kg.m.s^{-1},kg.m^2.s^{-1}]
$\underline{\underline{B}}$	Generalized damping matrix with respect to the $\mathbf{s}$ frame	[kg.s^{-1},kg.m.s^{-1},kg.m^2.s^{-1}]
$\underline{\underline{B}}_\phi$	Additional generalized damping matrix acounting for roll motion with respect to the $\mathbf{s}$ frame	[kg.s^{-1},kg.m.s^{-1},kg.m^2.s^{-1}]

$\underline{\underline{B}}^*$	Generalized damping matrix with respect to the $\mathbf{h}$ frame	[kg.s^{-1},kg.m.s^{-1},kg.m^2.s^{-1}]
$\underline{\underline{\tilde{B}}}$	Generalized damping matrix at infinit frequency with respect to the $\mathbf{s}$ frame	[kg.s^{-1},kg.m.s^{-1},kg.m^2.s^{-1}]
B_s	Ship beam	[m]
$\mathscr{C}$	Kite trajectory	[–]
C_8	Center of the kite trajectory	[m]
C_b	Ship block coefficient	[–]
C_e	Kite effective saving	[$]
$C_{i,t}$	Shipping income per unit of time	[$.s^{-1}]
C_k	Kite retail cost	[$]
C_{l0}	Kite lift coefficient with a zero time derivative of the heading	[–]
C_λ	Closest point of the kite trajectory $\mathscr{C}$ at the curvilinear abcissa λ	[m]
C_{lk}	Kite lift coefficient	[–]
$\underline{\underline{C}}$	Generalized restoring matrix with respect to the $\mathbf{s}$ frame	[kg.s^{-2},kg.m.s^{-2},kg.m^2.s^{-2}]
$\underline{\underline{C}}^*$	Generalized restoring matrix with respect to the $\mathbf{h}$ frame	[kg.s^{-2},kg.m.s^{-2},kg.m^2.s^{-2}]
$\tilde{C}_p$	Shipping profit with kite	[$]
C_p	Shipping profit without kite	[$]
C_{sa}	Kite fuel saving	[$]
$C_{s,t}$	Shipping cost per unit of time	[$.s^{-1}]
C_t	Tether curve	[m]
$\underline{D}_k$	Kite aerodynamic drag	[N]
D_p	Propeller diameter	[m]
d_t	Tether diameter	[m]
E_i	Amplitude of the ith componant of the Froud-Krilov and diffraction force	[N,N.m^{-1}]
$\underline{F}^*$	Sum of the acting on the ship with respect to the $\mathbf{h}$ frame	[N,N.m]
$\underline{\bar{F}}^*$	Mean force acting on the ship	[N,N.m]

$\mathfrak{F}_{LP}$	Low pass filter function	[–]
$\underline{g}$	Acceleration of gravity	[m.s^{-2}]
G	Ship center of gravity	[m]
GM_t	Ship metacentric height	[m]
H_{ij}	Rational transfer function fitting the retardation matrix data K_{ij}	[kg.s^{-2},kg.m.s^{-2},kg.m^2.s^{-2}]
H_m	Mean height of the windage lateral surface with respect to the free surface	[m]
H_m	Mean height of the windage lateral surface	[m]
J	Propeller advance ratio	[–]
K	Kite position	[m]
$\underline{\underline{K}}$	Generalized retardation matrix with respect to the $\mathbf{s}$ frame	[kg.s^{-2},kg.m.s^{-2},kg.m^2.s^{-2}]
K_Q	Propeller torque factor	[–]
K_T	Propeller thrust factor	[–]
k_w	Wave number	[m^{-1}]
$\underline{L_k}$	Kite aerodynamic lift	[N]
L_{oa}	Overall ship length	[m]
L_{oa}	Ship length overall	[m]
L_{pp}	Ship length between perpendiculars	[m]
L_t	Tether length	[m]
l_z	Vertical distance of O_s with respect to the baseline	[m]
l_z	Vertical position of O_s with respect to the baseline	[m]
LCB	Longitudinal position of center of buyancy	[m]
M_k	Kite mass	[Kg]
$\underline{\underline{M^*_S}}$	Generalized ship mass matrix with respect to the $\mathbf{h}$ frame	[kg,kg.m,kg.m^2]
m_t	Tether mass per unit length	[Kg.m^{-1}]
$\underline{\underline{MA}}$	Sum of the generalized added mass matrix and ship mass matrix with respect to the $\mathbf{s}$ frame	[kg,kg.m,kg.m^2]

$\underline{\mu}$	Fluid memory forces with respect to the $\mathbf{s}$ frame	[N,N.m]
n_p	Propeller rotation speed	[rps]
n_v	Wind gradient power law parameter	[–]
O_{wa}	Intersection of the ship symmetry plane, the midship section and the free surface	[–]
$\underline{q}$	Total tether load per unit length	[N.m^{-1}]
$\underline{q}_g$	Tether gravity load per unit length	[N.m^{-1}]
$\underline{q}_w$	Tether aerodynamic load per unit length	[N.m^{-1}]
$R_{\mathcal{C}}$	Radius of curvature of the kite trajectory	[m]
R_e	Reynolds number	[–]
$\underline{\underline{R}}^{\mathbf{s}}_{\mathbf{c}}$	Transformation matrix of the Euler's angle time derivatives to the ship turning rate	[–]
$\underline{S}$	Generalized position vector of the ship with respect to the $\mathbf{c}$ frame expressed in the $\mathbf{c}$ frame, $\underline{S} = [s_x,\ s_y,\ s_z,\ \phi_s,\ \theta_s,\ \psi_s]^T$	[m, rad]
s	Tether curvilinear abscissa	[m]
s_h	Height of the windage lateral plane centroid	[m]
s_l	Longitudinal position of the windage lateral-plane centroid from the midship section	[m]
S_w	Wave spectrum	[s.m^2]
s_w	Wave steepness	[–]
$\underline{T}$	Tension along the tether	[N]
t_d	Kite lifetime	[s]
$\underline{T}_k$	Tether force $\in \mathbb{R}^3$	[N]
$\underline{t}_\lambda$	Tangent unit vector to the trajectory $\mathscr{C}$ at the curvilinear abcissa λ	[–]
T_m	Ship draft at midship	[m]
$\underline{\underline{T}}^{\mathbf{c}}_{\mathbf{s}}$	Direct cosine matrix from the $\mathbf{s}$ frame to the $\mathbf{c}$ frame	[–]
t_p	Propeller thrust deduction factor	[–]
$\underline{U}_a$	Tether attachment point velocity	[m.s^{-1}]
$\underline{U}_c$	Current velocity	[m.s^{-1}]

U_d	Desired ship velocity	[rad]
$\underline{U}_h$	Mean ship forward speed	[m.s^{-1}]
$\underline{U}_k$	The relative velocity of the kite K with respect to the tether attachment point A	[m.s^{-1}]
$\underline{U}_{ref}$	True wind speed at the altitude of measurment z_{ref}	[m.s^{-1}]
$\underline{U}_{rw,xy}$	At a point X, the relative wind speed referring to a position on the ship Y	[m.s^{-1}]
$\underline{U}_s$	Velocity vector of the ship at O_s with respect to the $\mathbf{c}$ frame expressed in the $\mathbf{s}$ frame	[m.s^{-1}]
$\underline{U}_{tw}$	True wind speed	[m.s^{-1}]
$\underline{V}_s$	Generalized velocity vector of the ship at O_s with respect to the $\mathbf{c}$ frame expressed in the $\mathbf{s}$ frame	[m.s^{-1}, rad.s^{-1}]
w	Wake fraction	[-]
$\underline{W}_k$	Kite weight	[N]
$\underline{x}_{vk}$	Kite velocity direction	[–]
z_{ref}	Altitude of wind measurement	[m]

Reference frames and parameterizations

In this thesis, if no simplifications are mentioned, following notations hold by default:

- $\underline{a}$: represents a vector.
- $\underline{\underline{a}}$: represents a matrix.
- $\mathbf{a}$: represents an orthogonal frame. The origin of the frame is denoted O_a, and each vector are denoted by $\underline{x}_a$, $\underline{y}_a$ and $\underline{z}_a$.
- $\underline{a}^{(\mathbf{b})}$: denotes the vector $\underline{a}$ expressed in the frame $\mathbf{b}$. In this case $\underline{a}^{(\mathbf{b})} \in \mathbb{R}^3$.
- $\underline{\underline{T}}_{\mathbf{a}}^{\mathbf{b}}$: represents the square transformation matrix from the $\mathbf{a}$ frame to the $\mathbf{b}$ frame. Consequently, any vector $\underline{n}^{(\mathbf{a})}$ expressed in $\mathbf{a}$ can be transformed in $\mathbf{b}$ as follows: $\underline{n}^{(\mathbf{b})} = \underline{\underline{T}}_{\mathbf{a}}^{\mathbf{b}} \underline{n}^{(\mathbf{a})}$. Moreover, $\underline{\underline{T}}_{\mathbf{a}}^{\mathbf{b}}$ is orthogonal, consequently $\left(\underline{\underline{T}}_{\mathbf{a}}^{\mathbf{b}}\right)^T = \left(\underline{\underline{T}}_{\mathbf{a}}^{\mathbf{b}}\right)^{-1} = \underline{\underline{T}}_{\mathbf{b}}^{\mathbf{a}}$.
- $\underline{a} \cdot \underline{b}$: denotes the scalar product.
- $\times$: denotes the cross product.
- $\circ$: denotes the Hadamard product.
- Two matrices side by side means a matrix product
- $\dot{x}$: denotes the time derivative of the scalar x.
- $\dot{\underline{a}}$: denotes the time derivative of $\underline{a}$. If it is not precised, the time derivative is performed with respect to a Galilean frame.

Earth fixed frame: $\mathbf{n}$-frame

The mathematical developments assume that the orthogonal reference frame $\mathbf{n}$ is Galilean. $\mathbf{n}$ is centered on O_n, somewhere on the mean sea level surface. The three unit vectors of $\mathbf{n}$

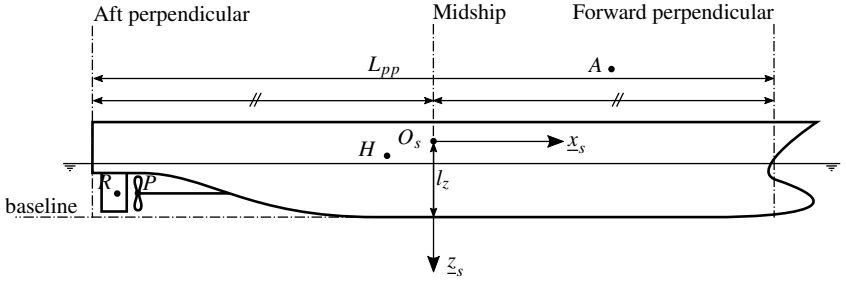

Figure 1.: Ship reference frame $\mathbf{s}$ and parameterization

are denoted by $\underline{x}_n$, $\underline{y}_n$ and $\underline{z}_n$. $\underline{z}_n$ is pointing downward with respect to the earth gravity. Consequently, the earth gravity $\underline{g}$ can be expressed as follows:

$$\underline{g} = g\underline{z}_n, \tag{1}$$

where $g = 9.81$ m.s^{-2}. Moreover, any other frame experiencing a rectilinear and uniform motion with respect to the $\mathbf{n}$ is assumed to be Galilean as well.

Current reference frame: c-frame

The current reference $\mathbf{c}$ centered on O_c is translating at the constant velocity $\underline{U}_c$. The three unit vectors of $\mathbf{c}$ are denoted $\underline{x}_c$, $\underline{y}_c$ and $\underline{z}_c$. Consequently, at any time we have:

$$\left[\underline{x}_c, \underline{y}_c, \underline{z}_c\right] = \left[\underline{x}_n, \underline{y}_n, \underline{z}_n\right]. \tag{2}$$

The current velocity is assumed to be horizontal, thus we have $\underline{U}_c \cdot \underline{z}_c = 0$.

Ship reference frame: s-frame

$\mathbf{s}$ is the ship fixed frame, $\underline{x}_s$ is pointing forward in the ship symmetry plane, $\underline{z}_s$ is pointing downward and $\underline{y}_s$ completes the direct orthogonal basis. $\underline{z}_s$ is normal to the free surface when the ship is at the hydrostatic equilibrium. The origin of $\mathbf{s}$ denoted by O_s is in the ship symmetry plane at mid-ship and at a vertical distance up to the baseline l_z. The mid-ship is a plane normal to $\underline{x}_s$ positioned at the half distance between aft perpendicular and the forward perpendicular. The aft perpendicular is normal to $\underline{x}_s$ at the transom. The forward perpendicular is the intersection of the stern with the free surface when the ship is at the hydrostatic equilibrium. Figure 1 illustrates the ship reference frame.

The generalized position vector of the ship denoted by $\underline{S} = [s_x,\ s_y,\ s_z,\ \phi_s,\ \theta_s,\ \psi_s]^T_{\mathbf{c}}$ is the assembly of the position of O_s and the ship Euler's angles with respect to the $\mathbf{c}$ frame. The generalized ship velocity at O_s expressed in $\mathbf{s}$ with respect to the $\mathbf{c}$ frame is denoted by $\underline{V}_s = [u_s,\ v_s,\ w_s,\ p_s,\ q_s,\ r_s]^T$, where the first three components are the linear velocities $\underline{U}_s^{(\mathbf{s})}$ and the last three components are the turning rates $\underline{\Omega}^{(\mathbf{s})}_{\mathbf{s/c}}$.

The transformation of a vector expressed in the $\mathbf{s}$ frame denoted by $\underline{n}^{(\mathbf{s})}$ can be expressed is the $\mathbf{c}$ frame with $\underline{n}^{(\mathbf{c})} = \underline{\underline{T}}^{\mathbf{c}}_{\mathbf{s}}\underline{n}^{(\mathbf{s})}$, where $\underline{\underline{T}}^{\mathbf{c}}_{\mathbf{s}}$ is the direct cosine matrix (cf. Eq. (3)).

$$\underline{\underline{T}}^{\mathbf{c}}_{\mathbf{s}} = \begin{bmatrix} \mathrm{c}\psi_s\mathrm{c}\theta_s & -\mathrm{s}\psi_s\mathrm{c}\phi_s + \mathrm{c}\psi_s\mathrm{s}\theta_s\mathrm{s}\phi_s & \mathrm{s}\psi_s\mathrm{s}\phi_s + \mathrm{c}\psi_s\mathrm{c}\phi_s\mathrm{s}\theta_s \\ \mathrm{s}\psi_s\mathrm{c}\theta_s & \mathrm{c}\psi_s\mathrm{c}\phi_s + \mathrm{s}\phi_s\mathrm{s}\theta_s\mathrm{s}\psi_s & -\mathrm{c}\psi_s\mathrm{s}\phi_s + \mathrm{s}\theta_s\mathrm{s}\psi_s\mathrm{c}\phi_s \\ -\mathrm{s}\theta_s & \mathrm{c}\theta_s\mathrm{s}\phi_s & \mathrm{c}\theta_s\mathrm{c}\phi_s \end{bmatrix} \tag{3}$$

where, c and s denote the cosine and the sine functions. The turning rates and the time derivatives of the ship Euler's angles satisfy the following relationship:

$$\begin{bmatrix} p_s \\ q_s \\ r_s \end{bmatrix} = \underline{\underline{R}}^{\mathbf{s}}_{\mathbf{c}} \begin{bmatrix} \dot{\phi}_s \\ \dot{\theta}_s \\ \dot{\psi}_s \end{bmatrix}, \tag{4}$$

where,

$$\underline{\underline{R}}^{\mathbf{s}}_{\mathbf{c}} = \begin{bmatrix} 1 & 0 & -\mathrm{s}\theta_s \\ 0 & \mathrm{c}\phi_s & \mathrm{c}\theta_s\mathrm{s}\phi_s \\ 0 & -\mathrm{s}\phi_s & \mathrm{c}\phi_s\mathrm{c}\theta_s \end{bmatrix}. \tag{5}$$

The point A is the tether attachment point. The position of A with respect to O_s is $\underline{O_sA} = \left[a_x^{(\mathbf{s})}, a_y^{(\mathbf{s})}, a_z^{(\mathbf{s})}\right]^T$ expressed in $\mathbf{s}$. R denotes the rudder position, $\underline{O_sR} = \left[r_x^{(\mathbf{s})}, r_y^{(\mathbf{s})}, r_z^{(\mathbf{s})}\right]^T$ expressed in $\mathbf{s}$. P denotes the propeller position, $\underline{O_sP} = \left[p_x^{(\mathbf{s})}, p_y^{(\mathbf{s})}, p_z^{(\mathbf{s})}\right]^T$ expressed in $\mathbf{s}$

Seakeeping reference frame: $\mathbf{h}$-frame

The seakeeping reference frame, $\mathbf{h} = \left(O_h,\ \underline{x}_h,\ \underline{y}_h,\ \underline{z}_h\right)$, is centered on O_h. This frame is translating at the constant mean ship forward speed U_h and the following relationship holds at any time:

$$\underline{z}_h = \underline{z}_c \tag{6}$$

At the reference ship position, O_h coincides with a point H fixed to the ship (Fig. 1). The position of H is defined with respect to O_s in the ship reference frame as follows:

$$\underline{O_s H} = [h_x,\ 0,\ h_z]^T \tag{7}$$

At the mean ship heading in the reference position, $\underline{x}_h = \underline{x}_s$.

Wind reference frames

tw-frame

$\mathbf{tw}$ denotes the true wind basis. In this study the true wind speed is assumed to be horizontal, consequently $\underline{z}_n = \underline{z}_{tw}$ holds. The true wind speed is orientated by $\underline{x}_{tw} = \frac{\underline{U}_{tw}}{\|\underline{U}_{tw}\|}$ and $\underline{y}_{tw}$ completes the orthogonal basis. The true wind velocity $\underline{U}_{tw}$ may depend on the position within the wind field and notably due to the wind friction with the free surface. However, in this thesis, the true wind speed is assumed to vary only with the altitude with respect to the $\mathbf{n}$ frame in terms of magnitude. Therefore, the true wind direction is independent of the altitude and the associated $\mathbf{tw}$ frame is constant with the altitude. Assuming the true wind direction $\underline{x}_{tw}$ is equal to $\underline{x}_n$ or $\underline{x}_n$, the true wind angle β_{tw} is defined as follows:

$$\beta_{tw} = \pi - \psi_s \tag{8}$$

rw-frame

The relative wind speed is a composition of the true wind velocity and the ship speed with respect to the current frame $\mathbf{c}$. Consequently, the relative wind speed depends on a position within the wind field and on a position on the ship. At a point X, the relative wind speed referring to a position on the ship Y can be written as follows:

$$\underline{U}_{rw}\left(X, Y\right) = \underline{U}_{tw}\left(X\right) - \underline{U}_y - \underline{U}_c, \tag{9}$$

where $\underline{U}_y$ denotes the velocity of the point Y fixed to the ship with respect to the $\mathbf{c}$ frame. The notation of $\underline{U}_{rw}\left(X, Y\right)$ can be simplified by $\underline{U}_{rw,xy}$. The relative wind basis is denoted $\mathbf{rw}_{xy}$. Since $\underline{U}_y$ is not necessarily horizontal, $\underline{z}_{rw,y}$ can be different from $\underline{z}_n$, the orthogonal basis of the $\mathbf{rw}_{xy}$ frame is defined as follows: $\underline{x}_{rw,xy} = \frac{\underline{U}_{rw,xy}}{\left\|\underline{U}_{rw,xy}\right\|}$, $\underline{y}_{rw,xy} = \frac{\underline{z}_n \times \underline{x}_{rw,xy}}{\left\|\underline{z}_n \times \underline{x}_{rw,xy}\right\|}$ and $\underline{z}_{rw,xy} = \underline{x}_{rw,xy} \times \underline{y}_{rw,xy}$.

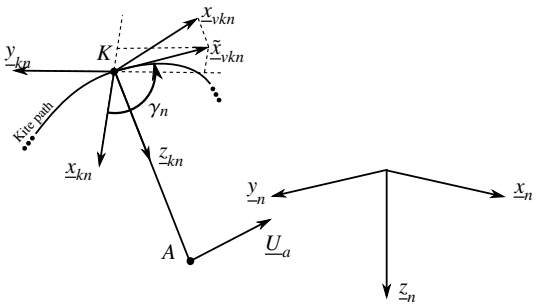

Figure 2.: Schema of the kite reference frame **kn**

The apparent wind speed $\underline{U}_{aw}$ is the wind speed relative to the kite:

$$\underline{U}_{aw} = \underline{U}_{tw}(K) - \underline{U}_a - \underline{U}_c - \underline{U}_k \tag{10}$$

where, $\underline{U}_a$ is the velocity of the tether attachment point on the ship and $\underline{U}_k$ is the relative velocity of the kite K with respect to A.

Kite reference frame: kn-frame

kn is a kite reference frame (Fig. 2) centered on K with $\underline{z}_{kn} = \frac{\underline{AK}}{\|\underline{AK}\|}$, $\underline{y}_{kn} = \frac{\underline{z}_{kn} \times \underline{z}_n}{\|\underline{z}_{kn} \times \underline{z}_n\|}$ and $\underline{x}_{kn} = \underline{y}_{kn} \times \underline{z}_{kn}$. The direction of the velocity K with respect to O_n is denoted by $\underline{x}_{vkn}$. The projection of $\underline{x}_{vkn}$ on the plane $\left(\underline{x}_{kn}, \underline{y}_{kn}\right)$ is denoted by $\tilde{\underline{x}}_{vkn}$. The angle of $\tilde{\underline{x}}_{vkn}$ with respect to $\underline{x}_{kn}$ is denoted byγ_n.

k is a kite reference frame (Fig. 3) centered on K and $\underline{z}_k = \frac{\underline{AK}}{\|\underline{AK}\|}$, $\underline{y}_k = \frac{\underline{z}_k \times \underline{z}_{rw,ka}}{\left\|\underline{z}_k \times \underline{z}_{rw,ka}\right\|}$ and $\underline{x}_k = \underline{y}_k \times \underline{z}_k$. The kite velocity is directed by $\underline{x}_{vk}$. The kite elevation angle is given by:

$$\theta_k = \frac{\pi}{2} - \arccos\left(\underline{z}_k \cdot \underline{z}_{rw,ka}\right) \tag{11}$$

The kite azimuth angle is defined as follows:

$$\phi_k = \arccos\left(\underline{y}_k \cdot \underline{y}_{rw,ka}\right) \tag{12}$$

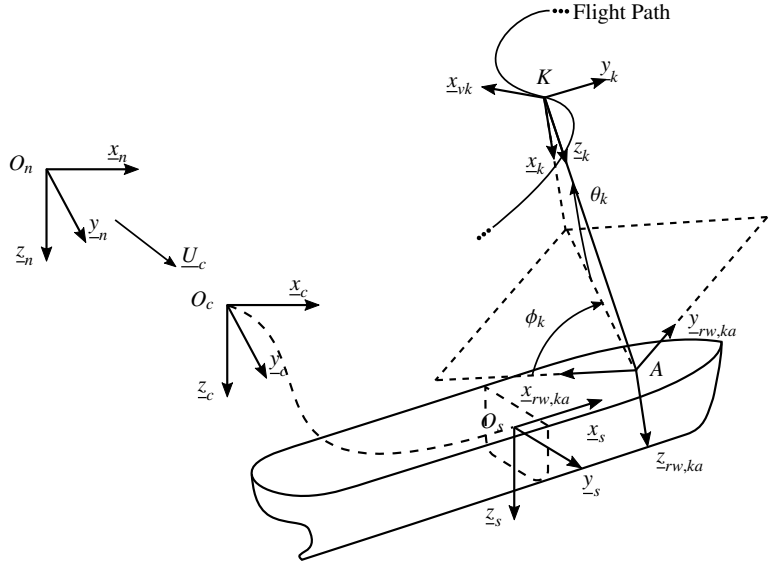

Figure 3.: Schema of the kite reference frame **k** and kite azimuth angle ϕ_k and elevation angle θ_k. This schema summarized the main coordinates systems.

Part I.

Introduction

1. Context

1.1. Preliminaries

To reduce the carbon footprint and the fuel consumption, the beyond the sea® project attempts to set up kites on commercial ships as an auxiliary propulsion device for fuel savings.

The concept was first introduced by Pocock (1827) to tow ships and buggys. Then, this concept of kite towing of ship was revisited for pleasure purposes by a group of four friends from United Kingdom and notably by Ian Day and Martin Rayment with the Jacob's Ladder project[1] in 1978. They started the project setting up a ram air kite called at this time a "flexifoil". In order to increase the power they added kites to form a stack. Then, they tried the concept on different catamaran boats to increase the speed. In 1982, in Portland UK at the Speed Week event, on a 30 ft hull, they performed their best speed, 25 knots. Figure 1.1b is picture of Ian Day and Martin Rayment during their record. Figure 1.1a shows how the launching phase can be sensitive.

(a) Launching phase

(b) Speed record at Portland during the Speed Week in 1982: 25 knots

Figure 1.1.: The first project of ship towed by kite: the Jacob's Ladder project

In the literature, the concept of kite towing was introduced by Duckworth (1983) and Wellicome and Wilkinson (1984). Duckworth (1983) argued that the installation of a kite on ship requires less modification than for a classical rig, and that a kite can be recovered in case

[1] http://www.panduj.plus.com/jladder/jl.htm

of storm insuring the ship safety. This study was focused on the use of axi-symmetric stable parachutes. Consequently, the operabilty of the kite was focused on downwind sailing only. Latter, Wellicome and Wilkinson (1984) performed a theoretical study about kite and introduced the so-called zero-mass kite model. In (Wellicome, 1985), Wellicome provides an analysis of the performance of different wind devices, such as conventional soft sail rig, Prossl rig, rigid wings and static kite classified into the passive device category, and flettner rotor, wind turbine and active maneuvered kite into the active category. His study leads to the conclusion that the kite is one of the best candidate. The benefits of a kite can be listed as follows:

- For a refitted ship, a kite requires less general arrangement modifications than a classical rig.
- Since the tether attachment point is at the deck level, the mean heeling angle induced by a kite is small compared to a classical rig.
- With an active maneuvered kite performing a dynamic flight, the towing forces are greater than the force developed by a classical rig of the same area (Leloup et al., 2014).
- Depending on the tether length, the kite can catch faster winds thanks to the wind gradient.

Fuel saving predictions have been carried out in the literature by Naaijen et al. (2006), Leloup et al. (2016) and Podeur et al. (2016). They all predicts significant fuel saving predictions. The most realistic fuel predictions has been performed by Podeur et al. (2016) on a 2200 TEU container ship towed by a kite of 800 m^2. Indeed, in that case using the 4 years weather database provided by the European Center for Medium range Weather Forecast (ECMWF), the mean fuel saving is 12.1 % for a ship forward speed of 8.2 $m.s^{-1}$ and 6.7 % for a ship forward speed of 9.8 $m.s^{-1}$.

Figure 1.2.: A Skysails kite of 320 m^2 on a 90 m long cargo ship

Despite all the advantages offer by a kite, quite few ships have been equipped with a kite. The most advanced project dedicated to the use of kites as an auxiliary propulsion device

for merchant ship was led by the Skysail® company[2] (cf. Fig. 1.2). In 2008, this company equipped a bulk carrier of 90 m long with a ram air kite of 320 m^2 (Erhard and Strauch, 2012). Actually, two experimental vessels promoting the energy transition are equipped with a kite. The first vessel is the Race For Water[3] vessel (cf. Fig. 1.3a) launched in spring 2017. The second vessel is Energy Observer[4], launched during the summer 2017 and is equipped with a kite provided by the beyond the sea® project (cf. Fig. 1.3b).

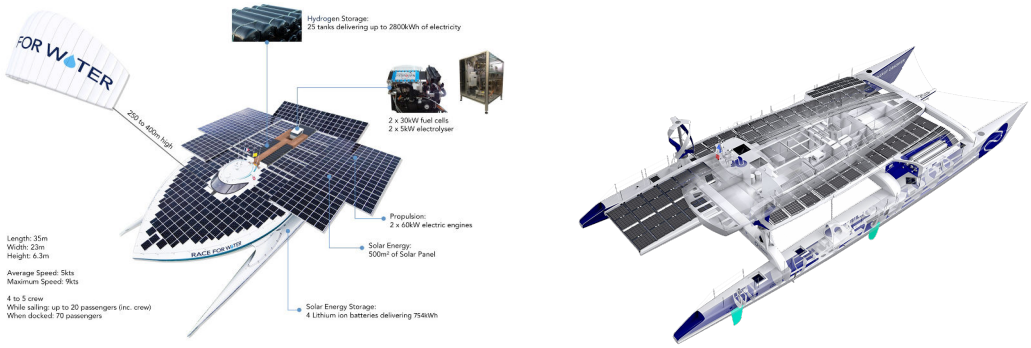

(a) Vessel of the Race For Water project

(b) Vessel of the Energy Observer project

Figure 1.3.: Experimental vessels equipped with a kite

1.2. Ecological interests

The seaway is one of the most efficient way of transport in terms of CO_2 emmissions. Figure 1.4 shows that a ship emits regarding the payload less than 10% of CO_2 emitted by a truck and 2% of CO_2 emitted by an airplane. According to (Smith et al., 2014), the overall maritime emission of CO_2 per year over the period 2007-2012 is 810 million tonnes, which represents 2.6% of the global emission. For a ship, Ronen (2011) shows that the fuel consumption may represent more than 75% of the operating costs. In addition, the CO_2 emissions could be considered as proportional to the fuel consumption. An estimation of the ratio of the fuel consumption and CO_2 emissions can be found in Corbett et al. (2009). Consequently, the ecological and economical interests are joint.

According to the International Maritime Organisation (Smith et al., 2014), CO_2 emissions could increase drastically due to an important raise of gross domestic products. Indeed, depending on the socioeconomic scenario considered in Smith et al. (2014), the gross domestic production should be multiplied between three and seven. An important effort should be performed by the shipping industry to improve the fuel-efficiency of the world fleet. The effect of improving the fuel efficiency is investigated in (Smith et al., 2014). 16 scenarios

[2] http://www.skysails.info
[3] www.raceforwater.com
[4] http://www.energy-observer.org/

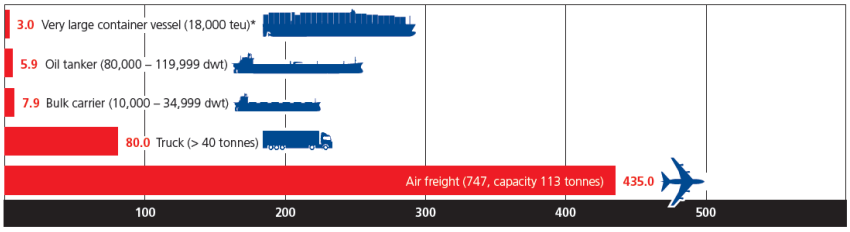

Figure 1.4.: Typical CO_2 emission in grams per ton kilometers for different modes of transport; Source: (Buhaug et al., 2009)

for the period 2012-2050 were considered. These scenarios assume different input parameters such as the Representative Concentration Pathways (RCP, see (Moss et al., 2008)), the Shared Socioeconomic Pathway (SSP, see (Ebi et al., 2014)), a Fuel-Efficiency Improvement (FEI) compared to fleet average in 2012, the roll out of Emission Control Area (ECA) and the use of Liquefied Natural Gas (LNG) engine.

RCP is a resultant radiative forcing in $W.m^{-2}$ due to greenhouse gas. For instance, an RCP of 2.6 $W.m^{-2}$ corresponds to a raise of the mean temperature on earth of 1.5° and is the most optimistic scenario. The most pessimistic RCP considered is 8.5 $W.m^{-2}$. According to a RCP level, Smith et al. extrapolated the oil and coal demand. Five SSP were considered from 1 to 5, respectively named *sustainability*, *middle of the road*, *fragmentation*, *inequality* and *conventional development*. A SSP is a qualitative parameter. A narrative description of different SSP can be found in (Kriegler et al., 2012; Smith et al., 2014). For instance, the SSP *middle of the road* corresponds to "*A world that sees the trends typical of recent decades continuing, with some progress towards achieving development goals. Dependency on fossil fuels is slowly decreasing. Development of low-income countries proceeds unevenly*." The full method of combining RCP and SSP is detailed in (Smith et al., 2014) according to the method proposed by Kriegler et al. (2012).

Here only 4 scenarios are reported. For each scenario, the development of the LNG and ECA are not considered. The best and the worst combination of RCP and SSP are considered, respectively RCP2.6 with SSP2 and RCP8.5 with SSP5. For this two combinations of RCP and SSP, two fuel-efficiency improvement are considered, 40% and 60%. Figure 1.5 shows for this 4 scenarios the CO_2 emissions projections.

The RCP and SSP combination are relatively independent of the maritime industry since the maritime industry represents only 2.6% of the total CO_2 emissions. For the most optimistic scenario, an increasing of 35% of CO_2 emissions is expected in 2050, with the combination RCP2.6, SSP2 and FEI 60%. For the worst case, RCP8.5, SSP5 and FEI 40%, an increase of 245% of CO_2 is expected in 2050. Comparing the two equivalent combinations of RCP and SSP, the effect of the fuel-efficiency improvement can be assessed. In 2050, the effect of an improvement of the fuel efficiency from 40% to 60% leads to a drop of the CO_2 emissions between 400 and 900 million of tons depending on the scenario.

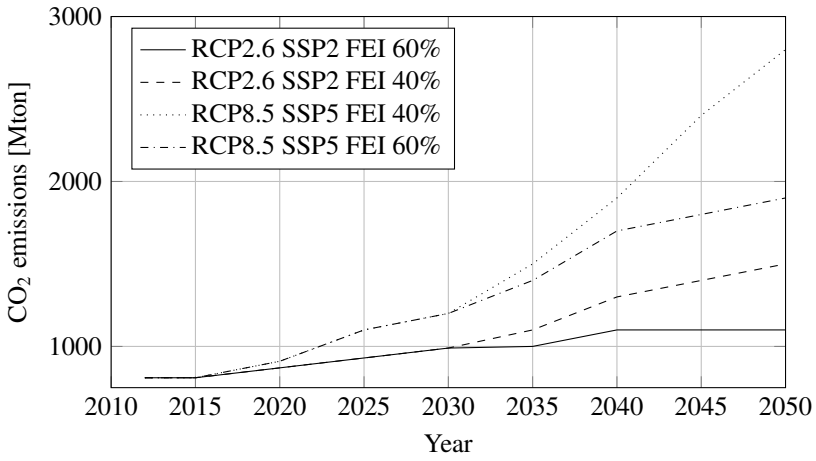

Figure 1.5.: CO_2 emissions projections between 2012 and 2050; results of Smith et al. (2014)

These CO_2 emissions forecasts show how it is important to improve the fuel efficiency of the shipping industry. Therefore, the development of new devices and notably kites in order to decrease the carbon footprint of ships is important. As highlighted by Traut et al. (2014), the use of kite on merchant ships is one of the most promising wind device for fuel saving and a kite is compatible with most of other saving fuel devices, for instance with LNG engine or flettner rotor.

1.3. Economical interest

The interest of a kite for fuel saving has been investigated in the past by (Naaijen et al., 2006; Naaijen and Koster, 2010; Leloup, 2014; Leloup et al., 2016). They showed that the kite towing could provide significant fuel savings without compromising the safety of merchant ship in terms of mean equilibrium of the system. Their studies have been performed on a 225 m long cargo ship, the British Bombardier. Leloup et al. (2016) investigated the fuel saving with a kite of 320 m^2 , the biggest ever manufactured at the time, with a tether length of 300 m. This kite area were considered since the Skysail® company had already proven the validity of the kite towing concept on a bulk carrier of 90 m long. The expected fuel saving ratio were estimated from 10% with a true wind speed of 9.8 $m.s^{-1}$and up to 60 % with a true wind speed of 15 $m.s^{-1}$. Later, Podeur et al. (2016) investigated the fuel saving along an ocean trip between Halifax (Canada, Nova Scotia) and Le Havre (France), back and forth over 4 years.

However in these studies, the kite and its operability costs have not been considered. Here a very simple approach is proposed. It can be defined an effective saving C_e as follows:

$$C_e = C_{sa} - C_k \tag{1.1}$$

where C_k is the kite cost and the C_{sa} is the fuel saving. The fuel saving can be expressed as follows:

$$C_{sa} = \bar{\eta}_{kf} t_d C_{s,t} \tag{1.2}$$

where $\bar{\eta}_{kf}$ is the mean fuel saving ratio, t_d is kite lifetime and $C_{s,t}$ is ship operating cost per unit of time.

Meyer et al. (2012) investigated the effect of the ship speed on the profit and operating cost of a container ship. They show the existence of an optimal speed taking into account economical aspects. It should be possible to perform the same work to determine an optimal ship speed with a kite. The ship operating cost can be represented as an increasing function of the fuel price c_f.

The kite cost is directly function of the material cost. The kite cost and the lifetime of a kite are very important to assess the economical interests of a kite. It can be assumed that the higher the wind loading considered for the design is, the higher the retail cost of the kite will be. Consequently, the kite retail cost can be expressed by an increasing function of the wind loading specs for kite design $C_k\left(\sigma_d\right)$. The kite lifetime is dependent on many parameters, but probably the most important one is the following factor of safety, σ_d/σ_k which is the kite wind loading compared to its wind loading of design. Then it can be assumed that the kite lifetime can be given by a decreasing function of the factor of safety, $t_d\left(\sigma_d/\sigma_k\right)$.

The counterpart of an important kite wind loading design, is that for given materials used for the kite and the tether, the weight of the kite system increases. Additionally the minimum operating wind speed required increases with the kite weight W_k. Consequently, the mean kite power saving ratio is a function of the kite wind load design as well. Moreover, as shown by the kite fuel saving studies, the kite fuel saving ratio depends on the weather condition and on the ship speed.

According to previous discussion studies, the ship profit without kite can be expressed as follows:

$$C_p = \left[C_{i,t}\left(U_s\right) - C_{s,t}\left(U_s,\ c_f\right)\right] t_d\left(\sigma_d/\sigma_k\right) \tag{1.3}$$

where, $C_{i,t}$ is the operating income of the merchant per unit of time represented as an increasing function of the ship speed, which means more round trips per annum. The ship profit with kite $\tilde{C}_p$ can be expressed as follows:

$$\tilde{C}_p = C_p + \bar{\eta}_{kf} t_d C_{s,t}\left(U_s,\ c_f\right) - C_k\left(\sigma_d\right) \tag{1.4}$$

Thus a kite profit ratio $\eta_p = \tilde{C}_p / C_p$, being the profit with kite divided by the profit without kite can be expressed as follows:

$$\eta_p = 1 + \frac{1}{C_{i,t}\left(U_s\right) - C_{s,t}\left(U_s,\ c_f\right)} \left[\bar{\eta}_{kf}\left(U_{tw},\ U_s,\ \sigma_d\right) C_{s,t}\left(U_s,\ c_f\right) - \frac{C_k\left(\sigma_d\right)}{t_d\left(\sigma_d/\sigma_k\right)} \right] \tag{1.5}$$

This kite ratio profits makes sense only if $C_{i,t}\left(U_s\right) > C_{s,t}\left(U_s,\ c_{oil}\right)$. The kite towing technology has an economical interest if the kite profit ratio η_p is higher than 1. This economical criteria can be simplified as follows:

$$\bar{\eta}_{kf}\left(U_{tw},\ U_s,\ \sigma_d\right) C_{s,t}\left(U_s,\ c_f\right) \frac{t_d\left(\sigma_d/\sigma_k\right)}{C_k\left(\sigma_d\right)} > 1 \tag{1.6}$$

Results presented by Podeur et al. (2016) show that the kite fuel saving ratio decreases with the ship speed. The evolution of the kite profit ratio with the ship speed are less obvious since the ship operating cost per day increases with the speed. According to Meyer et al. (2012), the ship operating costs of a 8000 TEU container ship is around 50 k$ per day at a ship speed of 10 m.s^{-1}. Figure 1.6 shows the minimum kite fuel saving ratio to make profits as function of the kite cost and for different kite lifetime is day. For instance, with a kite cost of 200k$, the kite should have at least an efficiency of 11.5% and a lifetime of 35 days or five days of lifetime with 80 % of fuel saving efficiency.

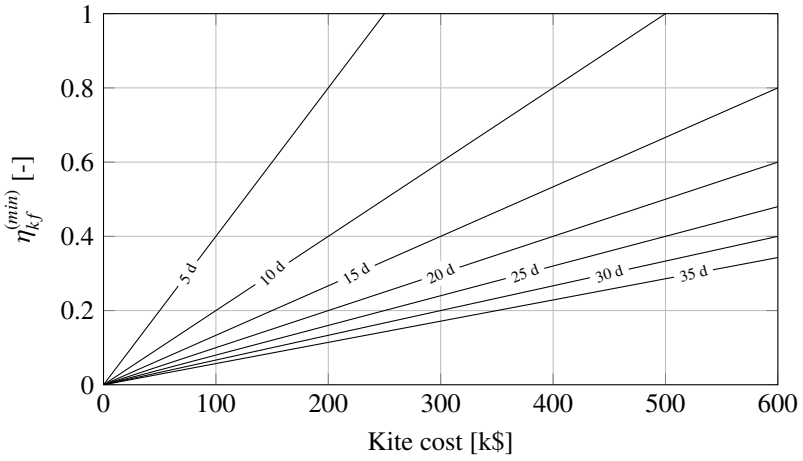

Figure 1.6.: Minimum required kite fuel saving ratio as function of the kite cost and different kite lifetime for a 8000 TEU container ship with ship operating cost of 50k$ per day.

Moreover an increase of the fuel price is a benefit for the kite towing technology. Figure 1.7 shows the oil price evolution over the period 2005-2017. The oil price was stabilized

around 90-100 USD between 2011 and 2014 and dropped drastically around 45-50 USD since 2015. This important price drop was caused by output growth of the OPEP and Russia to protect their market from the oil shale producers. Since 2017, the oil shale producers improved their process, now they make profit from an oil price per barrel of 30 USD. Consequently, the oil price per barrel may stay relatively low for a while. The kite towing technology might be delayed since its profits are dependent of the oil price.

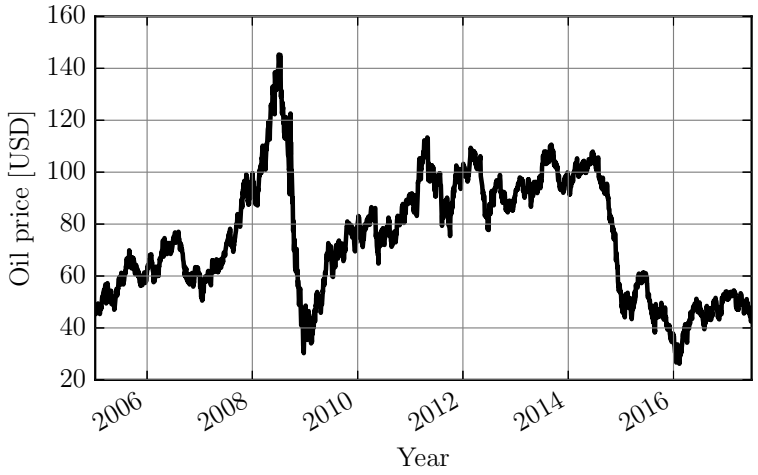

Figure 1.7.: Oil price per barrel since 2005

1.4. Beyond the sea® project

The beyond the sea® project began in 2007 under the initiative of the french navigator Yves Parlier. In 2014, a consortium of industrial partners and research center joined the beyond the sea® project with the sponsorship of the French Environment and Energy Management Agency (ADEME). ADEME ranked the beyond the sea® project as the more convincing project to succeed in the call for project "ship of the future". This consortium is composed of french industrial and academic partners able to offer expertise and technology to develop the system. The industrial and academic partners of the beyond the sea company are:

- Cousin Trestec, manufacturer of innovative ropes and braids.
- Porcher Industries, manufacturer of innovative fabrics.
- Bopp, designer and manufacturer of hydraulic and electrical winches and deck equipment for marine applications.
- CMA-CGM, worlwide shipping group.

- ENSTA Bretagne, a french national graduate engineering institute and the Dupuy de Lôme Research Institute.

- DAAM, a company handling a fleet of competition sailing boats. DAAM is in charge of trials carried out at sea.

The Beyond the sea® company is in charge of the practical knowledge for the kite design, control, launching and recovery procedures. To solve the associated technological challenges, the company works in close cooperation with research laboratories. The launching and recovery procedures have been investigated by Du Pontavice (2016) at the Ladhyx the research laboratory of the Ecole Polytechnique. The control of the kite is investigated by the IMS laboratory by Cadalen et al. (2017).

The theoretical understanding of the ship towed by a kite system is managed by the ENSTA Bretagne laboratory IRDL in close cooperation with the industrial partner and the ENSM (Ecole Nationale Supérieure Maritime), with trains merchant ship officers. Leloup (2014) developed the first theoretical knowledge on the fuel saving predictions and the fluid structure interaction on the kite for the Beyond the sea® project. The research program managed at the ENSTA Bretagne can be split into three fields. The kite is a very flexible structure, its geometry is highly dependent on its aerodynamic loading. The prediction of the kite flying shape, deformations and stresses constitute one a of the major scientific and technical issue to address. A second major scientific issue concerns the influence of the kite on the ship, both in terms of fuel savings and in terms of ship motions and operability. The third field of research concerns the experimental study of the dynamic kite flight and ship towed by kite. Since 2014, these three fields are the purpose of three PhD programs. Among these scientific challenges, the present PhD dissertation deals with the prediction of the ship motions induced by a towing kite and its operability.

2. Position of the problem and strategy

2.1. State of the art

The state of the art section is focused on the theoretical knowledge of the ship towed by a kite system. A more extensive literature review could have been achieved for each subsystems but it was preferred to provide these reviews in each dedicated chapters.

The first theoretical work about a kite can be found early in the eighties with Loyd (1980). This work was focused on the wind power production. Then Wellicome and Wilkinson (1984) used a zero mass kite model to estimate the kite towing force during a dynamic kite flight. This model neglects the mass of the kite and assumes straight and inelastic tethers. Then, in (Wellicome, 1985), they compared different wind system for the propulsion of ship. They showed that the kite is one of the most promising technology for fuel savings.

Later, Naaijen et al. (2006); Naaijen and Koster (2010) applied the mean kite towing force obtained with a zero mass kite model to solve the ship equilibrium in terms of surge, sway and yaw motions. The promising fuel savings were confirmed despite the induced resistance due to the ship drift. Their work was the first theoretical result predicting the fuel saving for different sailing conditions. Moreover, they argued that a kite should be attached at the bow to limit the rudder angle to counteract the kite yaw moment. Dadd (2013) paid attention to the validation of the zero mass kite model, and to the associated fuel saving solving only the surge equilibrium. The comparison of the zero mass kite model with experiments is presented in (Dadd et al., 2010). Results show, despite the simplicity of the modeling, a good agreement. Consequently, Leloup et al. (2014) used the zero mass kite model to compare a kite with a classical rig on a sailing yacht. Leloup (2014) solved the longitudinal equilibrium of a cargo ship over a transatlantic trip to estimate the mean fuel savings.

The most advanced work in terms of ship modeling were achieved by Ran et al. (2013) using the SEAMAN maneuvering and seakeeping in-house code of the Swedish Ship Testing Institute (SSPA) described in (Ottoson and Bystrom, 1991). The kite force was estimated with a zero-mass kite model on a predefined trajectory. The coupling between the ship and the kite was partially taken into account by means of the instantaneous horizontal ship velocity. The considered position to compute the ship velocity was not detailed. The influence of the vertical ship velocity were neglected. Their results have been presented in terms of mean equilibrium. This work was a first attempt to study the dynamic motions of a ship towed by kite and only few details on the methodology were provided,which are too few to

be useful. Unfortunately, no further work from the authors was published on the topic, as far we know.

2.2. Scientific issue and objectives of the thesis

As shown by the literature review, the existing knowledge about ships towed by kites had been motivated by the demonstration of the economical interest of the kite by solving the equilibrium of the ship according to a mean kite towing force. To consider a mean towing force is a strong assumption. A kite performing a dynamic a flight imposes to the ship an oscillatory excitation. The coupling between a ship and a kite may modify the mean equilibrium of the system. The dynamic motions of the system, may have an impact on the fuel saving estimation. Moreover, the kite oscillatory excitation may represent a risk for the ship safety in terms of seakeeping and maneuverability, and crews must be trained about how the kite system works and interacts.

From the kite design point of view, ship motions due to the kite and the sea state may modify the kite flight leading to an increase of the wind loading applied on the kite. The dynamic loading will probably leads to a heavier design. Consequently, the wind velocity required to launch the kite will increase. As discussed in Sec. 1.3, the kite cost increases with the wind loading and may have a significant impact on the kite profit.

The aim of this thesis is therefore to investigate the effect of the dynamic motions of a ship towed by kite on safety, profits and fuel savings. The dynamic motions of a ship towed by kite depends on parameters such as the kite area, tether length and tether attachment point. The scientific issue is to determine the influence of these parameters on the dynamic motions of the systems and on its operability.

The chosen strategy is to investigate this problematic with quasi-analytical and numerical modeling approaches. As much as possible, employed methods should be transferable as in-house code to provide dedicated tools to design kite towing systems for ships. Therefore, the modeling must be open for different types of ship. Moreover, in applied physics, numerical methods are generally developed to describe an identified phenomenon. On the contrary, for this scientific issue, the practical knowledge on the kite towing of large ship is almost nonexistent or confidential[1] Consequently, methods developed in this study should be fast enough to run a large number of configurations and accurate enough to represent the important physics phenomena related to the system. The trade off between computational time and accuracy associated to this work is therefore arbitrary.

[1] Cargo ship, MS Beluga Skysails

2.3. Organization of the thesis

The thesis is organized in three major parts:

- The part II deals with the kite system modeling including the tether. The zero mass kite model is presented in Chap. 3. In this chapter a comparison with experimental data at full scale is performed. Since the zero mass kite model assumes straight and inelastic tether, the Chap. 4 investigates the relevancy of these assumptions with a quasi-analytical model based on the catenary equation. Thanks to the quasi-analytical tether model, a low wind limit to enable a static kite flight is developed in Chap. 5.

- The part III focuses on the development of a dynamic ship model in time domain to perform a monolithic coupling with the kite model. Chapter 6 introduces a time domain method to take into account seakeeping motions. The model is compared to towing tank experimental results. Chapter 7 presents a method mixing the maneuvering equations of motions with the presented time domain seakeeping modeling. The mixed model is compared to free sailing results and other empirical methods.

- The part IV is dedicated to the coupling of the kite modeling with the ship modeling. First, based on the presented ship model, the mean equilibrium of a ship is performed in Chap. 8. The influence of the sailing condition, the tether attachment position and the windage force are investigated. In Chapter 9, the interactions between the kite and the ship are studied in both calm water and waves conditions with the presented ship modeling limited to heave, roll and pitch motions. To take into account the 6 degrees of freedom (dof) of the ship, the course keeping stability is investigated in Chap. 10. The last chapter 11 presents results of free sailing simulations in calm water and regular waves. The influence of the dynamic motions on ship and kite performances are compared to the mean equilibrium approach. The interactions phenomenon highlighted in Chap. 9 are studied modeling the 6 dof with different tether lengths.

The conclusion summarizes the results of each chapter and proposes several recommendations to continue and enhance the presented work.

Part II.

Kite modeling

3. Zero-mass kite model

Résumé: Modélisation du kite sans masse

Un cerf-volant est une structure légère et flexible. La canopée du cerf-volant est généralement fabriquée en toile légère. La structure du cerf-volant peut être renforcée par des boudins gonflables et un réseau de brides. Sa forme en vol est très dépendente du chargement aérodynamique et de façon réciproque le chargement aérodynamique est très dépendent de la forme en vol. Ainsi, pour calculer les performances en vol du cerf-volant il faudrait en toute rigueur résoudre le problème couplé : fluide et structure. Cependant de telles méthodes sont coûteuses en termes de temps de calcul. D'autres méthodes plus simples ont été développées dans la littérature pour estimer les performances d'un cerf-volant : vitesse et force de traction. La plus simple d'entre-elles fait l'hypothèse d'un cerf-volant sans masse avec des lignes droites et inélastiques (Wellicome and Wilkinson, 1984; Dadd et al., 2011; Leloup et al., 2016). Cette approche est utilisée dans l'ensemble de la thèse.

Dans ce chapitre l'équation cinématique du vol du cerf-volant est introduite, cf. Eq. 3.1.Cette équation analytique est ensuite analysée pour mettre en évidence un majorant analytique du maximum de traction (Eq. 3.18) ainsi que le maximum de force propulsive (Eq. 3.19) en tenant compte d'une loi d'évolution de la vitesse du vent avec l'altitude en puissance 1/7. Il est ensuite montré qu'au vent arrière, un cerf-volant peut fournir par exemple 3.67 fois plus d'effort propulsif qu'une voile de Laser (dériveur olympique), à support nautique identique.

L'équation cinématique du cerf-volant dépend de la finesse aérodynamique du cerf-volant et la traction du cerf-volant dépend du coefficient de portance. Il est donc important d'estimer correctement ces deux paramètres. Précédemment, à travers la littérature consacrée, ces deux coefficients ont été considérés constants au cours du vol de façon à obtenir en moyenne la même vitesse de cerf-volant et la même force de traction. Ici, en suivant la même démarche, une comparaison avec des essais de vol de cerf-volant instrumenté ont permis de montrer que les amplitudes de vitesse et de force de traction ne pouvait être correctement représentées avec un modèle à coefficient constant, cf. Fig. 3.5.

Pour l'étude des mouvements dynamiques d'un navire tracté par cerf-volant, l'estimation des amplitudes d'effort est pourtant cruciale. En effet, en théorie linéaire, les amplitudes de mouvement d'un navire sont proportionnelles aux amplitudes d'excitation. Ainsi, une formulation linéaire de l'angle de finesse et du coefficient de portance en fonction de la

valeur absolue de la dérivée de la direction de la vitesse est proposée. Les coefficients de la loi linéaire sont adimensionnés par le rapport entre une longueur caractéristique du cerf-volant et la vitesse du vent relatif perçue par le navire. La longueur caractéristique du cerf-volant choisie est la racine carrée de sa surface. A dérivée de la direction constante, la perte de performance aérodynamique en virage augmente avec la taille du cerf-volant et diminue avec la vitesse du vent. Comparé au cas de vol dynamique choisi, la correction est satisfaisante, cf. Fig. 3.6. Cependant afin de valider cette approche, une étude traitant plusieurs cas de vol dynamique serait nécessaire.

3.1. Introduction

A kite is mainly composed of flexible and light materials such as fabric. The canopy is made with a very light fabric. Eventually, a kite is also composed of inflatable tubes as battens in the chord direction and at the leading edge. The bridle lines connect the kite structure to the tethers. A kite is controlled by the variations of the bridle line length or tether lengths. This adjustement of bridle line can be performed by a control pod below the kite (cf. Fig. 3.1a) or directly with the back tethers (cf. Fig. 3.1b). Since only a small part of the aerodynamic force is distributed to the back tethers or the bridle lines closed to the trailing edge (around 20-30%), they are controlled to modify the kite flying shape. In this way, the actuator has low energy consumption. This modification of the kite flying shape leads to a dissymetric aerodynamic loading which enables a modification of the kite heading.

The most advanced kite models take into account the complete kite Fluid Structure Interaction (FSI). The kite FSI problem is usually solved by iterative processes coupling a structural solver, generally a Finite Element (FE) model, and a fluid solver in order to describe the aerodynamic pressure distribution (Bosch et al., 2014; Chatzikonstantinou, 1989; Breukels et al., 2013). These methods are very usefull to evaluate the stress in the fabric and in the inflatable tubes.

However, all these approaches are time consuming. Consequently, many studies focusing on the global kite system performance use simpler approaches. These simple approaches can be classified into three groups: zero-mass model (Wellicome and Wilkinson, 1984; Dadd et al., 2011; Leloup et al., 2016), point-mass model (Williams et al., 2008) and rigid body model (Williams et al., 2008; Terink, 2009; Terink et al., 2011). The zero-mass model neglects the mass of the kite and assumes that the tether is straight and inelastic. These assumptions lead to a kinematic equation of the kite motion. The influence of the ship motions on the kite flight can then be taken into account trough the tether attachment point velocity. This model has the advantage of being very fast to compute.

First, the zero-mass model such as formulated by Leloup et al. (2016), dynamic kite trajectory and the control of the kite are detailed. According to the zero mass model, a convenient upper bound of the tether tension during a dynamic flight is developed. Then, a comparison

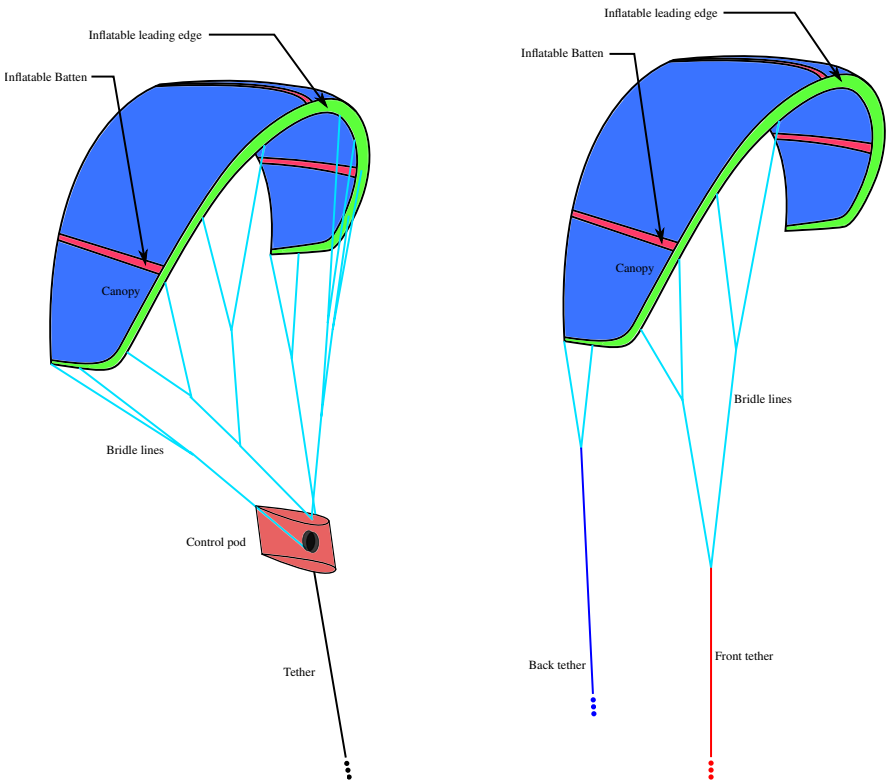

(a) Schema of an inflatable kite with a single tether controlled by a pod

(b) Schema of an inflatable kite controlled by the two back tethers

Figure 3.1.: Tether and bridle lines

with experimental data is provided. Based on experimental data, a correction of the lift to drag angle and lift coefficient as functions of the kite yaw turning rate are proposed.

3.2. Kite velocity and force

This section summarizes the development of the zero-mass model as formulated in (Leloup, 2014; Leloup et al., 2016). The masses of the tether and the kite are neglected. The tether is assumed to be straight and of constant length L_t. Consequently, the kite velocity is normal to $\underline{z}_k$ and for any configurations the tether tension is opposed to the aerodynamic kite force. Assuming that the apparent wind velocity is in its symmetry plane, Leloup et al. (2016) expressed the kite velocity $\underline{U}_k$, with respect to tether attachment point velocity $\underline{U}_a$, as follows:

$$\underline{U}_k = U_{rw,ka}\left[\underline{x}_{vk}\cdot\underline{x}_{rw,ka} + \sqrt{\left(\underline{x}_{vk}\cdot\underline{x}_{rw,ka}\right)^2 + \left(\frac{\underline{z}_k\cdot\underline{x}_{rw,ka}}{\sin\epsilon_k}\right)^2 - 1}\right]\underline{x}_{vk}, \tag{3.1}$$

where $\underline{U}_{rw,ka}$denotes the relative wind speed, $\underline{U}_{rw,ka} = \underline{U}_{tw}(K) - \underline{U}_a - \underline{U}_c$ and $\underline{x}_{vk}$ is the kite velocity direction with respect to A. ϵ_k denotes the lift to drag ratio angle. This equation constitutes the kite kinematic equation of motion and can be integrated numerically.The kite velocity is a real number if the following condition is satisfied:

$$\left(\underline{x}_{vk}\cdot\underline{x}_{rw,ka}\right)^2 + \left(\frac{\underline{z}_k\cdot\underline{x}_{rw,ka}}{\sin\epsilon_k}\right)^2 - 1 \geqslant 0. \tag{3.2}$$

Then, the tether tension is given by the following formula:

$$\underline{T}_k = -\frac{\rho_a C_{lk} A_k U_{aw}^2}{2\cos\epsilon_k}\underline{z}_k \tag{3.3}$$

The generalized tether force vector acting on the ship at O_S with respect to the $\mathbf{s}$ frame is expressed as follows:

$$\underline{F}_k = \begin{bmatrix} \underline{T}_k^{(\mathbf{s})} & \underline{O_S A}^{(\mathbf{s})} \times \underline{T}_K^{(\mathbf{s})} \end{bmatrix}^T \tag{3.4}$$

According to this model, the kite flight is modified by the ship motions through the tether attachment point velocity with the expression of the relative wind speed:

$$\underline{U}_{rw,ka} = \underline{U}_{tw}(K) - \underline{U}_a - \underline{U}_c \tag{3.5}$$

3.3. Wind gradient

The wind above the sea increases with the altitude due to the friction stress on the free surface within the atmospheric boundary layer. This phenomenon, called wind gradient can have a significant effect on the kite performance. A common way to take into account this effect is to use a wind gradient power law as investigated by Peterson and Hennessey (1978):

$$\underline{U}_{tw} = \underline{U}_{ref} \left(\frac{x_z^{(\mathbf{n})}}{z_{ref}} \right)^{n_v} \tag{3.6}$$

where $\underline{U}_{ref}$ denotes the true wind speed at the altitude of reference z_{ref}. According to a multi-site study Peterson and Hennessey (1978) suggested that a power law exponent $n_v = 1/7$ is realistic. This simple formulation of the wind gradient is suggested by the Ittc (2014) as well.

3.4. Kite trajectory and control

3.4.1. Control

The kite velocity direction $\underline{x}_{vk}$ is controlled in order to follow a trajectory denoted by $\mathscr{C}$. The kite velocity direction is defined by the target point $\tilde{K}$ expressed as follows:

$$\tilde{K} = \mathscr{C}\left(\lambda + \|\underline{U}_k\|\, dt\right), \tag{3.7}$$

where λ is the curvilinear abscissa of C_λ the closest point of the trajectory from the current kite position K. Hence, the kite velocity direction $\underline{x}_{vk}$ is defined as follows:

$$\underline{x}_{vk} = \frac{\left(\underline{K\tilde{K}} \cdot \underline{x}_k\right) \underline{x}_k + \left(\underline{K\tilde{K}} \cdot \underline{y}_k\right) \underline{y}_k}{\left\| \left(\underline{K\tilde{K}} \cdot \underline{x}_k\right) \underline{x}_k + \left(\underline{K\tilde{K}} \cdot \underline{y}_k\right) \underline{y}_k \right\|} \tag{3.8}$$

The point C_λ is determined according to the following equation:

$$\underline{KC_\lambda} \cdot \underline{t}_\lambda = 0, \tag{3.9}$$

where $\underline{t}_\lambda$ is the tangent vector to the trajectory at curvilinear abscissa λ. Equation (3.9) is solved numerically with a Newton-Raphson algorithm.

Any trajectory can be considered thanks to the use of a numerical solver to determine C_λ. Hence, the trajectory $\mathscr{C}$ can be experimental or theoretical.

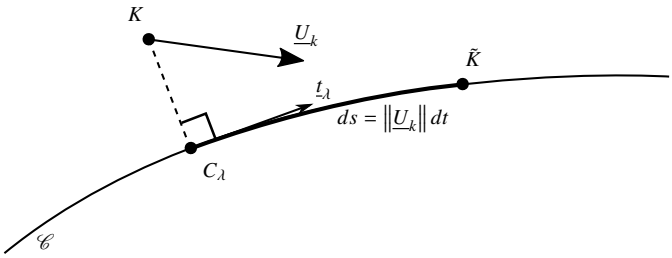

Figure 3.2.: Schema describing the target point to control the kite direction $\underline{x}_{vk}$

3.4.2. Trajectory

To perform a dynamic flight, the considered theoretical trajectory is the eight shape Lissajous curve as used by Argatov et al. (2009) and Leloup (2014). This type of trajectory has the advantage to avoid twists of the tether system. The Lissajous trajectories, is defined by the elevation θ_C and the azimuth ϕ_C as follows:

$$\begin{cases} \theta_C &= \Delta\theta_8 \sin(2\alpha) + \theta_8 \\ \phi_C &= \Delta\phi_8 \sin(\alpha) + \phi_8 \end{cases}, \tag{3.10}$$

where, $\alpha \in [0; 2\pi]$. θ_8 and ϕ_8 are the elevation and the azimuth of the center of the trajectory denoted by C_8. The trajectory is defined with respect to $\mathbf{rw}_{ra}$, the relative wind basis with accordingly to the tether attachment position A at the reference wind measurement altitude[1]. On a sphere of radius L_t, a point C of the trajectory is defined as a function of elevation θ_C and azimuth ϕ_C with respect to $\mathbf{rw}_{ra}$ frame as follows:

$$\underline{C} = \begin{bmatrix} L_t \cos\theta_C \cos\phi_C \\ L_t \cos\theta_C \sin\phi_C \\ -L_t \sin\theta_C \end{bmatrix}_{\mathbf{rw}_{ra}}, \tag{3.11}$$

As shown in Fig. 3.3, the Lissajous trajectories can be rotated by an angle χ_8 around $\underline{C_8 A}$.

Any point of the trajectory must agree with Eq. (3.2) insuring the realness the kite velocity. The benefit to define the trajectory with respect to the relative wind basis is that the realness of the kite velocity along the trajectory does not depend significantly on the ship motions. Nevertheless, ship motions may modify significantly the shape of the trajectory with respect to the earth fixed frame $\mathbf{n}$. Consequently, two trajectory definitions are investigated further in the paper. The first definition takes into account all components of the tether attachment point velocity. The second definition takes only the horizontal components of the tether attachment point velocity with respect to the earth fixed frame $\mathbf{n}$ to compute the relative

[1]The subscript r in $\mathbf{rw}_{ra}$ denotes the altitude of wind measurement and should not be confused with the subscript r for the rudder.

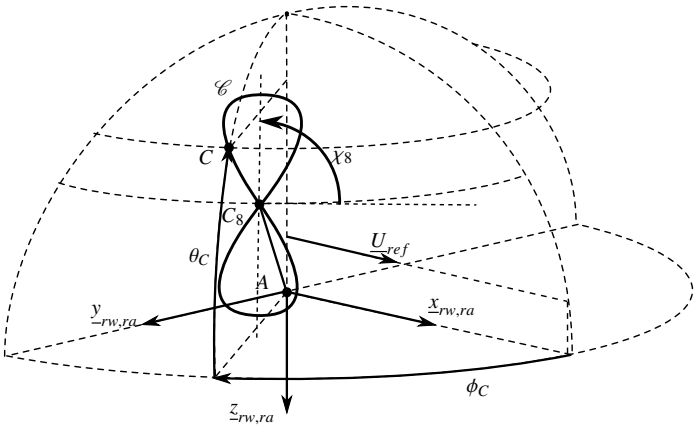

Figure 3.3.: Schema of the Lissajous trajectory parameterization

wind basis. This modified relative wind basis of trajectory definition is denoted by $\mathbf{r\tilde{w}}_{ra}$ and is given as follows:

$$\underline{\tilde{U}}^{(\mathbf{n})}_{rw,ra} = \underline{U}^{(\mathbf{n})}_{tw}\left(z_{ref}\right) - \left[u_a^{(\mathbf{n})},\ v_a^{(\mathbf{n})},\ 0\right]^T \tag{3.12}$$

3.5. An upper bound of the kite force

For design purposes, maximizing the traction provided by a given kite could be interesting. Leloup et al. (2016) showed that the apparent wind speed can be expressed as follows:

$$U_{aw} = U_{rw,ka}\frac{\underline{x}_{rw}\cdot\underline{z}_k}{\sin\epsilon_k}, \tag{3.13}$$

which can be written in terms of elevation and azimuth as follows:

$$U_{aw} = U_{rw,ka}\frac{\cos\left(\phi_k\right)\cos\left(\theta_k\right)}{\sin\epsilon_k} \tag{3.14}$$

In the case of a zero ship speed with no current $\underline{U}_c$, the apparent wind speed limit is driven by:

$$U_{aw} \leq U_{tw}\left(K\right)\frac{\cos\theta_k}{\sin\epsilon_k} \tag{3.15}$$

The true wind speed vary with the altitude due to the wind gradient. Consequently, it exists a kite elevation to maximize the apparent wind speed. Using the wind gradient expression

in Eq. 3.6, and assuming that the altitude tether attachment point is zero, Eq. (3.15) can be expressed as a function of the kite elevation:

$$U_{aw} \leq U_{ref} \left(\frac{L_t \sin \theta_k}{|z_{ref}|} \right)^{n_v} \frac{\cos \theta_k}{\sin \epsilon_k} \tag{3.16}$$

The maximum of $\sin^{n_v} \theta_k \cos \theta_k$ is reached for $\theta_k = \arctan \sqrt{n_v}$. As recommended by the Ittc (2014), typical value for the power law parameter above the sea is $n_v = \frac{1}{7}$, which leads to an optimal elevation angle of $20.7°$. According to the trigonometrical relationship, $\cos \theta_k = \sqrt{\frac{1}{n_v+1}}$ and $\sin \theta_k = \sqrt{\frac{n_v}{n_v+1}}$, the upper bound of the apparent wind velocity is:

$$U_{aw} \leq U_{ref} \left(\frac{L_t \sqrt{\frac{n_v}{n_v+1}}}{|z_{ref}|} \right)^{n_v} \frac{\sqrt{\frac{1}{n_v+1}}}{\sin \epsilon_k} \tag{3.17}$$

In terms of kite force magnitude, the upper bound is:

$$T_k \leq \frac{\rho_a C_{lk} A_k}{2 \cos \epsilon_k \sin^2 \epsilon_k \left(n_v + 1\right)} U_{ref}^2 \left[\frac{L_t^2 n_v}{z_{ref}^2 \left(n_v + 1\right)} \right]^{n_v} \tag{3.18}$$

The maximum of kite towing force is obtained for $\theta_k = \arctan \sqrt{2n_v/3}$, consequently $\underline{T}_k \cdot \underline{x}_{tw}$ is maximized by:

$$\underline{T}_k \cdot \underline{x}_{tw} \leq \frac{\rho_a C_{lk} A_k}{2 \cos \epsilon_k \sin^2 \epsilon_k \left(\frac{2}{3} n_v + 1\right)^{3/2}} U_{ref}^2 \left[\frac{L_t^2 n_v}{z_{ref}^2 \left(n_v + \frac{2}{3}\right)} \right]^{n_v} \tag{3.19}$$

Just by the way as an illustrative example, the performance of a kite can be compared to the sail performance of the Olympic Laser Class at downwind. Performing s-turn maneuvers, Schutt and Williamson (2017) showed that the downwind force coefficient can reach a value of $C_{dc} = 2.5$. The s-turn is a maneuver performed by the athlete combining an oscillating yaw motion with an oscillating roll motion to increase the downwind force coefficient. Neglecting, the benefit from the wind gradient for the kite, and considering the same sail area, the ratio of propulsive force between a kite and a Olympic Laser Class rig is at downwind is written as follows:

$$\frac{\underline{T}_k \cdot \underline{x}_{tw}}{\frac{1}{2} \rho_a C_{dc} A_k U_{ref}^2} < \frac{C_{lk}}{C_{dc}} \frac{1}{2 \cos \epsilon_k \sin^2 \epsilon_k} \tag{3.20}$$

Referring to the literature, Dadd et al. (2010) measured on a classical kite a lift to drag angle of $12°$ and a lift coefficient of 0.776. This example leads then to the statement that a kite is up to 3.68 times more powerful than a classical rig at downwind. A more comprehensive

comparison was performed by Leloup et al. (2014). They compared the performance of a keel yacht Beneteau First Class 8 and its classical rig with the same keel yacht but equipped with a kite of 25 m^2. The classical sail area of the Beneteau First Class 8 is 34 m^2 at upwind and 65 m^2 at downwind. With the kite, the authors argued that the ship performance is increased by 40% at upwind and by 250% at downwind.

3.6. Comparison with experimental data

The zero-mass kite model is compared to the experimental data obtained by Behrel et al. (2017). As shown in this section, the zero mass kite model dependends on two parameters, the kite lift coefficient C_{lk} and the lift to drag angle ϵ_k. These coefficients must be adapted in order to fit the data. The onshore full scale trials (Behrel et al., 2017) was performed with a classical kite Cabrinha® Switchblade of 5 m^2 designed for kite-surfing. The tether length was 80 m long. During the run, the kite performed eight shape trajectories controlled by an autopilot based on the algorithm proposed in (Fagiano et al., 2013). The experimental kite position is determined with a 3D load cell assuming that the tethers are straight, which seems reasonable as a first approach. The evolution of the wind velocity with the altitude was identified thanks to a SOnic Detection And Ranging (SODAR). Experimental results presented here correspond to a phase averaging post-processing of a 5 minutes kite flight run.

Figure 3.4 shows the evolution of the wind velocity with respect to kite altitude on the average trajectory. The SODAR measured the wind velocity at altitudes of 48 m, 53 m and 58 m. The cross represents the wind velocity at kite positions during the run. Hence, for the presented case, the wind velocity has been fitted with a linear function such as:

$$U_{tw} = 3.16 - 0.035 k_z^{(\mathbf{n})} \tag{3.21}$$

The wind gradient function in Eq. (3.21) was therefore used for following simulation results.

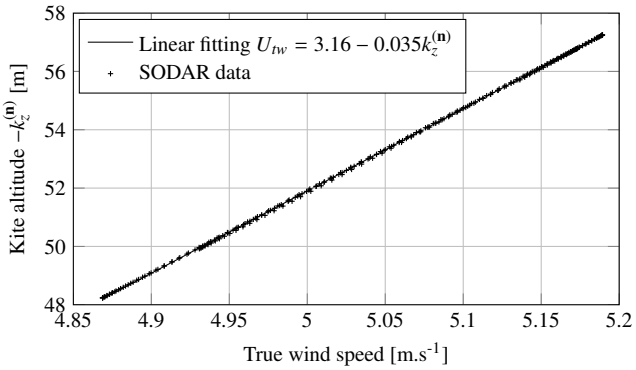

Figure 3.4.: Linear evolution of the wind velocity along the altitude of the average trajectory

3.6.1. Comparison with the zero-mass model

The zero-mass model presented in (Leloup et al., 2016) assumes a constant lift to drag angle and a constant kite lift coefficient. The kite velocity is only dependent of ϵ_k. Consequently, zero-mass model results presented are obtained with a lift to drag angle which enables kite trajectories to be done in the same time of 5.86 seconds than the experimental data. The kite towing force is dependent on the kite lift coefficient. Hence, the kite lift coefficient is adjusted in order to obtain the same mean towing force. Note that the kite trajectory used for the simulation is the same than the kite trajectory of the experimental measurements. The position of the kite is integrated with the 4$^{\text{th}}$ order Runge-Kutta scheme with a time step of 0.1 s. According to the convergence time step performed in Annex B.1, a time step of 0.1 s is small enough.

Figure 3.5 shows the evolution of the kite velocity and the evolution of the tether tension at point A on the average trajectory. The experimental velocity is obtained by finite differentiation, which induces some noise in the signal sampled at 50 Hz. This noise in terms of speed and tension for the simulated results still exists since the simulation uses the average kite trajectory of the experimental data. However, this noise is barely visible as the sampling frequency of the simulation is only 10 Hz. The kite lift to drag angle and the lift coefficient used for the zero-mass model are respectively 12.45° and 0.855. Relative margins in terms of tension and velocity between simulation results and average experimental data are respectively around 1% and 0.1%.

The main difference between experiments and results concerns the tether tension and kite velocity oscillatory amplitudes. Amplitude predicted by the simulation is slightly underestimated for velocity results but is less satisfying for tension results. The error in terms of amplitude of tether tension is more significant.

The tether tension given by Eq. 3.3 is a linear function of the square of the apparent wind velocity, consequently a tension error is linearly dependent on the square of the kite velocity

error. In order to perform an eight pattern trajectory, the back tether are steered. The difference of the two back tether lengths leads to an important deformation of the kite flying shape. Hence, a modification of the kite lift coefficient and of kite lift to drag ratio angle can be expected..

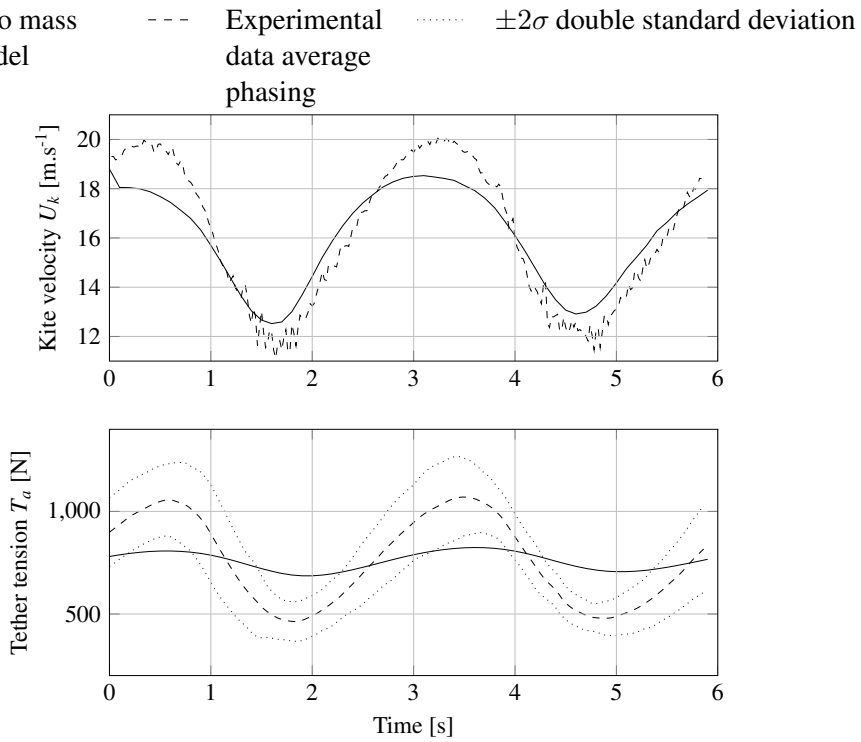

Figure 3.5.: Evolution of the kite velocity and the evolution of the tether tension at point A along the average trajectory: comparison of the zero mass model set with constant lift to drag angle and lift coefficient with the average phasing of the experimental data.

3.6.2. Modification of the kite aerodynamic specs

When the back tethers are steered to impose a yaw rate to the kite, the flying shape is highly modified. This shape modification leads to an evolution of the aerodynamic specs of the kite. Even without considering tip vortices, the yaw rate induces an evolution of the local inflow velocity along the kite span. According to Eq. (3.1), the kite velocity is independent of its area. Consequently, for a given radius of curvature of the trajectory, the evolution of the local inflow along the span and the effect of the flying shape deformation are more consequent with larger kites. Here it is assumed that the evolution of the kite lift to drag angle $\epsilon_k = \arctan\left(C_{dk}/C_{lk}\right)$ and lift coefficient are proportional to the ratio of a characteristic length of the kite with the radius of curvature of the trajectory. For a given

aspect ratio, the characteristic length of the kite can be $\sqrt{A_k}$. To be more precise, the radius of curvature to consider is the radius of curvature of the projected trajectory on the plane $\left(K, \underline{x}_k, \underline{y}_k\right)$. Let us denote this radius of trajectory $\tilde{R}_{\mathscr{C}}$. The lift to drag angle and the lift coefficient could written as follows:

$$\begin{cases} \epsilon_k & = \epsilon_0 + \kappa_\epsilon^{'} \frac{\sqrt{A_k}}{\tilde{R}_{\mathscr{C}}} \\ C_{lk} & = C_{l0} + \kappa_l^{'} \frac{\sqrt{A_k}}{\tilde{R}_{\mathscr{C}}} \end{cases} \tag{3.22}$$

where, $\kappa_\epsilon^{'}$ and $\kappa_l^{'}$ are two coefficients. Eq. (3.22) can be rewritten in terms of heading rate according to the relationship between the radius of curvature of the trajectory and the kite velocity. Using the Fresnet's relationships, $\tilde{R}_{\mathscr{C}}$ can be rewritten as function of the turning rate of the kite velocity direction around the axis $\underline{z}_{kn}$ denoted $\dot{\gamma}_n$, where γ_n is the angle of $\underline{x}_{vkn}$ with respect to $\underline{x}_{kn}$. Furthermore, according to Eq. (3.1), the kite velocity is proportional to the relative wind speed, thus the correction proposed can be rewritten as function of $\dot{\gamma}_n$ and the relative wind speed as follows:

$$\begin{cases} \epsilon_k & = \epsilon_0 + \frac{\sqrt{A_k}}{U_{rw}} \kappa_\epsilon \left|\dot{\gamma}_n\right| \\ C_{lk} & = C_{l0} + \frac{\sqrt{A_k}}{U_{rw}} \kappa_l \left|\dot{\gamma}_n\right| \end{cases} \tag{3.23}$$

The determination of coefficients ϵ_0, κ_ϵ, C_{l0} and κ_l can be evaluated by comparison with the experimental data set. First, ϵ_0 and κ_ϵ are identified in order to obtain respectively the same maximum and minimum speed than the experiments. Then, C_{l0} and κ_l are identified in order to obtain respectively the same maximum and minimum tether tension than the experiments. According to this method, following values were identified:

$$\begin{cases} \epsilon_0 & = 0.2013 \text{ rad} \\ \kappa_\epsilon & = 0.0422 \\ C_{l0} & = 0.9856 \\ \kappa_l & = -0.3718 \end{cases} \tag{3.24}$$

The results in terms of kite velocity and tether tension are plotted in Fig. 3.5. With the modification introduced for the lift to drag angle and the lift coefficient, the noise in the kite velocity and the tether tension time series is more significant. Indeed, the computation of the kite yaw rate requires two finite differences of the kite position. However, as expected with the identification method of ϵ_0, κ_ϵ, C_{l0} and κ_l, the amplitude of the kite velocity and the amplitude of the tether tension are respected.

An overall good agreement is found in terms of velocity but a slight phase difference exists between simulation results and experimental data. Results presented by the modified model,

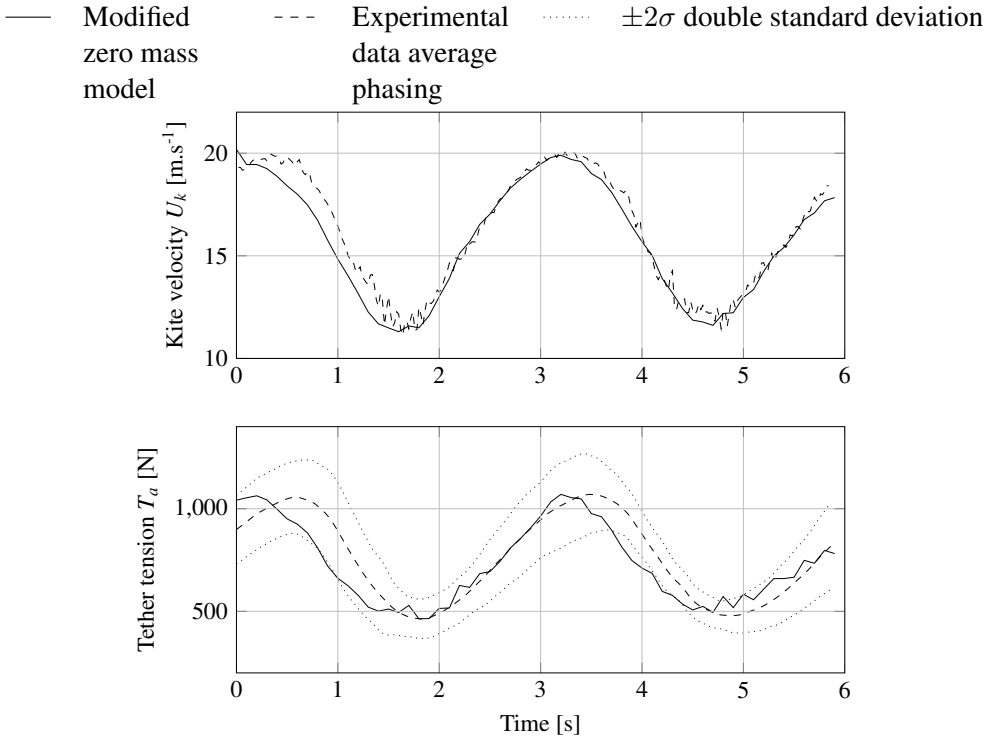

Figure 3.6.: Evolution of the kite velocity and the evolution of the tether tension at A along the average trajectory: comparison of the zero mass model with a lift to drag angle and a lift coefficient linarly depedent of the kite yaw rate with the average phasing of the experimental data.

are almost in the range of the $\pm 2\sigma$ of the tether tension. The linear modifications of the lift to drag angle and of the lift coefficient with the kite yaw rate lead to a main inprovement of the zero mass model. However, these modifications should be tested for more experimental cases. Finally, since at the first order ship motions are proportional to the amplitude of excitation forces, these modifications ,as they enhance the prediction of the kite excitation amplitude, are very crucial.

Moreover, the minimum allowable radius of curvature of the trajectory can be estimated according to Eq. (3.22). Indeed, during a kite flight C_{lk} must be positive. This means that the trajectory radius of curvature must satisfy the following condition:

$$\tilde{R}_{\mathscr{C}} \geqslant -\frac{\kappa_l^{'}}{C_{l0}}\sqrt{A_k} \tag{3.25}$$

As for numerical application, the maximum trajectory radius of curvature of the 5 m^2 Cabrinha® Switchblade is $2.23\sqrt{A_k} \approx 5.0$ m, which is approximately its span length. This is consistent with observations on kites dedicated to kite-surfing.

Coefficients ϵ_0, κ_ϵ, C_{l0} and κ_l are dimensionless quantities. Consequently, modifications presented in Eqns. (3.23) and (3.24) were kept for the next steps of this study.

3.7. Conclusion

In this chapter, the zero-mass kite model with straight and inelastic tether has been introduced. According to this model, an upper bound of the tether tension has been identified. Its classical version assumes a constant lift to drag angle and a constant lift coefficient. A comparison with experimental data have shown that this assumption is not realistic in terms of velocity amplitude and tether tension. Since ship motions are theoretically proportional to excitation forces, a correction of the classical zero mass model has been proposed. This modification assumes that the kite lift to drag angle and the kite lift coefficient are linearly dependent of the kite yaw rate. The resulting model is then dependent on four parameters. A good agreement is found between the experimental data and the modified zero mass model. However a phase difference is observed. This phase difference is probably due to the tether effect and the kite mass.

Tether effects are neglected with this kite model. Since the tether system is the link between the kite and the ship, it appears necessary to investigate the importance of the tether in such a system. Consequently, a tether analysis is provided in the next chapter.

4. Static analysis of tethers

Résumé: Analyse statique des lignes

Dans le chapitre précédent, pour obtenir une équation cinématique de vol de cerf-volant, une hypothèse de ligne droite et inélastique a été employée. Cette hypothèse est forte et mérite d'être discutée. Dans ce chapitre, un modèle analytique de ligne de cerf-volant est développé dans le cas d'un vol statique.

Le modèle de ligne se base sur l'équation de la chainette qui suppose une ligne inélastique et un chargement linéique constant. Ce modèle présente l'avantage d'être analytique. La forme de la ligne et la tension aux extrémités dépendent de la position du cerf-volant et du chargement aérodynamique sur la ligne. Ce problème peut également être résolu de façon inverse si la force aérodynamique du cerf-volant est connue. Le chargement aérodynamique varie le long de la ligne à cause du gradient de vent et de la direction locale de la ligne. Un modèle de chargement aérodynamique équivalent constant est donc proposé. Par ailleurs, la force aérodynamique du cerf-volant dépend de sa position, le problème est donc couplé. Ainsi, l'équation d'équilibre entre le cerf-volant et la ligne est résolue numériquement.

Dans un premier temps l'implémentation du modèle est vérifiée sur un cas académique d'une ligne soumis à son poids propre. Dans un second temps, le modèle de chargement équivalent est discuté au travers d'une comparaison avec une modélisation de ligne par éléments finis. Les résultats montrent que le fait de supposer un chargement aérodynamique constant n'est pas significatif sur les différences de tension et de direction entre les deux extrémités. En effet, les différences relatives entre les deux modèles en termes de tension et de direction sont respectivement inférieures à 2% et 1.2%.

Par la suite, avec le modèle de ligne présenté, les différences de tension et d'angle aux deux extrémités de la ligne sont étudiées en fonction du vent pour un cas de vol statique au zénith i.e. angle d'azimuth nul par rapport à la direction du vent. Pour se rapprocher d'un cas de vol dynamique, des vitesses de vent allant jusqu'à 65 $m.s^{-1}$ sont considérées. La différence de tension entre les deux extrémités tend vers zéro avec l'augmentation de la vitesse du vent. La différence d'angle entre les deux extrémités tend vers une valeur constante non nulle. En effet, la force aérodynamique du cerf-volant ainsi que le chargement aérodynamique de la ligne augmentent avec la vitesse du vent. Pour le cas considéré, à partir de 10 $m.s^{-1}$ de vent les lignes peuvent être considéré droites. En se basant sur le modèle cinématique de kite

sans masse, en vol dynamique, un vent apparent de 10 $m.s^{-1}$ correspond à un vent réel de 2 $m.s^{-1}$.

Par cette analyse on peut considérer que si les effets d'accélération sur lignes sont négligeables dans le cadre d'un vol dynamique, l'hypothèse de ligne droite nécessaire au développement du modèle cinématique de cerf-volant sans masse est raisonnable. Il serait alors intéreressant de poursuivre cette investigation pour quantifier l'effet de l'accélération sur les lignes en vol dynamique de cerf-volant.

4.1. Introduction

The tether is the interface between the kite and the ship. It seems crucial to investigate the role played by the tether in such a system. Using a classical kite, it can be observed that the tether sag is particularly important for a static kite flight configuration in a case of low wind speed. In a case of a dynamic kite flight, the tether sag may be quite small and the tether may be almost straight. This chapter is a first approach to investigate the effect of the tether on the kite flight. The benefit of the zero mass model (cf. Chap. 3) is its simplicity which is however due to some strong assumptions. The weight of the kite and the weight of the tether are neglected and the tether is assumed to be straight. Here, through a static analysis, the effect of the tether weight and shape on static kite flight configuration are investigated.

Tethers are currently made of fiber materials such as Dyneema® (Ultra-high-molecular-weight polyethylene, UHMWPE). This means that compression, transverse shear, bending and torsional stiffness of the tether can be neglected compared to the tensile stiffness. In addition, the tether shape is highly dependent on aerodynamic loading acting on the tether surface and tether gravity acting on the tether volume. This kind of structure has been studied for other industrial applications such as electrical power lines, anchored offshore structures, tethered underwater vehicles or sling loads. Tether models for airborne wind energy applications were inspired by these applications. Williams et al. (2007) developed a so-called lumped mass model for dynamic flight. The mass of each element is concentrated on each node and the distance between each node remains constant. Breukels and Ockels (2007) used discrete element modelling with inelastic bar elements. Argatov et al. (2011) took into account sag due to wind load and tether weight, assuming that the tension along the tether is constant. They proposed a method to calculate wind load by neglecting the tangential wind component relatively to the line. They showed how tether effects decrease the electric power production for a dynamic flight. A model considering the tether as a single straight elastic spring to account for material stiffness has been used in order to study the stability of the kite during a dynamic flight by Terink et al. (2011). All these tether models have been developed for dynamic flight and are still valid for static flight. Nevertheless, for discrete models, an artificial structural damping needs to be added to reach the static equilibrium as reported by Breukels and Ockels (2007).

Considering low wind velocities, tether sag could be important, therefore a single straight elastic spring modelling the tether (Terink et al., 2011) could not become a realistic enough assumption. Varma and Goela (1982) developed a soft kite tether model for static kite flights at zero azimuth angle. Their model is based on the catenary curve. They considered a flexible tether of constant length and mass per unit length. Indeed, the average aerodynamic loading applied on the tether is not significantly modified by increasing the length of the tether due to its tensile stiffness. Hobbs (1986) studied the influence of the wind velocity gradient effect on the tether shape for static kite flights at zero azimuth angle. He concluded his study on the wind profile influence arguing that the main factor influencing the tether shape is the mean quadratic wind velocity according to the altitude. On the other hand, being quasi-analytical, the model proposed by (Varma and Goela, 1982) has the potential to sufficiently reduce computation times in order to perform tether analysis at the early stage of the design.

This chapter provides a quasi-analytical formulation of the catenary curve (Irvine, 1981; Varma and Goela, 1982) to model a flexible tether of a constant length for any static kite flight position, with an arbitrary attachment point altitude on the ship deck, and with a wind velocity gradient law for kite towing forces estimation. The determination of tether's shape and tension only requires the solution of a one-dimensional transcendental equation with a fixed-point algorithm. This procedure improves the reliability and the convergence rate of 2D Newton's method suggested in (Irvine, 1981). A closed-form solution is presented to evaluate a mean aerodynamic loading on the tether according to the wind velocity gradient effect.

4.2. Mathematical model

4.2.1. Reformulation of the catenary

The tether model is based on the well-known catenary curve (Irvine, 1981). A constant load per unit length is applied on the tether. A and K points denote joint connections at each extremities of the tether, respectively for ship attachment point and kite position. The tether is assumed to be flexible, of a constant length and with no transverse shear and no bending stiffness. Consequently, the tether remains in a plane defined by $(A, \underline{x}_t, \underline{z}_t)$ of the reference frame $\mathbf{t}$. It is assumed that the ship is sailing at a constant speed on a straight course. Consequently, the ship fixed frame $\mathbf{s}$ is Galilean and $\left[\underline{x}_s, \underline{y}_s, \underline{z}_s\right] = \left[\underline{x}_n, \underline{y}_n, \underline{z}_n\right]$. The unit vector $\underline{z}_t$ is defined by the load per unit length $\underline{q}$ in Eq. (4.1).

$$\underline{q} = -\left\|\underline{q}\right\| \underline{z}_t = -q\underline{z}_t \tag{4.1}$$

The unit vector $\underline{y}_t$ is defined as $\underline{y}_t = \left(\underline{z}_t \times \underline{AK}\right) / \left\|\underline{AK}\right\|$, where "$\times$" denotes the cross product operator. In order to obtain a direct orthonormal coordinate system, the unit vector $\underline{x}_t$ is given by $\underline{x}_t = \underline{y}_t \times \underline{z}_t$. Figure 4.1 illustrates the coordinate systems $\mathbf{s}$ and $\mathbf{t}$.

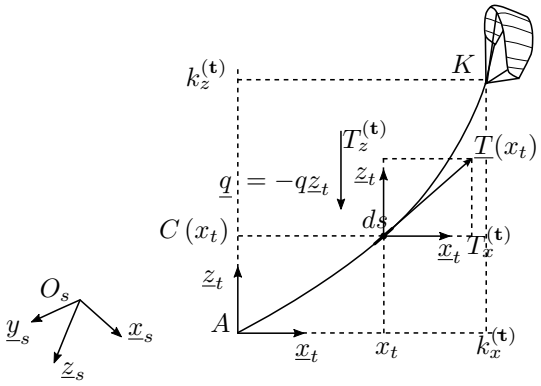

Figure 4.1.: Tether reference frame $\mathbf{t}$ and notations used for the development of the catenary equation

With the tension $\underline{T}$ along the tether and s the curvilinear abscissa, Eqns. (4.2) and (4.3) define respectively the static equilibrium of an infinitesimal tether length ds projected on $\underline{x}_t$ and $\underline{z}_t$. $T_x^{(\mathbf{t})}$ and $T_z^{(\mathbf{t})}$ denote respectively $\underline{T} \cdot \underline{x}_t$ and $\underline{T} \cdot \underline{z}_t$.

$$\frac{dT_x^{(\mathbf{t})}}{ds} = 0 \tag{4.2}$$

$$\frac{dT_z^{(\mathbf{t})}}{ds} - q = 0 \tag{4.3}$$

According to Eqns. (4.2) and (4.3), a catenary function C must verify the following equation:

$$\frac{q}{T_x^{(\mathbf{t})}} = \frac{C''(x_t)}{\sqrt{1 + C'(x_t)^2}} \tag{4.4}$$

Therefore, by integration of Eq. (4.4), C could be expressed as follows:

$$C(x_t) = \frac{T_x^{(\mathbf{t})}}{q} \cosh\left(\frac{q}{T_x^{(\mathbf{t})}} x_t + K_1\right) + K_2 \tag{4.5}$$

where K_1 and K_2 are two constants of integration. They are determined by the boundary conditions: constant tether length L_t, coordinates of $\underline{A} = [0, 0, 0]_{\mathbf{t}}^T$ and $\underline{K} = \left[k_x^{(\mathbf{t})}, 0, k_z^{(\mathbf{t})}\right]_{\mathbf{t}}^T$, which leads to:

$$0 = \frac{T_x^{(\mathbf{t})}}{q}\cosh\left(K_1\right) + K_2 \tag{4.6}$$

$$k_z^{(\mathbf{t})} = \frac{T_x^{(\mathbf{t})}}{q}\cosh\left(\frac{q}{T_{y_t}}k_x^{(\mathbf{t})} + K_1\right) + K_2 \tag{4.7}$$

$$L_t = \int_0^{k_x^{(\mathbf{t})}} \sqrt{1 + \left[C'\left(x_t\right)\right]^2} dx_t = \frac{T_x^{(\mathbf{t})}}{q}\left[\sinh\left(\frac{q}{T_x^{(\mathbf{t})}}k_x^{(\mathbf{t})} + K_1\right) - \sinh\left(K_1\right)\right] \tag{4.8}$$

Using trigonometric identities, constants K_1 and K_2 can be expressed thanks to the boundary conditions in order to obtain the function C. The function C can be expressed by following Eq. (4.9):

$$C_t\left(x_t\right) = \frac{k_z^{(\mathbf{t})}\sinh\left(\kappa x_t\right) + \lambda\left\{\sinh\left(\kappa y_t\right) - \sinh\left(\kappa k_x^{(\mathbf{t})}\right) + \sinh\left[\kappa\left(k_x^{(\mathbf{t})} - x_t\right)\right]\right\}}{\sinh\left(\kappa k_x^{(\mathbf{t})}\right)} \tag{4.9}$$

where λ and κ are defined by Eqns. (4.10) and (4.11):

$$\lambda = \frac{L_t\sinh\left(\kappa k_x^{(\mathbf{t})}\right) - k_z^{(\mathbf{t})}\left[\cosh\left(\kappa k_x^{(\mathbf{t})}\right) - 1\right]}{2\left[\cosh\left(\kappa k_x^{(\mathbf{t})}\right) - 1\right]} \tag{4.10}$$

$$\kappa^2\left[\left(k_x^{(\mathbf{t})}\right)^2 - L_t^2\right] = 2\left[1 - \cosh\left(\kappa k_x^{(\mathbf{t})}\right)\right] \tag{4.11}$$

It can be noticed that the catenary function does not depend on the load per unit length, q. Equation (4.11) can be rearranged in order to compute the value of κ. With $u = \kappa^2\left(k_x^{(\mathbf{t})}\right)^2$, $\bar{L}_t = \frac{L_t}{k_x^{(\mathbf{t})}}$ and $\beta = \frac{k_z^{(\mathbf{t})}}{k_x^{(\mathbf{t})}}$, Eq. (4.11) becomes:

$$u = \left\{\operatorname{argcosh}\left[\frac{u\left(\bar{L_t}^2 - \beta^2\right)}{2} + 1\right]\right\}^2 \tag{4.12}$$

The value of u is computed by applying the fixed-point algorithm to Eq. (4.12). The convergence is achieved for all positive values of u. Thus, for a given kite position K and a given ship attachment point position A, tether tension can be expressed by:

$$\underline{T}\left(x_t\right) = \left[\frac{q}{\kappa}, 0, \frac{q}{\kappa} C_t'\left(x_t\right)\right]_{\mathbf{t}}^{T} \tag{4.13}$$

It can be noticed that the inverse of κ is directly proportional to the tension in the $\underline{x}_t$ direction with the factor q. Consequently, tether shape and tension along the tether are determined for any kite and ship attachment point.

By contrast to the previous approach, an expression giving the kite location K, for a known tension at K, could be relevant in order to determine the minimal wind velocity required for a static flight. This expression is then developed. The tension is tangential to the tether, which means at K:

$$C_t'\left(k_x^{(\mathbf{t})}\right) = \sinh\left(\frac{q}{T_x^{(\mathbf{t})}} k_x^{(\mathbf{t})} + K_1\right) = \frac{T_z^{(\mathbf{t})}}{T_x^{(\mathbf{t})}} \tag{4.14}$$

Then, using Eqns. (4.6), (4.7) and (4.8), expressions for the kite location K with a given tether tension at K are:

$$k_x^{(\mathbf{t})} = \frac{T_x^{(\mathbf{t})}}{q}\left[\operatorname{argsinh}\left(\frac{T_z^{(\mathbf{t})}}{T_x^{(\mathbf{t})}}\right) - \operatorname{argsinh}\left(\frac{T_z^{(\mathbf{t})} - qL_t}{T_x^{(\mathbf{t})}}\right)\right] \tag{4.15}$$

$$k_z^{(\mathbf{t})} = \frac{T_x^{(\mathbf{t})}}{q}\left(\sqrt{1 + \left(\frac{T_z^{(\mathbf{t})}}{T_x^{(\mathbf{t})}}\right)^2} - \sqrt{1 + \left(\frac{T_z^{(\mathbf{t})} - qL_t}{T_x^{(\mathbf{t})}}\right)^2}\right) \tag{4.16}$$

Equations (4.15) and (4.16) are similar to Eqns. (1.27) and (1.28) given by Irvine Irvine (1981) in case of a flexible tether of a constant length and with a very large Young's modulus.

4.2.2. Tether Load Model

The load per unit length on the tether is given by Eq. (4.17), where $\underline{q}_w$ denotes the load per unit length due to wind and $\underline{q}_g$ denotes weight distribution, along the curvilinear abscissa.

$$\underline{q}\left(s\right) = \underline{q}_w\left(s\right) + \underline{q}_g = \underline{q}_w\left(s\right) + m_t g \underline{z}_n \tag{4.17}$$

where m_t denotes the mass per unit length of tether and g the acceleration due to gravity ($g = 9.81\ \mathrm{m\,s^{-2}}$).

Aerodynamic tether loading modeling q_w is rather tricky since a tether can encounter a wide range of Reynolds number. The flow around a circular cylinder has been widely studied in the past and is still a research topic as mentioned by Sarpkaya in his literature review

(2004). In addition, a textile rope has not exactly a circular section. Jung in (2009) performed wind tunnel experiments for various rope sections and various roughness surface at a Reynolds, $R_e = 84.0\ 10^3$. According to his measurements the drag coefficient can vary from 0.76 to 1.56 with orthogonal flow. Nevertheless, since the Reynolds effect and the surface roughness are out of the scope of the thesis, the Hoerner formulation (1965) was chosen similarly to many other authors involved in airborne wind energy. $\underline{U}_{rw}$ depends on altitude, and therefore $\underline{q}_w$ as well. Since the catenary tether model requires only constant load per unit length (*cf.* Sect.4.2.1), an approximation of constant wind tether load must be achieved. The determination of an equivalent altitude $\tilde{z}_n$ to evaluate $\underline{q}_w$ is proposed here. It is assumed that the tether is a straight line between A and K.

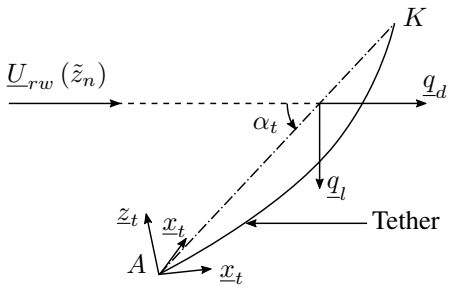

Figure 4.2.: Diagram of the tether wind load model

As illustrated in Fig. 4.2, wind load $\underline{q}_w$ can be decomposed into drag force $\underline{q}_d$ and lift force $\underline{q}_l$ (*cf.* Eq. (4.18)).

$$\underline{q}_w = \underline{q}_l + \underline{q}_d \tag{4.18}$$

$\underline{q}_d$ and $\underline{q}_l$ are determined thanks to Hoerner formulas (Hoerner, 1965), Eqns. (4.19) and (4.20), where a base drag coefficient of 1.1 is assumed for orthogonal flows ($\alpha_t = \pi/2$). ρ_a is the air density, d_t is the tether diameter and α_t is the angle of attack between the wind and the tether as described in Fig. 4.2.

$$\underline{q}_d = \frac{1}{2}\rho_a d_t \left[1.1\sin^3(\alpha_t) + 0.02\right] \|\underline{U}_{rw}(\tilde{z}_n)\|\, \underline{U}_{rw}(\tilde{z}_n) \tag{4.19}$$

$$\underline{q}_l = \frac{1}{2}\rho_a d_t \left[1.1\sin^2(\alpha_t)\cos(\alpha_t)\right] \|\underline{U}_{rw}(\tilde{z}_n)\| \frac{\underline{U}_{rw}(\tilde{z}_n) \times [\underline{U}_{rw}(\tilde{z}_n) \times \underline{AK}]}{\|\underline{U}_{rw}(\tilde{z}_n) \times \underline{AK}\|} \tag{4.20}$$

With respect to the ship velocity $\underline{U}_s$ and according to Eq. (3.6) , the relative wind velocity at the altitude $\tilde{z}_n$ is given by Eq. (4.21).

$$\underline{U}_{rw}(\tilde{z}_n) = \underline{U}_{ref}\left(\frac{\tilde{z}_n}{z_{ref}}\right)^{n_v} - \underline{U}_a \tag{4.21}$$

In order to conserve approximately the total force acting on the tether, $\tilde{z}_n$ is defined such that Eq. (4.22) is verified.

$$\left\|\underline{U}_{rw}\left(\tilde{z}_n\right)\right\|^2 = \frac{1}{\left(k_z^{(\mathbf{n})} - a_z^{(\mathbf{n})}\right)} \int_{a_z^{(\mathbf{n})}}^{k_z^{(\mathbf{n})}} \left\|\underline{U}_{rw}\left(z\right)\right\|^2 dz \tag{4.22}$$

This equation leads to Eq. (4.23), a second degree polynomial equation in $\tilde{z}_n^{n_v}$. Only the greatest root, which has a physical meaning is kept.

$$\begin{aligned} 0 = & \frac{\left\|\underline{U}_{ref}\right\|^2}{z_{ref}^{2n_v}} \tilde{z}_n^{2n_v} - 2\frac{\underline{U}_s.\underline{U}_{ref}}{z_{ref}^{n_v}} \tilde{z}_n^{n_v} - \left\|\underline{U}_{ref}\right\|^2 \frac{\left(k_z^{(\mathbf{n})}\right)^{2n_v+1} - \left(a_z^{(\mathbf{n})}\right)^{2n_v+1}}{(2n_v+1)\left(k_z^{(\mathbf{n})} - a_z^{(\mathbf{n})}\right) z_{ref}^{2n_v}} \\ & + 2\underline{U}_s.\underline{U}_{ref} \frac{\left(k_z^{(\mathbf{n})}\right)^{n_v+1} - \left(a_z^{(\mathbf{n})}\right)^{n_v+1}}{(n_v+1)\left(k_z^{(\mathbf{n})} - a_z^{(\mathbf{n})}\right) z_{ref}^{n_v}} \end{aligned} \tag{4.23}$$

It must be noticed that the definition of the equivalent altitude $\tilde{z}_n$, Eq. (4.22) is not correct to conserve the total force acting on the tether. Indeed, the load direction varies with the altitude which is not considered in Eq. (4.22). A better definition could have been:

$$\underline{U}_{rw}\left(\tilde{z}_n\right) = \frac{\underline{U}_2}{\sqrt{\left\|\underline{U}_2\right\|}} \tag{4.24}$$

with,

$$\underline{U}_2 = \frac{1}{\left(k_z^{(\mathbf{n})} - a_z^{(\mathbf{n})}\right)} \int_{S_{z_0}}^{K_{z_0}} \left\|\underline{U}_{rw}\right\| \underline{U}_{rw} dz \tag{4.25}$$

However, the previous proposition in Eq. (4.22) should be reasonable enough in order to achieve a closed-form formulation of the equivalent altitude $\tilde{z}_n$.

4.2.3. Aerodynamic Kite Model

For a static flight, forces acting on the kite must be opposed to the tether tension and vary with altitude due to the wind velocity gradient. Applying the first Newton's law to the kite, Eq. (4.26) is obtained:

$$0 = -\underline{T}\left(k_x^{(\mathbf{t})}\right) + \underline{L}_k + \underline{D}_k + \underline{W}_k \tag{4.26}$$

where:

- $\underline{T}\left(k_x^{(\mathbf{t})}\right)$ is the tether tension at kite location.
- $\underline{L}_k$ is the lift kite aerodynamic force.
- $\underline{D}_k$ is the drag kite aerodynamic force.
- $\underline{W}_k$ is the kite weight, $\underline{W}_k = +M_K g \underline{z}_n$ where M_K is the kite mass.

Kite weight is completely known. $\underline{D}_k$ is by definition in the direction of the relative wind and can be determined as follows:

$$\underline{D}_k = \frac{1}{2}\rho_a A_k C_{lk} \tan(\epsilon_k) \|\underline{U}_{rw}\| \underline{U}_{rw}, \tag{4.27}$$

where, ρ_a is the air density, A_k is the kite area and C_{lk} is the kite lift coefficient. According to the assumption of a constant lift-to-drag ratio, the magnitude of the lift, $\|\underline{L}\|$ can be determined by Eq. (4.28). In addition, by definition, the kite lift is orthogonal to the drag, which is expressed by Eq. (4.29).

$$\|\underline{L}_k\| = \frac{\|\underline{D}_k\|}{\tan(\epsilon_k)} \tag{4.28}$$

$$\underline{L}_k \cdot \underline{D}_k = 0 \tag{4.29}$$

One more equation is needed to determine the lift. As a balance is expected between kite forces and tether tension, we know that at least they must stay in the $\left(A, \underline{y}_t, \underline{z}_t\right)$ plane. This is a consequence of the projection of Eq. (4.26) on axis $\underline{y}_t$, which is expressed by the following Eq. (4.30):

$$(\underline{L}_k + \underline{D}_k + \underline{W}_k) \cdot \underline{y}_t = 0 \tag{4.30}$$

Thanks to the scalar Eq. (4.30), $L_{x,k}^{(\mathbf{t})}$ is given by Eq. (4.31):

$$L_{y,k}^{(\mathbf{t})} = -\left(D_{y,k}^{(\mathbf{t})} + W_{y,k}^{(\mathbf{t})}\right) \tag{4.31}$$

Equations (4.28) and (4.29) lead to a second order polynomial equation in $L_{z,k}^{(\mathbf{t})}$. $L_{z,k}^{(\mathbf{t})}$ solution is given by Eq. (4.32):

$$L_{z,k}^{(\mathbf{t})} = \frac{\sqrt{\Delta} - L_{y,k}^{(\mathbf{t})} D_{y,k}^{(\mathbf{t})} D_{z,k}^{(\mathbf{t})}}{\left[\left(D_{x,k}^{(\mathbf{t})}\right)^2 + \left(D_{z,k}^{(\mathbf{t})}\right)^2\right]}, \tag{4.32}$$

$$\Delta = \frac{\left(D_{x,k}^{(\mathbf{t})}\right)^2 \|\underline{D}_k\|^2}{\tan^2(\epsilon_k)} \left[\left(D_{x,k}^{(\mathbf{t})}\right)^2 + \left(D_{z,k}^{(\mathbf{t})}\right)^2 - \left(L_{y,k}^{(\mathbf{t})}\right)^2 \tan^2(\epsilon_k)\right], \tag{4.33}$$

where Δ, Eq. (4.33) is the discriminant of the second order polynomial equation in $L_{z,k}^{(\mathbf{t})}$. Finally, $L_{x,k}^{(\mathbf{t})}$ is expressed in Eq. (4.34) using Eq. (4.29):

$$L_{x,k}^{(\mathbf{t})} = -\frac{L_{y,k}^{(\mathbf{t})} D_{y,k}^{(\mathbf{t})} + L_{z,k}^{(\mathbf{t})} D_{z,k}^{(\mathbf{t})}}{D_{x,k}^{(\mathbf{t})}} \tag{4.34}$$

The condition $\Delta \geq 0$ is a necessary condition to allow a static kite flight.

4.2.4. Kite static equilibrium

The equilibrium equation of the kite, Eq. (4.26), can be solved by coupling these models. Since the tether force depends on the kite position into the plane $(\underline{x}_t, \underline{z}_t)$, the equilibrium must be searched in a plane. The plane $(\underline{x}_t, \underline{z}_t)$ is defined with the tether loading $\underline{q}$ depending on the kite position cf. Eqns. (4.19) and (4.20). The equilibrium solution can be searched in a arbitrary plane. Here, the equilibrium is searched into the plane $(A, \underline{x}_{\tilde{t}}, \underline{z}_{\tilde{t}})$ where, $\underline{x}_{\tilde{t}}$ and $\underline{z}_{\tilde{t}}$ are defined with the tether loading corresponding to the static kite position $\tilde{K}$ according to the zero mass modeling:

$$\begin{cases} \tilde{\phi}_k & = \pm \arccos\left(\frac{\sin \epsilon_k}{\cos \tilde{\theta}_k}\right) \\ \underline{\tilde{K}}^{(\mathbf{rw})} & = L_t \left[\cos\tilde{\theta}_k \cos\tilde{\phi}_k, \cos\tilde{\theta}_k \sin\tilde{\phi}_k, \sin\tilde{\theta}_k\right]^T + \underline{A}^{(\mathbf{rw})} \\ \underline{z}_{\tilde{t}} & = \frac{-\underline{q}}{\left\|\underline{q}\right\|} \\ \underline{y}_{\tilde{t}} & = \left(\underline{z}_{\tilde{t}} \times \underline{A\tilde{K}}\right) / \left\|\underline{A\tilde{K}}\right\| \\ \underline{x}_{\tilde{t}} & = \underline{y}_{\tilde{t}} \times \underline{z}_{\tilde{t}} \end{cases} \tag{4.35}$$

Then, this plane remains constant and can be denoted by $(A, \underline{x}_{\tilde{t}}, \underline{z}_{\tilde{t}})$. A Newton-Raphson algorithm, is used to solve the kite static equilibrium. The initial condition of the algorithm is defined by Eqns. (4.15) and (4.16), where the tension $\underline{T}$ is equal to the aerodynamic forces applied to the kite at position $\underline{\tilde{K}}^{(\mathbf{rw})}$ and $\mathbf{t}$ is equal to $\tilde{\mathbf{t}}$. After each iteration of the algorithm the frame $\mathbf{t}$ changes until convergence.

4.2.5. Verification of the implementation

The implementation of the presented model is verified thanks to experimental data provided by Irvine and Sinclair in Irvine and Sinclair (1976). In this experiment, the two extremities of a cable were horizontally attached. The cable length was 1.20 m, the cable cross sectional area was 1.58 10^{-6} m^2 and the Young's modulus of the cable was 1.00 10^{11} $N.m^{-2}$. The horizontal distance between the attachment points was 1.00 m. A total of 20 weights of 2.45

N were added to the cable with ferrules in order to neglect the cable bending stiffness. From the attachment point, the weights were attached with a distance of 0.03 m and the weights were equally spaced each other by a distance of 0.06 m. The weight of the cable, ferrules plus weights were 50 N. Figure 4.3 shows the cable corresponding to the experiment in (Irvine and Sinclair, 1976) (dashed line) and the corresponding cable shape predicted by the model, Eqns. (4.9 - 4.12). The experimental cable shape from (Irvine and Sinclair, 1976) has been graphically reported (digitized with a dedicated software).

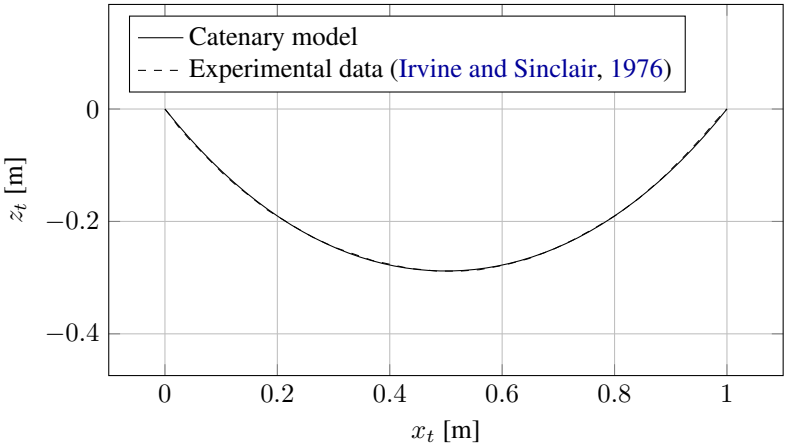

Figure 4.3.: Tether shape; comparison of the presented model with experimental data of Irvine and Sinclair (1976)

The presented model fits pretty well with the experimental data Irvine and Sinclair (1976) and can be considered as being validated. Nevertheless, a comparison between the whole presented model and static kite flight must be investigated as well.

4.3. Case of Study

The following application is based on the case study of Dadd (2013) where kite parameters have been extrapolated from experimental data measured on a *Flexifoil Blade III* in (Dadd et al., 2010). Kite and tether characteristics are presented in table 4.1. Tether features, line mass and diameter (cf. table 4.1), have been estimated using maximum wing loading of 1.10^3 N.m^{-2} with a safety coefficient of 2.

The ship attachment point altitude, $a_z^{(\mathbf{n})}$, is 10 m and the true wind speed is measured at an altitude of $z_{ref} = 10$ m. According to (Ittc, 2014), the wind velocity gradient parameter is $n = 1/7$. The air density is $\rho_a = 1.2$ kg.m^{-3}.

***Flexifoil Blade III* specs extrapolated by Dadd 2013**	
Kite surface	320 m^2
Kite mass*	150 kg
Tether length	300 m
Kite lift coefficient	0.776 $[-]$
Lift to drag ratio angle	12°
Tether specs (estimation)	
Line mass*	0.45 $kg.m^{-1}$
Diameter*	30.0 mm
Drag coefficient for orthogonal flow	1.1

Table 4.1.: Kite and tether characteristics for the study; (*) denotes estimation

4.4. Comparison with a finite element tether modeling

With the model presented in this study, the aerodynamic load is assumed to be constant along the tether. This section aims to assess the importance of neglecting the evolution of the aerodynamic load with the altitude and the angle between $\underline{U}_{rw,ka}$ and the local tangent vector direction of the tether. The modeling is compared with a finite element analysis of the tether where the evolution of the aerodynamic load is taken into account.

The finite element modeling is performed using quasi-elastic bars (linear truss) of constant length with the software Abaqus (Hibbett et al., 1998). A backward Euler implicit numerical scheme is used. The initial position corresponds to the catenary solution. The aerodynamic loading is gradually applied to the tether with a linear ramp. It is assumed that the static equilibrium is reached when the ratio between kinetic energy and the strain energy is less than 10^{-4}. For practical reasons, it was easier to apply an aerodynamic loading transversaly to the elements according to the Morison formula:

$$q_l = \frac{1}{2}\rho_a d_t U_{rw}^2 \cdot 1.1 \sin^2 \alpha_t \tag{4.36}$$

The comparison is performed with kite specs presented in Sec. 4.3 with no ship speed and an attachment point at zero altitude. The tether is considered to be in Dyneema® SK78. According to the manufacturers data and a linear regression in Annex B.2.3, the relationship between the mass per unit of length [$kg.m^{-1}$] and the diameter [m] can be expressed as follows:

$$d_t^2 = 1.98 \cdot 10^{-3} m_t \tag{4.37}$$

The two tether diameters tested are $30 \cdot 10^{-3}$ mm and $60 \cdot 10^{-3}$ mm corresponding respectively to 0.455 $kg.m^{-1}$ and 1.82 $kg.m^{-1}$. Since the presented model assumes the tether to

be inelastic, a Young modulus convergence is performed in Annex B.2.1 for making each element quasi-inelastic. Then, a mesh convergence is performed in Annex B.2.2. These convergence procedures lead to a Young's modulus of $10^4 E_{sk78}$ (where $E_{sk78} = 65.7$ GPa) and to 30 elements of equal length.

The equilibrium between the kite and the tether is performed with the presented model for different wind speed and different kite azimuth. All cases presented assume no ship forward speed. True wind speeds tested are $\{5,\ 7.5,\ 10\}$ m.s^{-1}. Three azimuth angles are tested, a first one at zero azimuth angle, a second one around 40° and 50° azimuth angle and a third one around 70° and 75°. The angles of azimuth are not identical as they are resulting from the equlibrium (cf. § 4.2.4). Boundary conditions applied to the finite element model are the position of the tether extremities computed with the presented model. The comparison between the two models is focused on the direction of the tether tension at the attachment point A and at the kite extremity K, both in terms of direction and magnitude. The difference of tension direction $\Delta\nu$ is expressed as follows:

$$\Delta\nu = \arccos\left(\frac{\underline{T}_{cat}\cdot\underline{T}_{fem}}{\|\underline{T}_{cat}\|\,\|\underline{T}_{fem}\|}\right), \tag{4.38}$$

where $\underline{T}_{cat}$ and $\underline{T}_{fem}$ denote respectively the tether tension obtained with the presented model and the finite element method. The relative difference of tension magnitude is expressed as follows:

$$\Delta T = \frac{\underline{T}_{cat} - \underline{T}_{fem}}{\left|\underline{T}_{fem}\right|} \tag{4.39}$$

Figure 4.4 contains plots of the difference of tension direction in degree and plots of the relative difference of tension magnitude in percentage. $\times$ denotes the results at the attachment point on the deck A and + denotes the results at the kite location. Each column corresponds to a true wind speed and each group of two rows corresponds to a tether diameter, 0.03 m and 0.06 m.

It can be noticed that the difference in terms of tension direction remains within a range of $\pm$ 1.2° and the relative difference of magnitude remains within a range of $\pm$ 2%. These differences are acceptable. The effect of the evolution of the aerodynamic wind load with the altitude is not very significant on the final equilibrium compared to an equivalent constant aerodynamic wind load obtained according to the method developed in the § 4.2.3. This comparison confirms the statement given by Hobbs (1986) arguing that the main factor influencing the tether shape is the mean quadratic wind velocity according to the altitude.

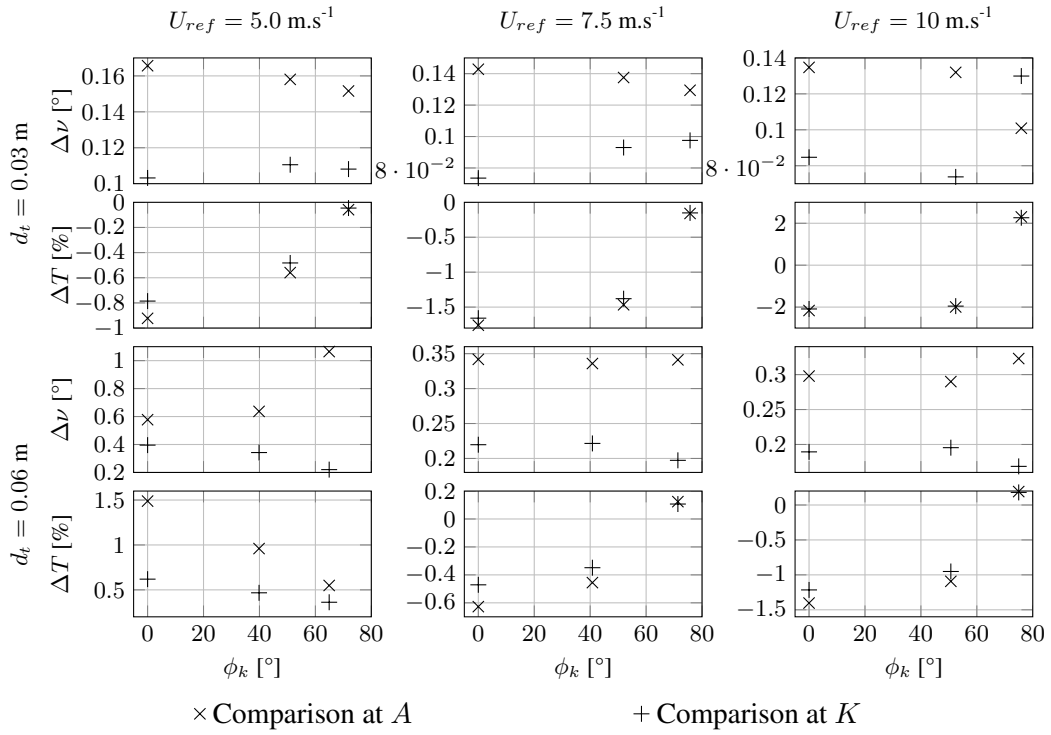

Figure 4.4.: Comparison of the presented model with a finite element tether simulations

4.5. Tether effect on static kite flight configurations

4.5.1. Results

Figure 4.5 represents static kite flight positions for different azimuth angles at wind condition $\underline{U}_{ref} = [7.5, 0, 0]^T_{\mathbf{n}}$ m.s^{-1} and ship velocity $\underline{U}_s = [0, 7.5, 0]^T_{\mathbf{n}}$ m.s^{-1}. Static kite flight positions define the flight window edge. Two models are compared: the zero mass model in dashed line and the catenary formulation in solid line.

The top of Figs. 4.6 and 4.7 show the angle between the tether tension at positions$A$ and K:

$$\nu = \arctan\left(C'\left(k_x^{(\mathbf{t})}\right)\right) - \arctan\left(C'\left(a_x^{(\mathbf{t})}\right)\right) \tag{4.40}$$

The bottom of Fig. 4.6 and the middle of Fig. 4.7 show the relative difference between the magnitude of the tether tension at K and A in percentage:

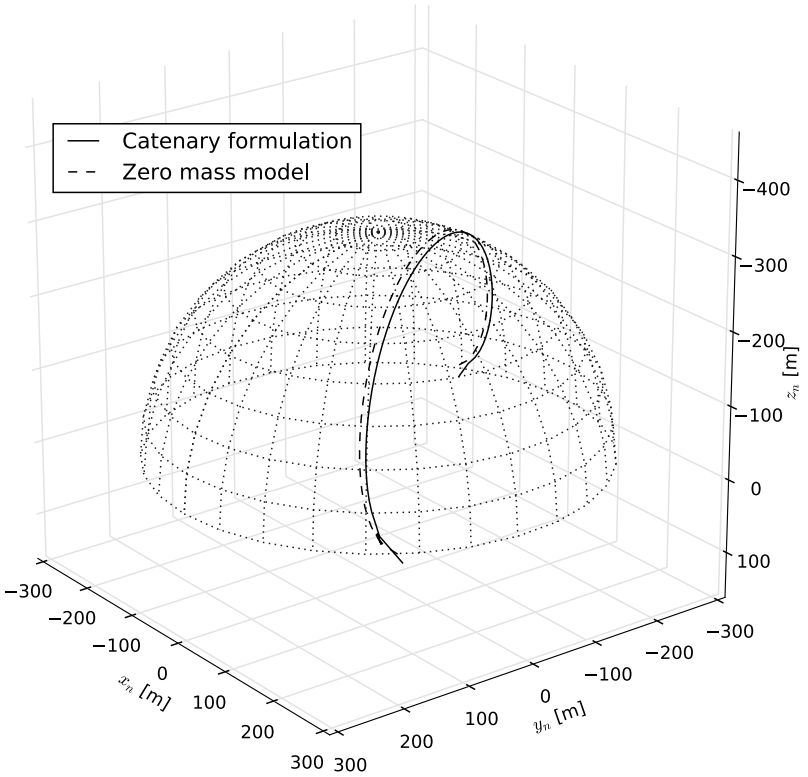

Figure 4.5.: Kite flight position for azimuth angles from -78° to 78° calculated with the catenary formulation in solid line and with the zero mass model in dashed line.

$$\Delta_T = \frac{\left\|\underline{T}\left(k_x^{(\mathbf{t})}\right)\right\| - \left\|\underline{T}\left(a_x^{(\mathbf{t})}\right)\right\|}{\left\|\underline{T}\left(k_x^{(\mathbf{t})}\right)\right\|} \tag{4.41}$$

Fig. 4.6 compares ν and Δ_T for azimuth angles from -78° to 78° in the same wind speed and ship velocity as in Fig. 4.5. Fig. 4.6 compares ν and Δ_T with zero ship speed and zero azimuth angle for different wind speeds from 0 m.s^{-1} to 65 m.s^{-1}. With this kite flight condition, the true wind speed, the relative wind speed and the apparent wind speed are the same. Neglecting the effect of the altitude of the tether attachment point and assuming straight lines, the apparent wind speed for a dynamic flight case can be maximized as follows (cf. Eq. (3.17)):

$$U_{aw} \leq U_{ref}\left(\frac{L_t\sqrt{\frac{n_v}{n_v+1}}}{z_{ref}}\right)^{n_v}\frac{\sqrt{\frac{1}{n_v+1}}}{\sin\epsilon_k} \tag{4.42}$$

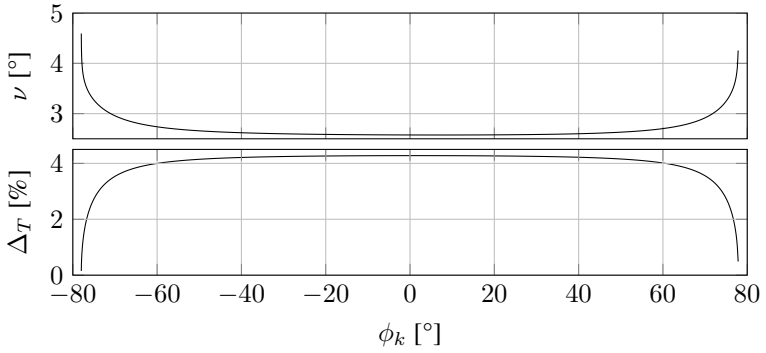

Figure 4.6.: Difference of tether tension between A and K for different kite azimuth angle; in terms of direction on the top; in terms magnitude on the bottom

At the bottom, Fig. 4.7 plots U_{ref}^{eqv} the equivalent true wind velocity corresponding to the highest apparent wind speed for a dynamic flight case according to the Eq. (4.42). Consequently, U_{ref}^{eqv} can be expressed as follows:

$$U_{ref}^{eqv} = \frac{U_{ref}}{\left(\frac{l_t\sqrt{\frac{n_v}{n_v+1}}}{z_{ref}}\right)^{n_v} \frac{\sqrt{\frac{1}{n_v+1}}}{\sin\epsilon_k}} \tag{4.43}$$

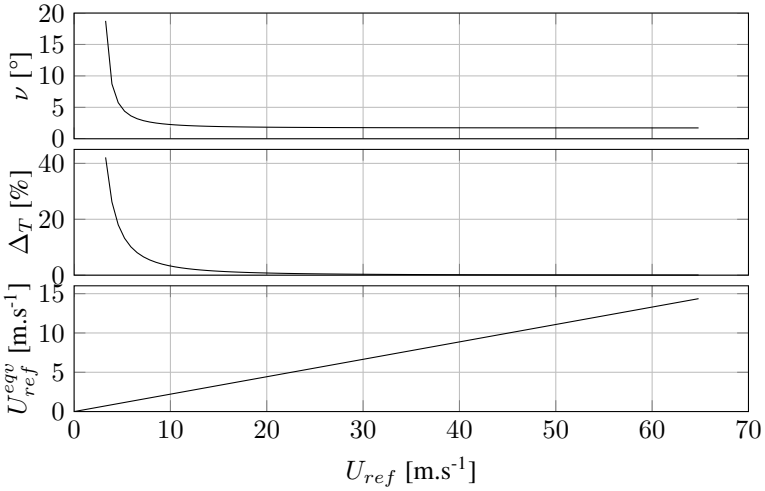

Figure 4.7.: Difference of tether tension between positions A and K for different wind speeds at the altitude of measurement z_{ref}. At the top side: angle between the tension direction at A and K. At the middle: relative difference of tension between A and K. At the bottom: equivalent reference wind speed in case of dynamic flight, cf. Eq. (4.43).

4.5.2. Analysis

Figures 4.5 and 4.6 investigates the influence of the kite position along the wind window edge. According to Fig. 4.5, the wind window obtained with the catenary formulation is smaller than the wind window obtained with the zero mass model. According to Fig. 4.6, the evolution of ν the angle between the tether tension at A and K, and the relative difference Δ_T between the magnitude of the tension at K and A, are almost symmetrical with respect to zero azimuth angle and remains almost constant between -70° and 70° of azimuth angle. ν has a minimal value of 2.58° at zero azimuth angle. Near the extreme azimuth angles, -78° and 78°, ν is slightly superior to 4°. The maximal value of Δ_T is 4.3% for a zero azimuth angle. The relative difference decreases for the extreme azimuth angles and tends to 0%.

Figure 4.7 investigates the influence of the true wind speed for a zero azimuth angle position and zero ship speed. The lower wind speed allowing a static flight is around 3 m.s^{-1}. For $U_{ref} = 3.27$ m.s^{-1}, ν is maximal and reaches 18.75°. Δ_T is maximum (43.14%) at $U_{ref} = 3.27$ m.s^{-1}. ν and Δ_T decreases when the wind speed increases. ν tends to a non zero value 1.7°. Δ_T tends to zero.

4.5.3. Discussion

At extreme azimuth values the tether is almost horizontal and the kite is low in terms of altitude. For these kite positions, the tether load per unit length is almost normal to $\underline{AK}$. Consequently, the difference of the tether tension norm at A and K tends to zero. The aerodynamic kite forces and the aerodynamic part of the tether load per unit length are lower due to the wind gradient. For a constant kite tension, the lower the tether load is , the lower the angle between the tether tension at A and K is . On the contrary, for a constant tether load per unit length, the lower the tether tension is, the more important is ν. At extreme azimuth angles the two phenomenon are in competition. For this case of study, results show that the decrease of aerodynamic forces is more significant than the decrease of tether load per unit length. Near zero azimuth angle, Δ_T is maximum whereas ν is minimum. Here again, the increase of the aerodynamic kite force is more significant than the increase of tether load per unit length.

Concerning the effect of the true wind speed, Fig. 4.7 shows the more important the wind speed is, the less significant is the tether effect in terms of tension. The relative difference between the tether tension norm at A and K tends towards zero and the angle between the tether tensions converges to a constant value. This shows that there is a balance between the increase of kite aerodynamic loading and the increase of the tether aerodynamic load per unit length. Nevertheless, at high wind speed, the constant angle between the tether tension is small, 1.7°. This shows that for high wind velocities (greater than 10 m.s^{-1}for static flight) a straight tether assumption is reasonable. Moreover the bottom of Fig. 4.7 shows the equivalent true wind speed for a dynamic flight. For instance, with a true wind speed of 10 m.s^{-1} at the reference altitude for static flight, the equivalent reference wind velocity is around 2 m.s^{-1} for dynamic flight. Consequently, if the effects of the tether acceleration are supposed negligible, even for reasonable true wind speed (greater than 2 m.s^{-1}), the straight tether assumption remains reasonable in case of a dynamic flight. However, a dynamic analysis of the tether should be carried out to confirm this assumption.

At low wind speed lower than 10 m.s^{-1}, in case of a static kite flight, the tether cannot be considered as a straight line. The difference of tension between positions A and K becomes significant. Under $U_{ref} = 3.27$ m.s^{-1}, no solution of kite equilibrium are found above the sea level. Kite and tether weights dominate the aerodynamic forces. However, since the kite launch step begins with a quasi static kite flight, a low wind limit of operability could be investigated according to the catenary formulation.

4.6. Conclusion

A static tether analysis has been performed according to an analytical modeling. The tether model was based on the well-known catenary equation. The tether load per unit length was assumed constant in order to be consistent with the catenary model requirements. The

kite was modeled assuming a constant lift to drag ratio and lift coefficient and taking into account its weight. Since the catenary model requires that the tether remains in a plane, an analytical method to determine the kite forces has been developed in order to complete this requirement. The determination of the kite position was performed in agreement with tether and kite models.

Results show that tether effects could be important at extreme azimuth angles. However, for high wind speed the effect of the tether on the difference of tension between the tether attachment point and the kite are not significant. Consequently, the straight tether assumption as used in the zero mass model should be reasonable for high wind speed greater than 10 $m.s^{-1}$. In a case of dynamic kite flight the straight tether assumption is relevant for reference wind speed greater than 2 $m.s^{-1}$. At low wind speed, the tether tension at the kite is clearly different from the tether tension at the attachment point. The tether weight can dominate the aerodynamic load on the tether.

Furthermore, this first approach shows that a low wind limit criterion enabling a static kite flight could be developed with this model by neglecting the aerodynamic load on the tether. Moreover, even if this model shows that the tether is almost straight for high wind speed and that a straight tether assumption seems reasonable, an investigation of the acceleration effect of the tether should be conducted.

5. Low wind limit of kite operability

Résumé: Vent minimum d'utilisation d'un cerf-volant

Le vol d'un cerf-volant pendant les procédures de lancement et de récupération peut être considéré comme quasi-statique. La flèche de la ligne peut être alors importante et ce d'autant plus que le vent est faible. Afin d'éviter l'accrochage et le ragage de la ligne qui pourrait entrainer une perte de control du cerf-volant, les lignes doivent malgré tout rester au-dessus du pont du navire. Dans ce chapitre cette contrainte d'utilisation en termes de vitesse de vent minimum est formalisée mathématiquement au travers du modèle de ligne chainette introduit au chapitre précédent.

En négligeant le chargement aérodynamique de la ligne devant son poids propre, un critère analytique dépendant des caractéristiques du cerf-volant et de la ligne est développé, cf. Eq. (5.9). En considérant un cerf-volant de 0.5 kg.m^{-2} avec un coefficient de portance de 0.7, la vitesse de vent minimum de lancement d'un cerf-volant en vol quasi-statique est de 3.4 m.s^{-1}.

L'hypothèse négligeant le chargement aérodynamique est discutée. Il est montré qu'en utilisant une ligne en Ultra-High-Molecular-Weight Polyethylene, la proportion entre l'effort aérodynamique et le poids propre de la ligne diminue en fonction du diamètre de la ligne. En considérent un vent de 3.4 m.s^{-1}, l'effort aérodynamique sur la ligne ne représente plus que 20% du poids propre à partir de 7 mm de diamètre.

5.1. Introduction

Most kite launch steps begin by a quasi-static flight at zero azimuth angle. Therefore, the low wind limit in terms of velocity for static kite flight at zero azimuth angle is an important parameter. It has been shown in Sec. 4, that at low wind speed, the tether weight dominates the aerodynamic tether load. Consequently, neglecting the aerodynamic load on the tether, an analytical criterion to estimate the low wind limit of operability is developed in this section.

5.2. An analytical criterion

Obviously, a tether should not touch the ship deck or the water. In that case, friction with the ship deck or the water could have a dramatic effect on the material durability and kite control. This leads to the mathematical condition that all points of the tether must be above the attachment point, as shown in Fig. 5.1. The mathematical expression of this limit is given by Eq. (5.1).

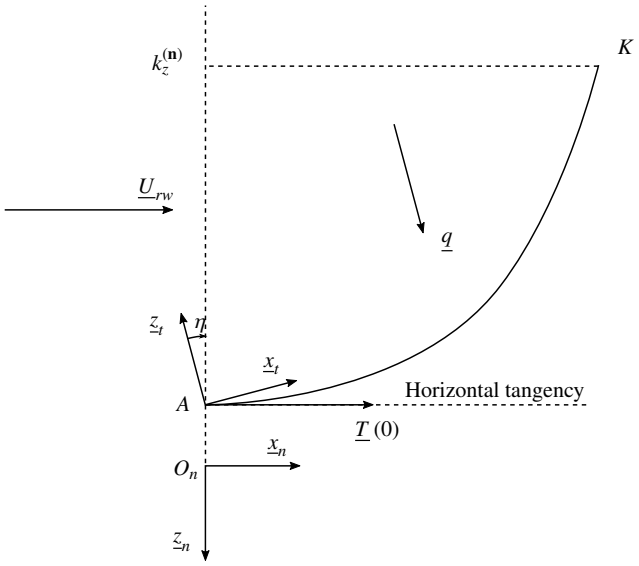

Figure 5.1.: Diagram of the lower limit static flight case

$$\underline{T}\,(0) \cdot \underline{z}_n = 0 \tag{5.1}$$

In the static kite flight case at zero azimuth angle, the first Newton's law applied to the tether and projected on axis $\underline{z}_n$, in accordance with the condition given by Eq. (5.1), leads to Eq. (5.2).

$$L_{z,k}^{(\mathbf{n})} + W_{z,k}^{(\mathbf{n})} + l_t q_z^{(\mathbf{n})} = 0 \tag{5.2}$$

Therefore, the relative wind at the kite location is given by Eq. (5.3).

$$U_{rw} = \sqrt{\frac{2\left|W_{z,k}^{(\mathbf{n})} + l_t q_z^{(\mathbf{n})}\right|}{\rho_a A_k C_{L,k}}} \tag{5.3}$$

In the static kite flight at zero azimuth angle, the kite position in frame $\mathbf{n}$, compared to the position in frame $\mathbf{t}$, is defined by the angle $\eta = \arctan\left(\underline{q} \cdot \underline{x}_n / \underline{q} \cdot \underline{z}_n\right)$. Kite altitude in $\mathbf{n}$ is given by:

$$k_z^{(\mathbf{n})} = a_z^{(\mathbf{n})} - k_x^{(\mathbf{t})} \sin(\eta) - k_z^{(\mathbf{t})} \cos(\eta) \tag{5.4}$$

Then, assuming $\underline{U}_{rw}$ and $\underline{U}_a$ are co-linear, the wind velocity at the measurement altitude is given by Eq. (5.5) by inserting Eqns. (5.2) and (5.3) into Eq. (4.21) and reorganizing:

$$U_{ref,min} = \frac{(-z_{ref})^{n_v}}{\left[-a_z^{(\mathbf{n})} + k_x^{(\mathbf{t})} \sin(\eta) + k_z^{(\mathbf{t})} \cos(\eta)\right]^{n_v}} \left[\sqrt{\frac{2\left(W_{z,k}^{(\mathbf{n})} + l_t \underline{q} \cdot \underline{z}_n\right)}{\rho_a A_k C_{L,k}}} + U_a\right] \tag{5.5}$$

Since $\underline{q}$ depends on $U_{ref,min}$ (cf. Eqns. (4.17 - 4.21)), this last equation needs to be solved. Thus, rather than to give a numerical solution of the problem, a closed-form approximation of the minimal wind velocity required for a static flight is provided assuming that the load per unit length on the tether is only due to the gravity. Therefore, $\underline{z}_t$ is equal to $\underline{z}_n$, η is equal to zero and the load per unit length, $\underline{q} = \underline{q}_g$, is constant. Then, the closed-form Eq. (5.3) becomes:

$$U_{rw} = \sqrt{\frac{2g\left(M_k + m_t l_t\right)}{\rho_a A_k C_{L,k}}} \tag{5.6}$$

where $g = 9.81$ m.s^{-2} is the acceleration due to gravity. Using Eqns. (4.16) and (4.21), the lower limit is:

$$U_{ref,min} = \frac{(-z_{ref})^{n_v} \left(\sqrt{\frac{2g(M_k + l_t m_t)}{\rho_a A_k C_{L,k}}} + U_a\right)}{\left\{-a_z^{(\mathbf{n})} + \tan(\epsilon_k)\left(l_t + \frac{M_k}{m_t}\right)\left[\sqrt{1 + \left(\frac{m_t l_t}{(m_t l_t + M_k)\tan(\epsilon_k)}\right)^2} - 1\right]\right\}^{n_v}} \tag{5.7}$$

For dimensional analysis, this last equation becomes non-dimensional, with:

$$\begin{cases} \tilde{U} & = U_{ref,min}\sqrt{\frac{A_k \rho_a C_{L_K}}{2gM_k}} \\ \tilde{l}_t & = \frac{m_t l_t}{M_k} \\ \tilde{a}_z & = \frac{a_z^{(\mathbf{n})}}{z_{ref}} \\ \tilde{U}_a & = U_a\sqrt{\frac{A_k \rho_a C_{L_K}}{2gM_k}} \\ \tilde{m} & = \frac{-z_{ref} m_t}{M_k} \end{cases} \tag{5.8}$$

Then $\tilde{U}$ could be expressed as follows:

$$\tilde{U} = \frac{\sqrt{1+\tilde{l}_t} + \tilde{U}_a}{\left\{ \tilde{a}_z + \tan(\epsilon) \frac{\left(1+\tilde{l}_t\right)}{\tilde{m}} \left[\sqrt{1 + \left[\frac{\tilde{l}_t}{\tan(\epsilon)\left(1+\tilde{l}_t\right)} \right]^2} - 1 \right] \right\}^{n_v}} \tag{5.9}$$

5.3. Analysis

The parameter $\tilde{L}_t$ can be considered as the dimensionless tether length. The attachment point altitude is non-dimensional using the wind measurement altitude, which leads to the parameter $\tilde{a}_z$. The parameter $\tilde{m}$ characterizes the tether mass per unit length compared to the kite mass. This last parameter provides information on the structural and material design priority between the tether and the kite, it increases when the ratio of safety factors between the line and the kite increases. $\tilde{U}$ and $\tilde{U}_a$ denote respectively the low wind limit parameter and the ship speed parameter.

$\tilde{U}$ increases with the parameter $\tilde{m}$. Analyzing the derivative of $\tilde{U}$ with respect to ϵ_k, it can be shown that $\tilde{U}$ increases with the lift to drag angle. On the contrary, $\tilde{U}$ decreases with $\tilde{a}_z$. At the beginning of a launch step, $\tilde{L}_t = 0$, and $\tilde{U}$ becomes:

$$\tilde{U} = \frac{1 + \tilde{U}_a}{\tilde{a}_z^{n_v}} \tag{5.10}$$

As expected, with no tether, the low wind limit is only dependent of the tether attachment point altitude and of the kite mass, area and lift coefficient. The derivative of $\tilde{U}$ with respect to $\tilde{L}_t$ at $\tilde{L}_t = 0$ is:

$$\left.\frac{\partial \tilde{U}}{\partial \tilde{L}_t}\right|_{\tilde{l}_t=0} = \frac{1}{2\tilde{a}_z^{n_v}} \tag{5.11}$$

Since $\tilde{a}_z$ is always positive for kite applications, near $\tilde{L}_t = 0$, the required wind speed increases with the tether length. When the tether length tends towards infinity, the non-dimensional low wind limit is equivalent to:

$$\lim_{\tilde{L}_t \to +\infty} \tilde{U} = \left(\frac{\tilde{m} \cos \epsilon_k}{1 - \sin \epsilon_k} \right)^{n_v} \tilde{L}_t^{\left(\frac{1}{2} - n_v\right)} \tag{5.12}$$

$\tilde{m}$ is always positive, consequently if $n_v < 1/2$, the required wind speed tends towards infinity. If $n_v > 1/2$ the required wind speed tends towards zero. In the special case

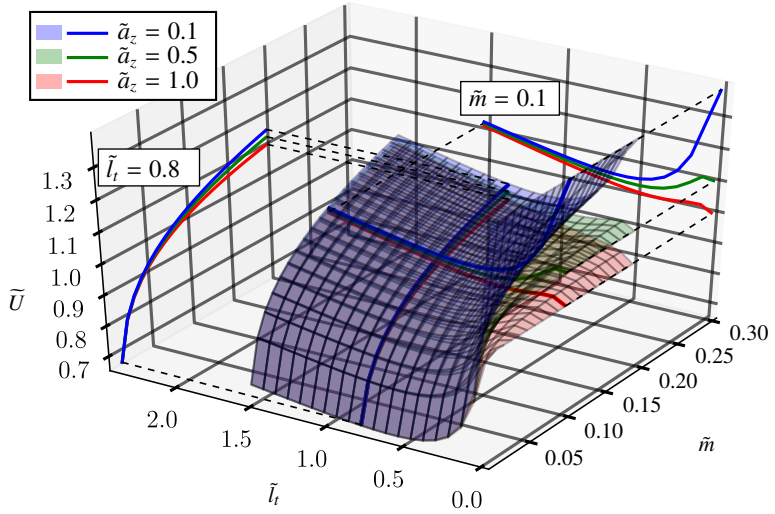

Figure 5.2.: Surface plots, for 3 fixed values of $\widetilde{a}_z$, 0.1, 0.5 and 1, of the non-dimensional minimum wind velocity $\widetilde{U}$ versus $\tilde{m}$ and $\tilde{l}_t$

$n_v = 1/2$, the non-dimensional limit tends towards the constant $\sqrt{\tilde{m}/\tan\epsilon_k}$. However, for a realistic wind gradient, the typical value of n_v is $1/7$, therefore the required wind speed should tend toward infinity.

For intermediate values of the tether length, the variation of the low wind limit according to the tether length is less obvious. Consequently a numerical analysis has been carried out. Figure 5.2 represents three surface plots of the non-dimensional minimal wind velocity $\tilde{U}$ defined in Eq. (5.9) versus the two non-dimensional parameters $\tilde{m}$ and $\tilde{L}_t$, for $\tilde{U}_a = 0$ and fixed values of $\tilde{a}_z$, 0.1, 0.5 and 1. The wind gradient parameter is taken to the classical value $n_v = 1/7$. An optimal tether length can appear to minimize $\tilde{U}$. Finally the effective minimal wind velocity $U_{ref,min}$ is obtained by dividing $\tilde{U}$ by the factor $\sqrt{A_k\rho_a C_{lk}/2W_k}$.

According to the specs of kite dedicated to the kite-surf with an inflatable leading edge and kites built within the beyond the sea® project, the ratio between the kite mass and the kite area is around 0.5 kg.m^{-2}. According to the experimental data in (Dadd et al., 2010) and (Behrel et al., 2016), the kite lift coefficient can be estimated around 0.7. Consequently, with an existing kite, the low wind limit is around $U_{ref,min} \approx 3.4\tilde{U}$. Assuming a wind measurement altitude of 10 m above the sea level, values of $\tilde{m}$ between 0.01 and 0.05 are investigated in Fig. 5.3.

In Fig. 5.3, the evolution of the non-dimensional low wind limit $\tilde{U}$ with the non-dimensional tether length is plotted for different values of $\tilde{m}$ and $\tilde{a}_z = 1$. Taking $\tilde{a}_z = 1$ makes sense with a wind measurement on the top of the launching mast. As expected, near $\tilde{L}_t = 0$, $\tilde{U} = 1$. Then, $\tilde{U}$ increases of less than 1% for $\tilde{m} = 0.05$, which is not very significant. A minimum can be observed near $\tilde{L}_t = 0.53$. This minimum, depends quasi-linearly on

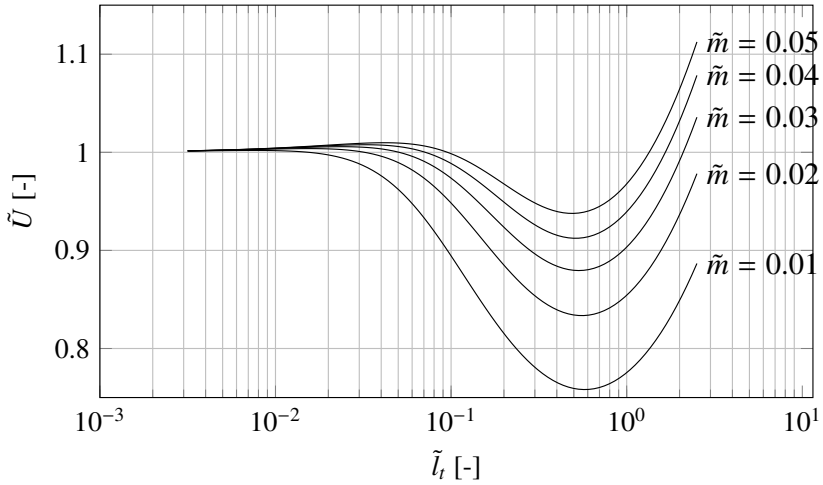

Figure 5.3.: Evolution of the non-dimensional low wind limit $\tilde{U}$ with the non-dimensional tether length $\tilde{L}_t$ for different values of $\tilde{m}$ from 0.01 to 0.05, $\tilde{U}_a = 0$ and $\tilde{a}_z = 1$.

the parameter $\tilde{m}$. By curve fitting, the linear relationship giving the optimal tether length is identified as follows:

$$\tilde{L}_{t,min} = -2.2\tilde{m} + 0.6 \tag{5.13}$$

In order to obtain a practical result, Eq. (5.13) can be expressed, reminding $\tilde{a}_z = 1$, as follows:

$$\tilde{L}_{t,min} = 0.6\frac{M_k}{m_t} + 2.2a_z^{(\mathbf{n})} \tag{5.14}$$

Beyond this minimum, since $n_v < 1/2$, the value of $\tilde{U}$ increases to infinity.

In order to obtain a closed-form low wind limit criterion, the aerodynamic load on the tether has been neglected. Consequently, it can be expected than the low wind limit is underestimated. According to the characteristics of diameter and mass per unit of length of dyneema® SK78 provided by tether manufacturer, the ratio, $\eta_{a/g}$, between the tether aerodynamic force per unit of lenght and the tether gravity per unit of length is plotted on Fig. (5.4). $\eta_{a/g}$ is estimated as follows:

$$\eta_{a/g} = \frac{\frac{1}{2}\rho_a d_t C_{dt} U_{ref,min}^2}{m_t g}, \tag{5.15}$$

where, $U_{ref,min} \approx 3.4\tilde{U}\left(\tilde{L}_t = 0\right) = 3.4$ m.s^{-1} and $C_{dt} = 1.1$. Figure (5.4) shows that tether aerodynamic forces are of the same order for low tether mass per unit of length.

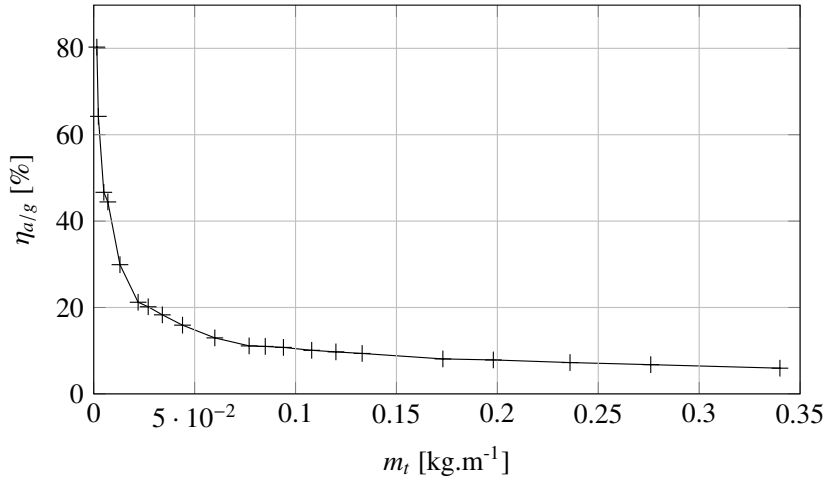

Figure 5.4.: Ratio of the tether wind loading with the tether weight as function of the tether mass per unit of length

Above $m_t > 25$ g.m^{-1} the tether aerodynamic load is less than 20% of the tether gravity load and above $m_t > 0.15$ kg.m^{-1}, the aerodynamic load is less then 10% of the tether gravity load. According to this result, the assumption of neglecting the aerodynamic force can be considered as being reasonable for a heavy tether.

5.4. Conclusion

A closed-formula has been developed in order to estimate the low wind limit to operate the kite in a static flight mode. A mathematical analysis has been perform to study the influence of parameters such as the tether mass per unit of length, the tether length, the kite mass, the aerodynamic specs of the kite and the tether attachment point altitude. This low wind limit increases with the ratio between the tether mass per unit of length and the kite mass and with the lift to drag ratio angle. However, the low wind limit decreases with the tether attachment point altitude. The effect of tether length are less obvious, but it has been shown that the low wind limit increases near zero tether length for any tether and kite characteristics. Performing a numerical analysis, with classical value of kite design, it has been shown that the low wind limit decreases to a minimum and finally increases to infinity for an infinite tether length.

Finally, since the criterion is based on the assumption that the aerodynamic load on the tether is negligible at low wind, the validity of this mathematical development is limited to heavy tether with small diameter. For instance, for a tether made of dyneema® the tether aerodynamic load is less than 20% of the gravity load for line mass per unit of length superior to 25 g.m^{-1} corresponding to 7 mm in diameter

Part III.

Ship modeling

6. Time domain seakeeping modeling

Résumé: Modélisation de la tenue à la mer dans le domaine temporel

La dynamique des navires est traditionnellement scindée entre mouvement de manœuvrabilité et mouvement de tenue à la mer. Pour étudier la manœuvrabilité, généralement uniquement les mouvements horizontaux du navire en mer calme sont modélisés. La tenue à la mer traite plus généralement des mouvements oscillants des corps flottants soumis à un état de mer. L'objectif de cette thèse est notamment de modéliser les mouvements d'un navire tracté par kite dans son environnement, i.e. état de mer et de vent. L'objectif global de cette partie est de modéliser les mouvements d'un navire seul dans son environnement. Cependant le kite peut représenter un risque pour la manœuvrabilité et la tenue à la mer d'un navire et par conséquent, une modélisation couplant la tenue à la mer et la manœuvrabilité des navires devra être mise en œuvre. Dans un premier temps, ce chapitre traite de la modélisation des mouvements de tenue à la mer par une approche temporelle. La méthode, doit pouvoir être étendue pour prendre en compte les mouvements de manœuvrabilité et permettre de rendre compte des interactions entre le navire et le cerf-volant.

Une façon courante et performante de modéliser les mouvements d'un navire soumis aux vagues est de faire l'hypothèse de fluide parfait irrotationnel et d'une réponse linéaire du navire par rapport à son excitation. Par l'hypothèse de linéarité, les mouvements d'un navire dû aux vagues sont obtenus par le principe de superposition : ils correspondent à la somme des mouvements dû aux potentiels des vitesses incidentes, diffractées et de radiées. En pratique, ce problème fluide est souvent résolu dans le domaine fréquentiel en supposant des mouvements harmoniques de petite amplitude. Les codes commerciaux résolvent l'amplitude et le déphasage du mouvement du navire par rapport à une vague monochromatique. Par fréquence, il est également possible de connaitre les efforts de vague, de diffraction et de radiation. Par ailleurs, en connaissant le spectre d'excitation du cerf-volant, il est alors possible de connaitre les mouvements du navire. Cependant, les mouvements du navire peuvent modifier le vol du cerf-volant et donc son spectre d'excitation. Une approche fréquentielle se limiterait donc à un couplage faible entre le cerf-volant et le navire. De plus, il n'est pas possible d'étendre une telle modélisation pour prendre en compte la manœuvrabilité.

Pour étudier les interactions entre un cerf-volant et un navire, une approche temporelle apparait donc nécessaire. Les méthodes temporelles résolvant les mouvements de tenue à

la mer peuvent être décomposées en trois types (Skejic, 2013): les méthodes CFD (Computational Fluid Dynamics), les méthodes potentielles temporelles et les méthodes basées sur les réponses impulsionnelles. Les méthodes CFD peuvent être précises mais requièrent d'importantes ressources informatiques et/ou de temps de calcul. Les méthodes potentielles temporelles présentent de l'intérêt car elles sont plus rapides que les méthodes CFD. Cependant, le développement d'un tel code dans le temps imparti d'une thèse a semblé être trop ambitieux. Les méthodes basées sur les réponses impulsionnelles peuvent être très rapide en termes de temps de calcul. Ces méthodes demandent des développements plus raisonnables. Ces méthodes ont été introduites par Cummins Cummins (1962) pour modéliser l'effet de n'importe quel type d'excitation sur la tenue à la mer des navires. Plus tard, Bailey et al. (1997) et Fossen (2005) ont étendu cette méthode pour prendre en compte la manoeuvrabilité des navires dans un état de mer formé. Une méthode proche de celle de Bailey et al. (1997) est mise en oeuvre dans ce chapitre.

Avec les méthodes basées sur les réponses impulsionnelles, les efforts de radiation sont calculés en temporel par des produits de convolution ce qui peut être coûteux en termes de temps de calcul. Pour contourner ce problème, Kristiansen et al. (2005) et Fossen et Smogeli (2004) ont introduit l'utilisation de systèmes d'état pour calculer le produit de convolution. Cette méthode est mathématiquement équivalente au calcul du produit de convolution tant que la fonction de transfert du navire est analytiquement connue. Ici, les fonctions de transfert du navire sont calculées au moyen de la méthode des tranches (Salvesen et al., 1970) avec le logiciel de tenue à la mer Shipmo développé par le Marin® qui résout le problème de tenue à la mer en fréquentiel. Ainsi la fonction de transfert du navire est connue pour des fréquences de mouvements particuliers. Il est donc nécessaire de réaliser une identification des fonctions de transfert sous forme de fractions rationnelles afin d'en obtenir une expression analytique. Différentes méthodes d'identification des fonctions de transfert ont été étudiées en détail par Pérez and Fossen (2008). Cependant, leurs travaux se sont limités aux fonctions de transferts de navires sans vitesse d'avance. Il est montré dans ce chapitre que la forme des fractions rationnelles doit être modifiée pour répondre aux propriétés des fonctions de transfert avec vitesse d'avance de navire. Une forme adaptée de fraction rationnelle est donc proposée dans ce chapitre. Une méthode d'indentification fréquentielle est utilisée. Cette méthode est initialisée par une méthode temporelle (Kung, 1978).

Un exercice de validation de l'ensemble de la méthode est par la suite proposé avec un navire militaire de surface le DTMB 5512. L'Université d'Iowa a mis à disposition en accès libre des données d'essais en bassin décrites par Irvine et al. (2008). Ces données concernent les mouvements de pilonnement et tangage avec et sans vitesse d'avance soumis à une houle régulière de face. Plusieurs, fréquence de vagues ont été investiguées. La résolution fréquentiel du problème de tenue à la mer avec la méthode des tranches de Salvesen et al. (1970) montre des résultats satisfaisant par rapport à l'expérimental. La transformation dans le domaine temporel du modèle de tenue à la mer est très satisfaisante car une excellente équivalence est trouvée avec la méthode de Salvesen et al. (1970).

Cette méthode qui est linéaire et qui se base sur une hypothèse de fluide parfait est connu pour ne pas être très adéquate pour modéliser les mouvements de roulis des navires. Cela

peut s'expliquer par le fait que le roulis est fortement non linéaire et visqueux par nature. Une façon de corriger la méthode est d'ajouter un amortissement de roulis supplémentaire à celui calculé par la résolution de l'écoulement potentiel. Les mouvements de roulis sont alors comparés aux prédictions du modèle de Ikeda et al. (1978).

6.1. Introduction

The aim of this thesis is to model the motions of a ship towed by kite under the influences of sea state and wind. The dynamic ship motions are traditionally split between maneuverability and seakeeping. To study the maneuverability of a ship, the modeling is restrained to the horizontal ship motions in calm water. Seakeeping motions concern the oscillating motions of floating bodies exposed to waves. The overall objective of this part is to model the ship motions since the kite may represent a risk for the ship safety in terms of seakeeping and maneuverability. Consequently, a modeling coupling the seakeeping and the maneuverability of ships is required. More specifically, the objective of this chapter is to develop a seakeeping modeling being able to be extended to take into account maneuvering motions and to study the interactions with the kite.

The seakeeping of ship is commonly studied with seakeeping codes based on the potential flow theory under the assumption of linear response of the ship to a given perturbation on a mean path. These studies are usually performed into the frequency domain in order to take benefit from the linear formulation to sum the motions. Nevertheless, since the kite and the ship may be strongly coupled, their interactions cannot be directly computed through a spectral description of the kite excitation. Consequently, the computation of ship motions due to a kite into the frequency domain is limited to a weak coupling between the kite and the ship. Here, the semantics of a *weak* and a *strong* coupling is based on the work of Markert (2010). A weak coupling can be performed by a segregated numerical scheme. In order to perform a strong coupling between the kite and the ship, a monolithic scheme into the time domain formulation is required.

As highlighted by Skejic in (2013), time-domain methods enabling to compute the 6 degrees of freedom (dof) combining horizontal and vertical motions of a ship are the linear convolution based methods (Bailey et al., 1997), the two time scale models (Skejic and Faltinsen, 2008) and the CFD methods. According to Skejic and Faltinsen (2008) the two time scale models are more appropriate to take into account the second order wave drift motion. However, this phenomenon is beyond the scope of the thesis. The linear convolution based methods are preferred since they are based on more widespread seakeeping tools. The linear convolution based methods applied to the ship motions have been introduced by Cummins (1962) in order to take into account any type of excitation. Later, Bailey et al. (1997) developed a method based on the linear convolution method and unifying the maneuvering and seakeeping coordinates systems. Thanks to this unified coordinate system, the formulation of the kite force into the ship coordinate system is more straight forward.

Nevertheless, the computation of a linear convolution product is time consuming. Consequently, Kristiansen et al. (2005) and Fossen and Smogeli (2004) introduced the state-space modeling to compute quickly the linear convolution integral of the Cummins equation of ship motion. Based on these developments, the linear convolution based method is faster than the real-time on a classical computer. Therefore, the convolution based method performed with state-space systems is suitable for design purposes. The identification of the state-space systems (Pérez and Fossen, 2008) has been detailed only for the zero forward speed case. Consequently, a slight modification of the structure of the state-space system is proposed to take into account the effects of the forward speed on the state-space systems.

First the dynamic ship equation of motion according to the classical frequency domain approach is introduced. Secondly, the time domain equation of motion based on the convolution method is presented. This section is an overview of the work achieved by Fossen (2005). Thirdly, the identification of the state-space systems and their new structure are introduced. Finally, a validation of the method in head waves regarding heave and pitch motions is presented. These comparisons are based on the experimental fluid dynamics (EFD) of the surface vessel combatant DTMB 5512 provided by the University of Iowa and studied by Irvine et al. (2008). The roll motion modeling is compared to the method of Ikeda et al. (1978).

6.2. Frequency domain solution

Assuming moderate sea states, the starting point of the mathematical model is the linearized equation for small amplitude ship motions in regular waves used notably by Salvesen et al. (1970):

$$\left[\underline{\underline{M}}_S^* + \underline{\underline{A}}^*\right] \ddot{\underline{\xi}} + \left[\underline{\underline{B}}^* + \underline{\underline{B}}_\phi^*\right] \dot{\underline{\xi}} + \underline{\underline{C}}^* \underline{\xi} = \underline{F}^* - \bar{\underline{F}}^*, \tag{6.1}$$

where, $\underline{\underline{M}}_S^*$, $\underline{\underline{A}}^*$, $\underline{\underline{B}}^*$ and $\underline{\underline{C}}^*$ denote respectively the generalized mass matrix, added mass matrix, damping matrix and the restoring matrix with respect to the $\mathbf{h}$ frame. $\underline{\underline{B}}_\phi^*$ is an extra generalized damping matrix accounting only for the roll motion as proposed in (Salvesen et al., 1970). $\underline{F}^*$ denotes the sum of the generalized external forces (forces and moments) applied to the ship expressed in the $\mathbf{h}$ frame. $\bar{\underline{F}}^*$ is the mean value of $\underline{F}^*$.

6.3. Time domain solution

This section is an overview of the work of Fossen (2005).

6.3.1. Transformation into the s and c frames: unified coordinates systems

Since Eq. (6.1) is linear, the ship motions can be summed with respect to a sum of excitation forces. Since, $\underline{\underline{A}}^*$and $\underline{\underline{B}}^*$ are frequency dependent matrices, Eq. (6.1) holds only for a given frequency of excitation, ω. Consequently, this assumption leads to the following relationship:

$$\underline{\ddot{\xi}} = -\omega^2 \underline{\xi} \tag{6.2}$$

And, the direct cosine matrix between the $\mathbf{h}$ frame and the $\mathbf{s}$ frame is equal to the direct cosine matrix between the earth fixed frame $\mathbf{n}$ and the ship fixed frame $\mathbf{s}$ for small angles defined in Eq. (3). Thus, the direct cosine matrix can be simplified considering small angles of oscillations:

$$\underline{\underline{T}}^{\mathbf{h}}_{\mathbf{s}} = \begin{bmatrix} 1 & -\xi_6 & \xi_5 \\ \xi_6 & 1 & -\xi_4 \\ -\xi_5 & \xi_4 & 1 \end{bmatrix} \tag{6.3}$$

Under the assumption of small amplitude of motions, the expression of the ship speed variation can be approximated by $\delta\underline{V}_s = [u_s - U_h,\ v_s,\ w_s,\ p_s,\ q_s,\ r_s]^T_{\mathbf{s}}$ with respect to the $\mathbf{s}$ frame. $\underline{\xi}$ can be expressed in terms of $\delta\underline{V}_s$ with Eq. (6.4). The detail of this transformation was presented in Fossen (2005) and is reported in Annex C.1.

$$\begin{cases} \dot{\underline{\xi}} = & \underline{\underline{J}}\delta\underline{V}_s - \frac{U_h}{\omega_e^2}\underline{\underline{L}}\delta\dot{\underline{V}}_s \\ \ddot{\underline{\xi}} = & \underline{\underline{J}}\delta\dot{\underline{V}}_s + U_h\underline{\underline{L}}\delta\underline{V}_s \end{cases}, \tag{6.4}$$

where,

$$\underline{\underline{J}} = \begin{bmatrix} 1 & 0 & 0 & 0 & z_H & 0 \\ 0 & 1 & 0 & -z_H & 0 & x_H \\ 0 & 0 & 1 & 0 & -x_H & 0 \\ 0 & 0 & 0 & 1 & 0 & 0 \\ 0 & 0 & 0 & 0 & 1 & 0 \\ 0 & 0 & 0 & 0 & 0 & 1 \end{bmatrix}, \tag{6.5}$$

and,

$$\underline{\underline{L}} = \begin{bmatrix} 0 & 0 & 0 & 0 & 0 & 0 \\ 0 & 0 & 0 & 0 & 0 & 1 \\ 0 & 0 & 0 & 0 & -1 & 0 \\ 0 & 0 & 0 & 0 & 0 & 0 \\ 0 & 0 & 0 & 0 & 0 & 0 \\ 0 & 0 & 0 & 0 & 0 & 0 \end{bmatrix} \tag{6.6}$$

Then, using Eq. (6.4), the ship equation of motion, Eq. (6.1), can be expressed in terms of $\delta\underline{V}_s$ as follows:

$$\left[\underline{\underline{M}}_S + \underline{\underline{A}}\right] \delta\dot{\underline{V}}_s + \left[\underline{\underline{B}} + \underline{\underline{B}}_\phi + \underline{\underline{D}}\right] \delta\underline{V}_s + \underline{\underline{C}}\,\underline{\xi} = \underline{F} - \bar{\underline{F}}, \tag{6.7}$$

where,

$$\begin{cases} \underline{\underline{M}}_S & = \underline{\underline{J}}^T \underline{\underline{M}}_S^* \underline{\underline{J}} \\ \underline{\underline{A}} & = \underline{\underline{J}}^T \underline{\underline{A}}^* \underline{\underline{J}} \\ \underline{\underline{D}} & = \underline{\underline{J}}^T \underline{\underline{M}}_S^* \underline{L} \\ \underline{\underline{B}} & = \underline{\underline{J}}^T \left[\underline{\underline{B}}^* + U_h \underline{\underline{A}}^* \underline{L}\right] \underline{\underline{J}} \\ \underline{\underline{B}}_\phi & = \underline{\underline{B}}_\phi^* \\ \underline{\underline{C}} & = \underline{\underline{J}}^T \underline{\underline{C}}^* \\ \underline{F} & = \underline{\underline{J}}^T \underline{F}^* \end{cases} \tag{6.8}$$

6.3.2. Impulse response function

Since a kite and a ship may have strong coupled motions, it is more convenient recommended to transform Eq. (6.7) into the time domain using the impulse response function as Cummins (1962), Ogilvie (1964) and Fossen and Smogeli (2004). Moreover, it is more convenient to use the parameterization for $\underline{V}_s$ instead of $\delta\underline{V}_s$. The steady state corresponds to $u_s = U_h$ and $\delta\underline{V}_s = \underline{0}$. Due to the special structure of $\underline{\underline{C}}$, it can be noticed that $\underline{\underline{C}}\,\underline{\xi} = \underline{\underline{C}}\,\underline{S}$. Consequently, the ship equation of motion for arbitrary motions and using the parameterization in $\underline{V}_s$ is:

$$\left[\underline{\underline{M}}_S + \underline{\underline{\tilde{A}}}\right] \dot{\underline{V}}_s + \left[\underline{\underline{\tilde{B}}} + \underline{\underline{B}}_\phi + \underline{\underline{D}}\right] \underline{V_s} + \underline{\mu} + \underline{\underline{C}}\,\underline{S} = \underline{F}, \tag{6.9}$$

where, $\underline{\underline{\tilde{A}}} = \lim_{\omega \to +\infty} \underline{\underline{A}}\,(\omega)$ and $\underline{\underline{\tilde{B}}} = \lim_{\omega \to +\infty} \underline{\underline{B}}\,(\omega)$. $\underline{\mu}$ is defined as follows:

$$\underline{\mu} = \int_{-\infty}^{t} \underline{\underline{K}}\,(t-\tau)\,\delta\underline{V_s}\,(\tau)\,d\tau, \tag{6.10}$$

where $\underline{\underline{K}}$ denotes the retardation matrix. Strictly speaking, the left boundary of the convolution term should be $-\infty$. However, for a causal system the left boundary can be replaced by 0. The expression of the retardation matrix is given in Eq. (6.11) and can be obtained by comparing Eq. (6.1) and Eq. (6.9) assuming sinusoidal motions. Mathematical details are developed in Annex C.2.

$$\underline{\underline{K}}\left(j\omega\right) = \underline{\underline{B}}\left(\omega\right) - \underline{\underline{\tilde{B}}} + j\omega\left[\underline{\underline{A}}\left(\omega\right) - \underline{\underline{\tilde{A}}}\right], \tag{6.11}$$

where $j^2 = -1$.

Reciprocally, the added mass and the damping matrix can be obtained with the Laplace transform of the retardation matrix as follows:

$$\begin{cases} A_{ij} = & \frac{1}{\omega}\Im\left(K_{ij}\right) + \tilde{A}_{ij} \\ B_{ij} = & \Re\left(K_{ij}\right) + \tilde{B}_{ij} \end{cases}, \tag{6.12}$$

where, $\Im$ and $\Re$ denote respectively the imaginary part and the real part.

The computation of the convolution product is time consuming. However, each convolution component $\mu_{i\in[\![1,6]\!]}$ can be approximated by a state space system in Eq. (6.13), as introduced by Kristiansen et al. (2005) for the radiation forces. The mathematical justification of this transformation can be found in (Sontag, 2013).

$$\mu_i \approx \begin{cases} \mu_i & = \sum_{j=1}^{6} \mu_{ij} \\ \dot{\underline{y}}_{ij} & = \underline{\underline{A}}'_{ij}\underline{y}_{ij} + \underline{B}'_{ij}\delta V_{s,j} \\ \mu_{ij} & = \underline{C}'_{ij}\underline{y}_{ij} \end{cases}, \tag{6.13}$$

where, $\left\{\underline{\underline{A}}'_{ij},\ \underline{B}'_{ij},\ \underline{C}'_{ij}\right\}$ represents a state-space model corresponding to a rational transfer function denoted by H_{ij} fitting the $K_{ij}\left(j\omega\right)$ data, for $i, j \in [\![1,6]\!]$. μ_i denotes the i$^{\text{th}}$ component of the vector μ_j. $\underline{y}_{ij}$ is the state vector of the state space system. In order to clarify the notation which might be slightly confusing, it should be mentioned that Eq. (6.13) does not use the Einstein summation convention.

6.4. Identification of the state-space systems

6.4.1. Structure of the state-space systems

Direct equivalences exist between a rational transfer function and a state-space system. For instance, for single input and output system, the corresponding canonical state-space system of a transfer function is given as follows:

$$\begin{cases} \underline{\dot{y}}_{ij} & = \begin{bmatrix} -b_{n-1} & -b_{n-2} & -b_{n-3} & \cdots & -b_0 \\ 1 & 0 & 0 & \cdots & 0 \\ 0 & \ddots & \ddots & \ddots & \vdots \\ \vdots & \ddots & \ddots & \ddots & 0 \\ 0 & \cdots & 0 & 1 & 0 \end{bmatrix} \underline{y}_{ij} + \delta V_{s,j} \begin{bmatrix} 1 \\ 0 \\ \vdots \\ 0 \\ 0 \end{bmatrix} \\ \mu_{ij} & = \begin{bmatrix} a_{n-1} & \cdots & a_0 \end{bmatrix} \underline{y}_{ij} \end{cases}. \tag{6.14}$$

Where the coefficient a_i and b_i are respectively the numerator and denominator coefficient of the following transfer function:

$$H_{ij} = \frac{a_{n-1}p^{n-1} + \ldots + a_1 p + a_0}{p^n + b_{n-1}p^{n-1} + \ldots + b_0} \tag{6.15}$$

Form of the transfer function at zero forward speed At zero forward speed, properties of the retardation function as described in Pérez and Fossen (2008) impose the form of the transfer function as follows:

$$H_{ij} = \frac{K_{ij}\left(t=0\right)p^{n-1} + \ldots + a_1 p}{p^n + b_{n-1}p^{n-1} + \ldots + b_0} \tag{6.16}$$

Moreover according to the Riemann-Lebesgue Lemma, the transfer functions must be stable. The denominator should respect the Routh-Hurwitz criterion.

Form of the transfer function with forward speed With forward speed, the retardation function may not tend towards zero at zero frequency. Indeed $B_{ij}\left(\omega = 0\right)$ can be different from $B_{ij}\left(\omega = \infty\right)$, consequently:

$$\lim_{p \to 0} H_{ij} \neq 0 \tag{6.17}$$

This condition is not satisfied with the form given in Eq. (6.16). In case of forward speed, H_{ij} should have the following form:

$$H_{ij} = \frac{K_{ij}\left(t=0\right)p^{n-1} + \ldots + a_1 p + a_0}{p^n + b_{n-1}p^{n-1} + \ldots + b_0}, \tag{6.18}$$

where the coefficient a_0 and b_0 should respect the following condition:

$$\frac{a_0}{b_0} = B_{ij}\left(\omega = 0\right) - B_{ij}\left(\omega = \infty\right) \tag{6.19}$$

Computation of the hydrodynamic data and extrapolation towards zero and infinite frequency The data $K_{ij}(j\omega)$ are obtained with the added mass and damping obtained according to the STF strip theory (Salvesen et al., 1970). The 3D added mass and damping are expressed in terms of sectional added mass and damping. For instance, the STF strip theory expressed $A^*_{33}$and B^*_{33} in terms of sectional added mass a_{33} and damping b_{33} as follows:

$$\begin{cases} A^*_{33}(\omega) & = \int_{L_{pp}} a_{33}(\omega,\ x)\,dx - \frac{U_h}{\omega^2} b_{33}(\omega,\ x_a) \\ B^*_{33}(\omega) & = \int_{L_{pp}} b_{33}(\omega,\ x)\,dx + U_h a_{33}(\omega,\ x_a) \end{cases}, \tag{6.20}$$

where x_a is the longitudinal position of the aft perpendicular section.

The sectional added mass and damping are obtained with the Shipmo seakeeping software developed by the Marin® assuming an infinite depth. The frequency range of the data depends on the ship size, but for a commercial ship, the low frequency limit is generally 0.1 rad.s^{-1} and the high frequency limit does not generally exceed 3 rad.s^{-1}. To improve the quality of the identification method an extrapolation of the hydrodynamic data towards the asymptotic value is necessary.

As shown by Newman (1977), assuming a potential flow, at zero and infinite frequency, the 2D sections damping is zero. At infinite frequency, the 2D sections infinite added mass are approximated with the highest frequency computed, which is justified since the added mass remain almost constant at high frequency. Each sectional added mass and damping are then extrapolated at high frequency with the function in Eq. 6.21, as used in (Pérez and Fossen, 2008) and originally proposed by Greenhow (1986):

$$f_e(\omega) = \frac{\beta_1}{\omega^4} + \frac{\beta_2}{\omega^2}, \tag{6.21}$$

where β_1 and β_2 are two constants chosen in order to provide continuity and differentiability.

Transfer function identification method The identification of H_{ij} can be identified either into the frequency domain or into the time domain, see Pérez and Fossen (2008). Here, a time domain identification method is used to initialize the frequency domain identification method.

A first identification of H_{ij} into the time domain is performed with the the singular value decomposition method proposed by Kung (1978). This step is performed with a modified Matlab® function "imp2ss" to impose the order. This method is efficient but the identified transfer function has the following form:

$$H_{ij} = \frac{a_n p^n + \ldots + a_1 p + a_0}{p^n + b_{n-1} p^{n-1} + \ldots + b_0}. \tag{6.22}$$

Consequently, to comply with the form imposed by Eq. (6.18), a_n is set to zero, a_{n-1} is set to $K_{ij}\left(t=0\right)$ and a_0 is set to $a_0 = b_0\left[B_{ij}\left(\omega=0\right) - B_{ij}\left(\omega=\infty\right)\right]$.

This first estimation of the transfer function is used as initial solution of the frequency domain identification method. The frequency identification step is performed with the "oe" function of the Matlab® system identification toolbox. This function uses a local optimization scheme based on gradient methods and constraints can be added. The structure of the transfer function, as proposed in Eq. (6.18), can be imposed to the frequency domain optimization algorithm.

These two steps are repeated for several transfer function orders, for instance from 2 to 10. Then, the best transfer function order is selected according to the normalized mean square error from:

$$\begin{cases} e_{tot} & = \frac{1}{2}\left(e_w + e_t\right) \\ e_w & = \frac{\sum_k \left[\left|H_{ij}(j\omega_k) - K_{ij}(j\omega_k)\right|\right]^2}{\sum_k \left|K_{ij}(j\omega_k)\right|^2} \\ e_t & = \frac{\sum_k \left[H_{ij}(t_k) - K_{ij}(t_k)\right]^2}{\sum_k K_{ij}(t_k)^2} \end{cases} \tag{6.23}$$

As an illustration of the identification method Annex C.4 provides the details about the David Taylor Model Basin (DTMB) 5512 for the term K_{33}. After the time domain identification, the best order found is 4 with an error $e_{tot} = 10.4$ %. After the frequency identification step, the error e_{tot} dropped to 1.87 %.

6.5. Incoming waves and diffraction

The Froude-Krilov and diffraction forces are obtained with the STF 2D strip theory Salvesen et al. (1970). Assuming an infinite depth, the dispersion relationship is $k_w g = \omega_w^2$, where k is the wave-number and g the gravity. ω_w and β_w denote respectively the wave angular frequency in rad.s^{-1} and the angle of the waves with respect to the ship heading. β_w is given by $\beta_w = \psi_s - \psi_w$, where ψ_w denotes the wave angle with respect to $\underline{x}_n$. With $i \in [\![1;6]\!]$, each component f_{wi} of the Froude-Krilov and diffraction forces generated by a single unit wave can be expressed by the following expression:

$$\begin{aligned} f_{wi}\left(u_s, \beta_w, \omega_w, t\right) = E_i\left(u_s, \beta_w, \omega_w\right) \cos\Big(& k_w \cos\left(\psi_w\right) s_x^{(\mathbf{n})} \\ & + k \sin\left(\psi_w\right) s_y^{(\mathbf{n})} - \omega_w t - \phi_w\left(u_s, \beta_w, \omega_w\right) + \epsilon_w\Big) \end{aligned} \tag{6.24}$$

where E_i is the amplitude of the i$^{\text{th}}$ component of $\underline{f}_w$ and ϵ is a random initial wave phase. ϕ_w is the reflection phase change of the Froude-Krylov and diffraction force with respect

to the free surface elevation. According to Eq. 6.24, the wave frequency of encounter is obtained by time derivation of the cosine function argument:

$$\omega_e = \omega_w - \frac{U_s}{g}\omega_v^2 \cos\beta_w \tag{6.25}$$

For any wave spectrum $S_w(\omega_w, \psi_w)$, the Froude-Krilov and diffraction forces can be expressed as follows:

$$\underline{F}_w(u_s, \psi_s) = \sum_{i=1}^{N} \sqrt{2S_w(\omega_{w,i}, \psi_{w,i})\,\Delta\psi_w \Delta\omega_w}\ \underline{f}_w(u_s, \psi_s - \psi_{w,i}, \omega_i) \tag{6.26}$$

where ϵ_i is a random phase equidistributed between 0 and 2π to obtain a Gaussian wave spectrum.

6.6. Time domain equation of motion

Equations describing the motion of the system can be transformed into a system of first order differential equations Eq. (6.27). This system is deduced from Eqns. (3, 4, 6.9, 6.13).

$$\begin{cases} \dot{\underline{S}} & = \begin{bmatrix} \underline{\underline{T}}^{\mathbf{c}}_{\mathbf{s}} & \underline{\underline{0}} \\ \underline{\underline{0}} & \underline{\underline{R}}^{\mathbf{c}}_{\mathbf{s}} \end{bmatrix} \underline{V}_s + [\underline{U}_c\ \underline{0}_3]^T \\ \dot{\underline{V}}_s & = \left[\underline{\underline{M}}_S + \underline{\underline{\tilde{A}}}\right]^{-1} \left[\underline{F} - \left[\underline{\underline{\tilde{B}}} + \underline{\underline{B}}_\phi + \underline{\underline{D}}\right] \underline{V}_s - \underline{\mu} - \underline{\underline{C}}\ \underline{S}\right] \\ \dot{\underline{y}}_{ij} & = \underline{\underline{A}}'_{ij}\underline{y}_{ij} + \underline{\underline{B}}'_{ij}\delta V_{s,j},\ \forall i,j \in [\![1;6]\!] \end{cases} \tag{6.27}$$

Equation (6.27) represents 12 scalar equations for the ship and 75 scalars equations for the state-space systems assuming that the order of each state space system is 5 and taking into account the ship symmetry. Thus, with the presented model, a ship towed by kite is described by approximately 90 scalar equations depending on the state space model orders.

This system of differential equations is numerically integrated with a Runge-Kutta scheme of order 4 with a fixed time step.

6.7. Time domain validation case

The presented ship model is compared to experimental fluid dynamics (EFD) data and with STF strip theory results on the David Taylor Model Basin (DTMB) 5512. The DTMB

model 5512 is a 1:46.6 scale model. The hull form and its specs are respectively plotted in Fig. 6.1 and summarized in Tab 6.1. The experimental data are provided by the University of Iowa The University of Iowa (2013) and are presented in Irvine et al. Irvine et al. (2008). The EFD data concern the heave and pitch motions in regular head waves, with and without forward speed.

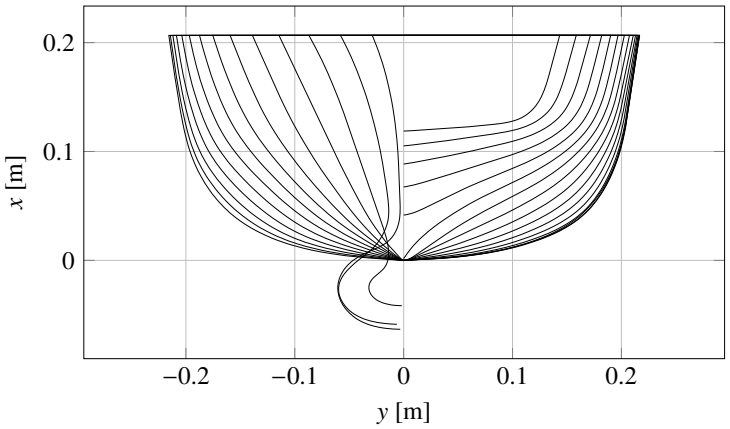

Figure 6.1.: DTMB 5512 hull sections at the scale of 1:46.6.

Parameter	Units	5512	Full Scale
Scale ratio	-	46.6	1
Length, L_{pp}	m	3.048	142.04
Beam, B	m	0.405	18.87
Draft, T	m	0.132	6.15
Weight	Kg - t	86.6	8763.5
LCG	m	1.536	71.58
VCG	m	0.162	7.55
Pitch radius of gyration, k_5	m	0.764	35.6

Table 6.1.: DTMB 5512 hull and full scale characteristics

6.7.1. Results

The computation of ship motions is performed at zero forward speed and at a Froude number of 0.28 which corresponds to $U_h = 1.53$ m.s^{-1} and with frequency head waves, ω_0, ranging from 1 rad.s^{-1} to 7.5 rad.s^{-1}. Figures 6.2 and 6.3 plot the heave and pitch transfer function obtained with the experimental data, with the STF strip theory and with the presented model. The experimental data are obtained for different wave steepness $s_w = \{0.025,\ 0.05,\ 0.075\}$. The amplitude of the transfer function for heave motion is directly the ratio of the heave amplitude motion to the wave amplitude. The RAO amplitude for the pitch motion is given by the ratio of the pitch motion amplitude (in radian) to the

wave amplitude multiplied by the wave number k. The phase angle of the presented model is obtained by cross correlation between the free surface elevation and the ship motion time series..

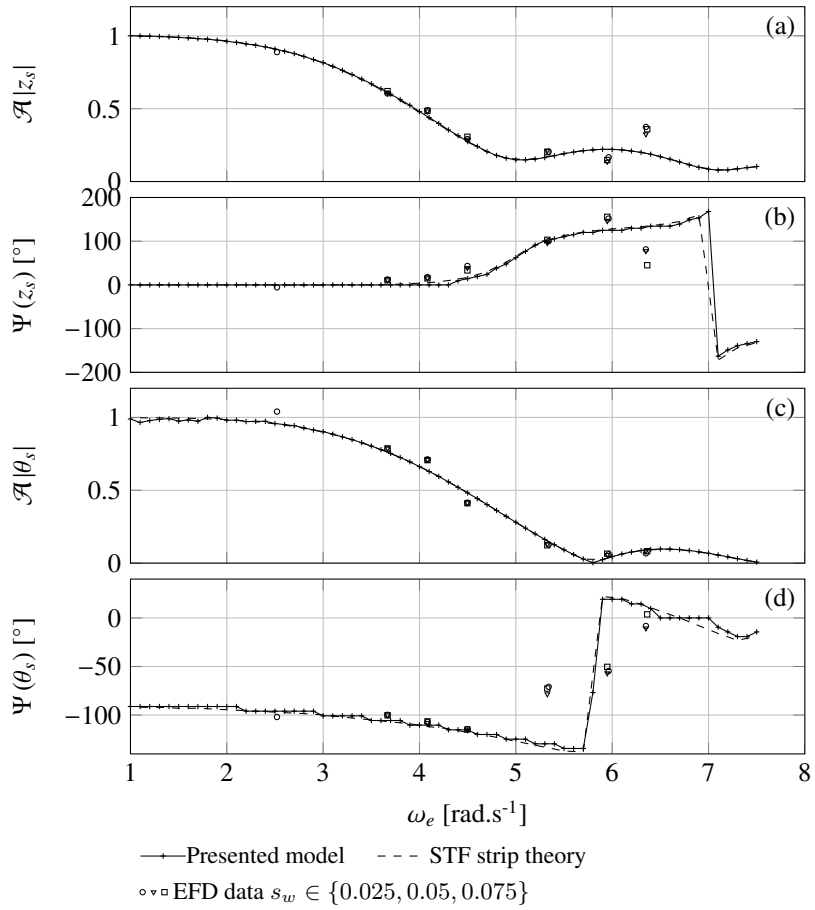

Figure 6.2.: Heave and pitch transfer function at $U_h = 0.0$ m.s^{-1}as function of the wave frequency of encounter w_e. The results are obtained with the frequency domain and time domain approaches, experimental data for different wave steepnesses s_w and with the STF strip theory.

The results presented in Fig. 6.4 shows the predicted roll motion with the strip theory using the damping predicted by the method of Ikeda et al. (1978). The results of Ikeda et al. (1978) are considered as a reference.

6.7.2. Analysis and Discussion

Concerning the amplitude, an overall good agreement is found with and without forward speed between the EFD data, the STF strip theory and the presented time domain seakeeping

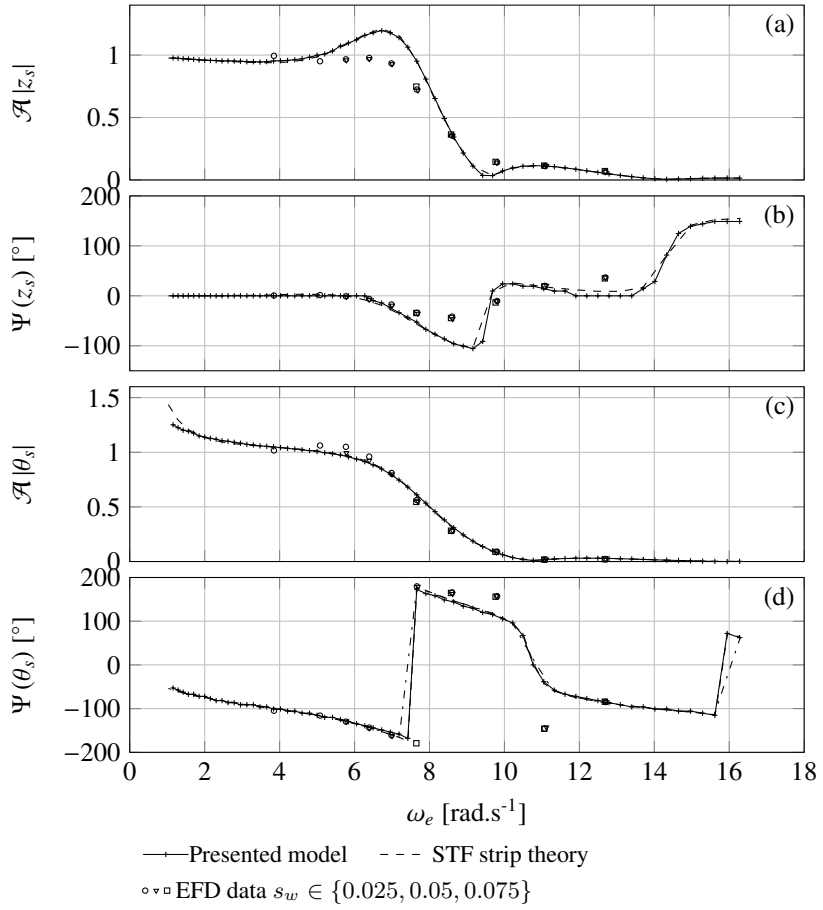

Figure 6.3.: Heave and pitch transfer function at $U_h = 1.53$ m.s^{-1} as function of the wave frequency of encounter w_e. The results are obtained with the frequency domain and time domain approaches, experimental data for different wave steepnesses s_w and with the STF strip theory.

model. For the considered waves, the influence of the wave steepness on the EFD data is not significant.

As it is theoretically expected, the STF strip theory and the time domain approach match perfectly for the amplitude. Very small differences can be observed in terms of phase angle, but these differences are caused by the accuracy of the post-processing method. The very small differences with the STF strip theory are due to the approximations performed with the identification method of the transfer functions H_{ij}.

As a conclusion for the heave and pitch motions, the very small differences between the STF strip theory and the presented time domain seakeeping model in Figs. 6.2 and 6.3 show that the transformation of the equation of motion into the s frame and the the state-space model identification method is consistent and accurate enough.

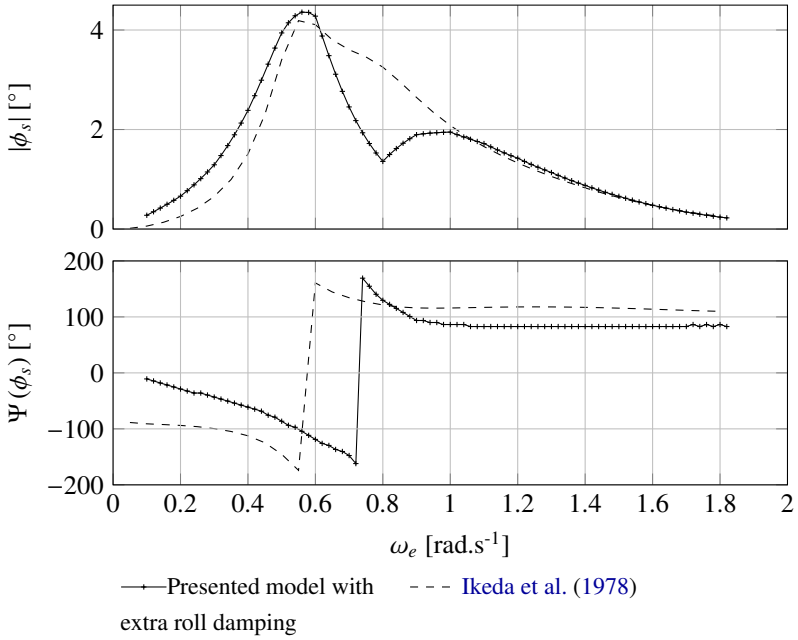

Figure 6.4.: Roll response amplitude operator and phase at $U = 7.716$ m.s^{-1} as function of the frequency of encounter w_e with DTMB 5512 at full scale. The results are obtained with the presented model and the STF strip theory with the roll damping modeled with the method proposed by Ikeda et al. (1978).

The roll motion is much more difficult to predict with a linear model. With the DTMB at full scale, results presented in Fig. 6.4 show the predicted roll motion with the strip theory using the damping predicted by the method of Ikeda et al. (1978). The results of Ikeda et al. (1978) are considered as a reference.

The extra roll damping is determined to obtain approximately the same roll motion amplitude at the natural roll ship frequency as the model of Ikeda et al. (1978). For the presented simulation the extra roll damping is set to $1.53 \cdot 10^8$ kg.m.s^{-1}. As shown in Fig. 6.4, at the natural roll ship frequency, $\omega_{roll} = 0.56$ rad.s^{-1}, the roll motion is well predicted. At high frequency, greater than 1 rad.s^{-1}, the roll motion amplitude is well predicted, only a slight difference in terms of phase is observable. Nevertheless, for the wave frequency in the range $]\,0;\ 1]$ rad.s^{-1}, predictions appear to be less accurate.

6.8. Conclusion

A time domain seakeeping model based on the Cummin's equation has been implemented with respect to the ship fixed coordinate system. The convolution product has been performed using state-space models. The state-model models have been identified with the

STF strip theory data. The structure of the state-space system has been modified to comply with the forward speed requirements.

A validation using EFD data has been performed on the DTMB 5512 in regular head waves. The results show that the heave and pitch motions predicted by the STF strip theory and the time domain approaches are consistent. Their comparisons with the EFD data are satisfactory. The approximations performed using state-space models are negligible. The ship model and its implementation give satisfactory results for the vertical ship motions. The predicted roll motion is less satisfactory, nevertheless the roll amplitude at the natural roll frequency of the ship is correctly estimated.

The STF strip theory (Salvesen et al., 1970) is based on the potential flow assumption and the horizontal ship motions dominated by viscous effects therefore the presented model is not adequate for the horizontal motions. The hydrodynamic model needs to be modified to take into account horizontal motions.

7. Extension of the time domain seakeeping for the maneuvering motions

Résumé: Prise en compte des mouvements de manœuvrabilité dans le modèle temporel de tenue à la mer

Ce chapitre présente une façon d'étendre le modèle de tenue à la mer pour modéliser les mouvements de manœuvrabilité. Les mouvements de manœuvrabilité sont des mouvements à basse fréquence. Ils correspondent aux efforts de radiation basse fréquence du modèle de tenue à la mer. Seulement, l'influence de la viscosité est significative sur les mouvements de manœuvrabilité. Comme le modèle de tenue à la mer suppose un écoulement non visqueux, il est nécessaire de modifier la formulation des efforts hydrodynamiques liés aux mouvements horizontaux du modèle temporel de tenue à la mer.

Deux types de modèles de manœuvrabilité peuvent être reconnus dans la littérature : les modèles du type Abkowitz (1980) et les modèles modulaires proposés par Kobayashi et al. (1995) également connu sous le nom de modèle MMG (Japanese research Mathematical Modeling Group). Les modèles du type Abkowitz (1980) représentent les efforts du safran, de l'hélice et de la coque sous forme de série de Taylor pour chaque composante de mouvement considéré. Les modèles modulaires se distinguent car le safran, l'hélice, la coque et leurs interactions sont modélisés de façon indépendante.

L'approche modulaire est préférée car elle s'implémente facilement en programmation orientée objet, ce qui présente un avantage pour la maintenance et l'évolution du code comme l'indique Sutulo and Soares (2005). Dans ce chapitre, les efforts correspondant aux composantes horizontales de mouvements sont remplacés par le modèle modulaire de Yoshimura and Masumoto (2012). Ce modèle a été choisi car Yoshimura and Masumoto (2012) propose une formulation paramétrique qui permet donc d'adapter le modèle pour différents types de navire. L'incorporation de ces modèles dans le modèle de tenue à la mer temporel est similaire à la méthode suivie par Sutulo and Guedes Soares (2006).

De plus le modèle temporel de tenue à la mer est valide autour d'une vitesse d'avance moyenne alors que la variation de vitesse d'avance au cours d'une manœuvre peut grandement varier. Plus précisément, les systèmes d'état correspondent à une vitesse d'avance. Ainsi, pour avoir une formulation continue en vitesse d'avance, les systèmes d'états correspondant à deux vitesses d'avance sont calculés au cours de la simulation. L'effort de radiation est ensuite linéairement interpolé.

Une validation de cette approche est proposée avec le porte conteneur KCS. Des essais zig-zag 15°/1° de navigation libre à l'échelle 1:52.667 effectué au bassin de Potsdam (Mofidi and Carrica, 2014; Shen et al., 2015) et des essais de giration avec un angle de barre à 35° et des essais zig-zag 20°/20° (Fukui et al., 2015, 2016) ont été utilisé comme cas de validation. De plus, en utilisant les résultats de manoeuvrabilité disponibles dans (Toxopeus and Lee, 2008; Stern et al., 2011) obtenus par différents codes et différents essais en bassin offrent des points de comparaisons supplémentaires.

L'extension du modèle temporel de tenue à la mer donne des résultats satisfaisants par rapport aux essais en bassin et aux autres codes.

7.1. Introduction

The aim of this chapter is to enhance and to complete the model developed in Chap. 6 to predict horizontal motions of a ship towed by a kite, since a kite might have an important impact on the maneuverability of the ship. The kite must be small enough to lead to small horizontal amplitude of ship motions in order to guarantee the ship safety. This requirement complies with the small amplitude of ship motions around a mean ship forward speed assumed by the time domain seakeeping model developed in chapter 6.

As highlighted by Bailey et al. (1997) the damping relative to the horizontal motions is dominated by viscous effects at low frequency. Hence, at low frequency, horizontal ship motions predicted with the time domain seakeeping model based on the potential flow theory introduced in Chap. 6 are overestimated. At least, the damping relative to the horizontal ship motion must be corrected to represent the viscous effects. An inclusion of the viscous effects into the time domain seakeeping model has been proposed by Bailey et al. (1997) and Fossen and Smogeli (2004). They suggested to add a viscous decaying ramp or viscous exponential decay to the frequency damping data. Their proposition has been implemented but results are not satisfactory as shown in Annex C.6. Another manner to model the 6 degrees of freedom of a ship is to mix time domain seakeeping equations of motion with maneuvering equations of motion. The mixed approach is introduced in this chapter. In addition, the ship forward speed may vary during a maneuver whereas the ship model of Chap. 6 is defined around a mean ship forward speed. Consequently, the formulation of the model must be transformed into a forward speed continuous model, which is proposed in this chapter.

To predict horizontal motions of a ship, rudder, propeller and hull advance resistance models should be introduced. In the literature, horizontal motions are basically studied by the maneuverability of ships. The maneuvering model can be classified into two groups. The first group of models is proposed by Abkowitz (1980), where the hydrodynamic forces of the bare hull, rudder and propeller are described by a single Taylor expansion for each component of the motion. The second type of model is the MMG model (Kobayashi et al.,

1995) proposed by the Japanese research Mathematical Modeling Group (MMG). MMG models are implemented in a modular way. The bare hull, the rudder, the propeller and their interactions are described by dedicated models. The bare hull is usually represented by Taylor expansions. The coefficients of the Taylor's expansions can be obtained with captive model tests, Computational Fluid Dynamics (Toxopeus, 2011) or parametric models such as (Clarke et al., 1983; Yoshimura and Masumoto, 2012).

Here, a modular approach such as proposed by the MMG model is preferred in order to offer an easier maintenance and future developments (Sutulo and Soares, 2005). Indeed, this approach offers the advantage to implement each model in a separated manner. Among MMG models proposed in the literature, the model of Yoshimura and Masumoto (2012) has the advantage to proposed a parametric description of the hull, rudder and propeller built with regressions based on differents types of ship, from fishing vessels to container ships. In addition, a parametric description of the interaction coefficient between the hull, propeller and rudder is also proposed. Consequently, in this thesis, in order to develop a tool dedicated to a wide variety of ships, the rudder, the propeller and their interactions are modeled with the parametric model proposed by Yoshimura and Masumoto (2012).

Firstly, the propeller, rudder and windage models are introduced. Secondly, the approach adding a viscous modification of the damping data is introduced with the equations of motion for a varying forward speed. Thirdly, the mixed maneuvering and seakeeping approach is introduced. Then, a validation exercise is proposed for the two approaches with free sailing EFD data performed by the Hokkaido University and by the Potsdam Model Basin (SVA). Results are then analyzed and discussed.

7.2. Maneuvering apparatus and other external forces modelings

7.2.1. Propeller model

The expression of the propeller thrust is given by Eq. (7.1).

$$X_P = (1 - t_p)\, \rho_w K_T D_P^4 n_p^2 \tag{7.1}$$

The open water propeller thrust factor is denoted by K_T. The thrust deduction factor is denoted by t_p. The thrust deduction factor represents the decrease of the propeller thrust due to the presence of the hull. The thrust factor is a function of the propeller advance ratio, denoted by J and expressed with the wake fraction w in Eq. (7.2).

$$J = (1 - w)\, \frac{u_S}{n_P D_P} \tag{7.2}$$

The thrust deduction factor and the wake fraction can be determined with a semi-empirical formula such as the one formulated by Harvald (1983) and Journée (1976).

The propeller torque is given by:

$$K_P = \rho_w K_Q D_P^5 n_p^2 \tag{7.3}$$

where K_Q is the propeller torque factor. The generalized force vector of the propeller thrust is given by:

$$F_p = [X_p,\ 0,\ 0,\ K_p,\ 0,\ 0]^T \tag{7.4}$$

The pitch moment due to the propeller thrust is not taken into account since the induced trim angle is small and no coupling with the other motion mode is further considered. This assumption holds for the following rudder and hull advance resistance sub-model.

7.2.2. Rudder model

According to Yoshimura and Masumoto (2012) rudder forces are expressed as follows:

$$\begin{cases} X_r &= -k_h\,(1-t_r)\,F_r^{'}\sin\delta \\ Y_r &= -k_h\,(1+a_h)\,F_r^{'}\cos\delta \\ N_r &= -k_h\left(x_r^{'}+a_h x_h^{'}\right)F_r^{'}\cos\delta \end{cases}, \tag{7.5}$$

where t_r, a_h and $x_h^{'}$ are coefficients representing the interactions of the rudder with the hull and the propeller. The symbol $^{'}$ denotes that a parameter is non-dimensional. Parametric expressions of these coefficients are provided in (Yoshimura and Masumoto, 2012). The non-dimensional rudder force $F_r^{'}$ is expressed as follows:

$$F_n^{'} = \frac{A_r}{L_{pp}T_m} f_{\lambda_r} U_r^{'2} \sin\alpha_r, \tag{7.6}$$

where, A_r is the lateral rudder area. f_{λ_r} is a coefficient modeling the effect of the rudder aspect ratio λ_r on the rudder lift coefficient. Yoshimura and Masumoto (2012) expressed this coefficient as follows:

$$f_{\lambda_r} = \frac{6.13\lambda_r}{2.25+\lambda_r} \tag{7.7}$$

U_r' is the non-dimensional rudder inflow velocity:

$$U_r^{'} = \frac{U_r}{U_s} = \sqrt{u_r^{'2} + v_r^{'2}}. \tag{7.8}$$

The determination of the rudder inflow velocity is not an easy task. Indeed, the inflow depends on the hull, propeller and rudder configuration and on the interactions between them. However, the determination of the exact inflow velocity in the whole fluid domain is out of the scope of this work. But, the modeling of these interactions cannot be avoided. It can be found in the literature several empirical formulas to describe this phenomenon. Here, the formulation provided in Yoshimura and Masumoto (2012), Eq. (7.9) is chosen in order to obtain a parametric formulation of the interaction coefficients.

$$\begin{cases} u_r^{'} & = \epsilon\,(1-w)\,\sqrt{\eta\left[1+\kappa\left(\sqrt{1+C_{th}}-1\right)\right]^2+(1-\eta)} \\ v_r^{'} & = \gamma_r\left(v_s^{'}+l_r^{'}r_s^{'}\right) \end{cases} \tag{7.9}$$

The dependency of the rudder inflow velocity with the propeller thrust is modeled thanks to the interactions coefficients ϵ and κ and the geometric ratio between the propeller diameter and the rudder span, $\eta = D_p/b_r$. Parametric expressions of ϵ and κ are provided in (Yoshimura and Masumoto, 2012). Downstream to the propeller the axial flow is increased, which can be noticed in Eq. 7.9. The axial rudder inflow velocity increases with the propeller thrust loading coefficient $C_{th} = 8K_T/\pi J^2$. The transverse rudder inflow velocity $v_R^{(\mathbf{s})}$ depends on the ship turning rate and ship transverse velocity. The hull tends to decrease the absolute value of the transverse rudder inflow velocity. This effect is represented by Yoshimura and Masumoto with the flow rectification factors, γ_r and $l_r^{'}$ in Eq. 7.9. The propeller walk effect can be take into account using a different value of γ_r according to the sign of $\left(v_s^{'}+l_r^{'}r_s^{'}\right)$. According to Fukui et al. (2016), the flow rectification factor may depend on the heeling angle. A correction can be given to the γ_r as follows:

$$\gamma_r = \gamma_r\,(\phi_s = 0)\,[1 + c_\gamma\,|\phi_s|] \tag{7.10}$$

The generalized force vector of the rudder is given by:

$$F_r = \left[X_r,\ Y_r,\ 0,\ -r_z^{(\mathbf{s})}Y_r,\ 0,\ N_r\right]^T \tag{7.11}$$

where $r_z^{(\mathbf{s})}$ is the componant along the $\underline{z}_s$ axis of the geometric center of the rudder.

7.2.3. Hull advance resistance

The hull advance resistance can be split into two parts: the steady hull advance resistance with no drift and the hull resistance due to drift and yaw rate. Since the propeller force is

already multiplied by $(1-t)$, where t is the thrust deduction factor, only the bare hull resistance must considered. The hull resistance due to drift and yaw rate is non-linear. Here this part of the hull resistance can be expressed with the non-linear Taylor expansion proposed by Yoshimura and Masumoto (2012). The hull advance resistance force is assumed to be oriented by the longitudinal ship axis $\underline{x}_s$, $\underline{F}_{hi} = [X_h, 0, 0, 0, 0, 0]^T$:

$$X_{hi} = X_{bh}(u_s) + k_h \left\{ X'_{\beta_s^2}\beta_s^2 + X'_{\beta_s r'_s}\beta_s r'_s + X'_{r'^2_s} r'^2_s + X'_{\beta_s^4}\beta_s^4 \right\} \tag{7.12}$$

where $k_h = \frac{1}{2}\rho_w L_{pp} T_m U_s^2$, with L_{pp} and T_m denoting respectively the waterline ship length and the draft at midship. The non-dimensional ship turning rate is expressed as follows:

$$r'_s = \frac{L_{pp}}{U_s} r_s. \tag{7.13}$$

The hull resistance part due to drift and yaw rate can be replaced by any other formulation of induced resistance due to the drift.

7.2.4. Windage model

The windage model used here is an empirical model proposed by Blendermann (1994). According to wind tunnel tests performed on various types of ships, Blendermann (1994) proposed a formulation of the windage force as follows:

$$\begin{cases} X_{wa} &= \frac{1}{2}\rho_a A_f U_{rw}^2 (H_m) \left[-D'_l \frac{A_l}{A_f} \frac{\cos\beta_{rw}}{1-\frac{\delta_w}{2}\left(1-\frac{D'_l}{D'_t}\right)\sin^2 2\beta_{rw}} \right] \\ Y_{wa} &= \frac{1}{2}\rho_a A_l U_{rw}^2 (H_m) \left[-D'_t \frac{\sin\beta_{rw}}{1-\frac{\delta_w}{2}\left(1-\frac{D'_l}{D'_t}\right)\sin^2 2\beta_{rw}} \right] \\ K_{wa} &= \frac{1}{2}\rho_a A_l H_m U_{rw}^2 (H_m) \left[-\kappa \frac{s_h}{H_m} D'_t \frac{\sin\beta_{rw}}{1-\frac{\delta_w}{2}\left(1-\frac{D'_l}{D'_t}\right)\sin^2 2\beta_{rw}} \right] \\ N_{wa} &= L_{oa} \frac{A_l}{A_f} \left[\frac{s_l}{L_{oa}} - 0.18\left(\beta_{rw} - \frac{\pi}{2}\right) \right] Y_{wa} \end{cases} \tag{7.14}$$

In this formulation, L_{oa} denotes the overall ship length. $H_m = A_l/L_{oa}$ defines mean height of the windage lateral surface. A_l and A_f denote respectively the lateral and the windage frontal area. s_l denotes the distance of the windage lateral-plane centroid from the main section. s_h is the height of the windage lateral plane centroid. The other parameters are tabulated dependenig on the type of ship.

K_{wa} and N_{wa} are expressed at O_{wa} defined by the intersection of the ship symmetry plane, midship section and the free surface. The generalized windage force can be expressed at O_s as follows:

$$\underline{F}_{wa} = \left[[X_{wa},\ Y_{wa},\ 0]\ [K_{wa},\ 0,\ N_{wa}] + \underline{O_s O_{wa}} \times [X_{wa},\ Y_{wa},\ 0]^T \right]^T \tag{7.15}$$

7.2.5. Modeling of a varying forward speed

The time domain seakeeping model is defined with respect to a given forward speed (cf. Chap. 6). To take into account a varying forward speed, a new formulation of the added mass and damping at infinite frequency and of the fluid memory force $\underline{\mu}$ is proposed here. Assuming that the ship forward speed is within the range $\left[U_h^{(1)};\ U_h^{(2)}\right]$, the added mass, the damping and the expression of the fluid memory force are approximated by linear interpolations. According to mean forward speeds $U_h^{(1)}$ and $U_h^{(2)}$, the ratio τ is defined as,

$$\tau = \frac{u_s - U_h^{(1)}}{U_h^{(2)} - U_h^{(1)}} \tag{7.16}$$

Each components of the fluid memory force are then calculated as follows:

$$\mu_i = (1-\tau)\,\mu_i^{(1)} + \tau \mu_i^{(2)} \tag{7.17}$$

where,

$$\begin{cases} \mu_i^{(1)} & = \sum_{j=1}^{6} \mu_{ij}^{(1)} \\ \mu_{ij}^{(1)} & = \underline{C}_{ij}^{\prime(1)} \underline{y}_{ij}^{(1)} \\ \mu_i^{(2)} & = \sum_{j=1}^{6} \mu_{ij}^{(2)} \\ \mu_{ij}^{(2)} & = \underline{C}_{ij}^{\prime(2)} \underline{y}_{ij}^{(2)} \end{cases}, \tag{7.18}$$

The interpolated added mass matrix is given from:

$$\underline{\underline{\tilde{A}}} = (1-\tau)\,\underline{\underline{\tilde{A}}}^{(1)} + \tau \underline{\underline{\tilde{A}}}^{(2)} \tag{7.19}$$

Finally, the damping matrix is given from:

$$\underline{\underline{\tilde{B}}} = (1-\tau)\,\underline{\underline{\tilde{B}}}^{(1)} + \tau \underline{\underline{\tilde{B}}}^{(2)} \tag{7.20}$$

The ship equations of motion is then transformed as follows:

$$\begin{cases} \dot{\underline{S}} & = \begin{bmatrix} \underline{\underline{T}}^{\mathbf{c}}_{\mathbf{s}} & \underline{\underline{0}} \\ \underline{\underline{0}} & \underline{\underline{R}}^{\mathbf{c}}_{\mathbf{s}} \end{bmatrix} \underline{V}_s \\ \dot{\underline{V}}_s & = \left[\underline{\underline{M}}_S + \underline{\underline{\tilde{A}}}\right]^{-1} \left[\underline{F} - \left[\underline{\underline{\tilde{B}}} + \underline{\underline{D}}\right] \underline{V}_s - \underline{\mu} - \underline{\underline{C}}\, \underline{S}\right] \\ \dot{\underline{y}}^{(1)}_{ij} & = \underline{\underline{A}}^{'(1)}_{ij} \underline{y}^{(1)}_{ij} + \underline{\underline{B}}^{'(1)}_{ij} V^{(1)}_{s,j},\ \forall i,j \in [\![2;6]\!] \\ \dot{\underline{y}}^{(2)}_{ij} & = \underline{\underline{A}}^{'(2)}_{ij} \underline{y}^{(2)}_{ij} + \underline{\underline{B}}^{'(2)}_{ij} V^{(2)}_{s,j},\ \forall i,j \in [\![2;6]\!] \end{cases} \tag{7.21}$$

The expression of the external forces, denoted by $\underline{F}$, can be precised as the sum of the first order wave force, rudder force, propeller force, hull advance resistance and windage forces, which leads to:

$$\underline{F} = \underline{F}_w + \underline{F}_r + \underline{F}_p + \underline{F}_{hi} + \underline{F}_{wa} + \underline{F}_{hnl} \tag{7.22}$$

7.3. A mixed seakeeping and maneuvering model

7.3.1. Maneuvering equations of motion

The maneuvering motion may lead to large horizontal ship motions: surge, sway and yaw. The maneuvering motions are at low frequency. Consequently, it is assumed that the maneuvering derivatives can be taken constant and that the zero frequency added mass are constant too. Consequently, ship equations of motion considered for the ship maneuvering can be written as follows:

$$\begin{cases} \dot{\underline{S}} & = m_h \circ \begin{bmatrix} \underline{\underline{T}}^{\mathbf{c}}_{\mathbf{s}} & \underline{\underline{0}} \\ \underline{\underline{0}} & \underline{\underline{R}}^{\mathbf{c}}_{\mathbf{s}} \end{bmatrix} \underline{V}_s \\ \dot{\underline{V}}_s & = m_h \circ \left[\underline{\underline{M}}_s + \underline{\underline{A}}_s\left(\omega \backsim 0\right)\right]^{-1} \left[\underline{F} - \underline{\underline{C}}_{rb,s}\, \underline{V}_s\right] \end{cases} \tag{7.23}$$

where m_h is the degree of freedom vector and $\circ$ denotes the Hadamard product. Generally, maneuvering models consider only the surge sway and yaw motion, consequently $m_h = [1,\ 1,\ 0,\ 0,\ 0,\ 1]^T$. The matrix $\underline{\underline{C}}_{rb,s}$ is the Coriolis and centripetal matrix defined as follows (Perez, 2006):

$$\underline{\underline{C}}_{rb,s} = \begin{bmatrix} \Delta_s \underline{\underline{I}}_3 & -\Delta_s \underline{\underline{S}}\left(\underline{G}^{(\mathbf{s})}_s\right) \\ \Delta_s \underline{\underline{S}}\left(\underline{G}^{(\mathbf{s})}_s\right) & \underline{\underline{I}}_s \end{bmatrix}. \tag{7.24}$$

where G_s is the ship center of gravity. The matrix $\underline{\underline{S}}$ denotes the three-by-three skew-symmetric matrix, for instance:

$$\underline{\underline{S}}\left(\underline{G}_s^{(\mathbf{s})}\right) = \begin{bmatrix} 0 & -g_{sz}^{(\mathbf{s})} & g_{sy}^{(\mathbf{s})} \\ g_{sz}^{(\mathbf{s})} & 0 & -g_{sx}^{(\mathbf{s})} \\ -g_{sy}^{(\mathbf{s})} & g_{sx}^{(\mathbf{s})} & 0 \end{bmatrix} \tag{7.25}$$

Into the sum the generalized external forces $\underline{F}$, the generalized hydrodynamic force of the hull $\underline{F}_h$ is taken into account. The hydrodynamic force of the hull can be expressed as series expansion of the ship velocity parameterization. For instance, the hull derivatives proposed in the MMG model of Yoshimura and Masumoto (2012) are given as function of the yaw turning rate r_s and the ship drift angle $\beta_s = -\arctan\frac{v_s}{u_s}$:

$$\begin{cases} Y_h & = k_h \left\{ Y'_{\beta_s}\beta_s + Y'_{r'_s} r'_s + Y'_{\beta_s^2 r'_s}\beta_s^2 r'_s + Y'_{\beta_s r_s'^2}\beta_s r_s'^2 + Y'_{\beta_s^3}\beta_s^3 + Y'_{r_s'^3} r_s'^3 \right\} \\ N_h & = k_h L_{pp} \left\{ Y'_{\beta_s}\beta_s + Y'_{r'_s} r'_s + Y'_{\beta_s^2 r'_s}\beta_s^2 r'_s + Y'_{\beta_s r_s'^2}\beta_s r_s'^2 + Y'_{\beta_s^3}\beta_s^3 + Y'_{r_s'^3} r_s'^3 \right\} \end{cases}, \tag{7.26}$$

where $k_h = \frac{1}{2}\rho_w L_{pp} T_m U_s^2$. The non-dimensional yaw turning rate is defined as $r'_s = \frac{L_{pp}}{U_s} r_s$.

To take into account the heeling moment due to the drift, it is assumed that the heeling moment is zero at $T_m/3$ below the free surface. Consequently, the generalized hydrodynamic force of the hull is written as follows:

$$\underline{F}_h = [0,\ Y_h,\ 0,\ z_m Y_h,\ 0,\ N_h]^T \tag{7.27}$$

where it is assumed that $z_m = l_z - \frac{2}{3}T_m$.

7.3.2. 6 dof mixed equations of motion

The mixed approach is based on the maneuvering equations of motion for horizontal motions and the seakeeping time domain equations of motion for the vertical motions. Equations of motions can then be written as follows:

$$\begin{cases} \dot{\underline{S}} &= \begin{bmatrix} \underline{\underline{T}}^{\mathbf{c}}_{\mathbf{s}} & \underline{\underline{0}} \\ \underline{\underline{0}} & \underline{\underline{R}}^{\mathbf{c}}_{\mathbf{s}} \end{bmatrix} \underline{V}_s \\ \dot{\underline{V}}_s &= \left[\underline{\underline{M}}_S + \underline{\underline{A}}_{hv}\right]^{-1} \left\{\underline{F} - \left[m_v \circ \left(\underline{\underline{B}}_{hv} + \underline{\underline{D}}\right) + m_h \circ \underline{\underline{C}}_{rb,s}\right] \underline{V}_s - \underline{\mu} - \underline{\underline{C}}\,\underline{S}\right\} \\ \dot{\underline{y}}^{(1)}_{ij} &= \underline{\underline{A}}^{\prime(1)}_{ij} \underline{y}^{(1)}_{ij} + \underline{\underline{B}}^{\prime(1)}_{ij} V^{(1)}_{s,j},\ \forall (i,j) \in [\![2;6]\!]^2 \setminus \{(4,2),(4,6)\} \\ \dot{\underline{y}}^{(2)}_{ij} &= \underline{\underline{A}}^{\prime(2)}_{ij} \underline{y}^{(2)}_{ij} + \underline{\underline{B}}^{\prime(2)}_{ij} V^{(2)}_{s,j},\ \forall (i,j) \in [\![2;6]\!]^2 \setminus \{(4,2),(4,6)\} \end{cases} \tag{7.28}$$

$\underline{\mu}$ is determined according to Eq. (7.17), where transfer functions H_{22}, H_{26}, H_{62} and H_{66} are set to zero. The degree of freedom vectors are defined as follows: $m_v = [0,\ 0,\ 1,\ 1,\ 1,\ 0]^T$ and $m_h = [1,\ 1,\ 0,\ 0,\ 0,\ 1]^T$. The added mass matrix $\underline{\underline{A}}_{hv}$ is a mix between $\underline{\underline{\tilde{A}}}$, the infinite frequency added mass for the vertical ship motion and $\underline{\underline{A}}_s(0)$, the zero frequency added mass for the horizontal ship motion. $\underline{\underline{A}}_{hv}$ is defined as follows:

$$\underline{\underline{A}}_{hv} = \begin{bmatrix} A_{11}(0) & 0 & 0 & 0 & 0 & 0 \\ 0 & A_{22}(0) & 0 & \tilde{A}_{24} & 0 & A_{26}(0) \\ 0 & 0 & \tilde{A}_{33} & 0 & \tilde{A}_{35} & 0 \\ 0 & 0 & 0 & \tilde{A}_{44} & 0 & 0 \\ 0 & 0 & \tilde{A}_{53} & 0 & \tilde{A}_{55} & 0 \\ 0 & A_{62}(0) & 0 & \tilde{A}_{64} & 0 & A_{66}(0) \end{bmatrix} \tag{7.29}$$

The damping matrix $\underline{\underline{B}}_{hv}$ defined as follows:

$$\underline{\underline{B}}_{hv} = \begin{bmatrix} \tilde{B}_{11} & 0 & 0 & 0 & 0 & 0 \\ 0 & \tilde{B}_{22} & 0 & \tilde{B}_{24} & 0 & \tilde{B}_{26} \\ 0 & 0 & \tilde{B}_{33} & 0 & \tilde{B}_{35} & 0 \\ 0 & 0 & 0 & \tilde{B}_{44} & 0 & 0 \\ 0 & 0 & \tilde{B}_{53} & 0 & \tilde{B}_{55} & 0 \\ 0 & \tilde{B}_{62} & 0 & \tilde{B}_{64} & 0 & \tilde{B}_{66} \end{bmatrix} \tag{7.30}$$

Since $\underline{\underline{A}}_{hv}$ and $\underline{\underline{B}}_{hv}$ vary with the ship speed, these matrices are defined by linear interpolation between two ship speeds as achieved in Eqns (7.19) and (7.20).

The sum of the generalized external forces $\underline{F}$ is expressed as follows:

$$\underline{F} = \underline{F}_w + \underline{F}_r + \underline{F}_p + \underline{F}_{hi} + \underline{F}_{wa} + \underline{F}_h \tag{7.31}$$

7.4. Case of study

The Kriso Container Ship was chosen as a case of study because this ship model is well documented in the literature.

7.4.1. Kriso Container Ship modeling

The case of study is the Kriso Container Ship (KCS) at test conditions used during the SIMMAN 2008 workshop. A summary of the hull particulars and test conditions is given in Tab. 7.1 and the hull sections are represented in Fig. Open water propeller curves are given in Annex C.7.1. The hull advance resistance is approximated with the regression model of Holtrop and Mennen (1982), the data are given in Annex C.7.2.

Hull		Rudder		Propeller		Test conditions	
L_{pp}	230 m	A_r	54.5 m^2	D_p	7.9 m	GM_t	0.60 m
B_s	32.2 m	λ_r	1.8	$p_x^{(s)}$	-110.8 m	$i_{zz} \approx i_{yy}$	57.5 m
T_m	10.8 m	$\dot{\delta}_r$	2.32 °/s	$p_z^{(s)}$	10.4 m	i_{xx}	12.9 m
∇_s	52030 m^3	$r_x^{(s)}$	-115 m	Open water propeller curve		U_s	24 knots
C_b	0.651	$r_z^{(s)}$	7.7 m	cf. Annex C.7.1		LCB	-3.4 m

Table 7.1.: Kriso Container Ship (KCS) particulars and test conditions

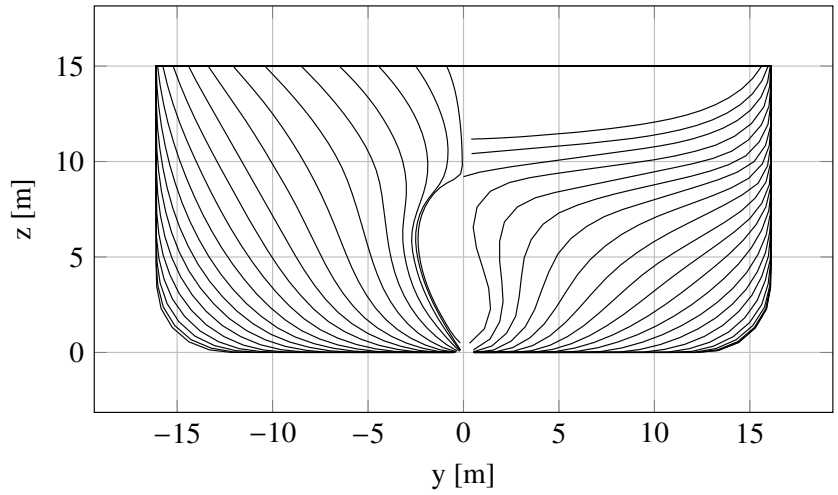

Figure 7.1.

Added masses at zero frequency have been estimated with the STF strip theory Salvesen et al. (1970) data at $\omega = 0.1$. The hull maneuvering derivatives of the KCS are taken from (Fukui et al., 2015). This model has the advantage to take into account the heel influence. The Taylor expansion modeling the surge, sway and yaw hydrodynamic force of the hull is given from:

$$
\begin{cases}
\frac{X_h}{k_h} = & c_{x0}\left|\phi_s\right| + X'_{\beta_s\phi_s}\beta_s\phi_s + X'_{r_s\phi_s}r_s\phi_s \\
& X'_{\beta_s\beta_s}\left(1 + c_{x\beta_s\beta_s}\left|\phi_s\right|\right)\beta_s^2 + X'_{\beta_s r_s}\left(1 + c_{x\beta_s r_s}\left|\phi_s\right|\right)\beta_s r'_s \\
& X'_{r_s r_s}\left(1 + c_{x r_s r_s}\right)r'^2_s + X'_{\beta_s\beta_s\beta_s\beta_s}\left(1 + c_{x\beta_s\beta_s\beta_s\beta_s}\left|\phi_s\right|\right)\beta_s^4 \\
\frac{Y_h}{k_h} = & Y'_{\phi_s}\phi_s + Y'_{\beta_s}\left(1 + c_{y\beta_s}\left|\phi_s\right|\right)\beta_s + Y'_{r_s}\left(1 + c_{yr_s}\left|\phi_s\right|\right)r'_s \\
& Y_{\beta_s\beta_s\phi_s}\beta_s^2\phi + Y'_{\beta_s r_s\phi_s}\beta_s r_s\phi_s + Y'_{r_s r_s\phi_s}r_s^2\phi_s \\
& Y'_{\beta_s\beta_s\beta_s}\left(1 + c_{y\beta_s\beta_s\beta_s}\left|\phi_s\right|\right)\beta_s^3 + Y'_{\beta_s\beta_s r_s}\left(1 + c_{y\beta_s\beta_s r_s}\left|\phi_s\right|\right)\beta_s^2 r_s \\
& Y'_{\beta_s r_s r_s}\left(1 + c_{y\beta_s r_s r_s}\left|\phi_s\right|\right)\beta_s r'^2_s + Y'_{r_s r_s r_s}\left(1 + c_{yr_s r_s r_s}\left|\phi_s\right|\right)r'^3_s \\
\frac{N_h}{k_h L_{pp}} = & N'_{\phi_s}\phi_s + N'_{\beta_s}\left(1 + c_{n\beta_s}\left|\phi_s\right|\right)\beta_s + N'_{r_s}\left(1 + c_{nr_s}\left|\phi_s\right|\right)r'_s \\
& N_{\beta_s\beta_s\phi_s}\beta_s^2\phi + N'_{\beta_s r_s\phi_s}\beta_s r_s\phi_s + N'_{r_s r_s\phi_s}r_s^2\phi_s \\
& N'_{\beta_s\beta_s\beta_s}\left(1 + c_{n\beta_s\beta_s\beta_s}\left|\phi_s\right|\right)\beta_s^3 + N'_{\beta_s\beta_s r_s}\left(1 + c_{n\beta_s\beta_s r_s}\left|\phi_s\right|\right)\beta_s^2 r_s \\
& N'_{\beta_s r_s r_s}\left(1 + c_{n\beta_s r_s r_s}\left|\phi_s\right|\right)\beta_s r'^2_s + N'_{r_s r_s r_s}\left(1 + c_{nr_s r_s r_s}\left|\phi_s\right|\right)r'^3_s
\end{cases}
\tag{7.32}
$$

where $k_h = \frac{1}{2}\rho_w L_{pp} T_m U_s^2$. The hull derivatives are given in Annex C.7.3. The interaction coefficients modeling the interaction between the hull, the propeller and the rudder are given in Annex C.7.4.

According to the STF strip theory and the considered maneuvering model in Eq. (7.32), transfer functions H_{ij} for the fluid memory forces can be estimated. Expressions of the transfer functions are given in Annex C.7.6. Corresponding impulse responses, added masses and damping are fitted with good agreement.

In following results, the mean ship speeds of reference are $\left[U_h^{(1)};\ U_h^{(2)}\right] = [10.29;\ 12.86]$ m.s^{-1} for the zig-zag tests and $\left[U_h^{(1)};\ U_h^{(2)}\right] = [5.15;\ 12.86]$ m.s^{-1} for the turning circle.

7.4.2. Benchmark results

Two benchmark results are used to compare and to validate the two approaches with time series of maneuvering motions. Free sailing tests of zig-zag 15°-1° were performed at the Potsdam Model Basin (SVA) with a KCS model at the scale of 1:52.667. These results can be found in (Mofidi and Carrica, 2014; Shen et al., 2015). Fukui et al. (2015) and Fukui et al. (2016) investigated the effect of the roll motion on the KCS maneuverability. Turning circle with a rudder angle of 35° and zig-zag 20°/20° maneuvers were carried out with a KCS scale model of 1:105 at the tank of the Japan Marine United Corporation (JMUC). These two free sailing results are used to compare the time series of the standard maneuvering motions obtained with the presented 6 dof dynamic ship models. The ship speed entry is 12.35 m.s^{-1}(Froude number 0.26) according to the Simman 2008 workshop cases Stern et al. (2011) and the rudder angle is zero at the beginning of the test maneuvers. Free sailing maneuver results are digitized from (Fukui et al., 2016) and (Shen et al., 2015).

A turning circle maneuver consists in turning the rudder at a given angle with ship motions let free. Generally, the considered rudder angle for a turning circle is $\pm 35°$. A zigzag X_{δ_r}/X_{ψ_s} test maneuver consists in turning the rudder at the angle X_{δ_r} until the ship experiences a heading modification of X_{ψ_s} and reversing the rudder angle until the ship experiences a heading deviation of $-X_{\psi_s}$ from the initial course and so on. A standard definition of this maneuver is provided in (ITTC, 2002).

Moreover standard KCS maneuvering results were presented in (Toxopeus and Lee, 2008; Stern et al., 2011). These results were obtained with experiments and empirical methods. Moreover, in (Toxopeus and Lee, 2008) statistical maneuvering results obtained with similar ship are presented..

7.5. Validation of the mixed seakeeping and maneuvering model

7.5.1. Results

During a turning circle maneuver with a rudder angle of 35°, Figs. 7.2 and 7.3 show respectively the ship path in the plane $\left(\underline{x}_n,\ \underline{y}_n\right)$ and time series of the drift angle β_s, surge velocity u_s, heel angle ϕ_s, surge velocity u_s and yaw turning rate r_s. Figs. 7.2 and 7.3 compare the results obtained thanks to the mixed seakeeping and maneuvering model (solid line) with the EFD data of the free running test at the JMUC (dashed line).

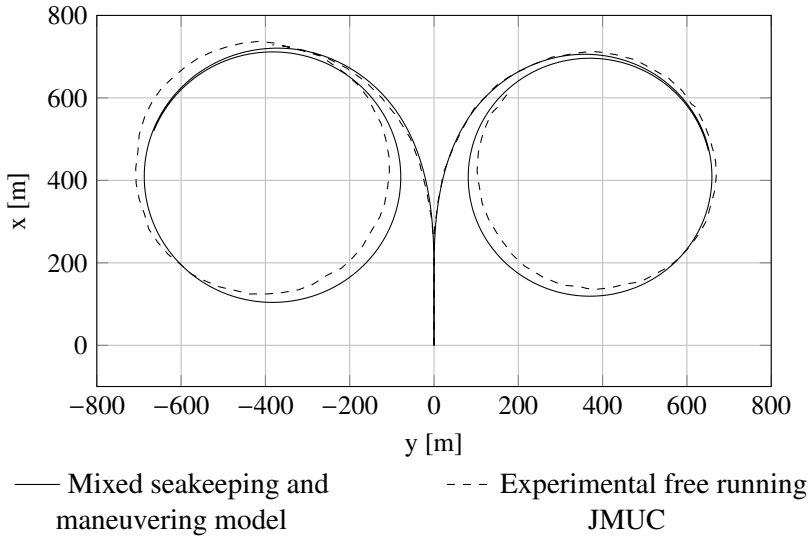

Figure 7.2.: Turning circle path with rudder angle $\delta_r = 35°$. The results obtained with the mixed seakeeping and maneuvering model (——) are compared with the free sailing EFD data of the JMUC (- - -).

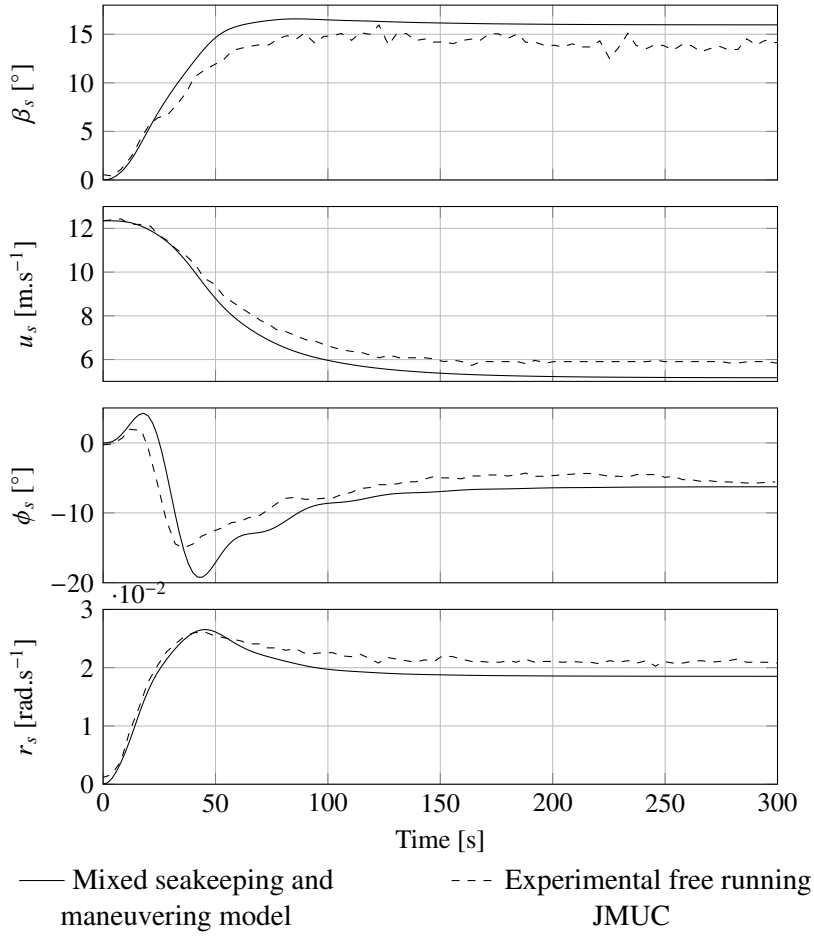

Figure 7.3.: Time history during a 35° turning circle maneuver of the: drift angle β_s, surge velocity u_s, heel angle ϕ_s, surge velocity u_s and yaw turning rate r_s. The results obtained with the mixed seakeeping and maneuvering model (——) are compared with the free sailing EFD data of the SVA (- - -).

Figure 7.4 shows, during a KCS zigzag 20/20° test maneuver, the time history of: the rudder angle δ_r, the ship heading ψ_s, the ship drift angle $\beta_s = -\arctan(v_s/u_s)$, the heeling angle ϕ_s and the ship longitudinal speed u_s. Solid lines correspond to the mixed seakeeping and maneuvering model. Dashed lines correspond to the free sailing data performed by the JMUC. Figure 7.5 shows, during a KCS zigzag 15/1° test maneuver, the time history of: the rudder angle δ_r, the ship heading ψ_s, the ship drift angle β_s, the heeling angle ϕ_s and the ship longitudinal speed u_s. Solid lines correspond to the mixed seakeeping and maneuvering model. Dashed lines correspond to the experimental free sailing data performed by the SVA.

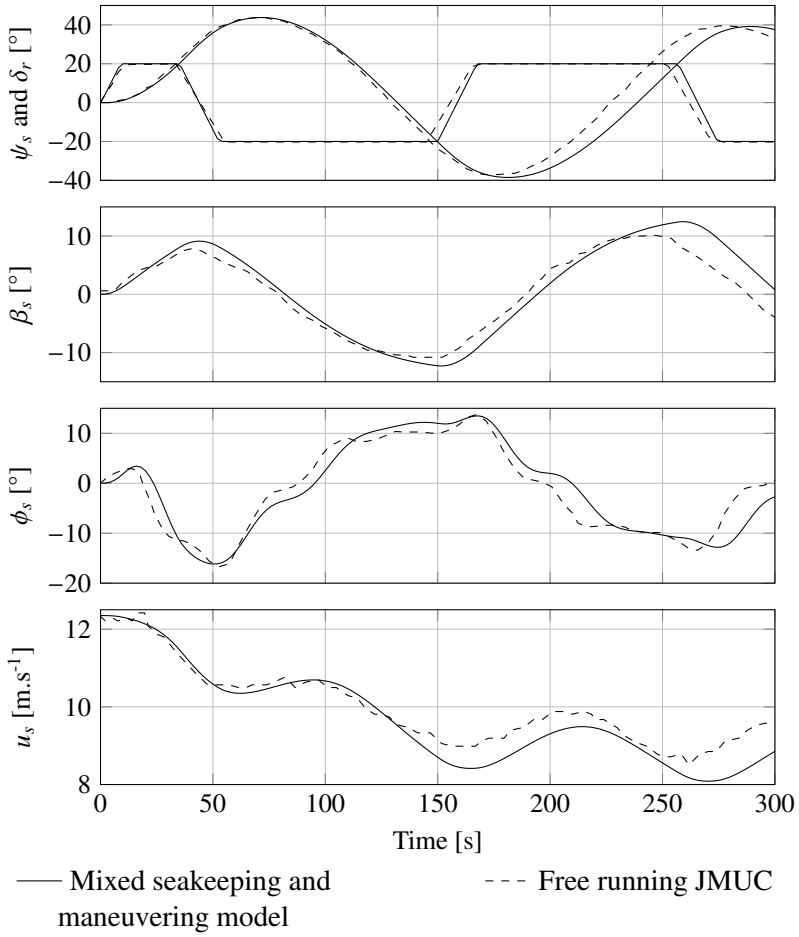

Figure 7.4.: Time history during a zigzag 20/20° maneuver of : rudder angle δ_r, heading ψ_s, drift angle β_s, heel angle ϕ_s and surge velocity u_s. Results obtained with the mixed seakeeping and maneuvering model (——) are compared with the free sailing EFD data of the JMUC (- - -).

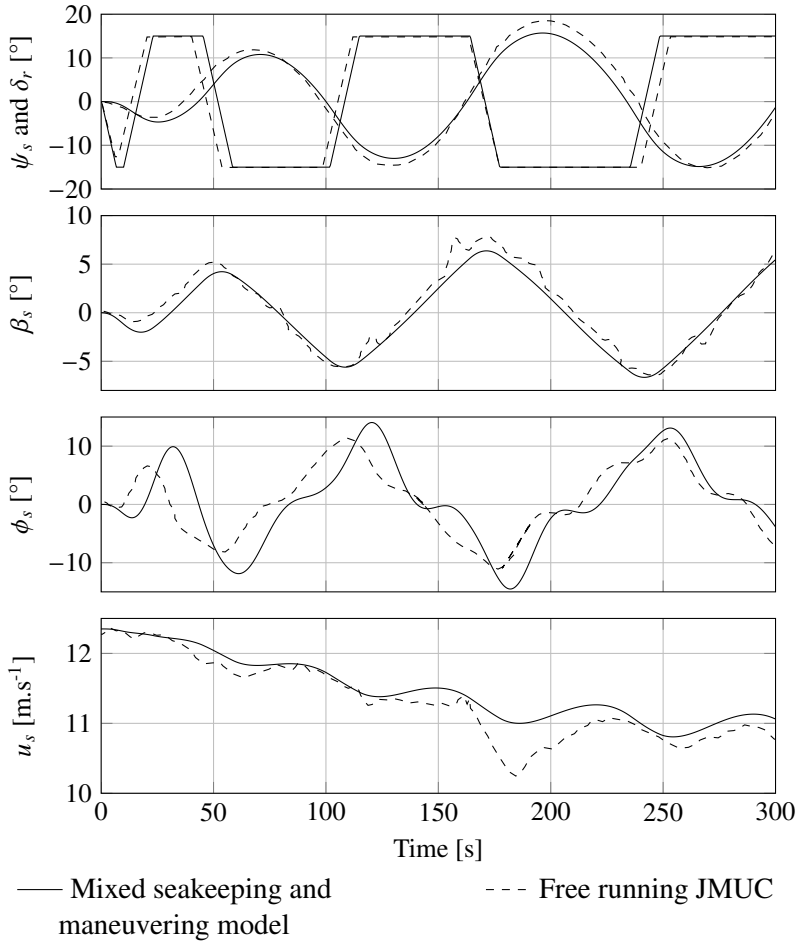

Figure 7.5.: Time history during a zigzag 15/-1° maneuver of : rudder angle δ_r, heading ψ_s, drift angle β_s, heel angle ϕ_s and surge velocity u_s. Results obtained with the mixed seakeeping and maneuvering model (——) are compared with the free sailing EFD data of the SVA (- - -).

7.5.2. Analysis and discussion

According to Figure 7.2, the transient part of the ship path is correctly estimated for both turning circles. The turning radius of gyration is correctly estimated. The only difference is the maximum transfer distance. In Figure 7.3, it can be shown that the transient part of the yaw turning rate and the surge velocity are accurately predicted until 50 seconds. However, transient parts of the drift angle and heeling angle are less well predicted. The predicted drift angle increases more rapidly than during the free sailing tests. Amplitudes of roll are more important and slower. Regarding steady states, the drift angle and the loss of surge velocity are overestimated. The turning rate is underestimated which is consistent with the predicted ship speed that is lower. The heeling angle seems to converge towards the same value.

According to the zig-zag maneuvers 20/20° and 15/-1°, respectively in Figs. 7.4 and 7.5, the predicted turning period is slightly longer. The predicted heading for both maneuvers is slightly longer. However, concerning the amplitude of the motions, observations are different. The loss of surge velocity and the drift angle are underestimated for the zig-zag test 15/-1° and overestimated for the zig-zag test 20/20°. For the zig-zag 15/-1°, the roll amplitude is overestimated and overshoot angles are underestimated, whereas for the zig-zag 20/20°, these motions are correctly predicted in terms of amplitude. Concerning the evolution of ship motions during these two zig-zag maneuvers, the same patterns than for the free sailing data are observed.

Despite the difference noticed between the predicted motions and the free sailing data of the SVA basin and JMUC basin, the mixed maneuvering and seakeeping approach shows a significant improvement compared to the direct extension of the time domain seakeeping model. The mixed seakeeping and maneuvering approach is satisfying. Finally, according to maneuvering results from different other empirical methods, PMM tests and free sailing results available in (Toxopeus and Lee, 2008; Stern et al., 2011) and compiled in Tab. 7.2, the mixed seakeeping and maneuvering approach is validated for the KCS.

Type	Source	Overshoot angles 1st 10/10°	10/-10°	2nd 10/10°	10/-10°	20/20°	Tactical diameter $\delta_r = 35°$
Empirical methods	SurSim	3.8°		4.2°		9.1°	3.88 L_{pp}
	SurSim sb	10.1°		15.1°		20.0°	2.77 L_{pp}
	FreSim	4.2°		5°		9.7°	4.36 L_{pp}
	FreSim sb	9.6°		13.0°		18.5°	2.96 L_{pp}
	MPP Marin	6.3°		7.7°		13.3°	3.01 L_{pp}
	Force SY Adv	-	-	16.7°	19.1°	-	-
	Force SY Sim	-	-	24.2°	29.8°	-	-
Circular Motion Tests	Hiroshima CMT	-	-	29.1°	18.7°	-	-
	MOERI CMT	-	-	8.0°	6.7°	-	-
	NMRI CMT	-	-	12.0°	9.2°	-	-
	Hokkaido Univ. CMT	-	-	12.0°	9.0°	-	-
Free Sailing Tests	SVA	-	-	17.0°	20.0°	-	-
	BSHC	-	-	20.3°	21.6°	-	2.74 L_{pp}
	Hokkaido Univ. (quasi 3dof)	-	-	11.7°	11.97°	-	3.34 L_{pp}
Statistics (Toxopeus and Lee, 2008)		**10°**		**15°**		**23.70°**	**2.8** L_{pp}
Presented model		**11.65°**	**9.65°**	**17.5°**	**21.05°**	**24.60°**	**2.82** L_{pp}

Table 7.2.: Compilation of KCS standard maneuvering results from (Toxopeus and Lee, 2008; Stern et al., 2011)

7.6. Conclusion

The time domain seakeeping approach developed in Chap. 6 has been enhanced to model the horizontal ship motion. First, rudder, propeller, windage models have been introduced. Parametric models, suitable with the presented approach have been introduced to enable the study of different ships. An approach mixing the modeling of the horizontal motion with a maneuvering model and the modeling of the vertical motion with the time domain seakeeping model has been developed. A validation exercise with experimental free sailing data and other empirical method was successfully performed.

The mixed approach uses constant maneuvering derivatives which is suitable for low frequency motions. Therefore, the evolution of the linear damping with the frequency of the motion is not represented. To verify this effect a second approach modifying the potential damping with viscous exponential decay such as proposed in (Bailey et al., 1997; Fossen and Smogeli, 2004) has been implemented in Annex C.6. At this time, results are not satisfactory and need further investigations.

Part IV.

Towards kite towing of ships

8. Mean equilibrium of a ship towed by kite

Résumé: Equilibre moyen d'un navire tracté par cerf-volant

Afin d'étudier les paramètres qui ont de l'importance sur les performances d'un navire tracté par cerf-volant, une étude de l'équilibre du navire est menée en considérant la force de traction moyenne au cours d'une trajectoire.

Dans un premier temps, la méthode de résolution de l'équilibre des 6 degrés de libertés est introduite. Dans un second temps, deux indicateurs permettant d'estimer la performance du système sont introduits. Le premier indicateur est le ratio d'économie de puissance. Le second indicateur est le facteur d'efficacité du cerf-volant correspondant au rapport entre l'effort propulsif du cerf-volant et la norme de la force de traction. Il est suggéré que pour optimiser le profit apporté par un cerf-volant, il est plus intéressant de maximiser l'efficacité du cerf-volant plutôt que le coefficient d'économie de puissance. En effet le facteur d'efficacité du cerf-volant est un compromis entre maximisation des économies de puissance et minimisation de la charge alaire pour augmenter la durée de vie du kite et diminuer son prix. Ensuite, l'influence du fardage, de la position longitudinale du point d'attache et de la vitesse du vent sont étudiés sur le porte conteneur KCS de 230 m tracté par un kite de 500 m2 avec 500 m de ligne.

L'influence du fardage est prépondérante devant celle du cerf-volant sur l'équilibre du navire en lacet et est du même ordre sur la dérive. Le fardage rend le navire ardent. Quand le point d'attache du cerf-volant est proche de l'étrave, l'influence du cerf-volant sur l'équilibre en lacet du navire est neutre. En revanche, en reculant le point d'attache, le navire devient plus ardent et l'angle de dérive diminue. La position longitudinale du point d'attache n'a que très peu d'effet sur la gîte et l'économie de puissance réalisée.

Sans surprise, la vitesse du vent augmente l'économie de puissance, l'angle de dérive, l'angle de barre et la gîte. L'allure la plus risquée pour l'équilibre du navire est le vent de travers. L'allure permettant de réaliser la plus grande économie de puissance hélice évolue du petit largue vers le grand largue quand la vitesse du vent augmente. L'efficacité du kite est maximale au vent arrière tant que la vitesse du vent est supérieure à la vitesse du navire. Si la vitesse du vent est plus faible que la vitesse du navire, le vent arrière n'est pas réalisable à moins de tirer profit du gradient de vent. Cependant, ces configurations n'ont pas été étudiées pour des restrictions d'implémentation. Dans ce cas, plus la vitesse du vent diminue plus le maximum d'efficacité est obtenu pour des allures proche du vent.

Le facteur d'efficacité du cerf-volant favorise donc les allures portantes où la charge allaire est minimale. On peut en déduire que la vitesse d'utilisation du navire est décisive pour définir l'intervalle de vent d'utilisation du cerf-volant et donc sa charge allaire nominale de conception.

8.1. Introduction

An important step of this thesis is to determine the mean equilibrium of a ship towed by a kite. Considering, the mean kite towing force, Naaijen and Koster (2010); Leloup et al. (2016) have investigated the mean equilibrium of a ship towed by a kite. Their analysis focused on the fuel saving prediction. In (Naaijen and Koster, 2010), the mean equilibrium was solved for the surge, sway and yaw motions. They showed that the additional resistance caused by the drift imposed by the transverse force of the kite is not significant. Consequently, Leloup et al. (2016) solved only the surge equilibrium. A short comment on the heeling equilibrium and mean rudder angle showed that the kite preserves the ship safety. Naaijen and Koster (2010) and Leloup et al. (2016) developed their analysis on the British Bombardier tanker (Leeuwen and Journée, 2001) with a given kite area, tether length and tether attachment point. A kite of 320 m^2 and a kite of 500 m^2 were used in these studies.

The ship modeling used in (Naaijen and Koster, 2010; Leloup et al., 2016), was simplified: windage and interactions between the hull, the propeller and the rudder were neglected. As shown in Chap. 7 the ship maneuvering is dependent on the interactions between the hull, the propeller and the rudder due to a modification of the local inflow velocity. Since, the kite towing force decreases the propeller thrust, the local inflow velocity at the rudder is modified. The first aim of this chapter is to assess the mean equilibrium of a ship towed by a kite, taking into account the windage and these interactions.

Moreover, the interest of these previous studies was to assess the fuel saving ratio. As highlighted in Sec. 1.3, the fuel saving ratio is important. Nonetheless, to evaluate the profits, the kite cost and the lifetime of the kite should also be regarded. The assessment of the cost and the lifetime of a kite is beyond the scope of the thesis. However, a criteria taking into account global parameters influencing the lifetime and the cost of a kite is developed and studied.

Consequently, in this chapter, the mean equilibrium of a ship towed by kite is solved considering its 6 degrees of freedom and the interactions between the hull, the propeller and the rudder. In this first approach, the coupling between the kite and the ship is neglected. Indeed, a mean kite towing force is computed considering that the tether attachment point is moving at a constant velocity. This first approach is fast and enable the study of a wide range of design parameters.

Firstly, the 6 dof equations of balance of a ship towed by a kite are introduced. Secondly, the criteria taking into account the fuel saving ratio, the lifetime and the cost of a kite is developed. With the case of study detailed in sections 8.4 and 8.5, investigations of the influence of the windage effect, longitudinal tether attachment point and true wind speed on the mean ship equilibirum are performed. In section 8.6 the evolution of the mean aerodynamic pressure and the kite efficiency criteria are investigated for different sailing conditions.

8.2. Equations of the mean equilibrium of a ship towed by kite

8.2.1. Equilibrium equation

The equation of balance is independent from ship positions in the horizontal plane $s_x^{(\mathbf{n})}$ and $s_y^{(\mathbf{n})}$. The mean vertical velocity of the ship is zero, hence $\dot{s}_z^{(\mathbf{n})} = 0$. At the equilibrium the ship turning rate is zero, $\left[\dot{\phi}_s,\ \dot{\theta}_s,\ \dot{\phi}_s\right]^T = \underline{0}$. Hence, the 6 scalar equations in Eq. 8.1 depend on the horizontal linear ship velocities, the vertical ship position and the three attitude angles of the ship: $\left[\dot{s}_x^{(\mathbf{n})},\ \dot{s}_y^{(\mathbf{n})},\ s_z^{(\mathbf{n})},\ \phi_s,\ \theta_s,\ \phi_s\right]^T$. Hence, using ship equations of motion Eq. (7.28), the balance equations of the ship is:

$$\underline{0} = \underline{F}\left(\dot{s}_x^{(\mathbf{n})},\ \dot{s}_y^{(\mathbf{n})},\ s_z^{(\mathbf{n})},\ \phi_s,\ \theta_s,\ \phi_s\right) - \underline{\underline{C}}\left[0,\ 0,\ s_z^{(\mathbf{n})},\ \phi_s,\ \theta_s,\ 0\right]^T \tag{8.1}$$

Since the aim of this chapter is to solve the mean equilibrium of a ship towed by kite, the mean kite force over a loop trajectory is considered. The mean generalized kite force is denoted by $\underline{\bar{F}}_k$. Since only the first order wave load is considered for the ship modeling, the mean generalized wave force is $\underline{0}$. Hence, the wave force is not represented in Eq. (8.1).

Here, the equilibrium is solved for a given ship speed $U_s = \sqrt{\left(\dot{s}_x^{(\mathbf{n})}\right)^2 + \left(\dot{s}_y^{(\mathbf{n})}\right)^2}$ and a given true wind angle β_{tw}. The surge balance, the sway balance and the yaw balance are adjusted respectively by the propeller rotational speed n_p, the ship drift β_s and the rudder angle δ_r. The heave, roll and pitch balances depend on the vertical position of the ship and on heeling and trim angles. Consequently, Eq. (8.1) can be transformed as follows:

$$\underline{0} = \underline{F}\left(n_p,\ \beta_s,\ s_z^{(\mathbf{n})},\ \phi_s,\ \theta_s,\ \delta_r\right) - \underline{\underline{C}}\left[0,\ 0,\ s_z^{(\mathbf{n})},\ \phi_s,\ \theta_s,\ 0\right]^T \tag{8.2}$$

Equation (8.2) is solved with a Newton-Raphson algorithm. The initial solution is $(\tilde{n}_p,\ 0,\ 0,\ 0,\ 0,\ 0)$, where $\tilde{n}_p$ corresponds to a propeller advance ratio J of 0.6:

$$\tilde{n}_p = (1-w)\,\frac{U_s}{0.6 D_p} \tag{8.3}$$

8.2.2. Kite efficiency

In (Naaijen et al., 2006; Naaijen and Koster, 2010; Leloup et al., 2016), the kite efficiency was studied through the fuel saving ratio. The fuel saving ratio is defined as the difference between the fuel consumption without and with the kite divided by the fuel consumption without the kite. To estimate this fuel saving ratio, transmission efficiency and the brake specific fuel consumption are required. Here, the power saving ratio is preferred, since it does not depend on the ship engine efficiency. The power saving ratio is defined from:

$$\eta_k = \frac{n_{p,wok} K_{p,wok} - n_{p,wk} K_{p,wk}}{n_{p,wok} K_{p,wok}} \tag{8.4}$$

where n_p and K_p are respectively the propeller rotational speed and the propeller torque. Subscripts wk and wok denote respectively the corresponding quantity with and without the kite. This power saving ratio expresses the relative decrease of the power delivered by the shaft to the propeller.

As it has been shown in Sec. 1.3, the kite profit is also dependent of the lifetime and the cost of the kite. It is assumed that the kite lifetime can be represented by an increasing function of the ratio σ_d/σ_k, where σ_d and σ_k are respectively the aerodynamic pressure specs for the design and the kite aerodynamic pressure at flight. The kite cost is supposed to be an increasing function of σ_d. Assuming that the lifetime and the cost of a kite are linear, the criteria in Eq. (1.6) can be rewritten as:

$$\frac{k_{td}}{k_{Ck}} \frac{\bar{\eta}_{kf}\left(U_{tw},\, U_s,\, \sigma_d\right)}{\sigma_k} C_{s,t}\left(U_s,\, c_f\right) > 1 \tag{8.5}$$

where k_{td} and k_{Ck} are the linear positive coefficient of the lifetime and cost functions of the kite. This criteria has to be maximized. Neglecting the propeller and the engine efficiency, at a given speed, the criteria can be expressed as follows:

$$\kappa \frac{\underline{T}_k \cdot \underline{x}_s}{\|\underline{T}_k\|} > 1 \tag{8.6}$$

where κ is a positive constant and the kite efficiency η_x is defined by:

$$\eta_x = \frac{\underline{T}_k \cdot \underline{x}_s}{\|\underline{T}_k\|} \tag{8.7}$$

The kite efficiency η_x has to be maximized. η_x enables to represent the trade off between a high kite power saving ratio and a high wind loading safety factor to extend the kite lifetime.

8.3. Case of study

The ship studied here is the Kriso Container Ship (KCS). The specs of the KCS are detailed in Sec. 7.4.1. The propeller, rudder, windage models and the modeling of the interaction with the hull is detailed in 7.2. The hydrodynamic model of the hull uses the Taylor expansions and the derivatives presented in Fukui et al. (2015). Coefficients required by the modeling of the ship are given in Annex C.7. The tether attachment point A is in the ship symetry plane at a height of 25 m above the baseline.

The kite model used to compute the mean kite towing force has been developed in Chap. 3. This model is based on the so-called zero-mass kite model. This model depends on two parameters, the lift to drag angle ϵ_k and the lift coefficient C_{lk}. Based on full scale experiments, significant evolution of ϵ_k and C_{lk} have been noticed according to the turning rate of the kite along a trajectory. Consequently, in 3.6.2 a linear modification with the kite turning rate has been proposed as follows:

$$\begin{cases} \epsilon_k & = \epsilon_0 + \frac{\sqrt{A_k}}{U_{rw}} \kappa_\epsilon \left| \dot{\gamma}_n \right| \\ C_{lk} & = C_{l0} + \frac{\sqrt{A_k}}{U_{rw}} \kappa_l \left| \dot{\gamma}_n \right| \end{cases} \tag{8.8}$$

ϵ_0, κ_ϵ, C_{l0} and κ_l have been identified on a kite of 5 m^2 with an inflatable leading edge dedicated to kite surfing. Same coefficients were taken and are reminded below:

$$\begin{cases} \epsilon_0 & = 0.2013 \text{ rad} \\ \kappa_\epsilon & = 0.0422 \\ C_{l0} & = 0.9856 \\ \kappa_l & = -0.3718 \end{cases} \tag{8.9}$$

The mean kite towing force is computed over a Lissajous trajectory as defined in Sect. 3.4. Trajectory amplitudes are arbitrarily set to $\Delta\phi_8 = 20°$ and $\Delta\theta_8 = 8°$. The center of the trajectory $[\phi_8,\ \theta_8]$ and the angle of the trajectory χ_8 around the axis $\underline{C_8 A}$ are determined by the optimization of the longitudinal kite towing force with a code similar to the one used by Leloup et al. (2016). A database of the optimized trajectory parameters ϕ_8, θ_8 and χ_8 according to different wind conditions, ship velocities and tether lengths is then used. Results presented in next sections use a linear interpolation of this database to determine the trajectory parameters. A part of this database is plotted in Fig. 8.1 for $L_t = 500$ m.

It can be noticed that the optimal trajectory at downwind, i.e. $\beta_{tw} > 150°$, is an horizontal Lissajous trajectory, i.e. $\chi_8 = 180°$. With $\chi_8 = 180°$, at the extremities of the trajectory, the kite is going down. When the ship heading is closer to the wind, i.e. $\beta_{tw} < 100°$, the kite orientation decreases down to $\chi_8 = 90°$. The faster the true wind speed is, the more the transition between the two orientations is pronounced and the closer to the wind the

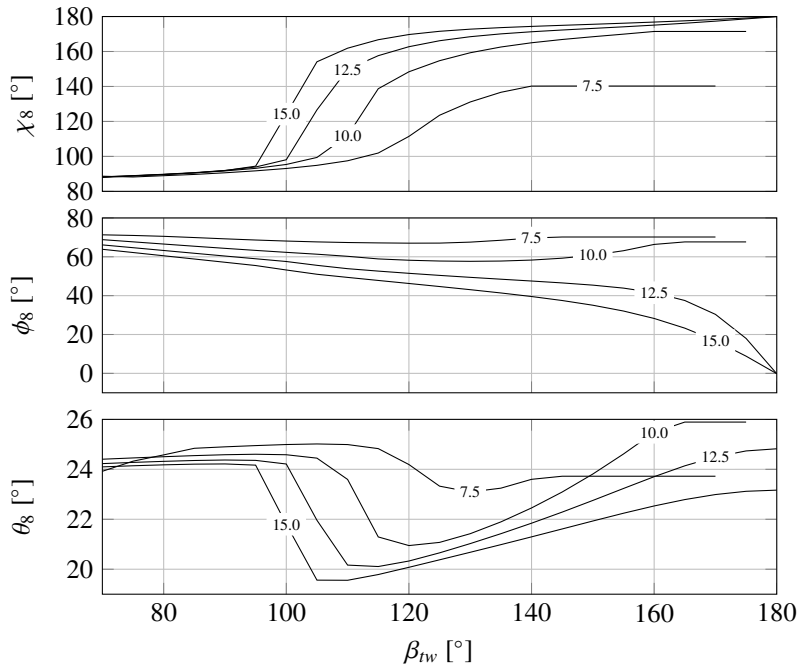

Figure 8.1.: For different true wind speed $U_{tw} \in \{7.5,\ 10.0,\ 12.5,\ 15.0\}$ m.s^{-1}, optimum kite flight trajectory parameters versus true wind angle β_{tw}: trajectory angle χ_8, azimuth of the center of the trajectory ϕ_8, elevation of the center of the trajectory θ_8.

transition is. The azimuth of the trajectory center decreases with the true wind angle. The evolution of the elevation trajectory center is less pronounced and remains within the range $\theta_8 \in [19°,\ 26°]$.

8.4. Influence of the windage force

Figures 8.2 and 8.3 show results of mean equilibrium, with and without considering the windage on the ship. Figure 8.2 shows the evolution of the mean equilibrium with respect to the true wind angle with the configuration $L_t = 500$ m, $A_k = 500$ m^2, $A^{(\mathbf{s})} = [110,\ 0,\ -10.6]^T$ m and $U_{tw} = 12.5$ m.s^{-1}. Figure 8.3 shows the evolution of the mean equilibrium with the longitudinal tether attachment position with the configuration $L_t = 500$ m, $A_k = 500$ m^2, $U_{tw} = 12.5$ m.s^{-1} and $\beta_{tw} = 90°$. The mean equilibrium are depicted in terms of power saving ratio η_k, drift angle β_s, rudder angle δ_r and heel angle ϕ_s.

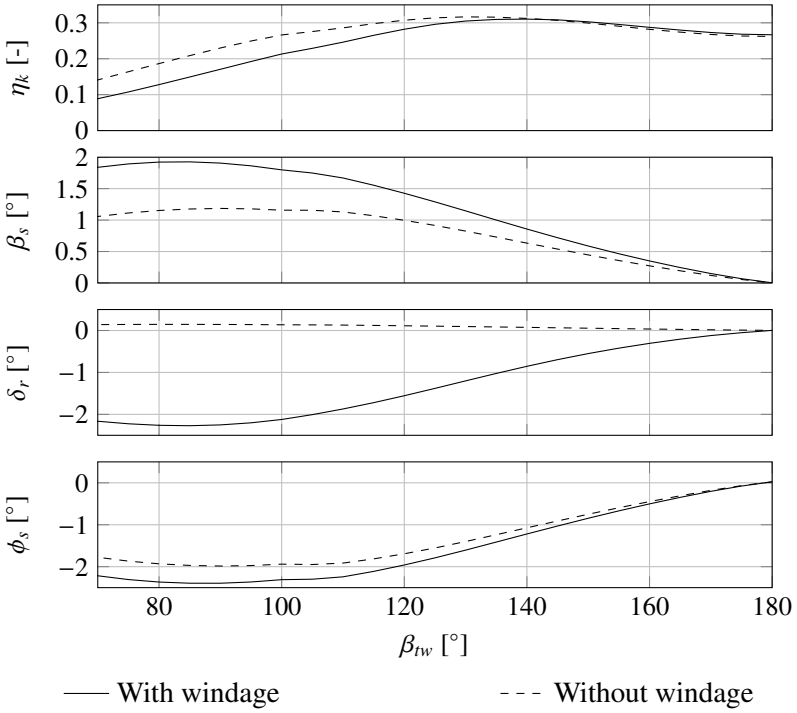

Figure 8.2.: Mean evolution of the kite power saving ratio η_k, drift angle β_s, rudder angle δ_r and heel angle ϕ_s with the true wind angle β_{tw}. The solid line is the mean equilibrium with the windage taken into account. The dashed line is the mean equilibrium without the windage effect. Configuration: $L_t = 500$ m, $A_k = 500$ m^2, $A^{(\mathbf{s})} = [110,\ 0,\ -10.6]^T$ m and $U_{tw} = 12.5$ m.s^{-1}

In Figure 8.2, the power saving ratio increases with the true wind angle to a maximum at broad reach and then decreases slightly until $\beta_{tw} = 180°$. The windage does not modify this evolution. The windage effect on the power saving ratio reduces significantly the kite power saving ratio until $\beta_{tw} = 140°$. For higher true wind angle, the windage has almost no effect on the power saving ratio. The windage causes an increase of the propeller demand

whereas the power supplied by the kite remains constant, which explains the loss of power saving ratio.

In Figure 8.2, the drift angle is defined as $\beta_s = -\arctan(v_s/u_s)$. Since, the drift motion is symmetrical with respect to the true wind angle, the results are discussed in terms drift angle modulus. The drift angle modulus increases slightly up to $\beta_{tw} = 90°$. Then, the drift angle modulus decreases continuously to zero until $\beta_{tw} = 180°$, which is trivial since the mean kite transverse force is zero at downwind. This evolution is directly driven by the evolution of the transverse windage and kite force. The windage effect is significant on the drift angle. Indeed, for $\beta_{tw} = 90°$, the drift angle is doubled by the effect of the wind load on the ship.

In Figures 8.2 and 8.3, it can be noticed that the windage effect is even more significant on the yaw equilibrium. With windage, the rudder angle becomes always negative for a starboard course. This results shows that the longitudinal tether attachment position leads to a weather helm ship. Indeed, according to the wind load model (Blendermann, 1994), the center of the wind load pressure is around 20 m, which is almost at mid-ship. Results shows that the windage effect dominates the yaw equilibrium of the ship.

The maximum heel angle with and without windage are respectively -2.9° and -2.25°. The windage increases the heel angle. The heel angle modulus reach a maximum value at $\beta_{tw} = 90°$. For the considered sailing conditions, the heel angle seems reasonable. The influence of the windage is less significant than the kite on the heel angle.

In figure 8.3, the effect of the longitudinal tether attachment position, $a_x^{(\mathbf{s})}$, on the mean equilibrium is studied. $a_x^{(\mathbf{s})} = 0$ m, corresponds to a tether attachment point at mid-ship and $a_x^{(\mathbf{s})} = 115$ m corresponds to a tether attachment point at the bow. The longitudinal position of A does not modify significantly the power saving ratio, as it stays at less than 2% of variation. However, the power saving ratio increases with $a_x^{(\mathbf{s})}$ and observed a maximum near the bow. The windage does not modify the evolution of the power saving ratio with the longitudinal position of A. The drift angle modulus increases with the longitudinal position of A. The rudder angle modulus decreases with the longitudinal position of A. The heel angle modulus increases slightly with the longitudinal position of A.

The evolution of the rudder angle confirms the fact that the KCS is a weather helm ship. As a consequence, with a backwards longitudinal position of A, the yaw generates a more important rudder angle modulus leading to a higher transverse force in opposition to the transverse kite towing force. Consequently, the ship drift angle decreases with backwards tether attachment position. The increase of rudder angle modulus with backward tether attachment position increases the rudder heeling moment. On the contrary, the decrease of drift angle modulus with backwards tether attachment position decreases the heeling moment. As shown by the results in terms of heel angle, the decrease of drift angle is slightly predominant over the increase of drift angle. Nevertheless, this effect may be different with a different ship.

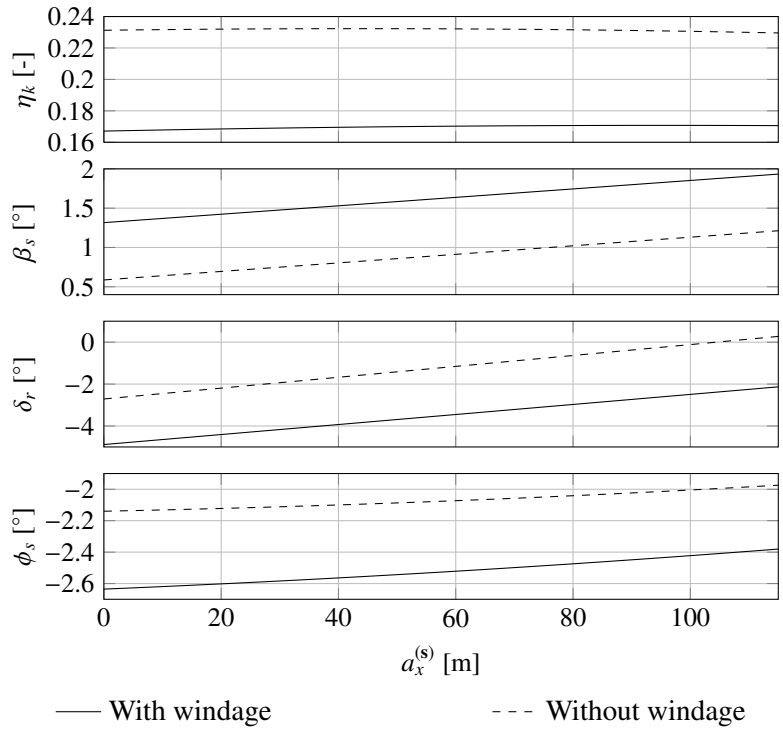

Figure 8.3.: For $U_{tw} = 12.5$ m.s^{-1}, $\beta_{tw} = 90°$, $L_t = 500$ m and $A_k = 500$ m: mean evolution of the kite power saving ratio η_k, drift angle β_s, rudder angle δ_r and heel angle ϕ_s with the longitudinal position of the tether attachment point $a_x^{(s)}$. The solid line is the mean equilibrium with the windage taken into account. The dashed line is the mean equilibrium without the windage effect.

As a partial conclusion, the windage effect is not negligible with respect to the kite towing force and particularly for the yaw equilibrium.

8.5. Influence of the true wind speed

The effect of the true wind speed is investigated in this section. Figure 8.4 shows the evolution of the mean equilibrium with true wind direction β_{tw} for different true wind speed $U_{tw} \in \{7.5,\ 10,\ 12.5,\ 15\}$ m.s^{-1}. For this results the windage effect is taken into account.

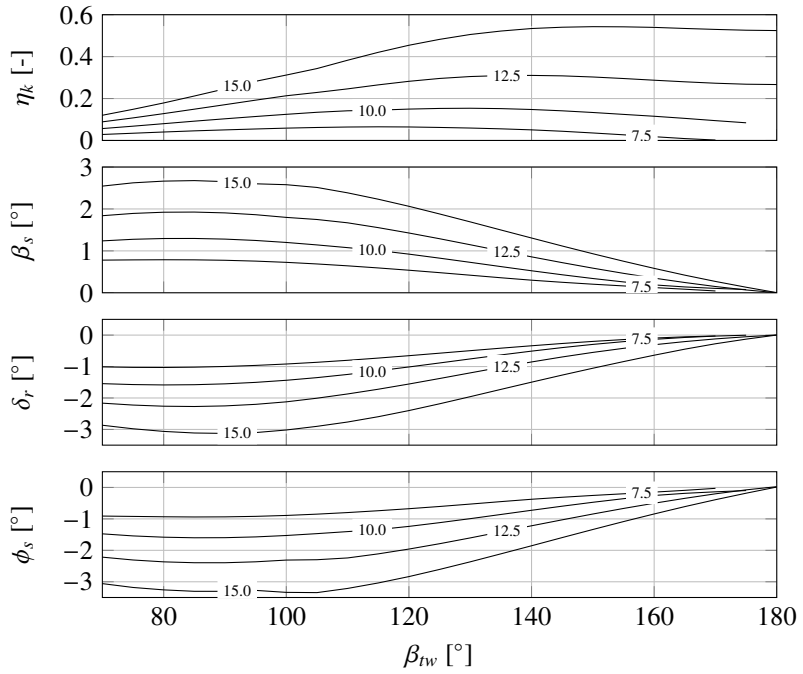

Figure 8.4.: For different true wind speed $U_{tw} \in \{7.5,\ 10,\ 12.5,\ 15\}$m.s^{-1}: mean evolution of the kite power saving ratio η_k, drift angle β_s, rudder angle δ_r and heel angle ϕ_s with the true wind angle.

In Figure 8.4, the global evolution of the kite power efficiency, drift angle, rudder angle and heel angle is similar for each true wind speed. As expected, the kite power efficiency, and the modulus of the drift, rudder and heel angles increase with the true wind speed. The optimum true wind angle in terms of kite power efficiency increases with the true wind speed. The optimal true wind angle with $U_{tw} = 7.5$ m.s^{-1} is around $\beta_{tw} = 115°$, whereas the optimal true wind angle with $U_{tw} = 15$ m.s^{-1} is around $\beta_{tw} = 145°$. Similarly, the true wind angle to obtain the maximum angle modulus of the drift, rudder and heel increases with the true wind speed. The evolution of the most critical true wind angle is not very significant and stay within a range of 20° around $\beta_{tw} = 90°$. With $U_{tw} = 15$ m.s^{-1}, the drift, rudder and heel angles are respectively $\beta_s = -3°$, $\delta_r = -4°$ and $\phi_s = -4°$.

8.6. Remarks on the kite efficiency and the mean aerodynamic pressure

In this section, the same navigation conditions as in Sec. 8.5 are used: the tether length is $L_t = 500$ m, the kite area $A_k = 500$ m^2. Figure 8.5 shows the mean aerodynamic pressure σ_k and the kite efficiency η_k as function of the true wind angle for different true wind speed.

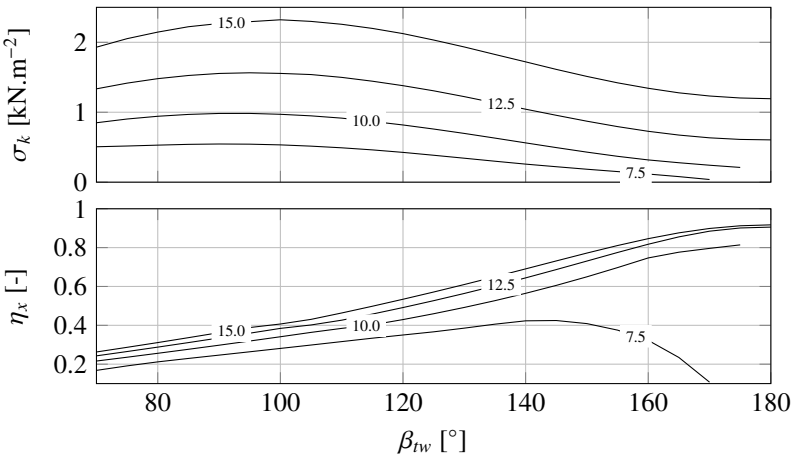

Figure 8.5.: For different true wind speed $U_{tw} \in \{7.5,\ 10,\ 12.5,\ 15\}$m.s^{-1}: evolution with the true wind angle of the mean aerodynamic pressure σ_k and of the kite efficiency η_x.

The mean aerodynamic pressure σ_k is given by the tether tension divided by the kite area. It can be shown that σ_k has a maximum between 100° and 90° of true wind angle. The minimum of σ_k is obtained at downwind. Consequently the safety factor of kite design is maximum at downwind. Even if, the dead downwind is not the optimal wind condition in terms of power saving ratio, the lifetime of the kite is increased, as discussed in Sec. 1.3. The trade off between the kite power saving ratio and the kite lifetime should be indicated by the kite efficiency η_k.

For all true wind speeds superior to the ship speed, the maximum of kite efficiency is obtained at dead downwind. In these cases, the kite efficiency is an increasing function of the true wind angle. For the true wind speed $U_{tw} = 7.5$ m.s^{-1}, the kite efficiency is maximum at $\beta_{tw} = 145°$. According to the definition of the kite efficiency η_k, the dead downwind is the best trade off between the kite power saving and the kite lifetime to make profits in the case of a true wind speed superior to the ship speed. When the true wind speed is less than the ship speed, the best trade off is shifted to lower true wind angle.

8.7. Conclusion

In section 8.4, the influence of the windage force has been investigated. It has been shown that the windage is not negligible at for kite sailing conditions. The windage effect is particularly important for a beam reach course. The ship drift angle is almost doubled. The windage effect on the yaw equilibrium dominates the kite effect.

The effect of the longitudinal tether attachment point is more pronounced on the ship drift and on the rudder angle than on the kite power saving ratio and the heel angle. Indeed a backwards tether attachment position decreases the ship drift angle. On the contrary, a forwards tether attachment position reduces the rudder angle. For a container ship, the general arrangement imposes a tether attachment point at the bow. The results complies with the analysis of Naaijen and Koster (2010). Even if the ship drift is maximum for an attachment position at the bow, the ship drift angle remains reasonable, less than 3° for the cases investigated in this study. As a first approximation, the ship drift angle and the rudder angle can be considered as linear with the transverse force. Consequently, it would mean that for a kite of 1000 m^2, the drift angle should be around 6°. From a more general point of view, the more critical sailing condition for the ship safety are obtained close to a beam reach sailing.

Through a brief economical analysis it has been shown that η_k, the ratio between the kite towing force along the ship axis and the kite force modulus, could be more relevant. The kite efficiency indicates the best trade off between power saving and kite lifetime. The results shows that this ratio is maximum at dead downwind in case of a true wind speed greater than the ship speed. In case of a true wind speed lower than the ship speed, the maximum is obtained at lower true wind angles. Eventually, despite a ship speed faster than the wind, the benefit from the wind gradient could enable a kite flight. However, these very special cases have not been considered. According to the kite efficiency criteria, it could be more relevant to design a kite only for downwind sailing courses. In this case, the use of kites is less critical for the ship safety and larger kites could be used. Consequently, the ship speed is decisive in defining the kite wind range for design and the aerodynamic wind loading for design σ_d.

This study considers the mean kite towing force to solve the static equilibrium of the ship. The amplitudes of the dynamic ship motions induced by a dynamic kite flight have not been considered. Since the kite induces ship motions, the kite flight can be modified, which can lead to a modification of the mean equilibrium. The kite power saving ratio and efficiency may be altered by dynamic motions. Consequently dynamic motions of a ship towed by kite and kite-ship interactions should be investigated. This work is the aim of the next chapters.

9. Interactions between a kite and a ship

Résumé: Etude des interactions navire-kite

Dans ce chapitre les interactions entre un cerf-volant et un navire sont étudiées. Pour mettre en évidence ces interactions, deux types de couplage entre le modèle de cerf-volant sans masse et le modèle de navire sont comparés : un couplage monolithique et un couplage dissocié. Le couplage dissocié intègre la force du kite comme une série temporelle prédéterminée en ne considérant que la vitesse moyenne du navire. Le couplage monolithique prend en compte le terme de couplage entre les deux modèles qui est la vitesse du point d'attache des lignes.

Le cas d'étude utilisé pour cette étude est un navire militaire de surface, le DTMB 5512 à pleine échelle. Ce navire a été choisi pour cette étude plutôt que le KCS car sa fréquence de résonnance en roulis (0.56 rad.s^{-1}) est plus proche des fréquences d'excitation du cerf-volant. Seuls les mouvements de roulis, pilonnement et tangage sont étudiés sur une route au travers. Un cas de navigation en mer calme et trois cas de navigation en houle régulière de travers sont étudiés avec les fréquences de vague 0.4, 0.56 et 0.8 rad.s^{-1}. En conservant les mêmes amplitudes angulaires de trajectoire, plus les lignes sont courtes plus les fréquences des harmoniques sont élevées. Ainsi en faisant varier la longueur de ligne, le domaine fréquentiel est balayé.

Sans interactions (couplage dissocié), le spectre d'excitation du kite en roulis est composé de plusieurs harmoniques. Les harmoniques paires ont le plus d'amplitudes. Le second harmonique est le plus important. En cas en mer calme, les interactions entre le kite et le navire sont faibles. On peut toutefois remarquer que le couplage diminue l'amplitude d'excitation du kite et l'amplitude de roulis du navire. Le couplage dissocié est alors conservatif par rapport au couplage monolithique en cas de mer calme.

En cas de houle régulière le mouvement de roulis est principalement causé par la vague. Dans ce cas il est préférable pour définir la trajectoire de vol du cerf-volant de négliger la vitesse verticale du point d'attache. Comme le mouvement de roulis du navire est quasi-harmonique à la fréquence de vague, un réseau de sous-harmoniques basse fréquence apparait. La fréquence fondamentale des sous-harmoniques est donnée par la différence entre la fréquence de vague et la fréquence de l'harmonique d'excitation la plus proche. Quand cette différence est suffisamment petite, un phénomène d'accrochage apparait. Les harmoniques

d'excitation du cerf-volant sont alors décalés à la fréquence de vague et le réseau de sous-harmoniques n'apparait pas. Ce phénomène d'accrochage de fréquence est bénéfique pour le cerf-volant et le navire quand le décalage des harmoniques d'excitation correspond à une augmentation. Le cerf-volant parcourt alors la trajectoire plus rapidement, et ainsi la force de traction est plus importante. Par ailleurs, le mouvement de roulis est atténué. L'amplitude de roulis peut dans certain cas devenir légèrement plus faible que sans cerf-volant. Avec un état de mer, le couplage monolithique apparait alors alors comme incontournable.

9.1. Introduction

Considering the mean kite towing force, Leloup et al. (2016) and Naaijen et al. (2006) solved the horizontal equations of balance of a ship towed by a kite to determine the fuel savings. Ran et al. (2013) studied the contribution of a kite to the mean ship thrust, drift angle and rudder angle. In the previous chapter, the 6 dof mean equilibrium has been solved. All these previous studies neglected the interactions between the kite and the ship. The kite force was imposed as a predefined external force to the ship. Nevertheless, motions of such a system are highly dynamic since a kite experiences a periodic dynamic flight. In Bigi et al. (2016), the influence of the kite attachment point on the deck was investigated on a fishing vessel equipped with a kite. This study was limited to horizontal ship motions, surge, sway and yaw, by means of a maneuvering model in calm water with a monolithic coupling approach between the ship and the kite. Nevertheless, even if the water was supposed to be calm, Bigi et al. (2016) did not take into account the effect of radiated waves on ship motions. Thus, the influence of the kite excitation frequency on the added mass and damping of the ship was neglected. Since hydrodynamic added mass and damping depend strongly on the frequency of the motion (Newman, 1977; Molin, 2002; Faltinsen, 2005; Bertram, 2012), this assumption is questionable.

The aim of this chapter is to investigate the interaction between a ship and a kite. Consequently a segregated coupling approach is compared to a monolithic coupling approach between the ship model (cf. Chap. 6) and the kite model (cf. Chap. 3). The term monolithic approach refers to the semantic developed in (Markert, 2010; Lewis et al., 1984) where the two interacting models are solved simultaneously in time with the same numerical scheme of integration. The monolithic approach solves the coupled system. By contrast, the segregated approach solves the motions of the whole system assuming that ship motions have no influence on the kite flight, consequently the kite flight is calculated considering only the mean tether attachment point velocity.

Section 9.2 presents the two coupling methods, the segregated approach and the monolithic approach. Section 9.3 presents the case of study. Sections 9.4 and 9.5 investigate respectively through a calm water case and a regular beam wave case, the coupling between ship and kite. The influence of the kite excitation frequencies is investigated with different tether

lengths and constant angular amplitudes of trajectory. In these sections Results are presented analyzed and discussed. A general discussion about methods and results is finally provided in Section 9.7.

9.2. Coupling methods

The tether tension induces motions to the ship. The expression of generalized kite force acting on the ship is expressed as follows:

$$\underline{F}_k = \left[\begin{array}{cc} \underline{T}_k^{(\mathbf{s})} & \underline{O_S A}^{(\mathbf{s})} \times \underline{T}_k^{(\mathbf{s})} \end{array} \right]^T \tag{9.1}$$

In addition, according to the zero-mass kite model (cf. Chap. 3 and Eq. (3.5)), the ship motions can modify the kite flight and the tether tension through the relative wind speed at the kite altitude with respect to the tether attachment point A:

$$\underline{U}_{rw}\left(k_z^{(\mathbf{n})}\right) = \underline{U}_{tw}\left(k_z^{(\mathbf{n})}\right) - \underline{U}_a \tag{9.2}$$

Two coupling approaches are investigated: a monolithic and a segregated approaches. The monolithic approach takes into account all the coupling terms between kite and ship models. As for the considered segregated approach, it assumes a predefined kite force and then solves ship equations of motion separately.

9.2.1. A monolithic approach

The whole system of equations ruling the motion of a ship towed by kite are obtained with Eqns. (6.27) and 3.1 as follows:

$$\begin{cases} \dot{\underline{S}} & = \begin{bmatrix} \underline{\underline{T}}_{\mathbf{s}}^{\mathbf{c}} & \underline{\underline{0}} \\ \underline{\underline{0}} & \underline{\underline{R}}_{\mathbf{s}}^{\mathbf{c}} \end{bmatrix} \underline{V}_s \\ \dot{\underline{V}}_s & = \left[\underline{\underline{M}}_S + \underline{\underline{\tilde{A}}}\right]^{-1} \left[\underline{F} - \left[\underline{\underline{\tilde{B}}} + \underline{\underline{B}}_\phi + \underline{\underline{D}}\right] \underline{V}_s - \underline{\mu} - \underline{\underline{C}}\,\underline{S}\right] \\ \dot{\underline{y}}_{ij} & = \underline{\underline{A}}_{ij}^{'} \underline{y}_{ij} + \underline{\underline{B}}_{ij}^{'} \delta V_{s,j},\ \forall i,j \in [\![1;6]\!] \\ \dot{\underline{K}}^{(\mathbf{c})} & = \underline{U}_A^{(\mathbf{c})} + U_{rw} \left[\underline{x}_{vk} \cdot \underline{x}_{rw} + \sqrt{\left(\underline{x}_{vk} \cdot \underline{x}_{rw}\right)^2 + \left(\frac{\underline{z}_k \cdot \underline{x}_{rw}}{\sin \epsilon_k}\right)^2 - 1} \right] \underline{x}_{vk}^{(\mathbf{c})} \end{cases} \tag{9.3}$$

Equation (9.3) includes 3 scalar equations for the kite. With the monolithic approach, the fully coupled system between ship and kite motions is solved. This monolithic system of differential equations is numerically integrated with the 4$^{\text{th}}$ order Runge-Kutta scheme with fixed time step.

9.2.2. A segregated approach

By contrast to the monolithic approach, the segregated approach considers only the mean tether attachment point velocity on the ship. Ship motions are computed by applying the time series of the kite towing force as an external force. Thus, ship equations of motion can be expressed as follows:

$$\begin{cases} \dot{\underline{S}} = \begin{bmatrix} \underline{\underline{T}}^{\mathbf{c}}_{\mathbf{s}} & \underline{\underline{0}} \\ \underline{\underline{0}} & \underline{\underline{R}}^{\mathbf{c}}_{\mathbf{s}} \end{bmatrix} \underline{V}_s \\ \underline{\dot{V}}_s = \left(\underline{\underline{M}}_S + \underline{\underline{\tilde{A}}}\right)^{-1} \left[\underline{F}_k(t) + \underline{F}^{'} - \left(\underline{\underline{\tilde{B}}} + \underline{\underline{B}}_{\phi} + \underline{\underline{D}}\right) \underline{V}_s - \underline{\mu} - \underline{\underline{C}}\, \underline{S}\right] \\ \dot{\underline{y}}_{ij} = \underline{\underline{A}}^{'}_{ij} \underline{y}_{ij} + \underline{B}^{'}_{ij} \delta V_{s,j}, \ \forall i,j \in [\![1;6]\!] \end{cases} \tag{9.4}$$

where $\underline{F}^{'}$ denotes external forces such as rudder, propeller and windage forces only and does not include the kite force applied as a time series $\underline{F}_k(t)$.

This segregated approach could be very practical to study the motions of ship towed by kite. Even if here, this approach is performed into the time domain, the segregated approach can be performed into the frequency domain by applying the kite excitation spectrum directly in Eq. (6.1). The validity of such an approach for the ship and kite system in comparison with the monolithic approach must however be assessed.

9.3. Case of study

In order to simplify the analysis, only vertical ship motions (heave, roll and pitch) of the DTMB 5512 at full scale are considered here. The analysis is focused on the roll motion. Thus, in the scope to observe significant roll motion, a true wind angle $\beta_{tw} = 90°$ is chosen. A true wind speed of reference U_{ref} =10 m.s^{-1} at the altitude $z^{(\mathbf{n})}_{ref}$ =10 m corresponding to the high range of a fresh breeze from the Beaufort scale is considered. The wind gradient parameter used here is $n_v = 1/7$. The ship speed is set to U_h =7.5 m.s^{-1} since it corresponds to a common sailing speed condition of the world merchant ship fleet (Smith et al., 2014). A kite with an area of A_k =500 m^2 and with the aerodynamic specs determined in Eq. (8.9) is used. The tether attachmentpoint A is 7.9 m above the water line.

The kite flight trajectory corresponds to a Lissajous trajectory as defined in Sec. 3.4.2. The amplitudes of the trajectory are arbitrarily set to $\Delta\phi_8 = 20°$ and $\Delta\theta_8 = 8°$. The critical radius of curvature of this trajectory is given by $L_t \Delta\theta_8$. Keeping a constant angular trajectory size and varying the tether length, the influence of the kite excitation frequency can be studied. Tether lengths between 360 m and 1000 m are investigated.

The center of the trajectory $[\phi_8,\ \theta_8]$ and the angle of the trajectory χ_8 around the axis $\underline{C_8 A}$ are determined by the optimization of the longitudinal kite towing force with a code similar

to the one used by Leloup et al. (2016). Figure 9.1 (a), (b) and (c) show respectively the evolution of ϕ_8, θ_8 and χ_8 with the tether length for the sailing condition mentioned before in this section.

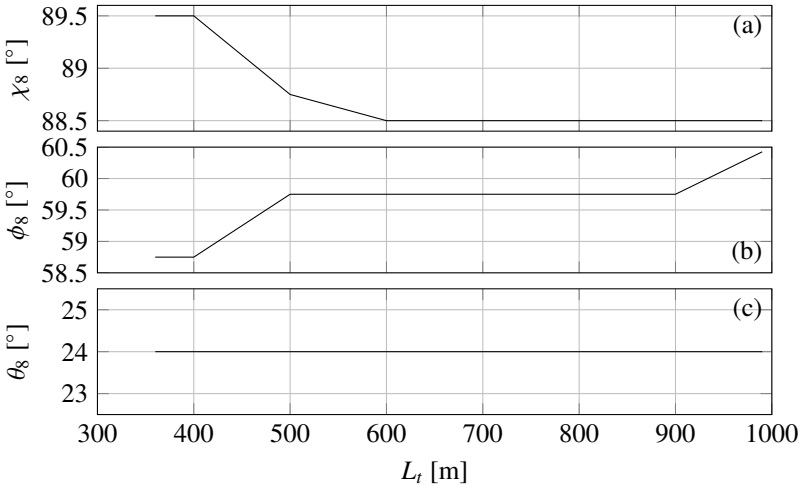

Figure 9.1.: Kite flight trajectory parameter versus tether length. (a): Trajectory angle χ_8; (b) Azimuth of the center of the trajectory; (c): Elevation of the center of the trajectory.

A calm water case and three regular beam wave cases of 2.5 m high consistent with a fresh breeze are considered. Three wave frequencies investigated are$\{0.4,\ 0.56,\ 0.8\}$ rad.s^{-1}. The 0.56 rad.s^{-1} wave frequency corresponds to the natural roll ship frequency.

For all following results, the simulation time is 1640 s with a time step of 0.3 s. Results are mainly studied into the frequency domain. Consequently, in order to correctly represent power spectrum results, the Fast Fourier Transform (FFT) is performed with a signal zero-padded 5 times longer than the initial data. In order to avoid the representation of the sine cardinal due to this numerical method, the signal is filtered with an Hamming window (Hamming, 1989).

9.4. Calm water case

9.4.1. Kite excitation spectrum

Figure 9.2 (a) and (b) respectively show the time series and the spectrum of the kite roll excitation moment obtained with the segregated approach for a tether length $L_t = 500$ m. Only the varying part of the kite excitation is taken into account to compute the kite excitation spectrum..

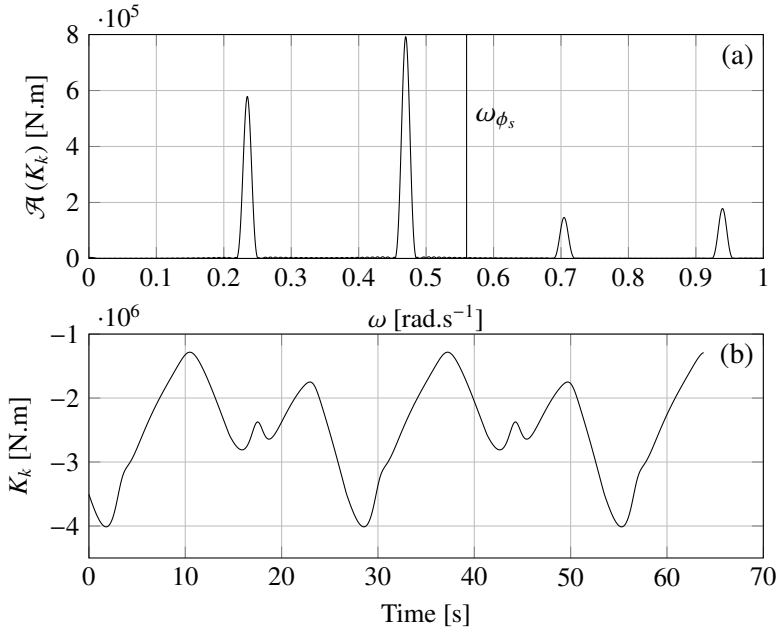

Figure 9.2.: With a tether length $L_t = 500$ m; (a): spectrum of the kite excitation moment around the longitudinal ship axis $\underline{x}_s$; (b): Time history of the kite excitation moment around the longitudinal ship axis $\underline{x}_s$ over the last loop.

With the segregated approach, the kite flight is not modified by the ship motions. It can be noticed in Fig. 9.2 (a) that the roll excitation moment is mainly composed of several harmonics. For convenience, harmonics are denoted ω_{ki} where i is a positive integer. Only the first, the second and the fourth harmonics are significant. The whole spectrum is not represented but harmonics at higher frequencies are not significant. The second and the fourth harmonics are the most powerful ones. The second harmonics appears to be the most critical for the ship motions due to its proximity with the natural roll ship frequency.

9.4.2. Comparison of the segregated approach with the monolithic approach

Figure 9.3 shows the evolution of the roll amplitude (a), of the first kite excitation harmonic frequency (b), and of the amplitude kite moment of excitation (c) with respect to the tether length. Three methods are compared: the segregated approach in dashed-dotted line and the two monolithic approaches with the kite trajectories defined in $\mathbf{r}\tilde{\mathbf{w}}_{ra}$ and in $\mathbf{r}\mathbf{w}_{ra}$ respectively in solid and dashed lines.

As expected, the first kite excitation harmonic ω_{k1} decreases with the tether length since the angular amplitude of the Lissajous trajectories is kept constant. No major difference can be noticed between the three approaches in terms of harmonics frequencies.

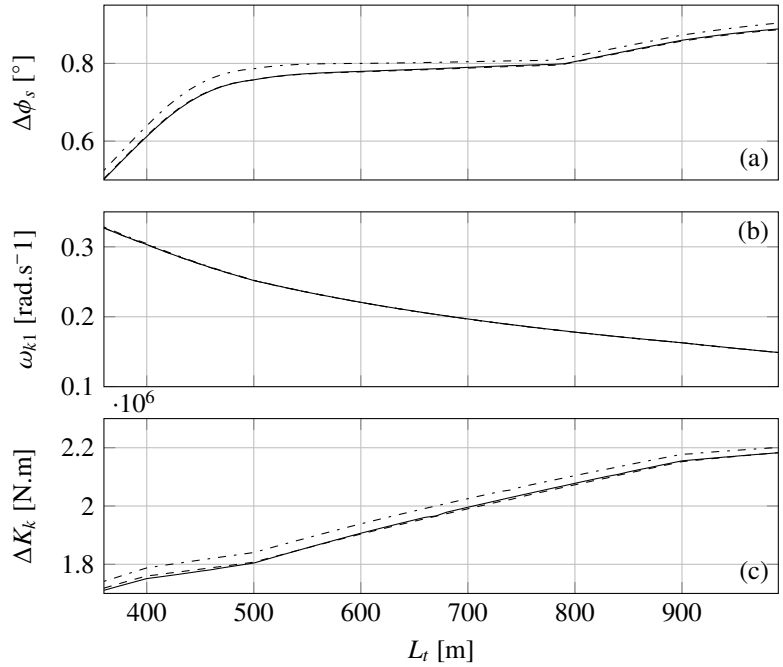

—— Monolithic approach with the simplified trajectory $\mathbf{r\tilde{w}}_{ra}$

- - - Monolithic approach with the trajectory in $\mathbf{rw}_{ra}$

- · - segregated approach

Figure 9.3.: (a) Amplitude of the ship roll motion, (b) first kite harmonic frequency and (c) amplitude of the kite moment of excitation for different tether lengths from 360 m to 990 m by step length of 10 m in calm water.

The roll amplitude $\Delta\phi_s$ and the amplitude of the kite roll moment ΔK_k predicted by the segregated are higher than those predicted by the two monolithic approaches. The two trajectory definitions in $\mathbf{r\tilde{w}}_{ra}$ and $\mathbf{rw}_{ra}$ give almost the same results both in terms of roll amplitude and kite roll moment amplitude.

For all the approaches presented, the evolution of the roll amplitude is similar. The kite moment amplitude increases quasi linearly with the tether length. Three ruptures can be observed on the evolution the kite moment amplitude. These ruptures correspond to the evolution of the trajectory with the tether length as shown in Fig. 9.1.

Due to the wind gradient, the longer the tether is, the larger the kite roll moment is. This raise in terms of the kite roll moment explains the continuous raise in terms of roll amplitude. However, two important slope variations can be noticed between $L_t = 360$ m and $L_t = 500$ m and around $L_t = 790$ m which do not correspond to any particular event in the kite roll moment curve. In fact, these two increases are due to the proximity of the two most powerful kite roll excitation harmonics from the natural roll ship frequency. Indeed, for $L_t = 440$ m the second harmonic frequency is almost equal to the natural roll frequency

of the ship. And for $L_t = 790$ m, the fourth harmonic frequency approaches the natural roll ship frequency.

In case of a slower true wind speed, the increase of the kite roll moment with the tether length would be less significant. In such a case, it could be observed a maximum of roll amplitude for tether length corresponding to a match between a kite harmonic frequency and the natural roll frequency of the ship.

According to these results, in calm water, the segregated apporach and the monolithic approaches lead to versy similar results. However, the segregated approach is slightly conservative in comparison to the monolithic approache.

9.5. Regular beam wave case

To investigate a case closer to a real ocean environment, the influence of regular beam waves is studied. The wave considered is 2.5 m high at frequencies of ω_w of 0.4 rad.s^{-1}, 0.56 rad.s^{-1} and 0.8 rad.s^{-1}. As for the calm water case, the frequency domain of kite excitation is scanned with different tether lengths ranging from $L_t = 360$ m to $L_t = 990$ m with a tether length step of 10 m.

9.5.1. Comparison between the trajectory definitions in $\mathbf{r\tilde{w}}_{ra}$ and $\mathbf{rw}_{ra}$

As outlined at the end of section 3.4.2, the definition of the kite trajectory with respect to the relative wind basis $\mathbf{rw}_{ra}$ may represent an issue. The trajectory definition in $\mathbf{r\tilde{w}}_{ra}$ takes only horizontal components of the tether attachment point velocity into account. The previous case of study in calm water did not highlight any major difference between the trajectory defined in $\mathbf{r\tilde{w}}_{ra}$ and the trajectory defined in $\mathbf{rw}_{ra}$. Indeed, in calm water the vertical amplitude of the ship motions is not significant. Nevertheless, in case of regular beam wave of 2.5 m high, the effects of the vertical ship motion on the trajectory definition is more important.

Figure 9.4 shows the trajectory defined in $\mathbf{r\tilde{w}}_{ra}$ in solid line and the trajectory defined in $\mathbf{rw}_{ra}$ in dashed line with respect to the $\mathbf{n}$ frame. A very clear difference of trajectory shape can be noticed between the two definitions. The local minimums of the radius of curvature along the trajectory defined in $\mathbf{rw}_{ra}$ are much smaller than those along the trajectory defined in $\mathbf{r\tilde{w}}_{ra}$.

Performing such a sharp trajectory represents no difficulty since the kite yaw motion is imposed. However, a real kite may be not able to perform such a trajectory with short radius of curvature. Therefore, a particular attention must be paid to the trajectory definition for the design of a kite auto-pilot dedicated to the towing of ship, as it has to be realistic. In the rest of the study, all the trajectories will be defined in $\mathbf{r\tilde{w}}_{ra}$.

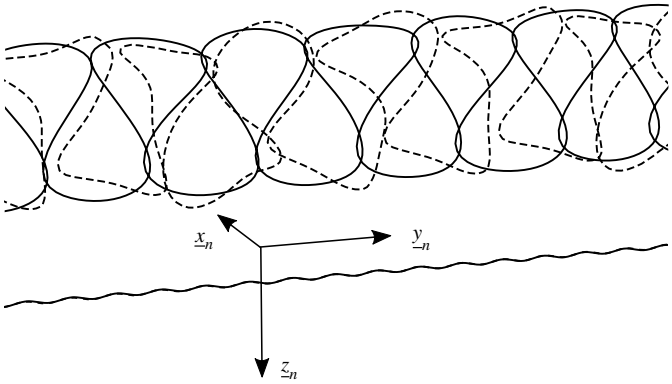

—— Monolithic approach with the simplified trajectory $\mathbf{r\tilde{w}}_{ra}$

- - - Monolithic approach with the trajectory in $\mathbf{rw}_{ra}$

Figure 9.4.: Kite and ship path with respect to $\mathbf{n}$ for $L_t = 390$ m with a wave of 2.5 m high at the frequency $\omega_w = 0.8$ rad.s^{-1}.

9.5.2. Interactions with regular beam waves

Figures 9.5, 9.6 and 9.7 show respectively for wave frequencies ω_w of 0.4, 0.56 and 0.8 rad.s^{-1}, the roll amplitude of the ship (a), the first kite harmonic frequency (b) and the roll moment amplitude of the kite (c). For each wave cases, the monolithic approach with the trajectory defined in $\mathbf{r\tilde{w}}_{ra}$ in solid line is compared to the segregated approach in dashed line. The dashed-dotted line corresponds to the roll amplitude of the ship due to the wave excitation without kite.

For all wave cases, the roll amplitude and the amplitude of the kite roll moment increases globally with the tether length as for the calm water case. In contrary to the calm water case, the amplitude of the kite roll moment obtained with the monolithic approach is globally larger than the amplitude of the kite roll moment obtained with the segregated approach. However, it should be noticed that the evolution of the roll amplitude and the evolution of the amplitude of the kite roll moment are sharp compared to the calm water case. For instance, in Fig. 9.6 (a), for the tether length $L_t = 440$ m, a significant drop of the roll amplitude of the ship can be noticed in the segregated case.

Concerning the evolution of the first harmonic frequency, no major difference can be noticed between the two approaches except locally at some tether length range. Indeed, for some ranges of tether length, harmonic frequencies obtained with the monolithic approach remain constant. For instance, on Fig. 9.5 (b), the first harmonic frequency remains constant at a value of $0.4/2 = 0.2$ for tether lengths within the range $[645; 710]$ m and on Fig. 9.6 (b), the first harmonic frequency remains constant at a value of 0.56/2 for tether lengths within the range $[390; 470]$ m.

Focusing on the segregated approach, brutal drops in terms of roll amplitude of the ship

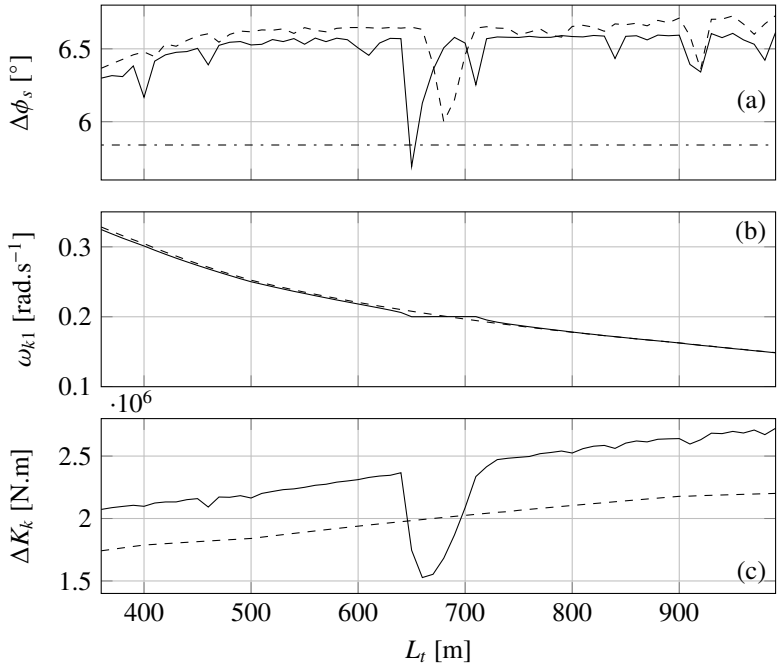

—— Monolithic approach with the simplified trajectory $\mathbf{r\tilde{w}}_{ra}$

- - - segregated approach

- · - Without kite

Figure 9.5.: (a) Amplitude of the ship roll motion, (b) first kite harmonic frequency and (c) amplitude of the kite moment of excitation for different tether lengths from 360 m to 990 m by step length of 10 m with a beam regular wave of 2.5 m high at a frequency of $\omega_w = 0.4$ rad.s^{-1}.

are explained by the proximity of a kite harmonic frequency from the wave frequency. For the case with the wave frequency $\omega_w = 0.56$ rad.s^{-1}, at $L_t = 440$ m, the second kite harmonic frequency is $\omega_{k2} = 0.562$ rad.s^{-1}. Consequently, depending on initial conditions, a difference in phase between the kite frequency and the wave frequency remains constant and has a significant effect. Longer simulations should be considered in order to be able to neglect the effect of initial conditions on the roll amplitude obtained with the segregated approach.

The sharp evolution of the roll amplitude of the ship concerns also results obtained with the monolithic approach. In contrary to the segregated approach, this phenomenon does not occur only when an harmonic frequency of the kite corresponds to the wave frequency. For the case with a wave frequency of 0.4 rad.s^{-1} and a tether length $L_t = 840$ m, a drop of the ship roll amplitude can be noticed. Indeed, Fig. 9.8 shows that no principal kite harmonic frequency corresponds to the wave frequency. However, due to the coupling between kite and ship motions, secondary harmonic network appears. The secondary harmonic frequencies are denoted ω'_{ki} and are given by:

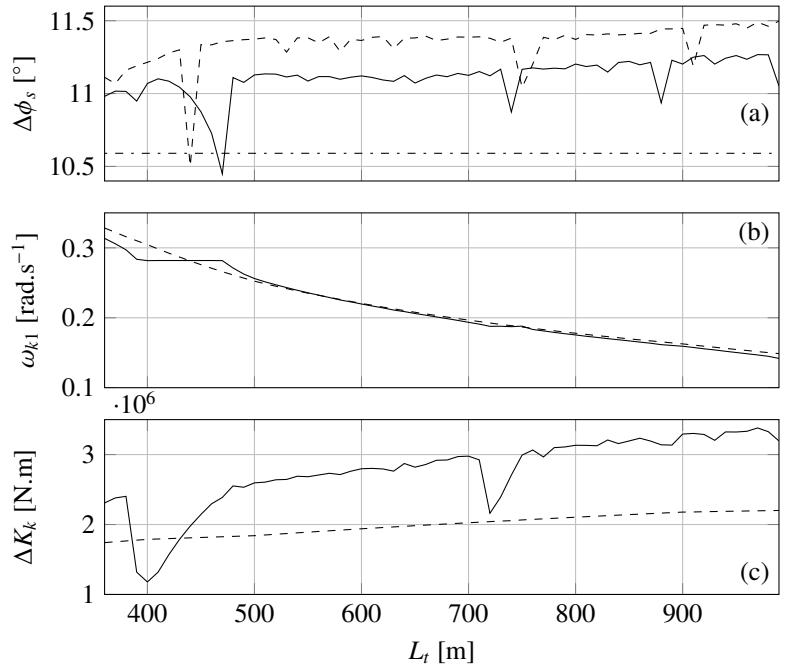

—— Monolithic approach with the simplified trajectory $\mathbf{r\tilde{w}}_{ra}$

- - - segregated approach

- · - Without kite

Figure 9.6.: (a) Amplitude of the ship roll motion, (b) first kite harmonic frequency and (c) amplitude of the kite moment of excitation for different tether lengths from 360 m to 990 m by step length of 10 m with a beam regular wave of 2.5 m high at a frequency of $\omega_w = 0.56$ rad.s^{-1}.

$$\omega_{ki}^{'} = i \min_{j \in N^{+*}} |\omega_w - \omega_{kj}| \tag{9.5}$$

This phenomenon occurs when the frequency difference between the closest principal harmonic frequency and the wave frequency is a submultiple of the first kite harmonic frequency. For the case presented in Fig. 9.8, $\omega_{k1} = 3\omega_{k1}^{'}$. With the monolithic approach, these drops are independent of the initial conditions. The most important drops of the roll amplitude occur when $\omega_{k1} = \omega_{k1}^{'}$ or $\omega_{k1} = 2\omega_{k1}^{'}$. The importance of the phenomenon occurring at $\omega_{k1} = n\omega_{k1}^{'}$ decreases with the increase of the integer value n. Moreover, the importance of the phenomenon decreases when the interaction with the wave concerns high harmonic orders. Indeed, the higher the order of the harmonic is, the less the harmonic intensity is.

This phenomenon of interaction between the kite and the ship can be explained by the fact that the monolithic approach predicts a smaller roll amplitude despite a larger kite roll moment amplitude compared to the segregated approach. Indeed, the secondary kite

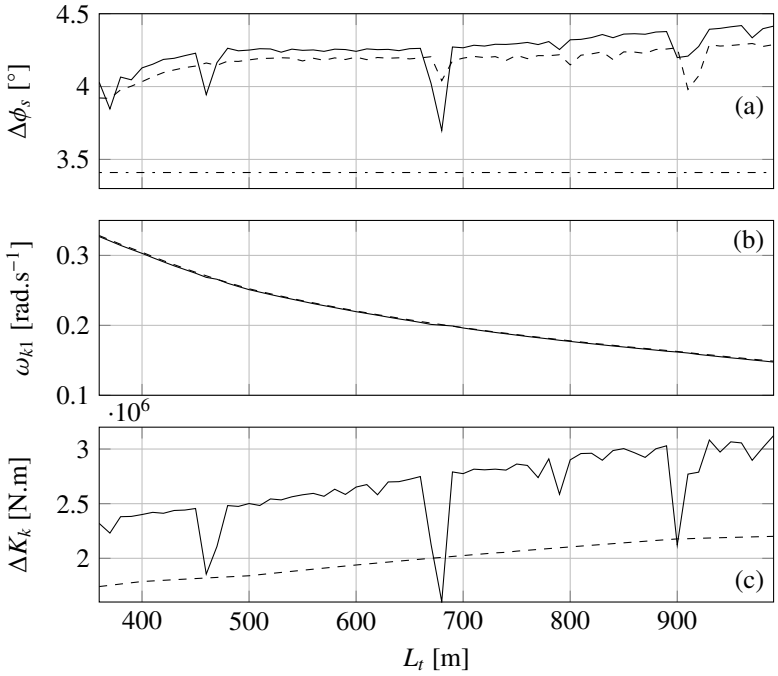

—— Monolithic approach with the simplified trajectory $\mathbf{r\tilde{w}}_{ra}$

- - - segregated approach

- · - Without kite

Figure 9.7.: (a) Amplitude of the ship roll motion, (b) first kite harmonic frequency and (c) amplitude of the kite moment of excitation for different tether lengths from 360 m to 990 m by step length of 10 m with a beam regular wave of 2.5 m high at a frequency of $\omega_w = 0.8$ rad.s^{-1}.

harmonic at the wave frequency has a relative phase with the ship motion. As an example, for the case plotted in Fig. 9.8, the difference in phase angle between the ship motion and the kite excitation at $\omega = 0.4$ rad.s^{-1} is 60.7°. For the case with the frequency wave $\omega_w = 0.8$ rad.s^{-1}, the interaction between the kite and the ship is less significant since the wave frequency is far from the most powerful kite harmonic frequency. According to these results, a ship and a kite are strongly in interaction when the ship experiences the effect of a wave. Moreover, in contrary to the calm water case, the segregated approach is not necessarily conservative with respect to the monolithic approach as shown by Fig. 9.7 (a).

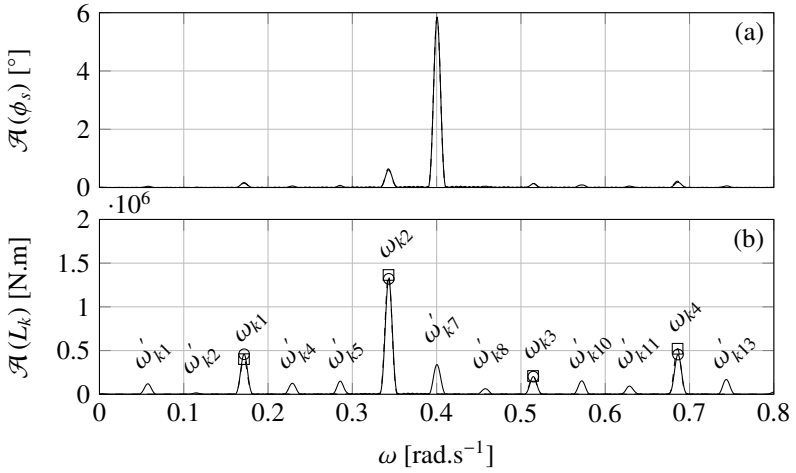

—— Monolithic approach with the simplified trajectory $\mathbf{r\tilde{w}}_{ra}$ (Principal harmonics ω_{ki}: ◦)

- - - segregated approach (Principal harmonics ω_{ki}: ▫)

Figure 9.8.: With a tether length $L_t = 840$ m at the wave frequency $\omega_w = 0.4$ rad.s^{-1}; (a) spectrum of the roll motion of the ship; (b) spectrum of the kite excitation moment around the longitudinal ship axis $\underline{x}_s$.

9.5.3. kite lock-in phenomenon

As shown in the previous section, an important interaction phenomenon between the kite and the ship occurs with the apparition of secondary harmonics ω'_{ki}. The interaction is particularly important when $\omega_{k1} = \omega'_{k1}$ or $\omega_{k1} = 2\omega'_{k1}$. The plateaus of the first kite harmonic with the tether length corresponds to these conditions. It can be shown in Figs. 9.5 (a) and 9.6 (a), respectively at $L_t = 650$ m and $L_t = 470$ m, that the drop of the roll amplitude predicted by the monolithic approach is important enough to lead to smaller roll amplitude than the case without kite.

A particular attention is paid to the case with wave frequency $\omega_w = 0.56$ rad.s^{-1} and $L_t = 470$ m because the interaction between the kite and the ship is a win-win one. Indeed, for this case the mean kite towing force predicted by the monolithic approach is 8.0% more important than the mean kite towing force predicted with the segregated approach. In addition, the ship roll amplitude is 1.4% less important than the case without kite.

Figure 9.9 shows the spectrum of the roll motion (a) and the spectrum of the kite excitation (b). It can be noticed that the second harmonic of the kite roll moment is attracted towards the wave frequency. Since the kite harmonic frequency is increased towards the wave frequency, the kite performed the whole trajectory faster. The time to perform the trajectory is decreased by 5.7%. This leads to a higher apparent wind speed and therefore to a higher mean kite towing force. Moreover, the difference in phase angle between the roll motion and the kite roll moment is 18.2° leading to a reduction of the roll amplitude.

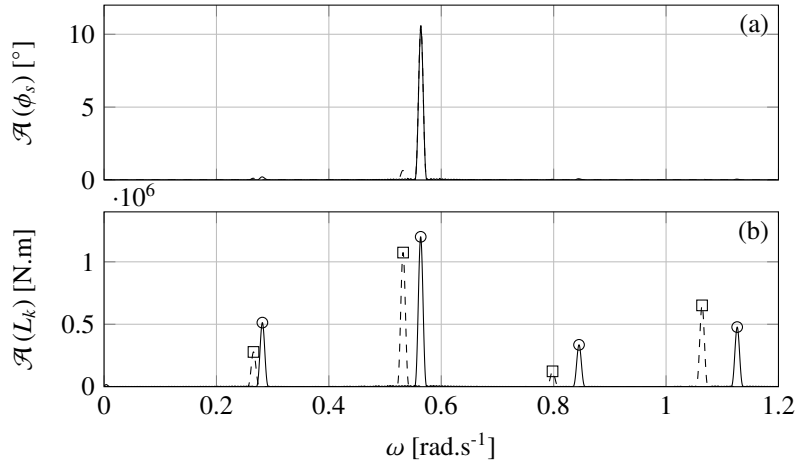

—— Monolithic approach with the simplified trajectory $\mathbf{r\tilde{w}}_{ra}$ (Principal harmonics ω_{ki}: ◦)

- - - segregated approach (Principal harmonics ω_{ki}: ▫)

Figure 9.9.: With a tether length $L_t = 470$ m at the wave frequency $\omega_w = 0.56$ rad.s^{-1}; (a) spectrum of the roll motion of the ship; (b) spectrum of the kite excitation moment around the longitudinal ship axis $\underline{x}_s$.

This attraction towards the wave frequency can be noticed also on the secondary harmonic corresponding to the case $\omega_{k1} = 2\omega_{k1}^{'}$. Indeed the kite harmonics can be shifted towards the wave frequency in order to fulfill the condition $\omega_{k1} = 2\omega_{k1}^{'}$. However, the effects are less significant than for the condition $\omega_{k1} = \omega_{k1}^{'}$.

This phenomenon is similar to the lock-in phenomenon happening with the vortex-induced vibrations (Bearman, 1984; Sarpkaya, 2004). Henceforth, this phenomenon is called the kite lock-in.

9.6. Discussion

9.7. Discussion

A method coupling a time domain seakeeping model and a zero-mass kite model has been developed to investigate the dynamic motion of a ship towed by a kite. The zero-mass kite model neglects the inertial forces, its deformation and the dynamic behavior of the tether. The ship model is based on the linear seakeeping STF strip theory (Salvesen et al., 1970), cf. Chap.6. A monolithic approach coupling the kite and ship models has been compared to a segregated approach which neglects the coupling term. The two methods enable a fast computing method. Implemented in Python, the monolithic approach is computed faster than the real-time. The computation of the considered cases are five time faster than the real

time on a processor Intel(R) Xeon(R) CPU E3-1220 v3 with a CPU frequency of 3.10 GHz and 8 Go Ram.

The ship model provides satisfactory results in terms of heave and pitch motions. Since the roll motion is highly nonlinear, the linear prediction of the roll motion is less accurate. However, in Chap. 6 a similar evolution of the predicted roll motion is noticed between the proposed roll motion modeling and the Ikeda et al. (1978) modeling used as a reference in this study. Consequently, a good confidence in the kite influence on the roll motion prediction could be attributed in terms of evolution. Nevertheless, the absolute value of the ship roll motion should be regarded with caution. Moreover, ship motions have been restricted to heave, pitch and roll motions, and existing couplings, such as roll and sway coupling, have been neglected.

In case of a dynamic flight, as shown in Chap. 4, the considered tether tensions lead to a small tether sag, which justifys the assumption of the tether as a straight inelastic line. However, the tether plays the role of interface between the kite and the ship. The acceleration of the tether may have a significant influence on the interaction between the kite and the ship. Further theoretical investigations should be performed to study the tether effects on the kite lock-in phenomenon.

Moreover, in order to validate the modeling approach proposed in this chapter, several strategies can be performed. Full scale experiments on a dinghy towed by kite has been performed by Behrel et al. (2017). However, measurement of the environment is challenging at full scale. In a towing tank test with a reduced scale model, similitude issues are also challenging to solve as it was highlighted by Martin et al. (2014) for offshore floating wind turbines. To get around the problem of similitude and to take benefit from the towing tank test conditions, the kite could be modeled like a hardware in the loop method such as proposed by Giberti and Ferrari (2015) for classical sailing yacht.

9.8. Conclusion

Different tether lengths have been tested with a constant angular trajectory size leading to an evolution of the kite excitation frequencies. In the case of calm water, the coupling between the ship and the kite decreases the kite towing force, consequently the segregated approach is conservative in comparison to the monolithic approach.

In case of regular beam waves, the interactions between the kite and the ship are more significant. The definition of the kite trajectory into the relative wind basis taking into account the vertical ship velocity can lead to unrealistic trajectories with very short radius of curvature. This issue is avoided by defining the kite trajectory into a relative wind basis neglecting the influence of the vertical ship motion. Moreover, strong interaction between kite flight and ship motions at the wave frequency is shown. A kite lock-in phenomenon

at the wave frequency has been discovered. However, the kite lock-in phenomenon can be win-win. Indeed, for some configurations of the kite lock-in phenomenon, the mean kite towing force is increased whereas the ship roll amplitude is getting smaller in comparison with no kite.

10. Course keeping stability

Résumé: Stabilité de route

Un navire tracté par cerf-volant peut être considéré comme un système proche d'un navire remorqué. La différence entre les deux systèmes est que le kite impose des perturbations harmoniques. Ainsi, les méthodes consacrées à la stabilité de route des bateaux remorqués ne peuvent pas être directement appliquées. Malgré tout en utilisant un critère de stabilité linéaire des navires remorqués, il est montré, en considérant uniquement la partie linéaire des forces hydrodynamiques de la carène, que le KCS ne peut être stable qu'à condition que le point d'attache soit légèrement en avant de l'étrave. Cependant, plusieurs positions de point d'attache du cerf-volant ont été testées numériquement au vent arrière, au grand largue et au travers. La seule configuration stable réaliste est au vent arrière. Pour les autres allures, le navire est instable. Des configurations de point d'attache plus en avant que l'étrave ont été testées par intérêt théorique. Quand le point d'attache est suffisamment devant, la stabilité de route est garantie, et pour des positions intermédiaires un phénomène de fishtailing est mis en évidence.

Ainsi pour garantir la stabilité de route il est nécessaire de contrôler activement le safran ou bien d'ajouter une dérive. Etant donné que les navires sont équipés de pilotes automatiques plusieurs conceptions de régulateur PID (Proportionnel Intégral Dérivé) ont été investiguées. Un régulateur qui rejoint rapidement le cap de consigne impose de forte amplitude de safran à cause des perturbations harmoniques du cerf-volant. Le filtrage de la partie dérivée permet d'atténuer les amplitudes de barre. En cas de mer de travers, les amplitudes de barre sont largement augmentées. Les perturbations du cerf-volant sur le lacet du navire deviennent alors négligeables.

10.1. Introduction

The course keeping stability of a ship towed by kite and the control of the heading with the rudder are investigated in this chapter.

A ship towed by kite is almost a similar system to a ship towed by tug boat. The course keeping of towed ships has been studied in the literature with differents levels of sophistication. A first investigation has been achieved by Strandhagen (1950) assuming that the

ship is towed at a constant towing force. Usually, the towed ship is modeled with the 3 dof of maneuverability where the tug boat follows a prescribed motion (Bernitsas and Kekridis, 1985, 1986; Lee, 1989). More recently, the tug has been also modeled with a 3 dof maneuvering model in (Yasukawa, 2007; Fitriadhy and Yasukawa, 2011; Fitriadhy et al., 2013). The elasticity of the line was taken into account in (Bernitsas and Kekridis, 1986). Often, ship forces are modeled in terms of Taylor expansion in order to use analytical stability analysis methods. Depending on the hydrodynamics of the towed ship, of the towline length and attachment position, the towed ship may be subjected to horizontal divergent motions and/or oscillatory motions called fishtailing. Furthermore, Fitriadhy et al. (2013); Sinibaldi and Bulian (2014) investigated the windage effect on the stability. Their results showed that a tug-ship system is significantly influenced by the relative wind direction. In case of a weak course keeping stability, the ship heading must be controlled with the rudder.

Due to a dynamic kite flight, no equilibrium of the ship towed by kite system can be found. Therefore, the stability analysis proposed in the literature as mentioned before is a priori not directly applicable. However, based on a first numerical approach with the monolithic coupling method, the course keeping stability of a ship towed by a kite is investigated in section 10.2. The influence of the longitudinal tether attachment position at different true wind angle is studied with the KCS container ship. Results are analyzed and discussed. Then in Sec. 10.3, the course keeping stability is studied with an active control of the rudder. Different Proportional Integrator Derivator (PID) designs are investigated in calm water and in case of a regular beam wave.

The study is performed with the Kriso Container Ship in the same conditions as presented in Chap. 8.

10.2. Self course keeping stability

10.2.1. Analytical requirements

Assuming a constant speed of the tug boat, an inelastic towline and no wind, Fitriadhy and Yasukawa (2011) investigated the parameters influencing the course keeping stability of the towed ship according to the Routh-Hurwitz criterion. This criterion leads to six inequalities:

$$\begin{cases} D_0, D_1, D_2, D_3, D_4 & > 0 \\ D_1 D_2 D_3 - D_1^2 D_4 - D_0 D_3^2 & > 0 \end{cases} \tag{10.1}$$

where,

$$\begin{cases} D_0 &= L_t^{'} MA_{22}^{'} MA_{66}^{'} \\ D_1 &= -L_t^{'} \left(MA_{22}^{'} N_{r_s}^{'} + MA_{66}^{'} Y_{v_s}^{'} \right) \\ D_2 &= L_t^{'} \left[\left(MA_{11}^{'} - Y_{r_s}^{'} \right) N_{v_s}^{'} + Y_{v_s}^{'} N_{r_s}^{'} \right] - X_{u_s u_s}^{'} \left[a_x^{(\mathbf{s})'} MA_{11}^{'} \left(a_x^{(\mathbf{s})'} + L_t^{'} \right) + MA_{66}^{'} \right] \\ D_3 &= X_{u_s u_s}^{'} \left[N_{r_s}^{'} - a_x^{(\mathbf{s})'} \left(Y_{r_s}^{'} - MA_{11}^{'} + MA_{22}^{'} \right) + \left(a_x^{(\mathbf{s})'} + L_t^{'} \right) \left(a_x^{(\mathbf{s})'} Y_{v_s}^{'} - N_{v_s}^{'} \right) \right] \\ D_4 &= X_{u_s u_s}^{'} \left(Y_{v_s}^{'} a_x^{(\mathbf{s})'} - N_{v_s}^{'} \right) \end{cases} \tag{10.2}$$

and,

$$MA_{11}^{'} = \frac{\Delta_s + A_{11}\,(\omega \sim 0)}{\frac{1}{2}\rho_w L_{pp}^2 T_m} \quad MA_{22}^{'} = \frac{\Delta_s + A_{22}\,(\omega \sim 0)}{\frac{1}{2}\rho_w L_{pp}^2 T_m} \quad MA_{66}^{'} = \frac{I_{z_s} + A_{66}\,(\omega \sim 0)}{\frac{1}{2}\rho_w L_{pp}^4 T_m}$$

$$L_t^{'} = \frac{L_t}{L_{pp}} \quad a_x^{(\mathbf{s})'} = \frac{a_x^{(\mathbf{s})}}{L_{pp}} \quad Y_{y_s}^{'} = \frac{Y_{y_s}}{\frac{1}{2}\rho_w L_{pp}^2 T_m U_s}$$

$$Y_{v_s}^{'} = \frac{Y_{v_s}}{\frac{1}{2}\rho_w L_{pp} T_m U_s} \quad N_{r_s}^{'} = \frac{N_{r_s}}{\frac{1}{2}\rho_w L_{pp}^3 T_m U_s} \quad N_{v_s}^{'} = \frac{N_{v_s}}{\frac{1}{2}\rho_w L_{pp}^2 T_m U_s}$$

This criteria is questionable since the windage and the rudder forces are neglected. Indeed, Fitriadhy et al. (2013) and Sinibaldi and Bulian (2014) showed that the windage may decrease the course keeping stability. They highlighted that under some configurations a fishtailing phenomenon can occur.

Since the windage force cannot be neglected for a ship towed by a kite especially for the yaw motion, only the condition D_4>0 is investigated. The condition $D_4 = 0$ is equivalent to the condition leading to a yaw equilibrium without rudder. In other words, this condition gives the hydrodynamic lever arm $X_{u_s u_s}^{'}$ which is always negative. Consequently, to get a stable configuration, the tether attachment point should be at least forwards $L_{pp} N_{v_s}^{'} / Y_{v_s}^{'}$. Using the KCS, this condition imposes that the tether attachment point should be located at $0.5421 L_{pp}$. Therefore, according to this linear criteria, no stable tether attachment configuration exists for the KCS. Adding a centerboard appendage could be investigated to obtain a stable configuration. A centerboard would increase the value of $Y_{v_s}^{'}$ and may not increase $N_{v_s}^{'}$. The ideal position of the centerboard could be determined to increase the ratio $N_{v_s}^{'} / Y_{v_s}^{'}$. However this study is beyond the scope of this thesis.

10.2.2. Results

The case of study is the KCS towed by a kite of 500 m^2 and a tether length of 500 m. For the following results, the ship speed is 10 m.s^{-1} and the true wind speed is 12 m.s^{-1}. True

wind angle $\beta_{tw} \in \{180°, 135°, 90°\}$ and tether attachment point $a_x^{(\mathbf{s})} \in \{0.5,\ 1,\ 2\}\ L_{pp}$ are tested.

First, for each configurations, the mean equilibrium of the ship towed by kite is solved to obtain the rudder angle and the propeller speed. Then, in calm water, 6 dof time domain simulations of the KCS are performed. The time step is 0.2 s and simulations are done over 10000 s. The rudder angle and the propeller rotational speed are summarized according to the tested sailing condition in Tab. 10.1. For information, the kite mean power saving ratio is also reported in Tab. 10.1.

	$a_x^{(\mathbf{s})} = 0.5L_{pp}$	$a_x^{(\mathbf{s})} = L_{pp}$	$a_x^{(\mathbf{s})} = 2L_{pp}$
$\beta_{tw} = 180°$	$\delta_r = 0.00°$ $n_p = 1.24$ rps $\eta_k = 35.4\%$	$\delta_r = 0.01°$ $n_p = 1.24$ rps $\eta_k = 35.4\%$	$\delta_r = 0.02°$ $n_p = 1.24$ rps $\eta_k = 35.4\%$
$\beta_{tw} = 135°$	$\delta_r = -0.81°$ $n_p = 1.23$ rps $\eta_k = 40.7\%$	$\delta_r = 1.94°$ $n_p = 1.23$ rps $\eta_k = 40.2\%$	$\delta_r = 7.42°$ $n_p = 1.25$ rps $\eta_k = 36.1\%$
$\beta_{tw} = 90°$	$\delta_r = -1.94°$ $n_p = 1.38$ rps $\eta_k = 21.4\%$	$\delta_r = 1.52°$ $n_p = 1.38$ rps $\eta_k = 20.9\%$	$\delta_r = 8.44°$ $n_p = 1.41$ rps $\eta_k = 14.7\%$

Table 10.1.: Mean rudder angle, propeller rotational speed and kite power efficiency for different true wind angle β_{tw} and longitudinal tether attachment point $a_x^{(\mathbf{s})}$

Figures 10.1a, 10.1b and 10.1c show respectively the time series of the ship heading for the tether attachment point $a_x^{(\mathbf{s})}$ =$0.5L_{pp}$, L_{pp} and $2L_{pp}$. From the top to the bottom, the heading times corresponding to true wind angles β_{tw} =180°, 135° and 90° are represented.

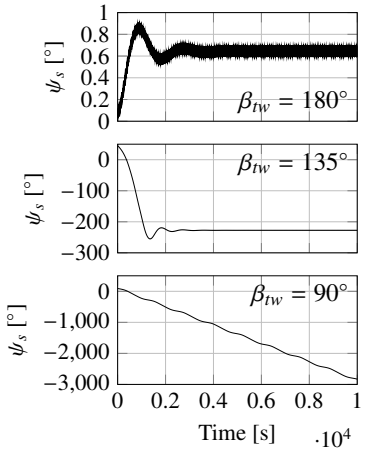

(a) $a_x^{(\mathbf{s})} = 0.5L_{pp}$

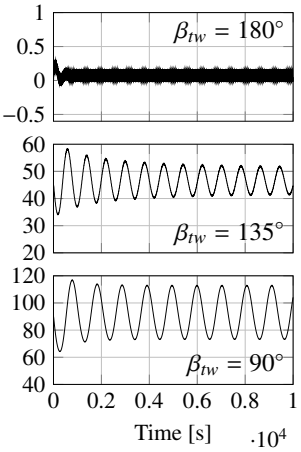

(b) $a_x^{(\mathbf{s})} = L_{pp}$

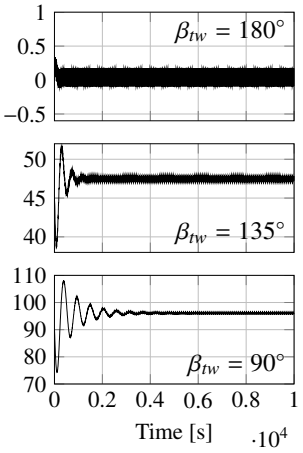

(c) $a_x^{(\mathbf{s})} = 2L_{pp}$

Figure 10.1.: From the top, heading time series ψ_s for the true wind angles β_{tw} =180°, 135° and 90°

10.2.3. Analysis and discussion

For each configuration it can be noticed a transitory phase since initial conditions for the time domain simulation are zero for the heave, heel and pitch instead of the mean equilibrium value. Moreover, as shown in the previous chapter (Chap. 9), the coupling between the kite and the ship leads to a different mean equilibrium than the one predicted by the mean equilibrium solver which neglects the coupling. For the 9 configurations tested, 3 types of behavior can be observed.

Stable configurations correspond to the cases $\left(a_x^{(\mathbf{s})};\ \beta_{tw}\right) = (0.5L_{pp}, 180°)$, $\left(a_x^{(\mathbf{s})};\ \beta_{tw}\right) = (L_{pp}; 180°)$ and $\left(a_x^{(\mathbf{s})};\ \beta_{tw}\right) = (0.5L_{pp};\ 180°, 135°, 90°)$. For these cases, after a transitory phase, the ship heading oscillation corresponds to the kite excitation. For a bounded excitation the response is bounded at the same frequencies of the excitation. At $\beta_{tw} = 180°$, the amplitude of the ship heading for $a_x^{(\mathbf{s})}$ =0.5L_{pp}, L_{pp} and 2L_{pp} are respectively 0.05° 0.09° and 0.132°. The amplitude the ship heading increases with the longitudinal tether attachment point $a_x^{(\mathbf{s})}$. With $a_x^{(\mathbf{s})}$ =2L_{pp}, the amplitude of ship heading for β_{tw} =180°, 135° and 90° are respectively 0.132°, 0.32° and 0.17°. The effect of the true wind angle on the ship heading amplitude is less obvious. Nonetheless, the ship heading amplitude increases with the yaw excitation amplitude of the kite.

Diverging configurations correspond to configurations $\left(a_x^{(\mathbf{s})};\ \beta_{tw}\right) = (0.5L_{pp}, 135°)$ and $\left(a_x^{(\mathbf{s})};\ \beta_{tw}\right) = (L_{pp}; 90°)$. For the case $\left(a_x^{(\mathbf{s})};\ \beta_{tw}\right) = (0.5L_{pp}, 135°)$, the ship heading diverges from the initial equilibrium state and found a stable mean equilibrium at $\psi_s = -227.5°$. For the case $\left(a_x^{(\mathbf{s})};\ \beta_{tw}\right) = (0.5L_{pp}; 90°)$, no new equilibrium was found and the ship performs turning circles.

Fishtailing phenomenon can be noticed for the configuration $\left(a_x^{(\mathbf{s})};\ \beta_{tw}\right) = (L_{pp}, 90°)$. The ship is subjected to oscillations at a frequency different from the kite excitation. This phenomenon is well-known for the ship towing operation with a tug boat. For the configuration $\left(a_x^{(\mathbf{s})};\ \beta_{tw}\right) = (L_{pp}, 135°)$, it seems that the fishtailing phenomenon can be noticed. Nevertheless, the amplitude of the heading is still decreasing after $10 \cdot 10^4$ s of simulation.

The cases with $a_x^{(\mathbf{s})}$ =L_{pp} and 2L_{pp} are purely theoretical. However, thanks to these cases, the existence of stable and fishtailing configuration is highlighted. Results gives a good confidence to apply the same analysis methods as those used for the tug-ship studies (Sinibaldi and Bulian, 2014; Fitriadhy et al., 2013) to a ship towed by kite.

Globally, a very poor course keeping stability is noticed for the KCS. Consequently, in order to perform free sailing simulations the rudder angle must be actively controlled. Hence, the next section investigates ship motions with an active control of the rudder angle. An alternative solution to the active control would have been to add a centerboard as mentioned before.

10.3. Ship active control

10.3.1. Controller

10.3.1.1. Rudder autopilot

The Proportional Integral Derivative (PID) controller is widely used in many applications. The development of this type of controller is well depicted in (Bennett, 1993). Just for the anecdote, one of the first theoretical developments of the PID controller was done in 1922 by Minorsky (1922) and was based on the observation of an helmsman steering a ship. For the ship heading control, the mathematical form of PID controller is given by:

$$\delta_r = K_p \left(\Psi_s - \psi_s + \beta_s\right) + K_i \int_0^t \left(\Psi_s - \psi_s + \beta_s\right) d\tau + K_d \frac{\mathrm{d}\left(\Psi_s - \psi_s + \beta_s\right)}{\mathrm{d}t}, \quad (10.3)$$

where, K_p, K_i and K_d are respectively the proportional, integrator and derivative terms[1]. Ψ_s denotes the heading target. Hence, the quantity $\psi_s - \Psi_s$ is the heading error. It is assumed here that the heading taget value is constant. Neglecting the time derivative of the drift, the heading error derivative is approximated to r_s.

The determination of coefficients K_p, K_i and K_d depends on the ship. For this purpose, a simplified yaw equation of motion is used:

$$MA_{66}\ddot{\psi}_s - N_{r_s}\dot{\psi}_s = \kappa_r \delta_r \quad (10.4)$$

κ_r is evaluated during the simulation with:

$$\kappa_r = \frac{N_r}{\alpha_r} \quad (10.5)$$

Here, the PID controller is designed with the Matlab® function “pidtune”. Different 0 dB gain crossover frequency ω_c can be chosen. The proportional term and the rudder angle amplitude increase with the crossover frequency. However, the response time decreases with the increase of the crossover frequency. The choice of the crossover frequency is a trade off between the response time and the amplitude of the rudder angle.

The derivative term amplified the noise of the signal. Since the kite may induced some noise, it could be interesting to filter the derivatives term with a low pass filter as proposed by Yun Li et al. (2006). Thus the rudder control can be rewritten as follows:

[1] In this chapter K_p should not be confused with the propeller moment around the $\underline{x}_s$ axis.

$$\delta_r = K_p\left(\Psi_s - \psi_s + \beta_s\right) + K_i \int_0^t \left(\Psi_s - \psi_s + \beta_s\right) d\tau + K_d \mathfrak{F}_{LP}\left(\frac{\mathrm{d}\left(\Psi_s - \psi_s + \beta_s\right)}{\mathrm{d}t}\right), \tag{10.6}$$

where, $\mathfrak{F}_{LP}$ denotes a low pass filter function.

10.3.1.2. Propeller autopilot

The propeller rotational speed is controlled by a PI controller to reach a target speed over ground:

$$n_p = K_p\left(U_d - U_s\right) + K_i \int_0^t \left(U_d - U_s\right) d\tau \tag{10.7}$$

10.3.2. Calm water case

Results presented aim to show the effect of the crossover frequency on the time response, rudder angle and heel angle. The sailing condition chosen is a case close to the most critical case for the course keeping stability studied in the first part of this chapter. The true wind angle is $\beta_{tw} = 90°$. The true wind speed is $U_{tw} = 12$ m.s^{-1}. The longitudinal tether attachment point is $a_x^{(\mathbf{s})} = 110$ m. The kite area is $A_k = 500$ m^2. The tether length is $L_t = 500$ m. The corresponding proportional, integrator and derivatives terms are reported in Tab. 10.2. The simulation time is 3000 s and the time step is 0.2 s. The initial condition is $u_s = 10$ m.s^{-1} and the initial heading angle is 90° with respect to the true wind speed. Four PID controllers are tested for the KCS, with the crossover frequency $\{0.4,\ 0.3,\ 0.2,\ 0.1\}$ rad.s^{-1} and with the "Design-focus" option set to "reference-tracking".

ω_c [rad.s^{-1}]	0.1	0.2	0.3	0.4
K_p	$3.15 \cdot 10^8$	$3.54 \cdot 10^8$	$7.96 \cdot 10^8$	$1.41 \cdot 10^9$
K_i	$4.75 \cdot 10^5$	$6.19 \cdot 10^5$	$2.09 \cdot 10^6$	$4.95 \cdot 10^6$
K_d	$2.52 \cdot 10^{10}$	$5.05 \cdot 10^{10}$	$7.58 \cdot 10^{10}$	$1.01 \cdot 10^{11}$

Table 10.2.: Rudder PID controller for the crossover frequency 0.1, 0.2, 0.3 and 0.4 assuming $\kappa_r = 1$; "Design focus" option: "reference-tracking".

Figure 10.2 shows the heading error time series, $\psi_s - \beta_s - \Psi_s$ for the 4 PID controller designs. Figures 10.3 and 10.4 are the amplitude of the Fourier transform of the rudder angle and heel angle.

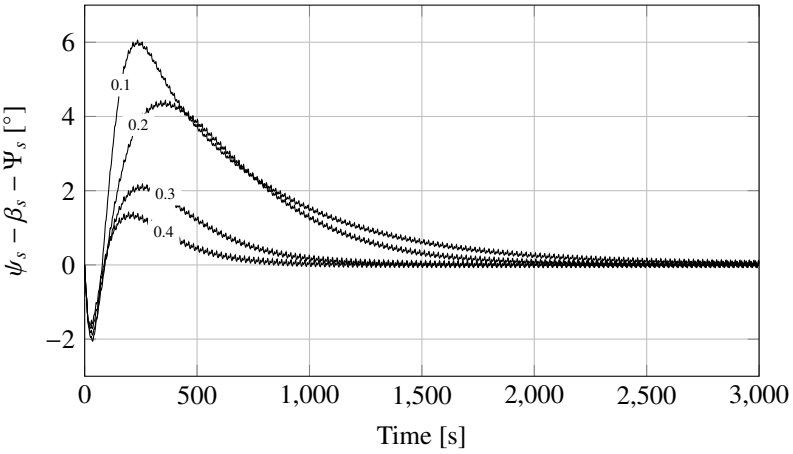

Figure 10.2.: Heading error time series for PID designs with crossover frequencies ω_c, 0.1, 0.2, 0.3 and 0.4 in calm water; “Design focus” option: “reference-tracking”.

For all PID controller designs, the evolution the heading error is similar. First the error decreases to reach a minimum around -2°. Then the heading error increases to reach a maximum. Afterwards the heading error decreases gently to reach a zero mean value. The yaw kite excitation induced small heading oscillations. Differences between PID designs can be noticed on the maximum error value and on the time reach a zero mean heading error. The maximum heading error and the time to reach a zero mean error increase with the decrease of the crossover frequency. According to the heading error time series, a higher crossover frequency should be preferred. Regarding the rudder angle, it can be noticed, that all PID controllers react at kite harmonic frequencies. A clear evolution of the rudder angle amplitude with the crossover frequency can be noticed. Indeed, the rudder angle amplitude response increases with the crossover frequency. In figure 10.4, it can be noticed that the heel angle decreases with the increase of the crossover frequency.

An usual manner to decrease perturbation effects is to filter derivative error terms with a low pass filter. Here, this method is not required, but it might be necessary for smaller ships. For illustrative purpose, Fig. 10.5 shows the heading error and rudder time series, with such a method where $K_p = 2.07 \cdot 10^9$, $K_i = 2.15 \cdot 10^7$ and $K_d = 5.00 \cdot 10^{10}$. The controller design, is obtained with the “Design-focus” option set to “balanced” and crossover frequency of 0.2 rad.s^{-1}. The low pass filter is a Butterworth filter of order 1 with a cutoff angular frequency of 0.1 rad.s^{-1}.

Compared to the standard PID controller with a crossover frequency of 0.4 rad.s^{-1}, the response time is divided by 2 with the filtered derivatives term. The rudder angle amplitude after 200 s of simulation is around 0.5°. The rudder angle amplitude and the time response are significantly reduced with the low pass filtering of the derivative term.

To sum up the analysis, a high crossover frequency is preferable for time response and the heel angle, and to limit the ruder angle amplitude a low crossover frequency is preferable.

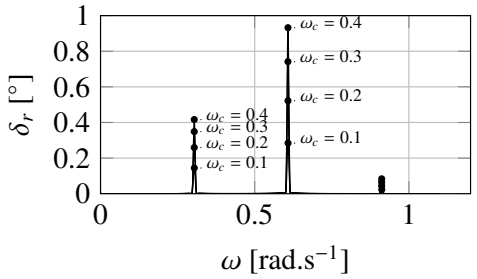

Figure 10.3.: Fourier transform amplitude of the rudder angle for PID designs with crossover frequencies ω_c, 0.1, 0.2, 0.3 and 0.4 in calm water. "Design focus" option: "reference-tracking".

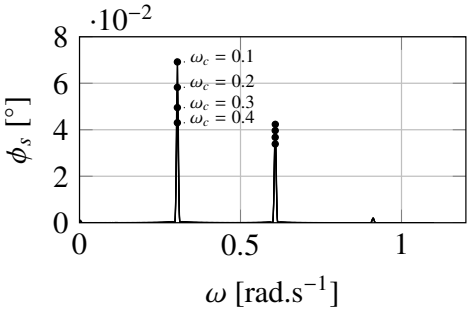

Figure 10.4.: Fourier transform amplitude of the heel angle for PID designs with crossover frequencies ω_c, 0.1, 0.2, 0.3 and 0.4.

However, the worse rudder angle amplitude is around 1° and heel angle amplitudes are small. To decrease the rudder angle amplitude, derivative terms have been filtered with a low pass filter. This usual method provides a significant improvement to the course keeping stability of the ship. Both the response time and the rudder angle amplitude are decreased.

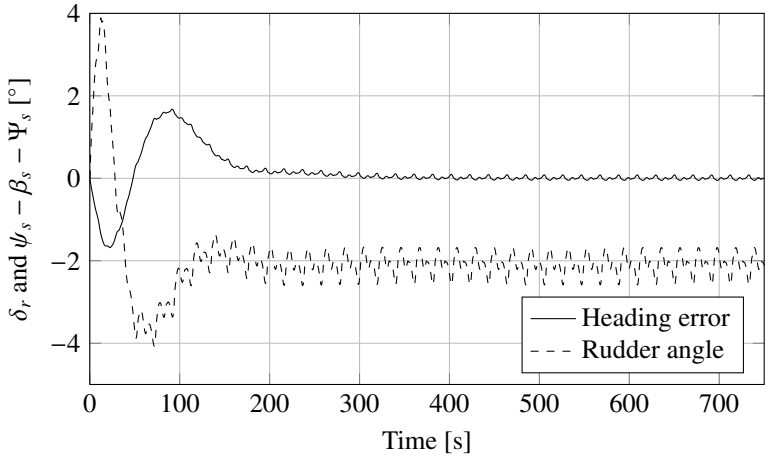

Figure 10.5.: Heading error and rudder time series with a low pass filter of the derivative term in calm water; “Design focus” option: “balanced”.

10.3.3. Regular beam wave case

To investigate a more realistic case, a regular beam wave case is studied. A regular beam wave with a frequency of 0.4 rad.s^{-1} and with an amplitude of 2.5 m is considered. As shown in Chap. 9, the wave excitation dominates the kite excitation. The course keeping stability may be affected by a wave. Two wave cases are investigated, a beam reach course $\beta_{tw} = \psi_w = 90°$ and a broad reach course $\beta_{tw} = \psi_w = 135°$. Four PID controller designs with the “design focus” option set to “balanced” are tested. They are obtained with following crossover frequencies $\{0.05,\ 0.075,\ 0.1,\ 0.2\}$ rad.s^{-1} and their coefficients are summarized in Tab. 10.3.

ω_c [rad.s^{-1}]	0.05	0.075	0.1	0.2
K_p	$1.81 \cdot 10^8$	$4.39 \cdot 10^8$	$7.60 \cdot 10^8$	$2.07 \cdot 10^9$
K_i	$6.55 \cdot 10^5$	$2.60 \cdot 10^6$	$5.84 \cdot 10^6$	$2.15 \cdot 10^7$
K_d	$1.24 \cdot 10^{10}$	$1.85 \cdot 10^{10}$	$2.47 \cdot 10^{10}$	$5.00 \cdot 10^{10}$

Table 10.3.: Rudder PID controller for the crossover frequency 0.1, 0.2, 0.3 and 0.4 assuming $\kappa_r = 1$. “Design focus” option: “balanced”.

Figure 10.6 shows the rudder angle an heading error time series. The plotted heading error is shifted of $+20°$ to make the plot more reader-friendly. As for the calm water case the crossover frequency decreases the response time and increases the rudder angle amplitude. The case in Fig. 10.6d is particular compared to the three others. For this case, to follow the rudder command, the maximum rudder turning rate is not high enough. Consequently, the rudder angle amplitude is important as it reaches 15°. For the three other cases, the rudder angle amplitude decreases with the crossover frequency. The rudder angle amplitude is notably reduced for the case in Fig. 10.6a with the crossover frequency $\omega_c = 0.05$

rad.s^{-1} compared to the case in Fig. 10.6b with the crossover frequency $\omega_c = 0.075$ rad.s^{-1}. Nevertheless, the heading error is barely reached after 1000 s with $\omega_c = 0.05$ rad.s^{-1} whereas the convergence is reached after only 300 s with $\omega_c = 0.075$ rad.s^{-1}. The case with the crossover frequency $\omega_c = 0.1$ rad.s^{-1} is not significantly faster than the case with $\omega_c = 0.075$ rad.s^{-1} whereas the rudder angle amplitude is significantly increased. The autopilot with the crossover frequency $\omega_c = 0.075$ rad.s^{-1} appears to be a good trade off to reduce the response time and the rudder angle amplitude.

Compared to the calm water case, the wave effect increases drastically the rudder angle amplitude and the heading error amplitude. The wave perturbation dominates significantly the kite perturbation on the course keeping stability. This shows that a kite does not represent a significant extra risk to the ship maneuvering safety.

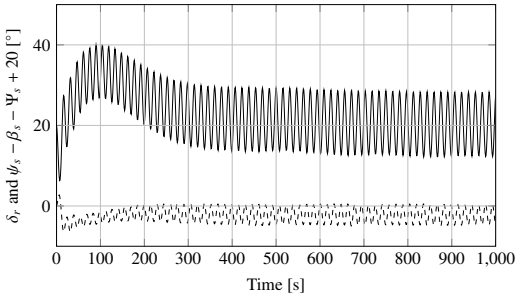

(a) $\omega_c = 0.05$ rad.s^{-1}

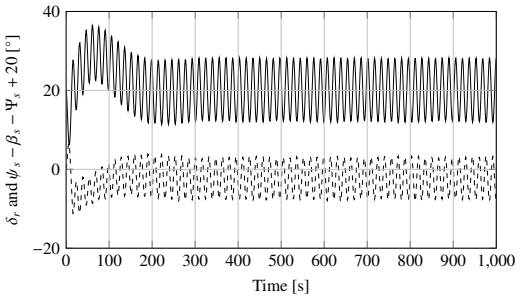

(b) $\omega_c = 0.075$ rad.s^{-1}

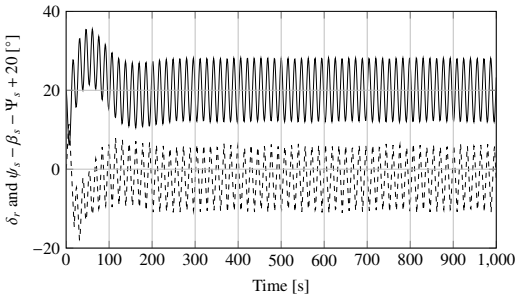

(c) $\omega_c = 0.1$ rad.s^{-1}

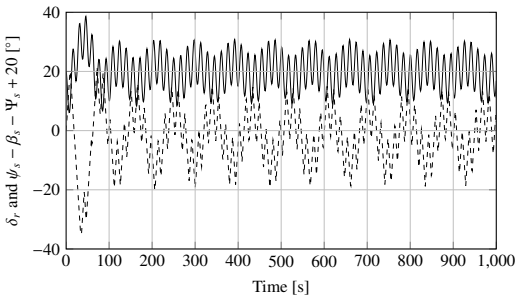

(d) $\omega_c = 0.2$ rad.s^{-1}

Figure 10.6.: Heading error and rudder angle time series for PID designs with crossover frequencies ω_c, 0.05, 0.075, 0.1 and 0.2 in regular wave on a beam reach case $\beta_{tw} = \psi_w = 90°$; "Design focus" option: "reference-tracking".

10.4. Conclusion

In this chapter, a simple investigation of the course keeping stability of a ship towed by a kite was performed. The self course keeping stability has been investigated performing simulations with a constant rudder angle and with active control of the rudder. The results on the KCS show that the self course keeping stability is very small with a tether attachment point at the bow. A self course keeping stability is only noticed at downwind. As theoretical study, tether attachment positions beyond the bow have been investigated. It has been highlighted that a fishtailing phenomenon can occur. When the tether attachment point is forwards enough, the ship towed by kite becomes stable. To increase the course keeping stability, the rudder could be actively controlled or a centerboard could be added to the ship. The self course keeping stability analysis deserves to be investigated for ships with shorter hydrodynamic lever harm. If the hydrodynamic lever arm is small enough, a study similar to the investigation performed on the ship towed by a tug boat (Fitriadhy et al., 2013; Sinibaldi and Bulian, 2014) could be interesting.

In the second part of this chapter the active control of the rudderwas investigated. PID controllers with different crossover frequencies have been investigated. The higher the crossover frequency is, the shorter the heading time response is. However, the higher the crossover frequency is, the higher the rudder amplitude is. To decrease the rudder angle amplitude due to kite perturbations, the method consisting in filtering the derivative term of the PID controller is successful. A case with a regular beam wave on a beam reach course has been investigated. It was shown that the wave perturbation dominates the kite perturbation on the heading. It means that modifications of the rudder and autopilot could be unnecessary for the refit of a merchant ship with a kite.

Secondarily, the presented study on the course keeping have led to the determination of a PID controller effective enough to simulate free sailing navigations of a ship towed by kite. Consequently, the next chapter investigates the free sailing performance of a ship towed by kite.

11. 6 dof free sailing simulations of ships towed by kite

Résumé: Simulation 6 degrés de liberté autopiloté

L'influence des mouvements dynamiques sur les performances du porte conteneur KCS tracté par un cerf-volant de 500 m et des lignes de 500 m est étudiée dans ce chapitre en prenant en compte les 6 degrés de libertés du navire. Dans le cas d'une force de traction constante, l'équivalence entre la résolution de l'équilibre statique et lemodèle dynamique est vérifiée avec succès.

Dans une première partie, pour une vitesse de vent de 12.5 $m.s^{-1}$ et une vitesse de navire de 10 $m.s^{-1}$, et pour des angles de vent réel allant de 70° à 180°, l'équilibre moyen obtenu par le modèle dynamique est comparé à la résolution de l'équilibre statique. Avec un état de mer calme, les deux approches donnent des résultats similaires. Avec une vague régulière de pulsation 0.4 $rad.s^{-1}$ et d'une hauteur de 2.5 m dans la direction du vent. L'équilibre moyen n'est pas significativement affecté. Il faut cependant noter que si l'équilibre moyen n'est que peu affecté par une vague, c'est que ne sont considérés que les efforts de vague du premier ordre. Avec le niveau de modélisation du système, le modèle dynamique ne présente qu'un intérêt limité pour calculer l'équilibre moyen. En revanche, le modèle dynamique permet d'obtenir les amplitudes de mouvement. En mer calme, les amplitudes des mouvements sont maximums pour des navigations travers au vent. En cas de houle régulière, les amplitudes des maximales des mouvements sont obtenues au largue, ce qui correspond ici à une mer de trois quart arrière.

Dans une deuxième partie, le phénomène d'accrochage est investigué par une mer trois quart arrière. Les fréquences d'excitations du cerf-volant sont balayées par variation de la longueur de ligne en gardant une amplitude angulaire de trajectoire constante. Le phénomène d'accrochage est bien présent à la fréquence de rencontre de la vague. Dans un intervalle de 200 m de ligne les harmoniques d'excitation du kite sont accrochées par la fréquence de vague. Dans cette configuration, la traction du cerf-volant est augmentée jusqu'à 34% et l'efficacité du kite est augmenté jusqu' 4% par rapport au cas en mer calme. L'amplitude de roulis est diminuée de 20% par rapport à une longueur en limite du phénomène d'accrochage.

11.1. Introduction

The aim of this chapter is to investigate the performance of a ship towed by a kite in case of 6 dof free dynamic sailing as predictedby the monolithic approach.

In Chap. 8, the mean equilibrium of a ship towed by a kite have been investigated. However, it has been shown in Chap. 9 that the dynamic motion of the ship may affect the kite flight. Since the study was focused on the roll motion only, the effect of the interactions between the ship and the kite with horizontal ship motions should be investigated. In Sec. 11.2, the mean equilibrium of a ship towed by kite obtained with the static approach is compared to the dynamic approach. First, assuming a constant towing force, the consistency of the two approaches are compared. Then, in calm water, the influence of dynamic motions on the mean performance are investigated. In Sec. 11.3 a similar analysis is performed to investigate the influence of a regular wave.

In Chap. 9, a kite lock-in phenomenon has been highlighted, but only the heave, roll and pitch motions were free. The kite lock-in phenomenon modifies the kite flight frequency towards the wave frequency. In Chap. 10 it has been shown that the influence of a wave induced significant rudder angle amplitude. The effect of the rudder angle on the roll motion, and more generally horizontal motions, may modify the kite lock-in phenomenon. Consequently, the kite lock-in phenomenon is studied in Sec. 11.4.

The case of study for this chapter is the Kriso Container Ship as presented before in Chap. 7.

11.2. Calm water case

11.2.1. Consistence of the dynamic modeling with the static modeling

This section aims to verify the consistency between, the mean equilibrium solution obtained with the static approach developed in Sec. 8.2.1 and the mean equilibrium obtained with the dynamic approach developed in Chap. 7. To perform this analysis, the mean kite towing force along a trajectory is applied to the ship. This mean kite towing force is a constant with respect to earth fixed frame $\mathbf{n}$. The two approaches are compared in terms of absolute relative margin defined as follows:

$$\delta E = \left| \frac{E_d - E_s}{E_s} \right| \tag{11.1}$$

where E stands for δ_r or β_s or ϕ_s.

$U_{tw} = 12.5$ m.s^{-1}	Absolute relative margin		
$U_s = 10$ m.s^{-1}	$\beta_{tw} = 90°$	$\beta_{tw} = 135°$	$\beta_{tw} = 180°$
δ_r	$9.4 \cdot 10^{-8}$	$3.8 \cdot 10^{-8}$	$5.2 \cdot 10^{-8}$
β_s	$1.5 \cdot 10^{-8}$	$5.2 \cdot 10^{-8}$	$3.4 \cdot 10^{-8}$
ϕ_s	$9.6 \cdot 10^{-6}$	$7.6 \cdot 10^{-6}$	$8.2 \cdot 10^{-6}$

Table 11.1.: Relative margins between the static and the dynamic approach in case of constant kite towing force

In Tab. 11.1 the relative margin between the two approaches is summarized in terms of rudder angle, drift angle and heel angle. Different true wind angle β_{tw} with a ship speeds of $U_s = 10$ m.s^{-1} and $U_{tw} = 12.5$ m.s^{-1} have been tested: beam reach, broad reach and downwind. For each cases the absolute relative margin are less than 10^{-5}, which gives an indication of the consistency of the two approaches.

11.2.2. Influence of the kite and ship interaction on the performance

With no wave, the true wind speed considered in this section is $U_{tw} = 12.5$ m.s^{-1}. Figure 11.1 shows the evolution with the true angle β_{tw} of the mean kite efficiency η_x, mean drift angle β_s, mean rudder angle δ_r and mean heel angle ϕ_s. The 6 dof dynamic approach and the static approach are compared. The amplitudes obtained with the 6 dof dynamic approach are plotted in dashed lines.

The static approach and the dynamic 6 dof dynamic approach are very closed for the mean value of all considered quantities. Relative margins are greater than to 10^{-5}, which shows that the differences are due to the modeling and not to the numerical accuracy. However, the relative margins are small enough, to consider that dynamic effects are negligible on the mean equilibrium. Consequently, the static approach is consistent to assess the mean equilibrium of a ship towed by kite.

Extreme values obtained with the 6 dof dynamic approach show the importance to consider the dynamic system. Kite efficiency η_x and drift angle β_s amplitudes are significant. Rudder angle and heel angle amplitudes are not significant. The kite efficiency amplitude reaches its maximum around a beam reach course $\beta_{tw} = 135°$. The minimum of kite efficiency amplitude is obtained at downwind. The drift angle is maximum at upwind and decreases with the increase of the true wind angle. These evolution in terms of amplitudes are partially dependent on the ship heading control strategy. As described in Sec. 10.3.1.1, the rudder is controlled with respect to the course over ground. A different heading control strategy could reduce the amplitude of drift angle and increase the heading amplitude.

This analysis shows that a static analysis approach is good enough for kite profit studies. However, to determine the kite design requirements regarding target specs, dynamic motions are important to investigate. Results give priority to the downwind sailing to limit dynamic effects and to increase kite efficiency.

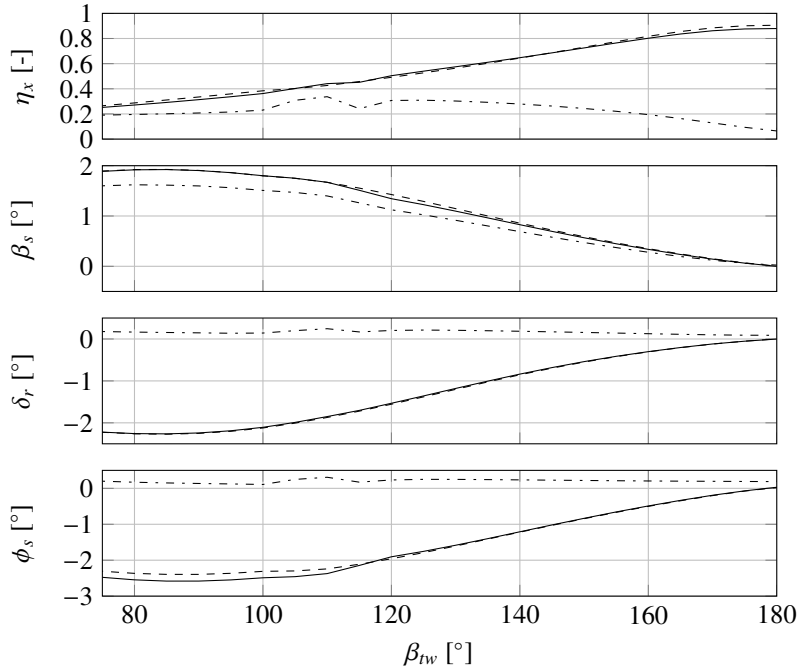

—— 6 dof dynamic approach: mean equilibrium
- - - Static approach: mean equilibrium
- · - 6 dof dynamic approach: amplitude

Figure 11.1.: For the calm water case, evolution of the mean kite efficiency η_x, mean drift angle β_s, mean rudder angle δ_r and mean heel angle ϕ_s with the true wind angle β_{tw}. The 6 dof dynamic approach (——) is compared to the static approach (- - -) in terms of mean equilibrium. The dashed-dotted lines correspond to the amplitudes obtained with the 6 dof dynamic approach (- · -). Kite configuration: $L_t = 500$ m, $A_k = 500$ m^2, $A^{(\mathbf{s})} = [110,\ 0,\ -10.6]^T$ m. Sailing condition: $U_{tw} = 12.5$ m.s^{-1}.

11.3. Regular wave case

With a regular wave of $A_w = 2.5$ m high and an angular frequency of $\omega_v = 0.4$ rad.s^{-1}, the true wind speed considered in this section is $U_{tw} = 12.5$ m.s^{-1}. Figure 11.2 shows the evolution with the true angle β_{tw} of the mean kite efficiency η_x, mean drift angle β_s, mean rudder angle δ_r and mean heel angle ϕ_s. The 6 dof dynamic approach and the static approach are compared. Amplitudes obtained with the 6 dof dynamic approach are plotted in dashed lines.

According to the results, the wave has no significant effect on the mean kite efficiency. The kite efficiency amplitude reach a maximum between a beam reach and a broad reach course. The minimum of kite efficiency amplitude is obtained at downwind. The ship drift angle

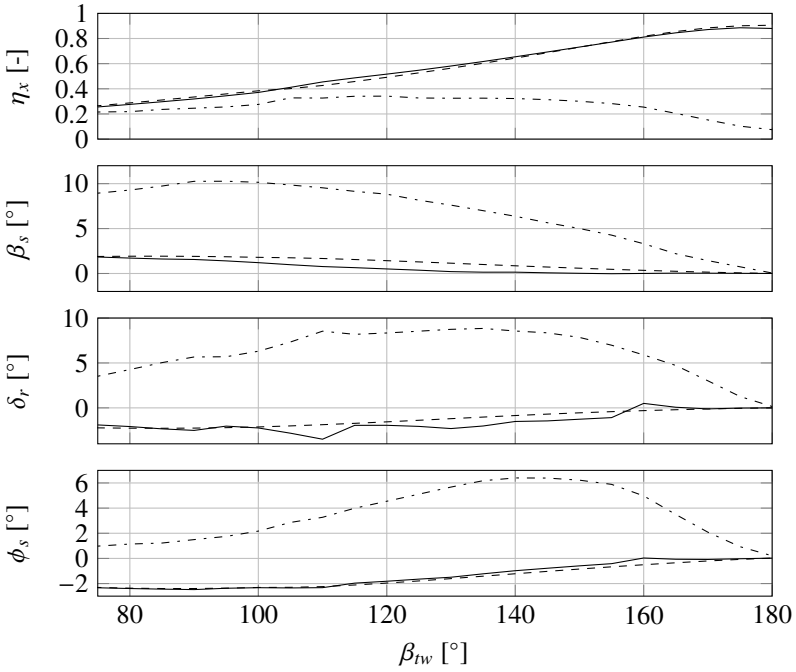

—— 6 dof dynamic approach: mean equilibrium
- - - Static approach: mean equilibrium
- · - 6 dof dynamic approach: amplitude

Figure 11.2.: For the regular wave case, evolution of the mean kite efficiency η_x, mean drift angle β_s, mean rudder angle δ_r and mean heel angle ϕ_s with the true wind angle β_{tw}. The 6 dof dynamic approach (——) is compared to the static approach (- - -) in terms of mean equilibrium. The dashed-dotted lines correspond to the amplitudes obtained with the 6 dof dynamic approach (- · -). Kite configuration: $L_t = 500$ m, $A_k = 500$ m^2, $A^{(\mathbf{s})} = [110,\ 0,\ -10.6]^T$ m. Sailing condition:$U_{tw} = 12.5$ m.s^{-1}, wave amplitude $A_w = 2.5$ m and wave angular frequency $\omega_w = 0.4$ rad.s^{-1}.

amplitude is maximum at beam reach course and is zero at downwind. The rudder angle evolution follows a sharp evolution. This sharp evolution could be explained by the kite and ship interactions as highlighted in Chap. 9. However, according to a global evolution, the rudder angle amplitude is maximum between a beam reach and a broad reach course. Comparing the rudder amplitude obtained in calm water to the one obtained with a regular wave, it can be noticed that the rudder angle amplitude is driven by the wave effect. The maximum heel angle amplitude is obtained for a broad reach course. As for the rudder angle, the heel angle is dominated by the wave force.

The wave effect dominates the kite effect. Consequently, as for the calm water case, Results are in favor to the downwind sailing. However, at downwind, the ship heading and heel stability can suffer from the parametric roll. The ship modeling used here is not accurate

enough to account for the parametric roll. Indeed, the parametric roll can be explained by the instantaneous modification of the metacentric height (Shin et al., 2004). Here, the hydrostatic is simply taken into account by a linear stiffness matrix, therefore the metacentric height is assumed constant.

A questionable result concerns the mean ship drift angle. The ship modeling does not take into account the mean second order wave drift load. Only the first order part of the incoming wave force is taken into account which is a zero mean value. Consequently, the mean ship drift angle due to a wave is zero which explains that almost no difference can be noticed between the calm water case and the regular wave case.

11.4. Influence of the kite lock-in phenomenon on the performance

This section aims to investigate the kite lock-in phenomenon revealed in Sec. 9.5.3 in case of a 6 dof free sailing. The kite excitation of a dynamic flight following a Lissajous trajectory is composed of several harmonics. When one of the kite excitation harmonic is close to the wave frequency, the interactions between the kite and the ship shifts this harmonic close to the ship main motion frequency. Since the ship motion is dominated by the wave effect, in case of a regular wave, the closest kite excitation harmonic is shifted towards the wave frequency. In Chap. 9 the considered ship degrees of freedom were the heave, roll and pitch motions. Consequently, the existence of this phenomenon has to be verified by modeling the 6 degrees of freedom of the ship.

The kite lock-in phenomenon is investigated on a broad reach course $\beta_{tw} = 135°$ with a true wind speed $U_{tw} = 12.5$ m.s^{-1}. The harmonics of the kite excitation are shifted from high frequencies to low frequencies by varying the tether length and keeping a constant angular amplitude of trajectory. In Figures 11.3, 11.4 and 11.5, the first kite roll excitation frequency ω_{k1} is plotted as function of the tether length. Globally, ω_{k1} decreases with the tether length. The wave frequency of encounter is obtained according to the following relationship:

$$\omega_e = \omega_w - \frac{u_s}{g}\omega_w^2 \cos\beta_w \tag{11.2}$$

According to the sailing condition, the frequency of encounter is $\omega_e = 0.285$ rad.s^{-1}. As it can be noticed in Fig. 11.3, the first harmonic of the kite roll excitation ω_{k1} observes a plateau at $\omega_{k1} = \omega_e$ between $L_t = 455$ m and $L_t = 665$ m. This particular evolution of the first kite harmonic shows that the kite lock-in phenomenon still exists in case of a 6 dof free sailing simulation. In Fig. 11.4, ω_{k1} is plotted with wave (in solid line) and in calm water (dashed line). The dashed lines shows the evolution of the first kite harmonic without the influence of a wave. The influence of the ship motion due to the wave is significant on the kite frequency.

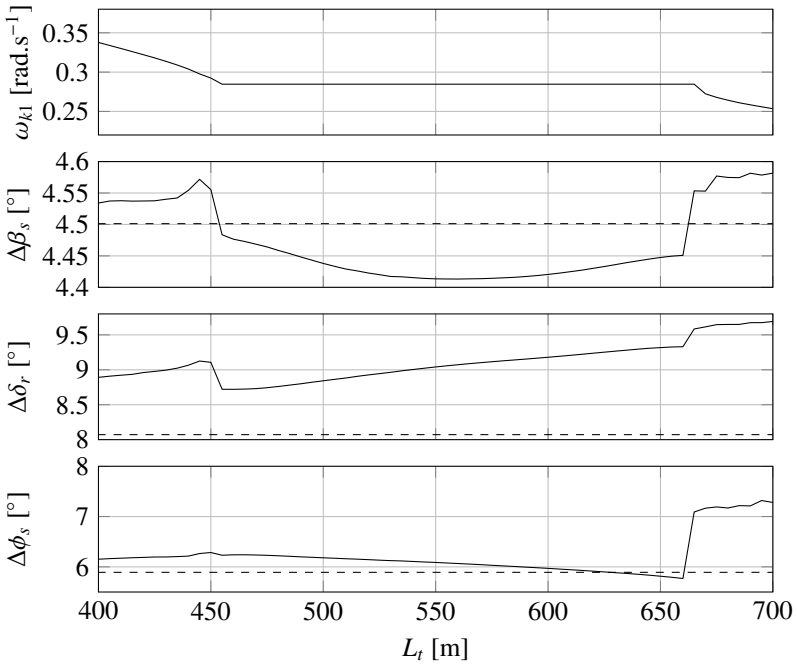

—— 6 dof dynamic approach with kite
- - - 6 dof dynamic approach without kite

Figure 11.3.: With a regular wave in the wind direction, evolution of the first kite roll excitation harmonic frequency ω_{k1}, drift angle amplitude $\Delta\beta_s$, rudder angle amplitude $\Delta\delta_r$ and heel angle amplitude $\Delta\phi_s$ with different tether lengths and a constant angular amplitude of trajectory. A configuration with kite (——) is compared to a configuration without kite (- - -). Kite configuration: $A_k = 500$ m^2, $A^{(\mathbf{s})} = [110,\ 0,\ -10.6]^T$ m. Sailing condition: $\beta_{tw} = 135°$, $U_{tw} = 12.5$ m.s^{-1}, wave amplitude $A_w = 2.5$ m and wave angular frequency $\omega_w = 0.4$ rad.s^{-1}.

As shown in Sec. 11.4, the kite lock-in phenomenon could be profitable as it can decrease the roll motion amplitude. In Fig. 11.3, the drift angle amplitude $\Delta\beta_s$, the rudder angle amplitude $\Delta\delta_r$ and heel angle amplitude $\Delta\phi_s$ are plotted as a function of the tether length. To make the analysis easier, the evolution of ω_{k1}, the first kite harmonic, with the tether length is plotted to identify the formation of the kite lock-in phenomenon. For short tether length, the heel angle amplitude is increased by the kite excitation. On the contrary, for long tether lengths and with the presence of the lock-in phenomenon and notably for $L_t = 660$ m, the heel angle is decreased compared to the case without kite. For $L_t = 660$ m, the heel angle is decreased by 20% compared to the case with $L_t = 665$ m. Consequently, the kite lock-in phenomenon is favorable in terms of roll motion. The same observation can be achieved for the drift angle amplitude. For all tether lengths concerned by the kite lock-in phenomenon the drift angle amplitude is lower than for the case without kite.

The rudder angle amplitude $\Delta\delta_r$ without wave is 8.1°. The rudder angle amplitude varies from 8.7° for $L_t = 455$ m to 9.7° for $L_t = 700$ m. For the considered tether lengths, the kite heading perturbation is responsible for 20% of the rudder angle amplitude compared to the wave perturbation.

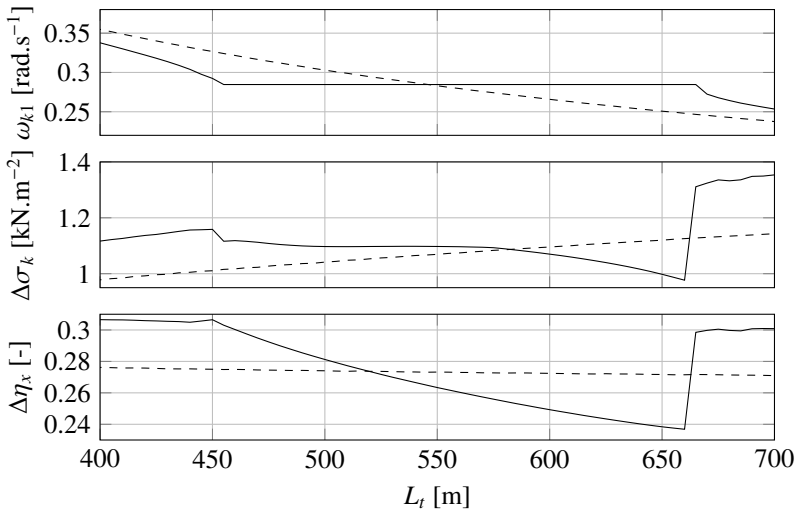

—— 6 dof dynamic approach with wave
- - - 6 dof dynamic approach without wave

Figure 11.4.: With a regular wave in the wind direction, evolution of the first kite roll excitation harmonic frequency ω_{k1}, kite wind loading amplitude $\Delta\sigma_k$, kite efficiency amplitude $\Delta\eta_x$ with different tether lengths and a constant angular amplitude of trajectory. A configuration with wave (——) is compared to a configuration without wave (- - -). Kite configuration: $A_k = 500$ m^2, $A^{(\mathbf{s})} = [110,\ 0,\ -10.6]^T$ m. Sailing condition: $\beta_{tw} = 135°$, $U_{tw} = 12.5$ m.s^{-1}, wave amplitude $A_w = 2.5$ m and wave angular frequency $\omega_w = 0.4$ rad.s^{-1}.

The influence of the lock-in phenomenon on the kite performance is investigated through the kite efficiency and the kite wind loading in Figs. 11.4 and 11.5. As a function of the tether length, the wind loading and the kite efficiency are plotted in solid lines in terms of amplitude and mean value respectively in Fig. 11.4 and in Fig. 11.5. For comparison purpose, these quantities without the effect of a regular wave are plotted in dashed lines.

Globally, the amplitude of the wind loading amplitude increases with the tether length in case of calm water (Fig. 11.4). The kite lock-in phenomenon decreases the kite wind loading amplitude. The minimum of wind loading amplitude is obtained for $L_t = 660$ m. Compared to the calm water case, with $L_t = 660$ m, the wind loading amplitude is decreased by 16%. Compared to the configuration with $L_t = 665$ m, the wind loading amplitude is decreased by 35% with $L_t = 660$ m.

In calm water, the kite efficiency remains almost constant with the tether length. The kite lock-in phenomenon decreases the kite efficiency amplitude (Fig. 11.4). The minimum of kite efficiency amplitude is obtained for $L_t = 660$ m. Compared to the calm water case, with $L_t = 660$ m, the kite efficiency amplitude is decreased by 14%. Compared to the configuration with $L_t = 665$ m, the kite efficiency is decreased by 26% with $L_t = 660$ m.

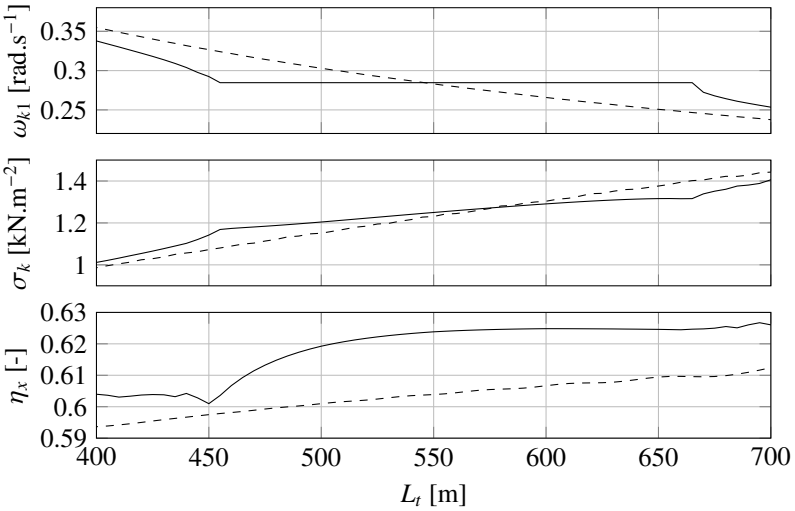

—— 6 dof dynamic approach with wave
- - - 6 dof dynamic approach without wave

Figure 11.5.: With a regular wave in the wind direction, evolution of the first kite roll excitation harmonic frequency ω_{k1}, mean kite wind loading σ_k, mean kite efficiency η_x with different tether lengths and a constant angular amplitude of trajectory. A configuration with wave (——) is compared to a configuration without wave (- - -). Kite configuration: $A_k = 500$ m^2, $A^{(\mathbf{s})} = [110,\ 0,\ -10.6]^T$ m. Sailing condition: $\beta_{tw} = 135°$, $U_{tw} = 12.5$ m.s^{-1}, wave amplitude $A_w = 2.5$ m and wave angular frequency $\omega_w = 0.4$ rad.s^{-1}.

As it can be noticed in Fig. 11.5, the mean kite efficiency, increased with the tether length. This tendency is not modified with the kite lock-in phenomenon. However, the increase of the mean wind loading is less significant within the tether length corresponding to the lock-in. For short tethers, the mean wind loading is increased by 7 % compared to the calm water case for $L_t = 455$ m. For long tethers, the mean wind loading is decreased by 8 % compared to the calm water case for $L_t = 660$ m.

The kite efficiency increases slightly with the tether length, 3% between $L_t = 400$ m and $L_t = 700$ with the calm water case (Fig. 11.5). The presence of waves increases the kite efficiency. Within the lock-in phenomenon, the increase of the kite efficiency increases significantly. Then, for longer tether than $L_t = 575$ m, the kite efficiency remains almost constant. For $L_t = 660$ m, the kite efficiency is increased by 4%.

Frequencies of the kite harmonics have been shifted with the tether length and keeping a constant angular amplitude of trajectory. This phenomenon could have been investigated by varying the angular amplitude of the trajectory and keeping a constant tether length. Within the range of the tether lengths concerned by the lock-in phenomenon, a long tether is a benefit. Indeed, for the case studied, the configuration $L_t = 660$ m is the best. The kite efficiency is maximum (Fig. 11.5), the kite wind loading amplitude and the kite efficiency amplitude are minimum (Fig. 11.4). The mean kite wind loading is smaller than in the calm water case. For the global kite performance this configuration seems to be favorable from a fatigue and a profit point of view. This configuration is also favorable for the ship. Indeed, the heel angle amplitude and the drift angle amplitude are decreased.

11.5. Conclusion

In this chapter, 6 dof free sailing simulations have been performed. In a first part, the influence of the true wind angle has been investigated in calm water and with a regular wave with the KCS container ship. The dynamic model with the monolithic coupling was first compared to the static approach in case of a constant kite towing force. The mean results are consistent, the relative margin between the two approaches being lower than 10^{-5}.

In calm water, the mean value of the kite efficiency, drift angle, rudder angle and heel angle obtained with the 6 dof dynamic approach are very close to those obtained with the static approach. Consequently, with the aim to obtain the mean performance of a ship towed by kite in calm water, a static approach is accurate enough since the interaction between the kite and the ship is small. In the presence of a wave, mean performances are slightly affected, but not significantly. On the contrary, the amplitudes of the performances are modified by the wave, especially for the ship heading and the rudder angle. The perturbations on the ship due to the wave dominate the perturbations due to the kite. Consequently, the ship safety is not significantly affected by the kite.

In a second part, the kite lock-in phenomenon highlighted in Chap. 9 has been investigated on broad reach course. The phenomenon still occurs leaving free the 6 dof of the ship. When this phenomenon occurs kite harmonic frequencies are attracted towards the wave frequency of encounter. When harmonic frequencies are increased to the wave frequency of encounter (compared to the calm water case), the kite lock-in phenomenon is a benefit for the ship and the kite. The heel angle amplitude can be smaller compared to the case without kite. The kite wind loading may be increased up to 34% and the kite efficiency may be increased up to 4% compared to the calm water case, within the investigated case.

Nevertheless, even if the kite lock-in phenomenon is verified in case of 6 dof free sailing, this phenomenon may be purely theoretical. This phenomenon has not been reported somewhere else and the existence of this phenomenon is entirely based on the presented kite and ship modeling. Consequently, a next step would be to verify the existence of this phenomenon by taking into account more physics into the tether and kite modeling.

Part V.

General conclusion and perspectives

12. Conclusion

The aim of this study was to investigate the operability of a ship towed by a kite through theoretical studies of the dynamic motions of the system. The first part of the thesis was dedicated to the kite modeling. The second part was dedicated to the ship modeling. The third part was dedicated to the coupling between the kite and ship modelings.

The zero mass kite model was presented. This model neglects the mass of the kite and assumes a straight and inelastic tether. Thanks to the analytical formulation of the zero mass kite model, an upper bound of the kite towing has been identified. A comparison of the kite model with full scale on-shore experiments was performed with a fixed tether attachment point. The comparison has shown that the kite velocity amplitude and the kite towing force over an eight pattern trajectory are underestimated with a constant lift to drag ratio angle and lift coefficient. Consequently, a correction of the lift to drag ratio angle and lift coefficient was proposed as a function of the kite velocity turning rate and this improvement provided satisfactory results. A more comprehensive validation should be performed on several kite trajectories and with a moving tether attachment point. Nevertheless, the proposed correction is conservative compared to a classical zero mass kite model with constant coefficients. Indeed, ship motions amplitude are in a first approximation proportional to the excitation amplitude.

The assumption of straight tether is a strong assumption. Therefore, the validity of this hypothesis was investigated with a quasi-analytical tether model based on the catenary. The catenary model assumes a constant tether load per unit length. In case of a static kite flight, the kite balance equation was solved numerically. Since the tether load varies with the altitude due to the wind gradient, an equivalent tether load was proposed. A comparison with a finite element method was performed to assess the effect of the varying tether aerodynamic load. Comparisons were performed for different wind directions, wind speeds and different tether mass per unit length. Relatives differences between the finite element method and the presented model remains within a range of $\pm$ 1.2° for tension direction and remains within a range of $\pm$ 2% for tension magnitude. Then, the influence of the tether is investigated on a 320 m^2 kite. Results show that the tether effects could be important at extreme azimuth angles. For high wind speed the effect of the tether on the difference in tension between the tether attachment point and the kite are not significant. Consequently, the straight tether assumption used in the zero mass model should be reasonable at high wind speeds greater than 10 $m.s^{-1}$for the static flight case. In a case of dynamic kite flight the straight tether assumption is relevant for reference wind speed greater than 2 $m.s^{-1}$.

According to the quasi-analytical tether model, a closed-form formula was developed in order to estimate the low wind limit to operate the kite in a static flight mode. Since the kite launching step begins by quasi-static flight at zero azimuth angle, the developed formula provides a practical and useful criterion. The development of th is criterion is based on the assumption that the aerodynamic load on the tether is negligible at low wind. The validity of this mathematical development is limited to heavy tether with small diameter. For instance, for a tether made of dyneema® the tether aerodynamic load is less than 20% of the gravity load for line mass per unit length greater than 25 $g.m^{-1}$ which corresponds to 7 mm in diameter for instance. According to this criterion, for a ship sailing at downwind, the launching step of kite can be impossible whereas the dynamic kite flight provides significant fuel savings. Therefore, first the ship should maneuver to increase the relative wind speed to launch the kite and start by a dynamic kite flight mode and then go back to downwind condition, following the planned route .

To perform a dynamic coupling of the zero mass kite model with a ship modeling, a time domain approach is required. Consequently, a time domain seakeeping model was developed. The developed ship model is based on linearized equations for small amplitude ship motions. The hydrodynamic problem was solved under the assumption of a potential flow into the frequency domain, the STF strip theory. Then, using the impulse response function of the ship, the ship modeling was transformed into the time domain. This method requires the computation of convolution products, which can be time consuming. To speed up the computation, convolution products are evaluated with the integration of state space models. A state space model identification is required. Identification methods were developed in the literature but only in case of zero ship forward speed. Consequently, the method was slightly modified to fit with the forward speed requirements. The method is compared to EFD data of the DTMB, a free surface combatant vessel, sailing in regular head wave. Results show that the transformation of the problem into the time domain is consistent and that the STF strip theory provides a good assessment of ship motions in terms of heave and pitch.

The time domain seakeeping model is suitable for vertical ship motions, however the horizontal ship motions are not well predicted. Indeed, the viscous effects are significant on the horizontal ship motions. Thus, a mixed approach was developed. Horizontal ship motions are modeled with a maneuvering model. The maneuvering model considered is based on a parametric MMG model. Hull, rudder, propeller and hydrodynamic interactions are represented by individual sub-models. The mixed approach was then compared to EFD data of free running turning circles and zig-zag tests with a container ship KCS. Comparisons gave satisfactory results.

Prior to perform a dynamic coupling between the kite model and the ship model, the mean equilibrium of a ship towed by kite was investigated considering the mean kite towing force. This approach is fast to compute and enables the study of a wide range of sailing configurations. The study was performed on the KCS. Windage effects were compared to kite towing effects on the mean equilibrium. The windage is not negligible for the lateral and yaw equilibrium. The effect of the longitudinal tether attachment point is more pronounced on the

ship drift and on the rudder angle than on the kite power saving ratio and the heel angle. To limit the mean rudder angle, the tether should be attached to the bow. In terms of mean rudder angle, drift angle and heel angle, the most critical sailing conditions are obtained on beam reach courses. The maximum of kite power saving ratio is obtained on broad reach courses. The maximum of kite efficiency is obtained on downwind courses if the true wind speed is faster than the ship speed, otherwise the maximum of kite efficiency is obtained at lower true angle. Finally, to minimize CO_2 emissions, the kite power saving ratio should be maximized whereas to maximize the profit, the kite efficiency has to be maximized.

Focusing on vertical ship motions (heave roll and pitch), a first study of the interactions between the kite and the ship was performed. The analysis was achieved in terms of spectrum of ship motion and kite excitation. The kite excitation is composed of the several harmonics ω_{ki} where i is a positive integer. The first harmonic is the most powerful one. Segregated and monolithic couplings were performed. The segregated approach consists in applying a predefined kite force time serie to the ship. The two coupling approaches were compared. In calm water, no significant difference between the two coupling approaches was found. Nevertheless, the segregated coupling is conservative compared to the monolithic approach. In case of a regular wave, ship motions are dominated by the wave excitation. Consequently, the ship motions spectrum is mainly composed of one harmonic at the wave frequency. With the monolithic coupling approach a sub-harmonic network appears with a fundamental frequency $\omega_{k1}^{'}$ corresponding to $\omega_{k1}^{'} = \min_i |\omega_w - \omega_{ki}|$. In case of a small $\omega_{k1}^{'}$, a strong interaction phenomenon was highlighted. The principal kite harmonic network is shifted towards the wave frequency. This phenomenon has been called kite lock-in. Only the monolithic coupling approach catches this phenomenon. Consequently, only the monolithic coupling was considered in the rest of the study.

To perform 6 degrees of freedom simulations, the course keeping stability of the ship was studied. According to an analytical linear criterion developed for the course keeping stability of ship towed by a tug boat, it was shown that the KCS container ship is not stable in that case. However, non-linear terms, the windage and the oscillatory towing force are not taken into account by this criterion. Consequently, the course keeping stability of the KCS towed by a kite of 500 m^2 was studied. Results have shown that the only stable configuration is at dead downwind with a longitudinal tether attachment position at the bow, otherwise the system is unstable. However, for theoretical interests longitudinal positions beyond the bow were tested. The ship is stable, when the tether attachment position is far enough above the bow which is unrealistic. Intermediate longitudinal position showed that a fishtailing phenomenon can appear. Nevertheless, the stable configuration is not realistic. Consequently, a design of a rudder autopilot based on a PID controller was investigated. The rudder autopilot is perturbed by the kite oscillatory excitation. A manner to decrease this effect is to filter the derivative term of the error with a low pass. This classical control method decreases the response time and the rudder angle amplitude. In calm water, the perturbations imposed by the kite are not significant. However, in case of a regular wave, the rudder angle amplitude increases drastically. The wave perturbation dominates the kite perturbation. Consequently, no modification of the existing rudder autopilot should be required.

In the final chapter, 6 dof simulations in calm water and regular waves were performed for different true wind angles. The mean equilibrium obtained with the dynamic coupling is not significantly modified compared to the static approach for both calm water and regular wave cases. Since only the first order wave loads have been taken into account, the average wave load is zero. The second order mean wave drift load may modify the mean equilibrium of the system. However, the static approach appears to be an accurate enough method for the mean effect of a kite regarding economic and fuel saving studies. Amplitudes of the rudder angle and heel angle are maximum on a broad reach course whereas the maximum of drift angle is maximum on a beam reach course. The apparition of the kite lock-in phenomenon was verified in case of a 6 dof simulations. An evolution of the frequencies of the kite harmonic network were performed with different tether lengths and keeping a constant angular trajectory size. On a broad reach course the kite lock-in phenomenon was noticed over a tether length range of 200 m. This phenomenon is a benefit for both kite and ship when kite harmonic frequencies are increased towards wave frequency. The best configuration is just at the boundary of the phenomenon. Indeed, the kite wind loading and the kite efficiency are increased respectively by 34% and 4%, and the roll amplitude of the ship is decreased by 23%. The kite lock-in phenomenon suggests that the tether and/or the kite trajectory should be chosen in relation to the sea state. However, this phenomenon has only been noticed with the presented modeling approach.

13. Perspectives

When it was possible, the modeling has been compared to experimental data or to more refined model, however, the validation of each sub-model can be enhanced.

The zero mass kite model should be compared to a larger number of kite flight cases to assess the validity of the linear modification of the kite aerodynamic specs. This investigation should be investigated on several kite shapes, at different scales and for different positions of the eight shaped trajectory.

A static analysis of the tether influence on the kite flight was conducted with catenary model. The effect of the tether acceleration was neglected. Since both tether attachment point and kite are subjected to large displacements, the assumption of straight and inelastic tether might be the strongest and most questionable assumption of the study. The existence of the kite lock-in phenomenon should be verified with a more sophisticated kite model.

Only the first order of wave force has been taken into account, therefore the mean equilibrium is not perturbed by the effect of a wave. At least the mean second order wave drift load should be taken into account. Moreover, a non-linear model should be considered to improve the roll prediction.

No validation of the whole ship towed by kite system modeling was performed. Using the real-scale experimental database acquired by Behrel et al. (2017), a validation of the ship towed by kite system modeling could be performed. However, some data are missing such as the sea state and the current. Therefore an exhaustive analysis of the comparison could be challenging. A promising alternative could be to use the so-called Hardware In the Loop (HIL) simulation method (Giberti and Ferrari, 2015; Johansen et al., 2005). This method is useful to validate complex systems. For the ship towed by kite application, two strategies could be employed:

- to simulate in real time and impose to the tether attachment the ship motions during kite flight experiments.
- to simulate in real time and impose to a ship sailing in a basin the kite towing force.

Nevertheless, the design of such experimental set-ups could also be challenging.

Moreover, the presented study shows that downwind sailings are favorable to the use of kite. In view of container ship speeds and of kite operating wind speeds, the sea state

should be significant. With these conditions, the ship might be subjected to a parametric rolling. Therefore, to study this critical ship motion, the instantaneous wetted hull surface should be known to compute the non-linear hydrostatic forces in an accurate manner.

Appendix

A. Onshore and offshore measurement set-up

This annex introduces the experimental set-up for the onshore and offshore measurements performed by Behrel et al. (2017). *The description of the experimental set-up is directly taken from (Behrel et al., 2017).*

The experimental set-up used for this measurement campaign is based on a kite control box with sensors and actuators, and two additional boxes containing batteries and data acquisition and control system. This trio can be deployed onshore, fixing the kite control box into the ground (Fig. A.2), or on board, embedding the system on the boat specifically designed for this purpose (Fig. A.1). The kite used for this study is a Cabrinha Switchblade®, with an area of 5 square meters, usually used by kite surfers for leisure sport. Other kites have been tested on the kiteboat. This kite has four tethers, two on each side of the kite: the first two are called front tethers, and have constant length. The two others, called back tethers, have variable length and are used for control purpose. Various length of tethers were tested during trials, from 25 meters to 80 meters.

Figure A.1.: Picture of the Kitelab, the experimental plateform specificaly designed to carried out measurements on effects and performances of kite propulsion. The 5-meter wind measurement mast is visible on the rear of the boat. The inflatable kite flying over the boat is a 5 m² one. Source: Behrel et al. (2017)

A.1. Main sensors

A.1.1. Forces Measurements

The major sensor of the experimental device is a three dimensional load cell, providing intensity and direction of the force into the front tethers. The load cell is a TR3D-B-1K

built by Michigan Scientific, with a range on each axis of 1,000 pounds (4,448 N), and a safe overload of 300% of the full scale. This product is similar to the one used on a previous study (Behrel et al., 2016), but with an smaller range of measurement suitable for forces generated by a 5 m² kite. This sensor has a non-linearity error specified by manufacturer as being under 0.5% of full scale, and hysteresis and repeatability errors under 0.05% of full scale each. A complete calibration of the measurement chain was not carried out before the trials, and sensibilities provided by manufacturer have been used. However a calibration control set-up is under development, using test machines available at ENSTA Bretagne's laboratory, and the sensitivity and accuracy of the sensor will be compared with manufacturer ones.

For back tethers, due to their variable lengths, another measurement system must be used. This one is based on two simple load cells (Futek LCM200) measuring forces after a return pulley. These load cells have a full scale load of 4,500 N, with a specified non-linearity error under 0.5% of full scale, an hysteresis error under 0.5% of full scale and repeatability error under 0.1% of full scale. Various set-ups for return pulley have been tested, leading to various return angles. These angles were all the time carefully measured to be able to retrieve the real load in tethers.

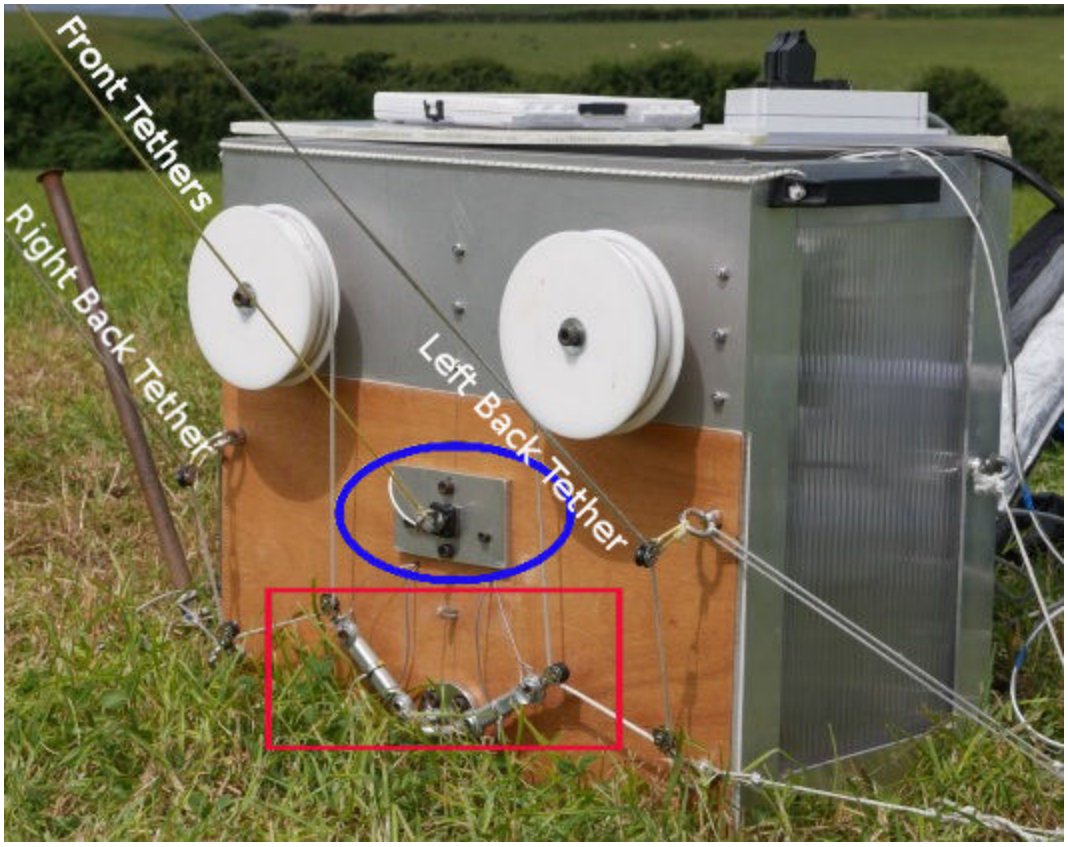

Figure A.2.: Kite control and measurement device deployed on shore. The two winches are visible , as well as the 3D front tether load cell (blue ellipse) and the two 1D back tether load cells (red rectangle). Source: Behrel et al. (2017)

A.1.2. Onshore Wind Measurements

Intensity and direction of the wind at kite altitude are important informations to get, in order to realize a valuable post processing, as it has been shown in previous work (Behrel et al., 2016). However with a kite flying between 10 and 80 meters above the ground, it is difficult to get a wind measurement with a good accuracy at any position of the kite. To deal with this problem, it was decided to use a wind profiler, based on sonic technology (Fig. A.3). This type of device is called SODAR, for SOnic and Detection And Ranging. In our case, the SODAR was able to measure a profile from 13 meters above the ground to 108 meters, with one point every 5 meters, and averaging data over a 5-minute-period. For each point of measurement, the direction, the intensity and the vertical component were available, but also the standard deviations for each data. It was particularly important to have a wind profiler for these onshore measurements because of the topographic configuration of the field where the trials were carried out. Indeed, it has been observed some variations of the

intensity and/or direction and/or vertical intensity of the wind along the altitude that could not have been easy to model.

Figure A.3.: The SODAR (SOnic and Detection And Ranging) device used fo the onshore kite measurements. Source: Behrel et al. (2017)

To catch higher rate wind variation, an ultrasonic three dimensional anemometer METEK USA-1 was also used. This anemometer was put in place on a mast at 8 meter above the ground, and had an acquisition rate of 20 hertz.

A.2. Kite control system

A.2.1. Control And Data Acquisition System

All the control system and the data acquisition system is driven by a National Instruments compactRIO motherboard, with additionally I/O modules, ensuring that all the recorded data are sampled synchronously. These modules provides analog and digital inputs, serial ports, and full bridge analog inputs for load cells data acquisition. The whole system is completely programmed using the National Instruments software LabVIEW.

The kite can be steered by applying a difference between the back tether lengths. For this purpose, each back tether is attached to an electric winch, and the winches are controlled in position, thanks to optical encoders with an accuracy of 4096 counts per revolution. Thus, for a given differential set-point δ, one winch shall shift by a value $\delta/2$ and the other winch by a value of $-\delta/2$. Each winch has a power of 800 watt, and are able to roll in or roll out tethers at a speed of 0.7 $m.s^{-1}$. The maximum differential speed is then 1.4 $m.s^{-1}$. A power card interfaces the compactRIO and the winches.

A.2.2. Dynamic Flight Automatic Pilot

The winches can be controlled by 2 joysticks for a manual control of the kite, but an automatic pilot can be also engaged, enabling the steering of 8-pattern trajectories with good reproducibility. This autopilot is mainly based on Fagiano work (Fagiano et al., 2014). To get a proper functioning of the autopilot, the kite position in the wind window has to be known at any time to ensure a feedback to the controller. More specifically, motions of the kite has to be known, because the kite is undergoing dynamic flight. That means that the kite position data shall be not too noisy to allow the computation of the first order time derivative process leading to the velocity. In our case, the kite position is obtained thanks to the 3D load cell, assuming that front tethers are straight, their lengths having been carefully measured. To reduce noise level on position data, load cell acquisition is done at 10 kHz, and then the signal is averaged at a frequency of 200 Hz. After the derivative process, the derivative signal is filtered with a 40 ms running average filter.

A.3. Kiteboat specific sensors

In addition to the experimental setup already described in the previous part, sensors are added to get the specific measurements associated with a moving platform, namely the KiteLab boat at sea.

A.3.1. Inertial Measurement Unit (IMU)

An IMU combined with a two GPS receivers provides boat orientations and velocity. This sensor is VectorNav VN-300 Rugged. Thanks to the MEMs inertial sensors, associated to advanced Kalman filtering algorithms provided by manufacturer, the heel and pitch orientation can be obtained. Data from MEMs (angular rate and acceleration) are also recorded at any time. The two GPS receivers, in addition to provide position and velocity of the boat, give also an accurate heading measurement, apart from any magnetic disturbance. With this accurate measurement of heading, it becomes possible to estimate the drift of the boat, relatively to the ground, comparing heading of the boat and course over ground obtained from

GPS receivers. The drift relatively to the sea water can be estimated taking into account currents. According to the specification sheet, the orientation static accuracies are under 0.5° RMS, and under 0.3° RMS in dynamic case. Velocity accuracy is 0.05 $m.s^{-1}$. It is planned for future work to benchmark the VN-300 with higher IMU grade.

A.3.2. Rudder Angle

A fully sealed linear potentiometer is set up into the steering system to get the rudder angle. This sensor was calibrated in the laboratory and the accuracy is lower than 0.5°.

A.3.3. Onboard Wind Measurements

As it has been recalled in part 2.1.2, wind estimation at kite altitude is one of the most important data required to get proper post processed data. However during sea trials, it is not possible to embedded the SODAR on board, due to insufficient room and technological issues (the SODAR needs to be set up in perfect horizontal position for a accurate measurements). Moreover, due to operational constraints, it was not relevant to set up a wind measurement mast higher than 5m. However wind gradient above the sea surface is less disturbed than onshore, and can be reasonably estimated using statistical formulas. To check the evolution of wind gradient, three sonic anemometers are fixed on the mast at three different elevations. This assembly provides also a redundancy of wind measurement. The three sonic anemometer are manufactured by Gill, but are different models. The higher one, with a measurement altitude of 5.5m above the sea level is a WindMaster, a three dimensional anemometer, fixed on the head of the mast. The second one is a 2D anemometer WindSonic placed at 4.2m above the sea level and deported from the mast by 0.6m. The last anemometer is a MaxiMet 500. This is also a 2D anemometer, and combines wind measurements with pressure, temperature and relative humidity measurements. This sensor is also fitted with a GPS sensor and a compass, and can provide the velocity of the wind into axis system attached to the earth, corrected from the boat velocity. This measurement is redundant when the measurement mast is set up on the kiteboat. The MaxiMet is located at 3.0m above sea level, and is also deported from the mast by 0.6m (see Fig. 1).

The misalignment angles of the sensors with respect to the axis of the mast have been measured in laboratory, as well as the misalignment angle of the mast with respect to the longitudinal boat axis. Data werer corrected accordingly during post processing.

B. Kite modelling

B.1. Zero-mass kite model: time step convergence

The influence of the time step on the mean simulated tether tension at A and the mean simulated kite velocity is investigated according to the following relative margins:

$$\begin{cases} \delta U_k &= \frac{\overline{U}_k^{(exp)} - \overline{U}_k^{(sim)}}{\overline{U}_k^{(exp)}} \\ \delta T_a &= \frac{\overline{T}_a^{(exp)} - \overline{T}_a^{(sim)}}{\overline{T}_a^{(exp)}} \end{cases} \tag{B.1}$$

The superscripts (sim) and (exp) denote respectively the results from simulation with the zero-mass model and the experimental results. Figure B.1 shows the evolution of the relative margins for differents sampling frequency.

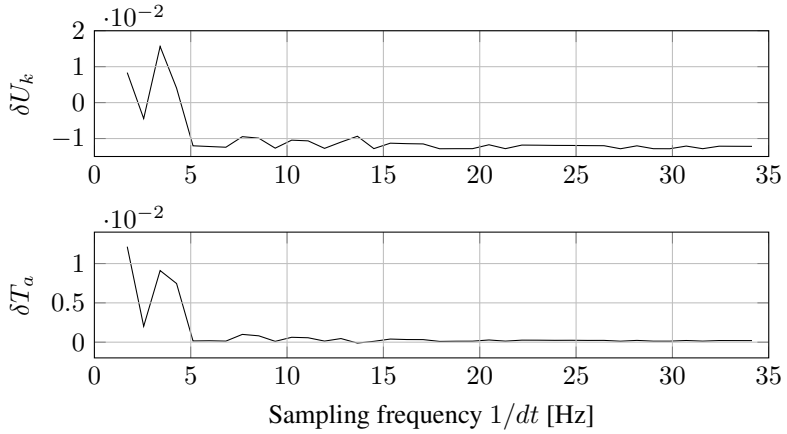

Figure B.1.: Evolution of the relative tether tension margin and relative kite velocity margin for different sampling frequency

It can be noticed that above 5 Hz, the relative margins are almost constant. For lower sampling frequency, the relative margins increase drastically. Finally according to these results a sampling frequency of 10 Hz is chosen.

B.2. Static analysis

B.2.1. Finite element method: Young modulus convergence

The aim of this convergence is to model a inelastic tether. An enoughly high tether Young modulus must be used. The air density is 1.225 kg.m^{-3}. The true wind speed is $U_{ref} = 10$ m.s^{-1} at the altitude of reference, z_{ref}, 10 m above the sea. The true wind velocity follows a wind gradient according to the power low $U_{tw} = U_{ref}\left(\frac{z}{z_{ref}}\right)^{1/7}$. The tether length is 300 m, the tether diameter is 0.03 m. The tether attachment point is at $[0, 0, 0]^T$, the kite position is set at $[78.89,\ 0,\ -289.31]^T$ m with respect to the relative wind frame $\mathbf{rw}$. The tether is supposed to be in Dyneema SK78 and to have a Young modulus $E_{sk78} = 102$ GPa.

Here, the Young modulus convergence consists in increasing the Young modulus by a coefficient 10^{λ}. In figure B.2, the relative difference tether tension for each components vertical and horizontal at the tether attachment point on the deck and at the kite is plotted for different value of λ from 1 to 5. The relative difference is defined as follows:

$$\Delta T_{\lambda} = \frac{T(\lambda) - T(\lambda - 1)}{T(\lambda - 1)} \tag{B.2}$$

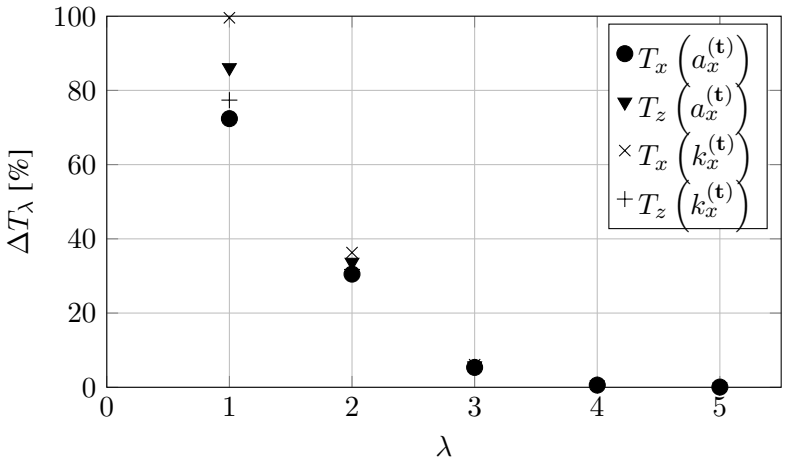

Figure B.2.: Young modulus convergence

Based on these convergence results, the Young modulus value $10^5 E_{sk78}$ leads to a convergence criteria less than 0.01 %. Consequentely, a Young Modulus of $10^5 E_{sk78}$ is then used.

B.2.2. Finite element method mesh convergence

Using the tether Young modulus $10^5 E_{sk78}$ in Annex B.2.1 a mesh convergence is performed. Here, the selected case leads to an important tether sag. The air density is 1.225 kg.m^{-3}. The true wind speed is $U_{ref} = 5$ m.s^{-1} at the altitude of reference, z_{ref}, 10 m above the sea. The true wind velocity follows a wind gradient according to the power low $U_{tw} = U_{ref}\left(\frac{z}{z_{ref}}\right)^{1/7}$. The tether length is 300 m, the tether diameter is 0.06 m. The tether attachment point is at $[0, 0, 0]^T$, the kite position is set at $[108.91,\ 232.83,\ 131.94]^T$ m. The tether is discretized in N_i linear bar (or truss in Abaqus) elements of equal length. In Figure B.3 the influence of the number of element $N_i \in \{5, 10, 20, 30, 40\}$ is investigated throught the following relative difference:

$$\Delta T_N = \frac{T\left(N_i\right) - T\left(N_{i-1}\right)}{T\left(N_{i-1}\right)} \tag{B.3}$$

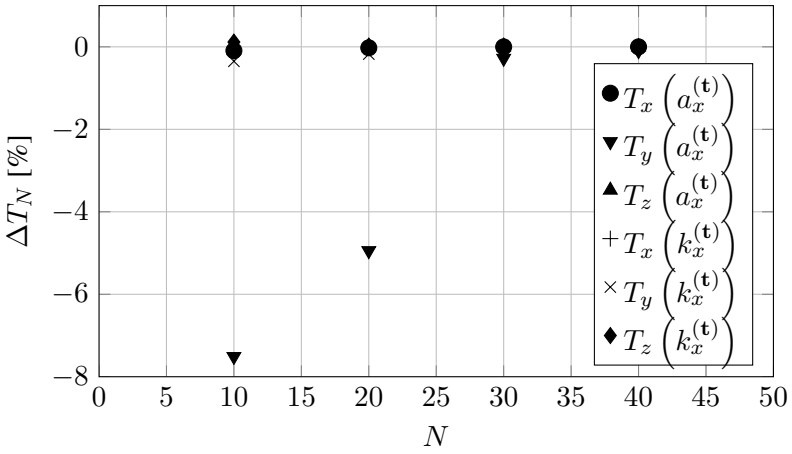

Figure B.3.: Tether mesh convergence; relative difference such as defined in Eq. versus the number of bar element

With 40 elements the relative difference is less than 0.01%.

B.2.3. Diameter and mass per unit of length of Dyneema® SK78

Figure B.4 shows the square of the diameter for different mass per unit of length. The solid line represents the linear regression estimating the relationship between the square of the diameter and the mass per unit of length.

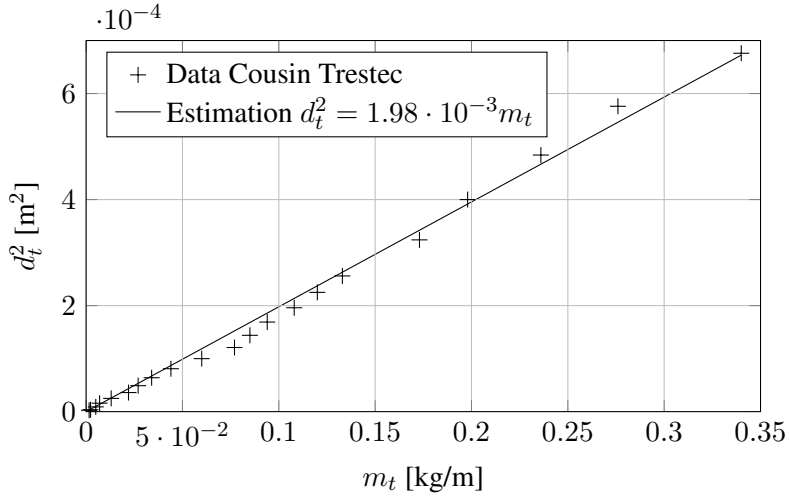

Figure B.4.: The square of the diameter versus mass per unit of length for a tether made of Dyneema® SK78; the data are provided by the manufacturer Cousin Trestec.

B.3. Low wind limit of kite operability

B.3.1. Ratio between the kite mass and the kite area

C. Ship motions

C.1. Transformation of the h to the s frame

The ship velocity at the point H with respect to the $\mathbf{c}$ frame is obtained as follows:

$$\begin{aligned}\mathcal{V}^{(\mathbf{s})}_{H\in\mathbf{s}/\mathbf{c}} &= \begin{bmatrix} u_s \\ v_s \\ w_s \end{bmatrix} - \underline{O_sH} \times \begin{bmatrix} p_s \\ q_s \\ r_s \end{bmatrix} \\ &= \begin{bmatrix} u_s + h_z q_s \\ v_s + h_x r_s - h_z p_s \\ w_s - h_x q_s \end{bmatrix} \end{aligned} \tag{C.1}$$

Thanks to the transformation matrix $\underline{\underline{T}}^{\mathbf{h}}_{\mathbf{s}}$ assuming small oscillations $\mathcal{V}^{(\mathbf{h})}_{H\in\mathbf{s}/\mathbf{c}}$ is:

$$\mathcal{V}^{(\mathbf{h})}_{H\in\mathbf{s}/\mathbf{c}} = \begin{bmatrix} 1 & -\xi_6 & \xi_5 \\ \xi_6 & 1 & -\xi_4 \\ -\xi_5 & \xi_4 & 1 \end{bmatrix} \cdot \mathcal{V}^{(\mathbf{b})}_{H\in\mathbf{s}/\mathbf{c}}, \tag{C.2}$$

and,

$$\begin{bmatrix} \dot{\xi}_4 \\ \dot{\xi}_5 \\ \dot{\xi}_6 \end{bmatrix} = \begin{bmatrix} p_s \\ q_s \\ r_s \end{bmatrix} \tag{C.3}$$

Decoupling the longitudinal modes (surge, heave and pitch) and lateral modes (sway, roll and yaw) and keeping only first order term $\mathcal{V}^{(\mathbf{h})}_{H\in\mathbf{s}/\mathbf{c}}$ can be simplified as follows:

$$\mathcal{V}^{(\mathbf{h})}_{H\in\mathbf{s}/\mathbf{c}} = \begin{bmatrix} u_s + h_z q_s \\ v_s + h_x r_s - h_z p_s + \xi_6 u_s \\ w_s - h_x q_s - \xi_5 u_s \end{bmatrix} \tag{C.4}$$

Moreover, the $\mathbf{h}$ frame is translating at a constant speed U_h with respect to the $\mathbf{c}$ frame. Consequently, $\mathcal{V}^{(\mathbf{h})}_{H\in\mathbf{s}/\mathbf{h}} = \begin{bmatrix} \dot{\xi}_1, & \dot{\xi}_2, & \dot{\xi}_3 \end{bmatrix}^T$ can be simplified as follows:

$$\begin{bmatrix}\dot{\xi}_1\\ \dot{\xi}_2\\ \dot{\xi}_3\end{bmatrix} = \begin{bmatrix}u_s - U_h + h_z q_s\\ v_s + h_x r_s - h_z p_s + \xi_6 U_h\\ w_s - h_x q_s - \xi_5 U_h\end{bmatrix} \tag{C.5}$$

and its time derivatives,

$$\begin{bmatrix}\ddot{\xi}_1\\ \ddot{\xi}_2\\ \ddot{\xi}_3\end{bmatrix} = \begin{bmatrix}\dot{u}_s + h_z \dot{q}_s\\ \dot{v}_s + h_x \dot{r}_s - h_z \dot{p}_s + r_s U_h\\ w_s - h_x \dot{q}_s - q_s U_h\end{bmatrix} \tag{C.6}$$

Assuming sinusoidal motions at the pulsation ω:

$$\begin{bmatrix}\dot{\xi}_1\\ \dot{\xi}_2\\ \dot{\xi}_3\end{bmatrix} = \begin{bmatrix}u_s - U_h + h_z q_s\\ v_s + h_x r_s - h_z p_s - \frac{U_h}{\omega^2}\dot{p}_s\\ w_s - h_x q_s + \frac{U_h}{\omega^2}\dot{q}_s\end{bmatrix} \tag{C.7}$$

Consequently,

$$\begin{cases}\underline{\dot{\xi}} = & \underline{\underline{J}}\delta\underline{V}_s - \frac{U_h}{\omega_e^2}\underline{\underline{L}}\delta\underline{\dot{V}}_s\\ \underline{\ddot{\xi}} = & \underline{\underline{J}}\delta\underline{\dot{V}}_s + U_h\underline{\underline{L}}\delta\underline{V}_s\end{cases}, \tag{C.8}$$

where,

$$\underline{\underline{J}} = \begin{bmatrix}1 & 0 & 0 & 0 & h_z & 0\\ 0 & 1 & 0 & -h_z & 0 & h_x\\ 0 & 0 & 1 & 0 & -h_x & 0\\ 0 & 0 & 0 & 1 & 0 & 0\\ 0 & 0 & 0 & 0 & 1 & 0\\ 0 & 0 & 0 & 0 & 0 & 1\end{bmatrix}, \tag{C.9}$$

and,

$$\underline{\underline{L}} = \begin{bmatrix}0 & 0 & 0 & 0 & 0 & 0\\ 0 & 0 & 0 & 0 & 0 & 1\\ 0 & 0 & 0 & 0 & -1 & 0\\ 0 & 0 & 0 & 0 & 0 & 0\\ 0 & 0 & 0 & 0 & 0 & 0\\ 0 & 0 & 0 & 0 & 0 & 0\end{bmatrix} \tag{C.10}$$

C.2. Laplace transform of the retardation function

Let's assume sinusoidal velocities of the form:

$$\begin{cases} \underline{V_s} & = \sin(\omega t)\,\underline{I}_6 \\ \underline{\dot{V}_s} & = \omega\cos(\omega t)\,\underline{I}_6 \end{cases} \tag{C.11}$$

Eq. (6.9) can then be transformed as follows:

$$\begin{aligned} &\left[\underline{\underline{M}}_S + \underline{\underline{\tilde{A}}}\right]\omega\cos(\omega t)\,\underline{I}_6 \\ &\quad + \left[\underline{\underline{\tilde{B}}} + \underline{\underline{D}}\right]\sin(\omega t)\,\underline{I}_6 \\ &+ \int_{-\infty}^{t} \underline{\underline{K}}(t-\tau)\sin(\omega\tau)\,d\tau\underline{I}_6 \\ &\qquad + \underline{\underline{C}}\,\underline{S} = \underline{F} - \underline{\bar{F}} \end{aligned} \tag{C.12}$$

Transforming the variable of integration τ into $\tau' = t-\tau$, the convolution product becomes:

$$\int_{-\infty}^{t} \underline{\underline{K}}(t-\tau)\sin(\omega\tau)\,d\tau = \int_{0}^{\infty} \underline{\underline{K}}\left(\tau'\right)\sin\left[\omega\left(t-\tau'\right)\right]d\tau' \tag{C.13}$$

According to the trigonometrical formula, $\sin\left[\omega\left(t-\tau'\right)\right] = \sin(\omega t)\cos\left(\omega\tau'\right) - \sin\left(\omega\tau'\right)\cos(\omega t)$, Eq. (C.12) becomes:

$$\begin{aligned} &\left\{\left[\underline{\underline{M}}_S + \underline{\underline{\tilde{A}}}\right] - \frac{1}{\omega}\int_{0}^{\infty} \underline{\underline{K}}\left(\tau'\right)\sin\left(\omega\tau'\right)d\tau'\right\}\omega\cos(\omega t)\,\underline{I}_6 \\ &\quad + \left\{\left[\underline{\underline{\tilde{B}}} + \underline{\underline{D}}\right] + \int_{0}^{\infty} \underline{\underline{K}}\left(\tau'\right)\cos\left(\omega\tau'\right)d\tau'\right\}\sin(\omega t)\,\underline{I}_6 \\ &\qquad + \underline{\underline{C}}\,\underline{S} = \underline{F} - \underline{\bar{F}} \end{aligned} \tag{C.14}$$

According to Eq. (6.7) with velocities and accelerations as in Eq. (C.11), Eq. (C.14) must be equivalent to:

$$\left[\underline{\underline{M}}_S + \underline{\underline{A}}\right] \omega \cos(\omega t)\, \underline{I}_6 + \left[\underline{\underline{B}} + \underline{\underline{D}}\right] \sin(\omega t)\, \underline{I}_6 + \underline{\underline{C}}\, \underline{\xi} = \underline{F} - \underline{\bar{F}}, \tag{C.15}$$

consequently, the retardation matrix must respect the following system:

$$\begin{cases} \underline{\underline{A}} & = \underline{\underline{\tilde{A}}} - \frac{1}{\omega} \int_0^\infty \underline{\underline{K}}\left(\tau'\right) \sin\left(\omega\tau'\right) d\tau' \\ \underline{\underline{B}} & = \underline{\underline{\tilde{B}}} + \int_0^\infty \underline{\underline{K}}\left(\tau'\right) \cos\left(\omega\tau'\right) d\tau' \end{cases} \tag{C.16}$$

By definition of the Laplace transform:

$$\begin{aligned} \underline{\underline{K}}(j\omega) &= \int_0^\infty \underline{\underline{K}}(t) \exp(-j\omega t)\, d\tau' \\ &= \int_0^\infty \underline{\underline{K}}(t) \cos(\omega t)\, dt - j \int_0^\infty \underline{\underline{K}}(t) \sin(\omega t)\, dt \end{aligned} \tag{C.17}$$

$$\underline{\underline{K}}(j\omega) = \underline{\underline{B}} - \underline{\underline{\tilde{B}}} + j\omega \left[\underline{\underline{A}} - \underline{\underline{\tilde{A}}}\right] \tag{C.18}$$

C.3. Infinite frequency added mass

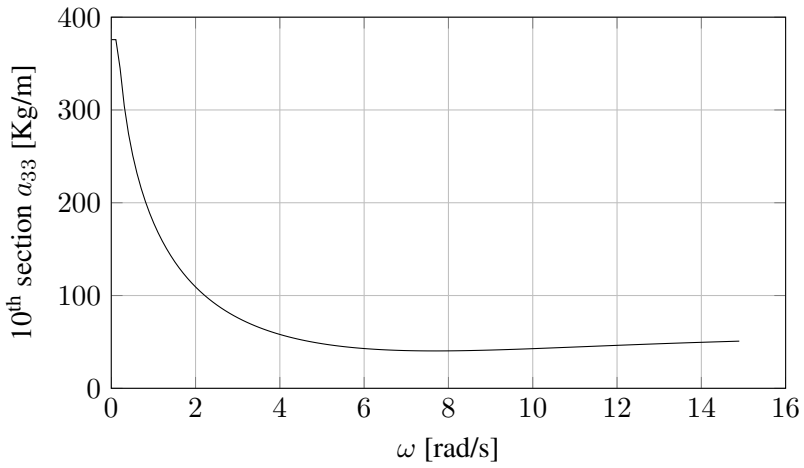

Figure C.1.: Sectional added mass of the 10th section of the DTMB5512 at full scale versus frequency of motion; result obtained with the Shipmo Marin® software.

Figure C.1 shows the added mass of the 10th section for different frequency from 0.01 to 14.9. For high frequency the added mass is quasi constant.

C.4. Illustrating example of the identification of the Laplace transform of the retardation matrix

The identification method of the rational transfer function fitting the retardation matrix is illustrated for the matrix coefficient K_{33} for $U_h = 1.53$ m/s.

C.4.1. First step: time domain identification

The Laplace transform of the retardation function is identified for different order from 2 to 10 in the time domain according to Kung (1978). For instance for the order 4, the identified transfer function is:

$$H_{33} = 10^3 \frac{6.823p^3 + 53.34p^2 + 41.4p}{p^4 + 15.03p^3 + 88.4p^2 + 124.8p + 30.55} \tag{C.19}$$

Figure C.2 shows the impulse response obtained with the data K_{33} and the impulse response of the estimated transfer function of order 4 with the time domain identification method, Eq (C.19). The corresponding results in terms of amplitude and phase of the Laplace transform are plotted in Figs. C.3 and C.4. As it can be observed on Figs. C.3 and C.4, the fit in terms of amplitude and phase amplitude is not very accurate for low frequencies.

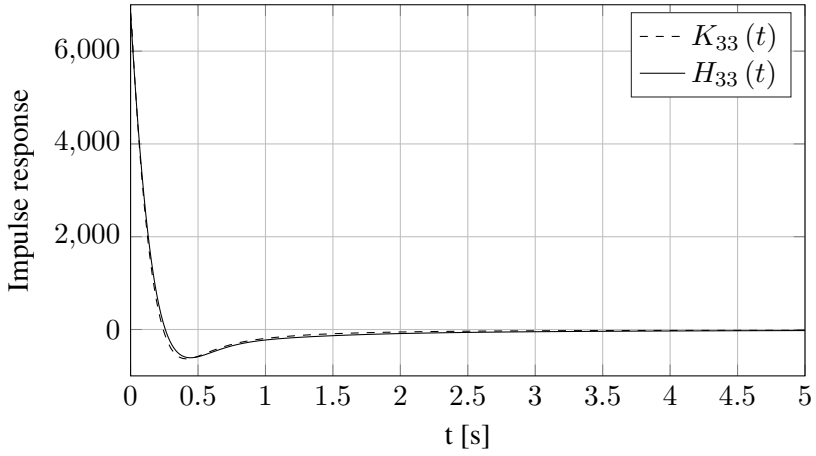

Figure C.2.: Comparison of the impulse response according to the data K_{33} in dashed line compared to the estimated transfert function of order 4 with the time domain method in solid line.

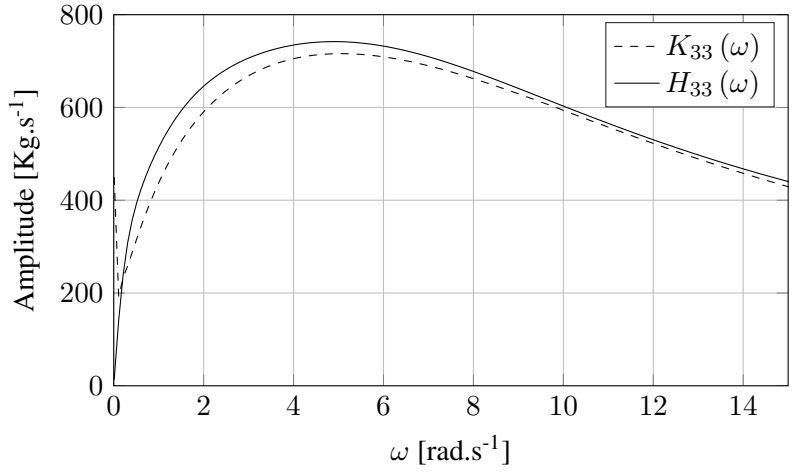

Figure C.3.: Comparison of the amplitude of the tranfert function K_{33} in dashed line with the identified transfert function in solid line H_{33} with the time domain method

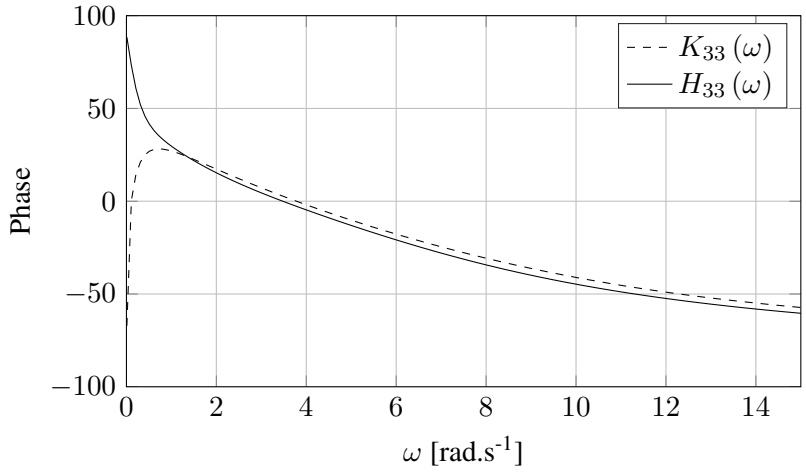

Figure C.4.: Comparison of the phase of the tranfert function K_{33} in dashed line with the identified transfert function in solid line H_{33} with the time domain method

C.4.2. Second step: frequency domain identification

In order to increase the accuracy of the identification method, a frequency domain identification is necessary. The frequency domain method uses as initial solution the best identification of the time domain method, for the considered case Eq. (C.19). Finally, with this step the identified function becomes:

$$H_{33} = \frac{7446p^3 + 6.34 \cdot 10^4 p^2 + 1.045 \cdot 10^5 p + 2.625 \cdot 10^4}{p^4 + 17.43p^3 + 112.2p^2 + 246.4p + 151} \tag{C.20}$$

After this step, the fitting error decreases to 1.87%. Figures C.5, C.6 and C.7 show the improvement.

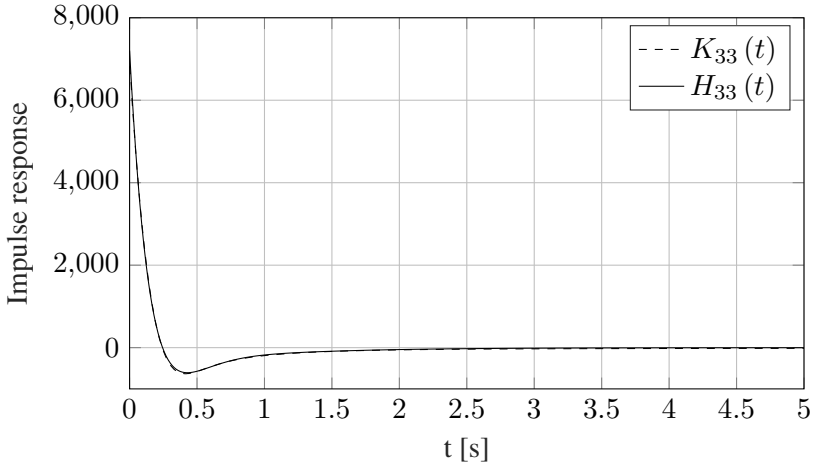

Figure C.5.: Comparison of the impulse response according to the data K_{33} in dashed line compared to the estimated transfert function of order 4 with the frequency domain method in solid line.

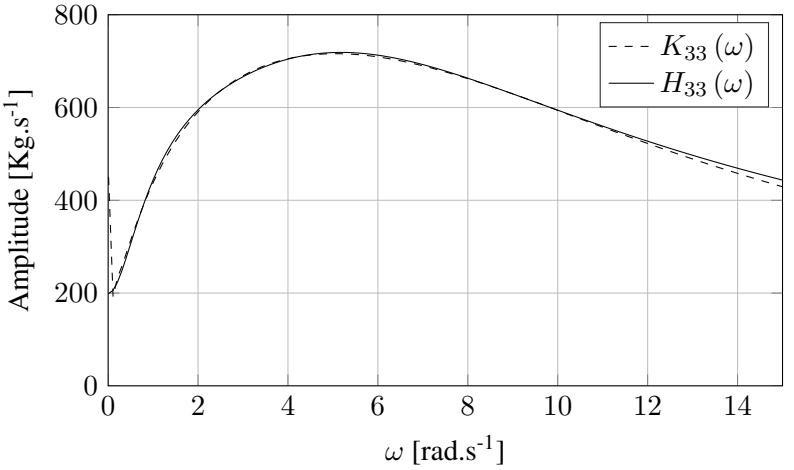

Figure C.6.: Comparison of the amplitude of the tranfert function K_{33} in dashed line with the identified transfert function in solid line H_{33} with the frequency domain method

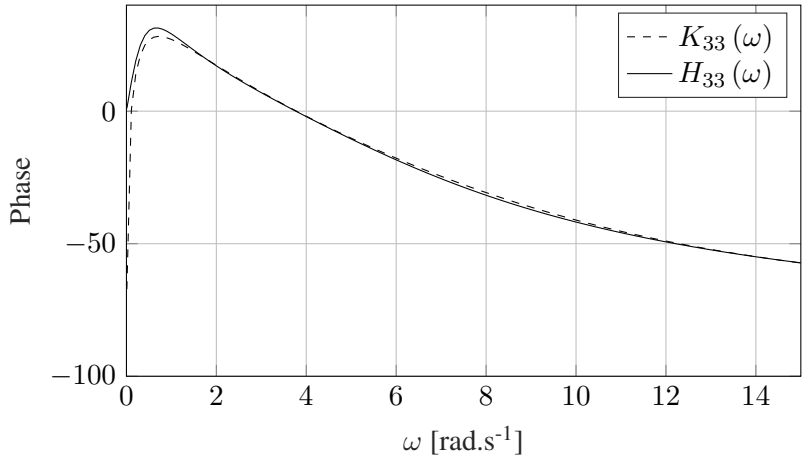

Figure C.7.: Comparison of the phase of the tranfert function K_{33} in dashed line with the identified transfert function in solid line H_{33} with the frequency domain method

C.5. DTMB 5512 transfer functions

C.5.1. Analytical expressions

	$U_s = 0$ m.s^{-1}	$U_s = 7.72$ m.s^{-1}
H_{33}	$\frac{1.567{\cdot}10^7p^3{+}1.686{\cdot}10^7p^2{+}1.965{\cdot}10^6p}{p^4{+}2.341p^3{+}2.051p^2{+}0.5028p{+}0.02567}$	$\frac{1.605{\cdot}10^7p^2{+}1.246{\cdot}10^7p{+}4.636{\cdot}10^5}{p^3{+}2.047p^2{+}1.503p{+}0.2333}$
H_{35}	$\frac{2.358{\cdot}10^8p^2{+}5.073{\cdot}10^8p}{p^3{+}2.893p^2{+}1.244p{+}0.0974}$	$\frac{2.496{\cdot}10^8p{+}1.28{\cdot}10^4}{p^2{+}2.498p{+}9.835{\cdot}10^{-5}}$
H_{55}	$\frac{2.567{\cdot}10^{10}p^3{+}1.047{\cdot}10^{10}p^2{+}2.411{\cdot}10^8p}{p^4{+}2.433p^3{+}1.414p^2{+}0.183p{+}9.855e{-}06}$	$\frac{2.619{\cdot}10^{10}p^3{+}1.627{\cdot}10^{10}p^2{+}2.283{\cdot}10^9p{+}8.57{\cdot}10^7}{p^4{+}2.524p^3{+}1.704p^2{+}0.3333p{+}0.01713}$
H_{53}	$\frac{2.358{\cdot}10^8p^2{+}5.073{\cdot}10^7p}{p^3{+}2.893p^2{+}1.244p{+}0.0974}$	$\frac{2.469{\cdot}10^8p^2{-}1.046{\cdot}10^8p{-}1.843{\cdot}10^7}{p^3{+}2.385p^2{+}0.8536p{+}0.04549}$
H_{44}	$\frac{7.103{\cdot}10^7p^4{+}1.536{\cdot}10^8p^3{+}1.715{\cdot}10^8p^2{+}8.002{\cdot}10^7p}{p^5{+}4.771p^4{+}8.429p^3{+}10.43p2{+}6.139p{+}2.898}$	$\frac{7.214{\cdot}10^7p^3{+}7.685{\cdot}10^7p^2{+}3.174{\cdot}10^7p{+}2.671{\cdot}10^6}{p^4{+}3.168p^3{+}3.669p^2{+}2.486p{+}0.8639}$

Table C.1.: Expressions of the identified analytical transfer function for the DTMB 5512 at full scale and at $U_s = 0$ m.s^{-1} and $U_s = 7.72$ m.s^{-1}

C.5.2. Heave

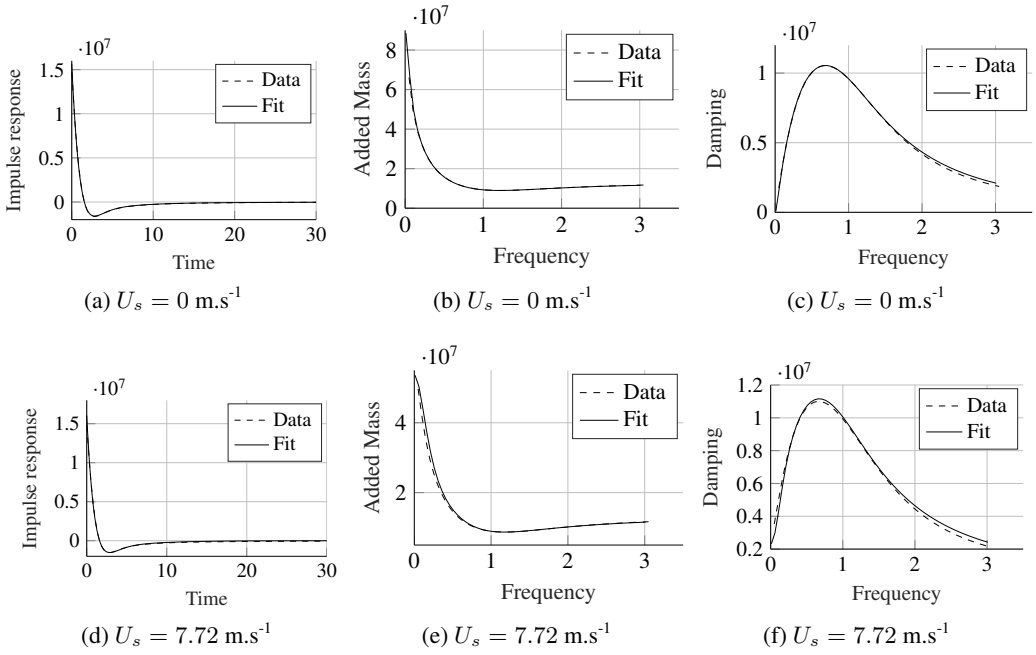

(a) $U_s = 0$ m.s^{-1} (b) $U_s = 0$ m.s^{-1} (c) $U_s = 0$ m.s^{-1}

(d) $U_s = 7.72$ m.s^{-1} (e) $U_s = 7.72$ m.s^{-1} (f) $U_s = 7.72$ m.s^{-1}

Figure C.8.: (a) and (d) plots of the impulse response function K_{33} from the data and the analytical fit H_{33}; (b) and (e) plots of the added mass A_{33} from the data and from the analytical fit; (c) and (f) plots of the damping A_{33} from the data and from the analytical fit

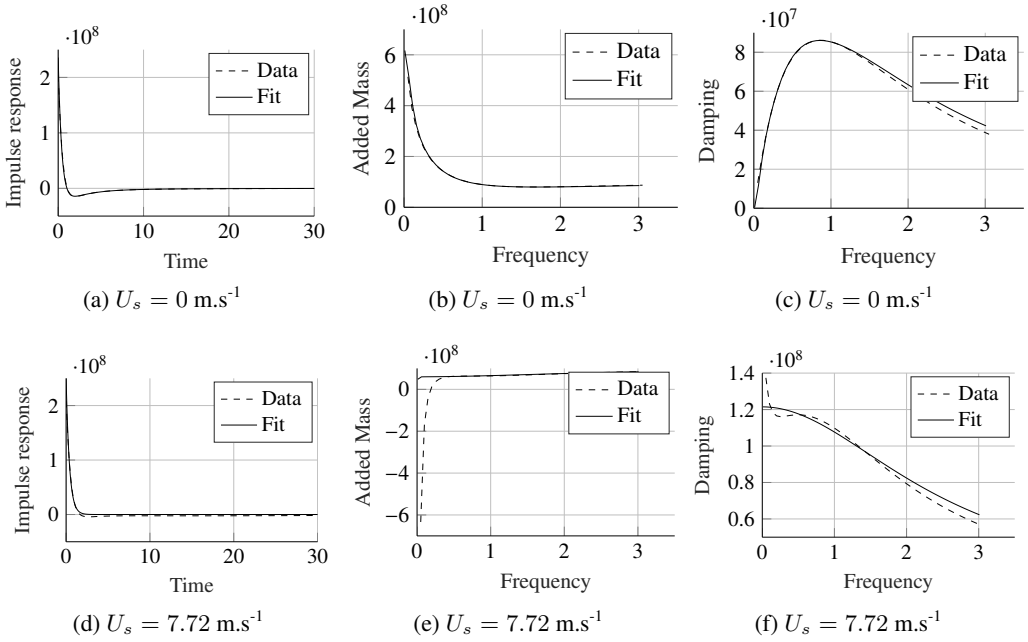

(a) $U_s = 0$ m.s^{-1} (b) $U_s = 0$ m.s^{-1} (c) $U_s = 0$ m.s^{-1}

(d) $U_s = 7.72$ m.s^{-1} (e) $U_s = 7.72$ m.s^{-1} (f) $U_s = 7.72$ m.s^{-1}

Figure C.9.: (a) and (d) plots of the impulse response function K_{35} from the data and the analytical fit H_{35}; (b) and (e) plots of the added mass A_{35} from the data and from the analytical fit; (c) and (f) plots of the damping A_{35} from the data and from the analytical fit

C.5.3. Roll

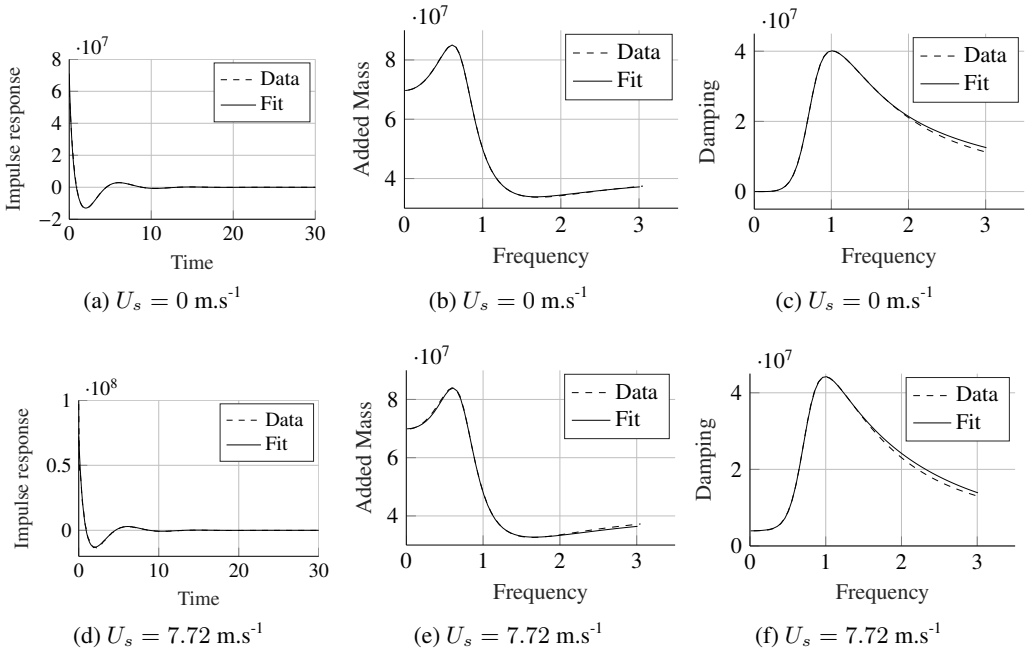

(a) $U_s = 0$ m.s^{-1} (b) $U_s = 0$ m.s^{-1} (c) $U_s = 0$ m.s^{-1}

(d) $U_s = 7.72$ m.s^{-1} (e) $U_s = 7.72$ m.s^{-1} (f) $U_s = 7.72$ m.s^{-1}

Figure C.10.: (a) and (d) plots of the impulse response function K_{44} from the data and the analytical fit H_{44}; (b) and (e) plots of the added mass A_{44} from the data and from the analytical fit; (c) and (f) plots of the damping B_{44} from the data and from the analytical fit

C.5.4. Pitch

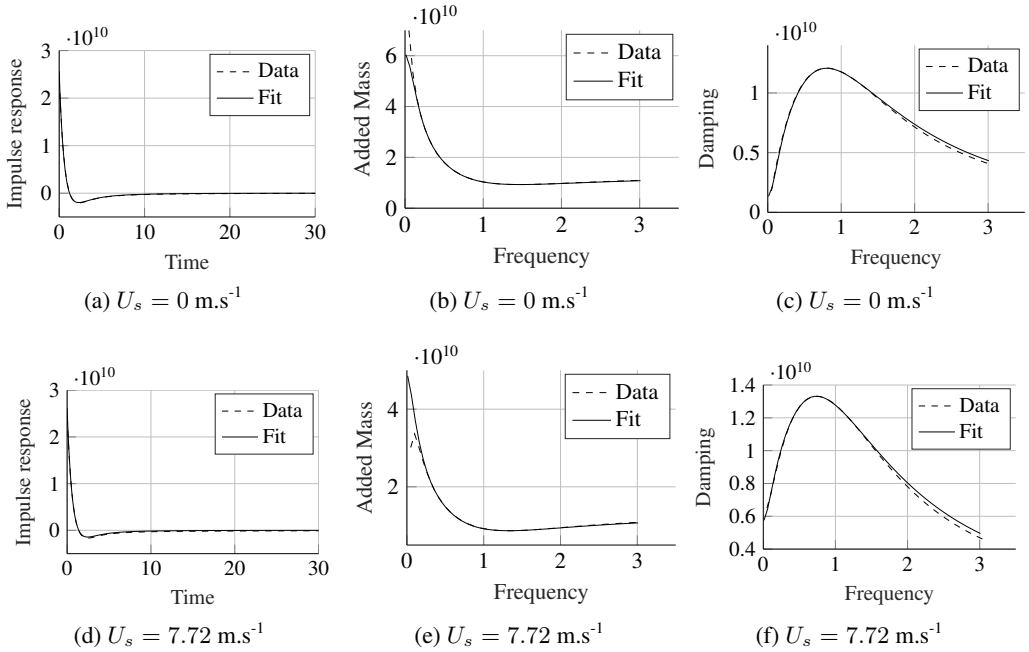

(a) $U_s = 0$ m.s^{-1} (b) $U_s = 0$ m.s^{-1} (c) $U_s = 0$ m.s^{-1}

(d) $U_s = 7.72$ m.s^{-1} (e) $U_s = 7.72$ m.s^{-1} (f) $U_s = 7.72$ m.s^{-1}

Figure C.11.: (a) and (d) plots of the impulse response function K_{55} from the data and the analytical fit H_{55}; (b) and (e) plots of the added mass A_{55} from the data and from the analytical fit; (c) and (f) plots of the damping B_{55} from the data and from the analytical fit

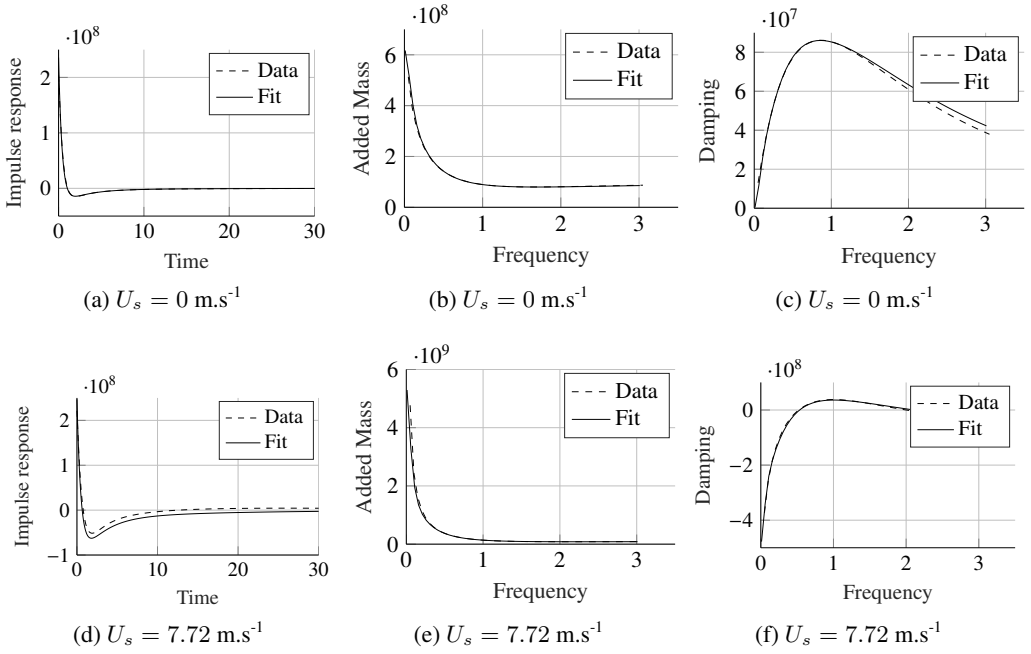

(a) $U_s = 0$ m.s^{-1} (b) $U_s = 0$ m.s^{-1} (c) $U_s = 0$ m.s^{-1}

(d) $U_s = 7.72$ m.s^{-1} (e) $U_s = 7.72$ m.s^{-1} (f) $U_s = 7.72$ m.s^{-1}

Figure C.12.: (a) and (d) plots of the impulse response function K_{53} from the data and the analytical fit H_{53}; (b) and (e) plots of the added mass A_{53} from the data and from the analytical fit; (c) and (f) plots of the damping A_{53} from the data and from the analytical fit

C.6. A direct extension of the time domain seakeeping model to maneuvering motions

C.6.1. Viscous effect modeling on the horizontal ship motions

The damping concerning the sway and the yaw motions is dominated at low frequency by viscous effects and may be non-linear. Since, the linear seakeeping theory of Salvesen et al. (1970) assumes a potential flow, the modeling of the hydrodynamic force of the hull with the time domain seakeeping model as presented in Chap. 6 is not consistent for horizontal ship motions. Consequently, Bailey et al. (1997) and Fossen and Smogeli (2004) proposed to take into account the viscous effect with a summation of the damping data from seakeeping theory denoted by $B_{ij}^{(sk)}$ and a viscous decaying ramp:

$$\begin{cases} B_{ij}(\omega) = B_{ij}^{(sk)}(\omega) + k_{ij} - \lambda_{ij}\omega & \text{if } k_{ij} - \lambda_{ij}\omega > 0, \\ B_{ij}(\omega) = B_{ij}^{(sk)}(\omega) & \text{otherwise,} \end{cases} \tag{C.21}$$

where $i, j \in \{2, 6\}$ are the component indices of motion (2: surge; 6: yaw). Fossen and Smogeli in (Fossen and Smogeli, 2004) proposed an alternative method as follows:

$$B_{ij}(\omega) = B_{ij}^{(sk)}(\omega) + k_{ij} e^{-\lambda_{ij}\omega}, \tag{C.22}$$

with $\lambda_{ij} > 0$.

No method has been provided to identify the coefficients k_{ij} and λ_{ij}. Consequently, a systematic method is proposed here. At zero frequency the sum of viscous damping with the seakeeping damping should equal to the linear maneuvering damping denoted by $B_{ij}^{(man)}$. Hence, k_{ij} can be estimated with the following formula:

$$k_{ij} = B_{ij}^{(man)} - B_{ij}^{(sk)}(\omega = 0), \tag{C.23}$$

The definition of the parameter λ_{ij} is more questionable but it can defined with the following formula:

$$\lambda_{ij} = \frac{1}{2} \frac{k_{ij} \omega_{max}^{(sk)}}{\max\limits_{\omega \in R^+} B_{ij}^{(sk)}}, \tag{C.24}$$

where $\omega_{max}^{(sk)}$ corresponds to the frequency such as $B_{ij}^{(sk)}(\omega_{max}) = \max B_{ij}^{(sk)}$. According to Eqns. (C.22), (C.23) and (C.24), comparisons of the presented correction method with the corrections presented in Bailey et al. (1997) are plotted in Figs. C.13 and C.14 respectively for B_{22} and B_{66}.

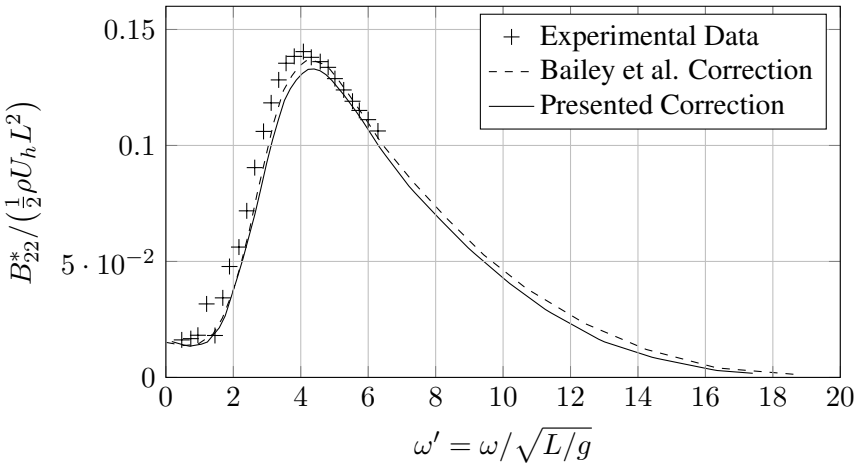

Figure C.13.: b_{22} damping coefficient against frequency of the motion; Comparison of the experimental data; with the Bailey et al. (1997) correction for viscous effects and with the present correction method for viscous effect.

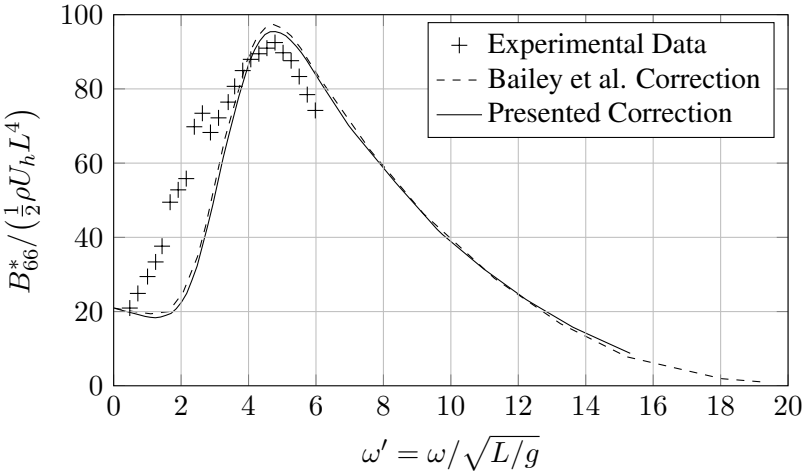

Figure C.14.: b_{66} damping coefficient against frequency of the motion; Comparison of the experimental data with the Bailey et al. (1997) correction for viscous effects and with the present correction method for viscous effect.

A good agreement is found with the presented correction and the considered data. According to this correction, at low frequency, the hull hydrodynamic forces relative to the horizontal motions should be equal to the hull forces predicted by the linear term of the maneuvering model used to determine k_{ij}.

With this modification of the damping, only the corresponding linear terms of a maneuvering model are taken into account. Consequently, the non-linear terms can be added as external force $\underline{F}_{hnl}$.

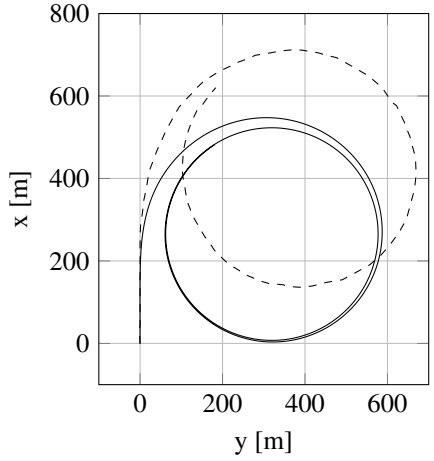

—— Direct extension of the time seakeeping model

- - - Free running JMUC

Figure C.15.: Turning circle path with rudder angle $\delta_r = 35°$. The results obtained with the mixed seakeeping and maneuvering model (——) are compared with the free sailing EFD data of the JMUC (- - -).

C.6.2. Results

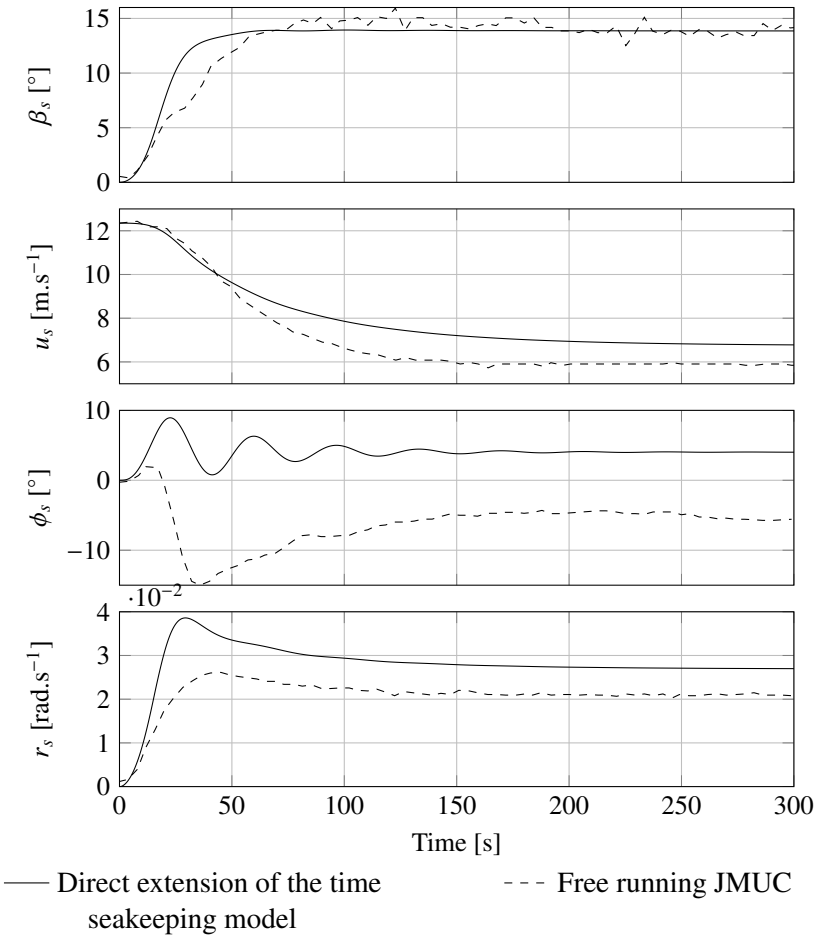

Figure C.16.: Time history during a 35° turning circle maneuver of the: drift angle β_s, surge velocity u_s, heel angle ϕ_s, surge velocity u_s and yaw turning rate r_s. The results obtained with the direct extension of the time seakeeping model (——) are compared with the free sailing EFD data of the SVA (- - -).

During a turning circle maneuver with a rudder angle of 35°, Figs. C.15 and C.16 show respectively the ship path in the plane $\left(\underline{x}_n,\ \underline{y}_n\right)$ and the time series of the drift angle β_s, surge velocity u_s, heel angle ϕ_s, surge velocity u_s and yaw turning rate r_s. Figs. C.15 and C.16 compare the results obtained with the direct extension of the time domain seakeeping model (solid line) with the EFD data obtained with the free running test at the JMUC (dashed line).

Figure C.17 shows during a KCS zigzag 15/1° test maneuver the time history of: the rudder angle δ_r, the ship heading ψ_s, the ship drift angle $\beta_s = -\arctan\left(v_s/u_s\right)$, the heeling angle

ϕ_s and the ship longitudinal speed u_s. The solid lines correspond to the direct extension of the time domain seakeeping model. The dashed lines correspond to the free sailing data performed by the SVA.

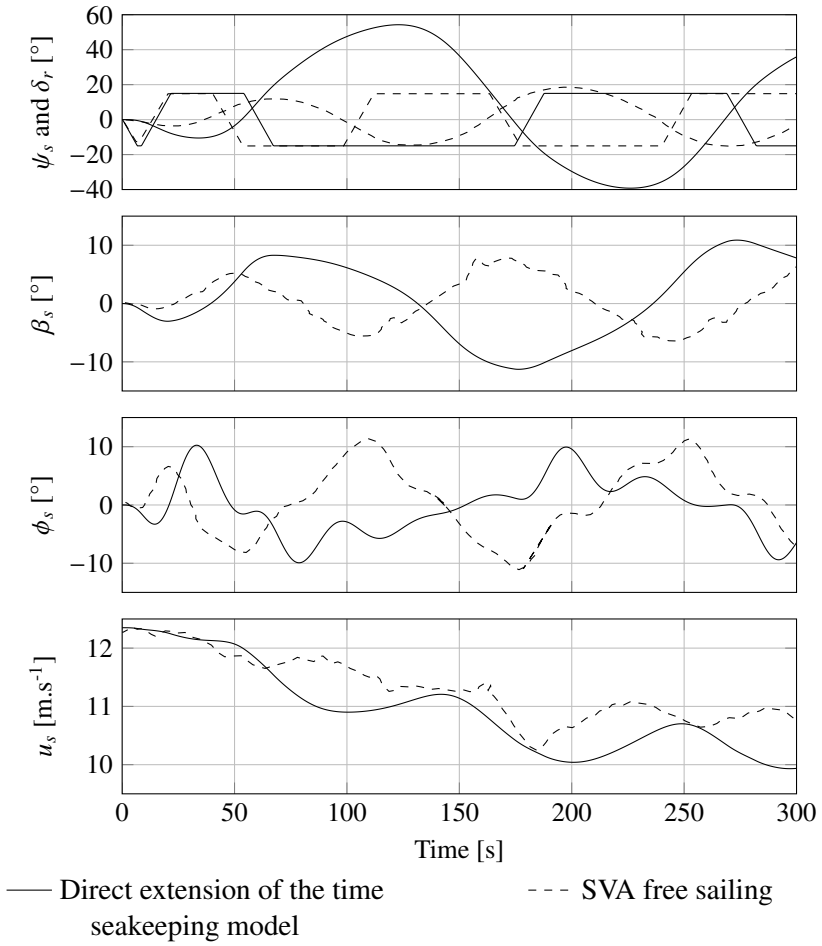

Figure C.17.: Time history during a zigzag 15/1° maneuver of the: rudder angle δ_r, heading ψ_s, drift angle β_s, heel angle ϕ_s and surge velocity u_s. The results obtained with the direct extension of the time seakeeping model (——) are compared with the free sailing EFD data of the SVA (- - -).

C.6.3. Analyse and discussion

In Fig. C.15, it can be noticed that the predicted turning radius of gyration with the direct extension of the time domain seakeeping model is slightly underestimated according to the free sailing results performed at the JMUC. The predicted transient part of the turning circle is shorter. This analysis is confirmed by the time series in Fig. C.16. Indeed, the

predicted evolution of the drift angle reaches sooner a steady state. The predicted loss of surge velocity is underestimated. The yaw turning rate is overestimated. Since, the steady part of the drift angle is correctly estimated, the higher surge velocity and the higher turning rate lead to an equivalent turning radius of gyration. The most important difference between the predicted motion and the free sailing data concern the heel angle. Indeed, the steady part of the predicted heel angle is around 4° whereas the free sailing heel angle is around -5°. Regarding the predicted ship motion during the 15/1° zig-zag test in Fig. C.17, the turning period and the overshoot angle are largely overestimated.

The important difference in terms of heel angle is due to an underestimation of the heel angle due to the drift and the yaw turning rate by the STF strip theory (Salvesen et al., 1970). The positive heel angle is due to the heeling moment impose by the rudder. Even if the hull heeling moment due to the drift and the yaw turning rate is negative with respect to the $\underline{x}_s$ axis, the heeling moment due to the rudder is positive and larger. Consequently, the term relatives to the mode "$2, 4$" should be examined.

The poor accuracy of the predicted motions during the transient part of the turning circle and the zig-zag maneuvers is clear. The transient parts of the motions are highly dependent of the added masses. With the direct extension of the time domain seakeeping model, the hull forces due to the accelerations are distributed on the infinite added mass and the state-space systems. As shown by Woodward (2014) the value of the yaw added mass is highly sensitive on the maneuvering results.

C.6.4. Conclusion

The accuracy provided by the implemented direct extension of the time seakeeping model is not satisfactory. Some key elements have been given to explain the importance differences between the direct extension of the time domain seakeeping model and the free sailing results. An extensive analysis of the ship modeling with the direct extension of the time domain seakeeping model should be performed. Nevertheless, since such an analysis can be very time consuming, this work is beyond the scope of this thesis. Consequently, the mixed seakeeping and maneuvering model is retained.

C.7. Kriso Container Ship

C.7.1. Open water propeller data

The considered open water propeller data are from the NMRI free sailing model (www.sim-man2008.dk).

J	K_t	K_q
0.0	0.5327	0.7517
0.10	0.4937	0.7058
0.15	0.4719	0.6813
0.20	0.4469	0.6538
0.25	0.4208	0.6232
0.30	0.3922	0.5895
0.35	0.3657	0.5589
0.40	0.3425	0.5314
0.45	0.3143	0.5008
0.50	0.2895	0.4702
0.55	0.2647	0.4396
0.60	0.2407	0.4090
0.65	0.2162	0.3784
0.70	0.1931	0.3478
0.75	0.1688	0.3172
0.80	0.1414	0.2805
0.85	0.1148	0.2468
0.90	0.0870	0.2132
0.95	0.0581	0.1704
1.00	0.0293	0.1275
1.05	-0.0033	0.0786

Table C.2.: Kriso Container Ship open water propeller data of the NMRI free sailing model

C.7.2. Kriso Container Ship hull adavance resistance

The hull advance resistance data have been calculated with the regression model of Holtrop and Mennen (1982).

u_s (m.s^{-1})	R_{bh} (N)
0.0	0.0
2.0	46110
4.0	166520
6.0	355480
8.0	634540
10.0	1094770
12.0	1881990
14.0	3218030

Table C.3.: Kriso Container Ship hull resistance

C.7.3. Kriso Container Ship maneuvering coefficients

Table C.4 gives the maneuvering coefficients of the KCS container ship according to Fukui et al. (2015).

		$c_{x0} = -0.12$
Surge coefficient	$X'_{\beta_s\beta_s} = -0.0603$	$c_{x\beta_s\beta_s} = 2.31$
	$X'_{\beta_s r_s} = -0.0603$	$c_{x\beta_s r_s} = -0.22$
	$X'_{r_s r_s} = -0.0162$	$c_{x r_s r_s} = 3.50$
	$X'_{\beta_s\beta_s\beta_s\beta_s} = -0.0760$	$c_{x\beta_s\beta_s\beta_s\beta_s} = -13.28$
		$Y'_{\phi_s} = -0.0052$
Sway coefficients	$Y'_{\beta_s} = 0.2162$	$c_{y\beta_s} = 0.05$
	$Y'_{r_s} = 0.0245$	$c_{y r_s} = -1.20$
		$Y_{\beta_s\beta_s\phi_s} = 0.3352$
		$Y'_{\beta_s r_s\phi_s} = 0.3123$
		$Y'_{r_s r_s\phi_s} = -0.0642$
	$Y'_{\beta_s\beta_s\beta_s} = 1.7028$	$c_{y\beta_s\beta_s\beta_s} = 0.36$
	$Y'_{\beta_s\beta_s r_s} = -0.5658$	$c_{y\beta_s\beta_s r_s} = 0.64$
	$Y'_{\beta_s r_s r_s} = -0.5658$	$c_{y\beta_s r_s r_s} = -0.22$
	$Y'_{r_s r_s r_s} = -0.0105$	$c_{y r_s r_s r_s} = -0.74$
		$N'_{\phi_s} = -0.0063$
	$N'_{\beta_s} = 0.1172$	$c_{n\beta_s} = 0.21$
	$N'_{r_s} = -0.0443$	$c_{n r_s} = -0.32$
		$N_{\beta_s\beta_s\phi_s} = -0.2532$
Yaw coefficients		$N'_{\beta_s r_s\phi_s} = 0.1152$
		$N'_{r_s r_s\phi_s} = -0.0120$
	$N'_{\beta_s\beta_s\beta_s} = 0.1710$	$c_{n\beta_s\beta_s\beta_s} = -0.09$
	$N'_{\beta_s\beta_s r_s} = -0.5602$	$c_{n\beta_s\beta_s r_s} = -0.09$
	$N'_{\beta_s r_s r_s} = 0.0200$	$c_{n\beta_s r_s r_s} = 2.52$
	$N'_{r_s r_s r_s} = -0.0369$	$c_{n r_s r_s r_s} = -0.23$

Table C.4.: KCS container ship maneuvering coefficient

C.7.4. Kriso Container Ship interaction coefficients

t	0.165
w	0.208
η	0.792
κ	0.713
ϵ	0.900
γ_r^+	0.55
γ_r^-	0.45
t_r	0.44
a_h	0.232
$x_h^{'}$	-0.711
$l_r^{'}$	-0.36
C_{ϕ_s}	-0.36

Table C.5.: KCS container ship maneuvering interaction coefficient

C.7.5. Kriso Container Ship windage coefficients

A_l	A_f	H_m	s_h	s_l	κ	δ_w	$D_t^{'}$	$D_l^{'}$
5245.4 m^2	893.9 m^2	20.0 m	10.08 m	-4.57 m	1.4	0.4	0.9	0.55

Table C.6.: KCS windage parameters

C.7.6. Kriso Container Ship transfer functions

C.7.6.1. Analytical expressions

	$U_s = 10.29$ m.s^{-1}
H_{22}	$\frac{4.544 \cdot 10^7 p^2 + 1.848 \cdot 10^7 p + 1.542 \cdot 10^6}{p^3 + 2.045 p^2 + 1.343 p + 0.56}$
H_{24}	$\frac{-5.098 \cdot 10^7 p^3 - 2.293 \cdot 10^8 p^2 - 9.098 \cdot 10^7 p + 1.013 \cdot 10^6}{p^4 + 3.598 p^3 + 6.007 p^2 + 3.807 p + 1.728}$
H_{26}	$\frac{4.931 \cdot 10^8 p^3 + 7.603 \cdot 10^8 p^2 + 3.173 \cdot 10^8 p - 2.328 \cdot 10^6}{p + 2.809 p^3 + 3.579 p^2 + 2.24 p + 0.985}$
H_{33}	$\frac{3.432 \cdot 10^7 p^2 + 1.806 \cdot 10^7 p + 7.087 \cdot 10^5}{p^3 + 1.217 p^2 + 0.5928 p + 0.06082}$
H_{35}	$\frac{1.599 \cdot 10^9 p^3 + 2.478 \cdot 10^9 p^2 + 1.647 \cdot 10^8 p + 196.6}{p^4 + 4.744 p^3 + 4.036 p^2 + 0.1008 p + 2.361 \cdot 10^{-7}}$
H_{42}	$\frac{-5.337 \cdot 10^7 s^3 - 2.312 \cdot 10^8 s^2 - 9.273 \cdot 10^7 s - 3.204 \cdot 10^5}{p^4 + 3.594 p + 5.966 p^2 + 3.781 p + 1.711}$
H_{44}	$\frac{1.208 \cdot 10^9 p^2 + 7.255 \cdot 10^8 p + 1.379 \cdot 10^8}{p^3 + 3.02 p^2 + 2.182 p + 1.239}$
H_{46}	$\frac{-5.03 \cdot 10^9 p^3 - 1.38 \cdot 10^{10} p^2 - 6.162 \cdot 10^9 p - 8.99 \cdot 10^7}{p^4 + 4.123 p^3 + 6.021 p^2 + 4.02 p + 1.837}$
H_{53}	$\frac{1.344 \cdot 10^9 p - 4.151 \cdot 10^8}{p^2 + 1.96 p + 0.2473}$
H_{55}	$\frac{1.839 \cdot 10^{11} p + 2.127 \cdot 10^{10}}{p^2 + 1.443 p + 0.3231}$
H_{62}	$\frac{-1.038 \cdot 10^9 p^2 + 4.258 \cdot 10^9 p + 1.121 \cdot 10^9}{p^3 + 11.76 p^2 + 11.49 p + 8.033}$
H_{64}	$\frac{-3.557 \cdot 10^9 p + 3.677 \cdot 10^8}{p^2 + 0.7965 p + 0.8216}$
H_{66}	$\frac{9.761 \cdot 10^{10} p^2 + 3.043 \cdot 10^{10} p + 5.954 \cdot 10^8}{p^3 + 1.622 p^2 + 1.217 p + 0.4785}$

Table C.7.: Expressions of the identified analytical transfer function for the KCS at full scale and at $U_s = 10$ m.s^{-1} and $U_s = 7.72$ m.s^{-1}

C.7.6.2. Sway

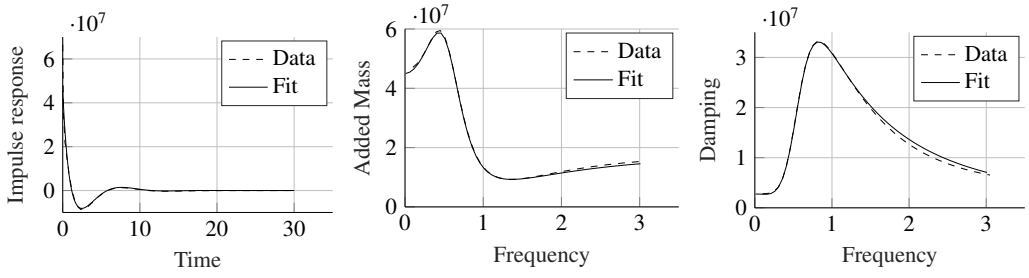

(a) $U_s = 10.29$ m.s^{-1} (b) $U_s = 10.29$ m.s^{-1} (c) $U_s = 10.29$ m.s^{-1}

Figure C.18.: (a) plot of the impulse response function K_{22} from the data and the analytical fit H_{22}; (b) plot of the added mass A_{22} from the data and from the analytical fit; (c) plot of the damping B_{22} from the data and from the analytical fit

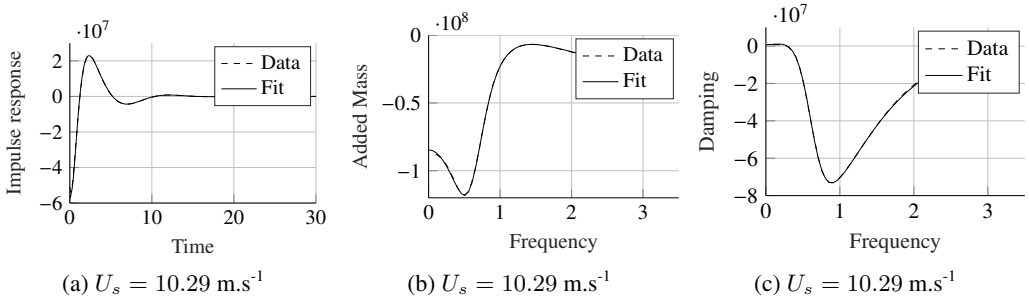

(a) $U_s = 10.29$ m.s^{-1} (b) $U_s = 10.29$ m.s^{-1} (c) $U_s = 10.29$ m.s^{-1}

Figure C.19.: (a) plot of the impulse response function K_{24} from the data and the analytical fit H_{24}; (b) plot of the added mass A_{24} from the data and from the analytical fit; (c) plot of the damping B_{24} from the data and from the analytical fit

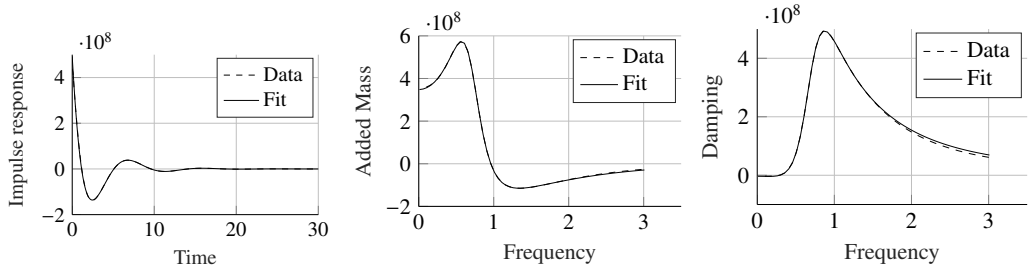

(a) $U_s = 10.29$ m.s^{-1} (b) $U_s = 10.29$ m.s^{-1} (c) $U_s = 10.29$ m.s^{-1}

Figure C.20.: (a) plot of the impulse response function K_{26} from the data and the analytical fit H_{26}; (b) plot of the added mass A_{26} from the data and from the analytical fit; (c) plot of the damping B_{26} from the data and from the analytical fit

C.7.6.3. Heave

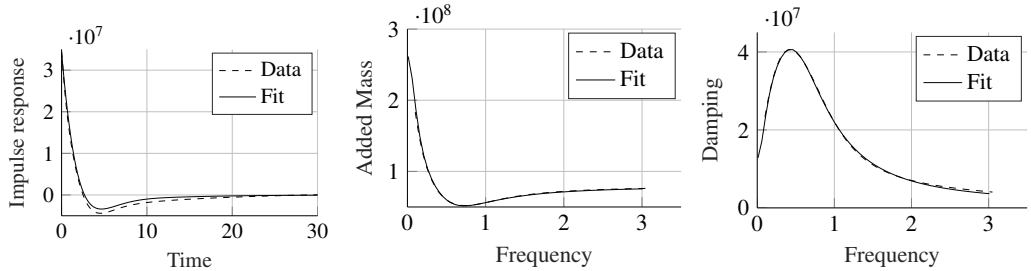

(a) $U_s = 10.29$ m.s^{-1} (b) $U_s = 10.29$ m.s^{-1} (c) $U_s = 10.29$ m.s^{-1}

Figure C.21.: (a) plot of the impulse response function K_{33} from the data and the analytical fit H_{33}; (b) plot of the added mass A_{33} from the data and from the analytical fit; (c) plot of the damping B_{33} from the data and from the analytical fit

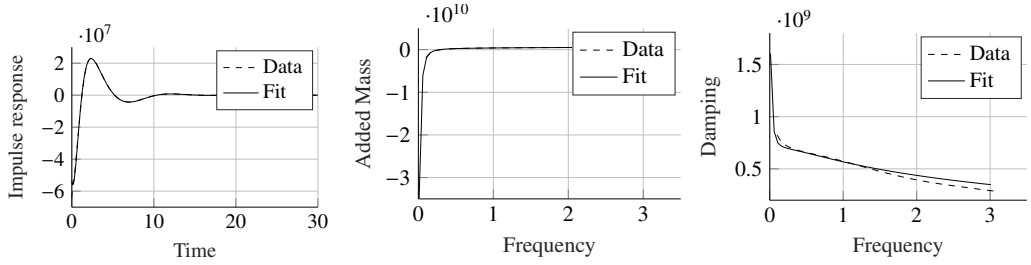

(a) $U_s = 10.29$ m.s^{-1} (b) $U_s = 10.29$ m.s^{-1} (c) $U_s = 10.29$ m.s^{-1}

Figure C.22.: (a) plot of the impulse response function K_{35} from the data and the analytical fit H_{35}; (b) plot of the added mass A_{35} from the data and from the analytical fit; (c) plot of the damping B_{35} from the data and from the analytical fit

C.7.6.4. Roll

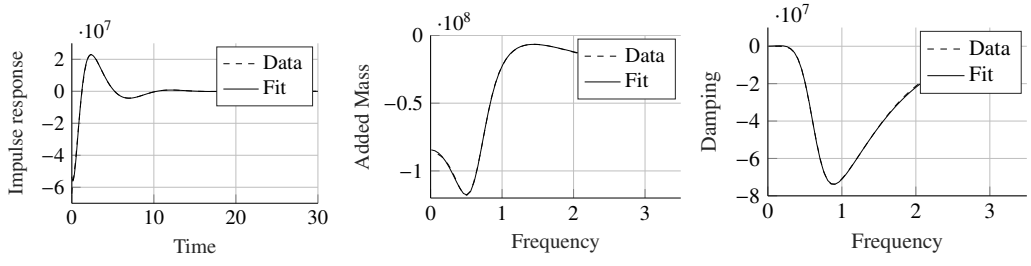

(a) $U_s = 10.29$ m.s^{-1} (b) $U_s = 10.29$ m.s^{-1} (c) $U_s = 10.29$ m.s^{-1}

Figure C.23.: (a) plot of the impulse response function K_{42} from the data and the analytical fit H_{42}; (b) plot of the added mass A_{42} from the data and from the analytical fit; (c) plot of the damping B_{42} from the data and from the analytical fit

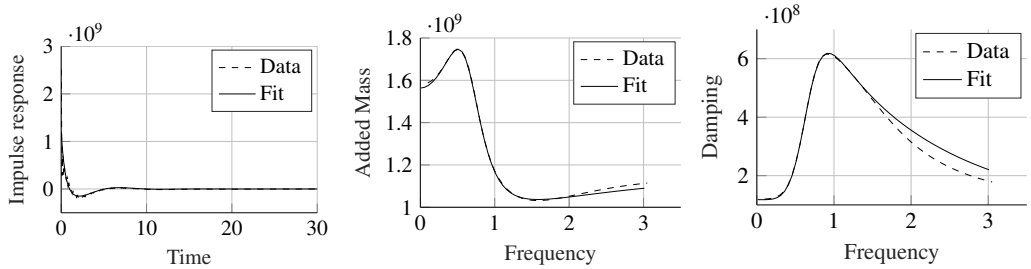

(a) $U_s = 10.29$ m.s^{-1} (b) $U_s = 10.29$ m.s^{-1} (c) $U_s = 10.29$ m.s^{-1}

Figure C.24.: (a) plot of the impulse response function K_{44} from the data and the analytical fit H_{44}; (b) plot of the added mass A_{44} from the data and from the analytical fit; (c) plot of the damping B_{44} from the data and from the analytical fit

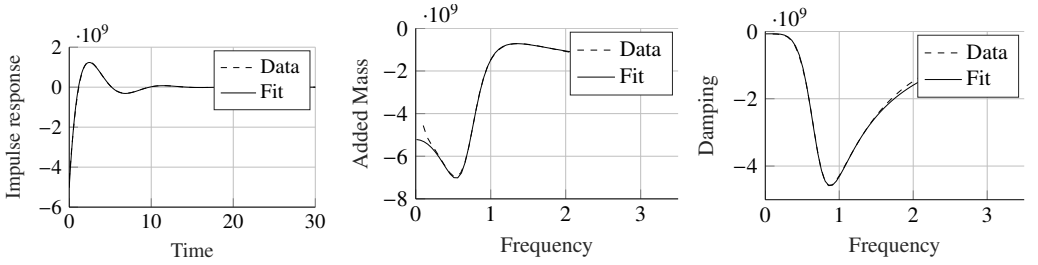

(a) $U_s = 10.29$ m.s^{-1} (b) $U_s = 10.29$ m.s^{-1} (c) $U_s = 10.29$ m.s^{-1}

Figure C.25.: (a) plot of the impulse response function K_{46} from the data and the analytical fit H_{46}; (b) plot of the added mass A_{46} from the data and from the analytical fit; (c) plot of the damping B_{46} from the data and from the analytical fit

C.7.6.5. Pitch

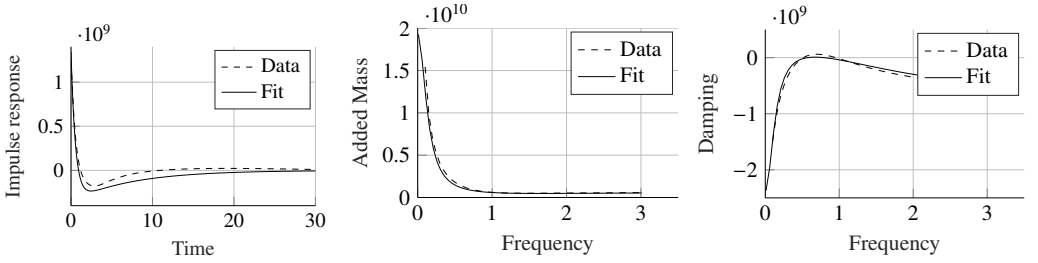

(a) $U_s = 10.29$ m.s^{-1} (b) $U_s = 10.29$ m.s^{-1} (c) $U_s = 10.29$ m.s^{-1}

Figure C.26.: (a) plot of the impulse response function K_{53} from the data and the analytical fit H_{53}; (b) plot of the added mass A_{53} from the data and from the analytical fit; (c) plot of the damping B_{53} from the data and from the analytical fit

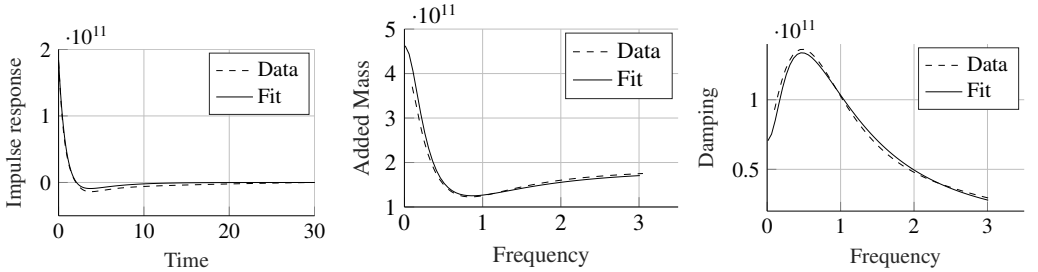

(a) $U_s = 10.29$ m.s^{-1} (b) $U_s = 10.29$ m.s^{-1} (c) $U_s = 10.29$ m.s^{-1}

Figure C.27.: (a) plot of the impulse response function K_{55} from the data and the analytical fit H_{55}; (b) plot of the added mass A_{55} from the data and from the analytical fit; (c) plot of the damping B_{55} from the data and from the analytical fit

C.7.6.6. Yaw

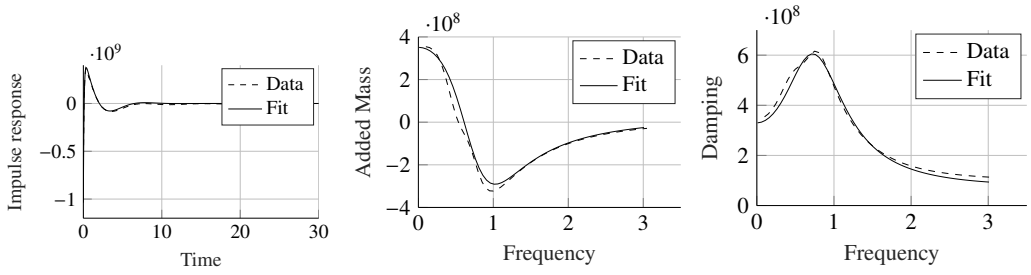

(a) $U_s = 10.29$ m.s^{-1} (b) $U_s = 10.29$ m.s^{-1} (c) $U_s = 10.29$ m.s^{-1}

Figure C.28.: (a) plot of the impulse response function K_{62} from the data and the analytical fit H_{62}; (b) plot of the added mass A_{62} from the data and from the analytical fit; (c) plot of the damping B_{62} from the data and from the analytical fit

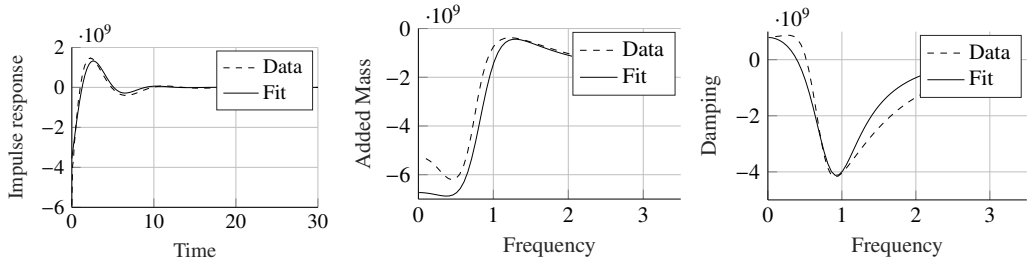

(a) $U_s = 10.29$ m.s^{-1} (b) $U_s = 10.29$ m.s^{-1} (c) $U_s = 10.29$ m.s^{-1}

Figure C.29.: (a) plot of the impulse response function K_{64} from the data and the analytical fit H_{64}; (b) plot of the added mass A_{64} from the data and from the analytical fit; (c) plot of the damping B_{64} from the data and from the analytical fit

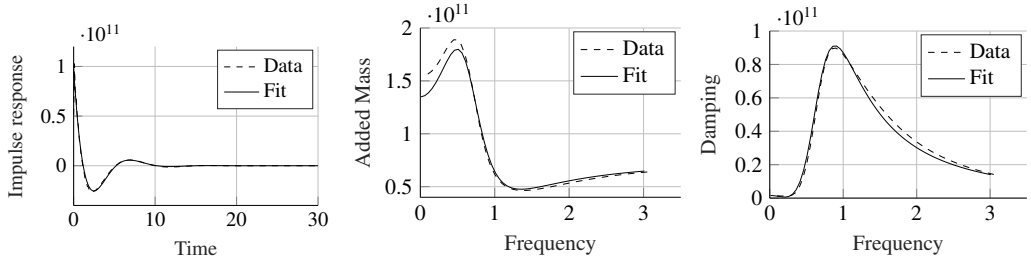

(a) $U_s = 10.29$ m.s^{-1} (b) $U_s = 10.29$ m.s^{-1} (c) $U_s = 10.29$ m.s^{-1}

Figure C.30.: (a) plot of the impulse response function K_{66} from the data and the analytical fit H_{66}; (b) plot of the added mass A_{66} from the data and from the analytical fit; (c) plot of the damping B_{66} from the data and from the analytical fit

Bibliography

Abkowitz, M. A. (1980). Measurement of hydrodynamic characteristics from ship maneuvering trials by system identification. Technical report.

Argatov, I., P. Rautakorpi, and R. Silvennoinen (2009). Estimation of the mechanical energy output of the kite wind generator. *Renewable Energy 34*(6), 1525–1532.

Argatov, I., P. Rautakorpi, and R. Silvennoinen (2011, oct). Apparent wind load effects on the tether of a kite power generator. *Journal of Wind Engineering and Industrial Aerodynamics 99*(10), 1079–1088.

Bailey, P., W. Price, and P. Temarel (1997). A unified mathematical model describing the manoeuvring of a ship travelling in a seaway. *Trans. RINA 140*, 131–149.

Bearman, P. W. (1984). Vortex shedding from oscillating bluff bodies. *Annual review of fluid mechanics 16*, 195–222.

Behrel, M., N. Bigi, K. Roncin, D. Grelon, F. Montel, A. Nême, J.-B. Leroux, C. Jochum, and Y. Parlier (2016). Measured Performance of a 50-m2 Kite on a Trawler. In *High-Performance Marine Vehicles Conference*.

Behrel, M., K. Roncin, J.-B. B. Leroux, F. Montel, A. Nême, C. Jochum, and Y. Parlier (2017). Experimental set up for measuring onshore and onboard performances of leading edge inflatable kites - Presentation of onshore results. In *Fourth International Conference on Innovation in High Performance Sailing Yachts (INNOV'SAIL)*, Lorient, France.

Bennett, S. (1993). Development of the PID Controller. *IEEE Control Systems 13*(6), 58–62.

Bernitsas, M. and N. Kekridis (1985). Simulation and stability of ship towing. *International Shipbuilding Progress 32*(369), 112–123.

Bernitsas, M. and N. Kekridis (1986). Nonlinear stability analysis of ship towed by elastic rope. *Journal of ship research 30*(2), 136–146.

Bertram, V. (2012). *Practical ship hydrodynamics*. Elsevier.

Bigi, N., M. Behrel, K. Roncin, J.-B. Leroux, A. Nême, C. Jochum, and Y. Parlier (2016). Course Keeping of Ship Towed by Kite. In *15e Journées de l'Hydrodynamique*, pp. 1–14.

Blendermann, W. (1994). Parameter identification of wind loads on ships. *Journal of Wind Engineering and Industrial Aerodynamics 51*, 339–351.

Bosch, A., R. Schmehl, P. Tiso, and D. Rixen (2014, sep). Dynamic Nonlinear Aeroelastic Model of a Kite for Power Generation. *Journal of Guidance, Control, and Dynamics 37*(5), 1426–1436.

Breukels, J. and W. J. Ockels (2007). A multi-body dynamics approach to a cable simulation for kites. *Proceedings of the IASTED Asian Conference ...*, 168–173.

Breukels, J., R. Schmehl, and W. Ockels (2013). Aeroelastic simulation of flexible membrane wings based on multibody system dynamics. *Green Energy and Technology*, 287–305.

Buhaug, Ø., J. Corbett, Ø. Endresen, V. Eyring, J. Faber, S. Hanayama, D. Lee, D. Lee, H. Lindstad, A. Markowska, A. Mjelde, D. Nelissen, J. Nilsen, C. Pålsson, J. Winebrake, W. Wu, and K. Yoshida (2009). Second IMO Greenhouse Gas Study 2009. *International Maritime Organization (IMO)*.

Cadalen, B., F. Griffon, P. Lanusse, and J. Sabatier (2017). Modelling and Control of a Tethered Kite in Dynamic. *Fourth International Conference on Innovation in High Performance Sailing Yachts (INNOV'SAIL)*.

Chatzikonstantinou, T. (1989). Numerical analysis of three-dimensional non rigid wings. In *10th Aerodynamic Decelerator Conference*, pp. 907.

Clarke, D., P. Gedling, and G. Hine (1983). The Application of manoeuvring criteria in hull design using linear theory. *Naval Architect*, 45–68.

Corbett, J. J., H. Wang, and J. J. Winebrake (2009). The effectiveness and costs of speed reductions on emissions from international shipping. *Transportation Research Part D: Transport and Environment 14*(8), 593–598.

Cummins, W. (1962). The impulse response function and ship motions. Technical report, DTIC Document.

Dadd, G. M. (2013). *Kite dynamics for ship propulsion*. Ph. D. thesis.

Dadd, G. M., D. A. Hudson, and R. A. Shenoi (2010, jan). Comparison of two kite force models with experiment. *Journal of aircraft 47*(1), 212–224.

Dadd, G. M., D. A. Hudson, and R. A. Shenoi (2011, oct). Determination of kite forces using three-dimensional flight trajectories for ship propulsion. *Renewable Energy 36*(10), 2667–2678.

Du Pontavice, E. (2016). *Propulsion par cerf-volant : envol et pérégrinations*. Ph. D. thesis, Université de Paris-Saclay.

Duckworth, R. (1983). The Application of Elevated Sails (Kites) for Fuel Savinf Auxiliary Propulsion of Comercial Vessels. *Journal of Wind Engineering and Industrial Aerodynamics 12*, 75–97.

Ebi, K. L., S. Hallegatte, T. Kram, N. W. Arnell, T. R. Carter, J. Edmonds, E. Kriegler, R. Mathur, B. C. O'Neill, K. Riahi, H. Winkler, D. P. van Vuuren, and T. Zwickel (2014). A new scenario framework for climate change research: Background, process, and future directions. *Climatic Change 122*(3), 363–372.

Erhard, M. and H. Strauch (2012). Control of Towing Kites for Seagoing Vessels. *IEEE Transactions on Control Systems Technology 21*(5), 1–1.

Fagiano, L., A. U. Zgraggen, M. Khammash, and M. Morari (2014). On control of tethered wings for airborne wind energy. *2013 American Control Conference 22*(4), 1430–1435.

Fagiano, L., A. U. Zgraggen, and M. Morari (2013). On modeling, filtering and automatic control of flexible tethered wings for airborne wind energy. *Green Energy and Technology*, 167–180.

Faltinsen, O. M. (2005). *Hydrodynamics of high-speed marine vehicles*. Cambridge University Press.

Fitriadhy, A. and H. Yasukawa (2011). Course stability of a ship towing system. *Ship Technology Research 58*(1), 4–23.

Fitriadhy, a., H. Yasukawa, and K. K. Koh (2013). Course stability of a ship towing system in wind. *Ocean Engineering 64*, 135–145.

Fossen, T. (2005). A Nonlinear Unified State-Space Model for Ship Maneuvering and Control in a Seaway. *International Journal of Bifurcation and Chaos 15*(09), 2717–2746.

Fossen, T. I. and Ø. N. Smogeli (2004). Nonlinear time-domain strip theory formulation for low-speed manoeuvring and station-keeping. *Modeling, Identification and Control 25*(4), 201–221.

Fukui, Y., H. Yano, T. Nakano, H. Yokota, M. Kondo, and Y. Yoshimura (2016). 4-DOF Mathematical Model for Manoeuvring Simulation including Roll Motion. *Journal of the Japan Society of Naval Architects and Ocean Engineers 24*, 167–179.

Fukui, Y., Y. Yoshimura, H. Yano, and M. Kondo (2015). Investigation of Effect of Roll Motion on Manoeuvrability using 4-DOF Mathematical Model. *Marsim 2015* (September).

Giberti, H. and D. Ferrari (2015). A novel hardware-in-the-loop device for floating offshore wind turbines and sailing boats. *Mechanism and Machine Theory 85*, 82–105.

Greenhow, M. (1986). High- and low-frequency asymptotic consequences of the Kramers-Kronig relations. *Journal of Engineering Mathematics 20*, 293–306.

Hamming, R. W. (1989). *Digital filters*. Courier Corporation.

Harvald, S. A. (1983). *Resistance and Propulsion of Ships*. New York: Wiley-interscience.

Hibbett, Sorensen, and Karlsson (1998). *ABAQUS/standard: User's Manual*. Hibbitt, Karlsson & Sorensen.

Hobbs, S. E. (1986). A Quantitative study of kite performance in natural wind with application to kite anemometry. *Ecological Physics Research Group*, 323.

Hoerner, S. F. (1965). Fluid Dynamic Drag.

Holtrop, J. and G. G. Mennen (1982). An Approximate Power Prediction Method. *International Shipbuilding Progress 29*(July), 166–170.

Ikeda, Y., Y. Himeno, and N. Tanaka (1978). A prediction method for ship roll damping. *Report of the Department of Naval Architecture, University of Osaka Prefecture*.

Irvine, H. (1981). Cable Structures.

Irvine, H. M. and G. B. Sinclair (1976). The suspended elastic cable under the action of concentrated vertical loads. *International Journal of Solids and Structures 12*(4), 309–317.

Irvine, M., J. Longo, and F. Stern (2008). Pitch and Heave Tests and Uncertainty Assessment for a Surface Combatant in Regular Head Waves. *Journal of Ship Research 52*(2), 146–163.

ITTC (2002). Recommended Procedures: Full Scale Measurements Manoeuvrability, Full Scale Manoeuvring Trials Procedure. Technical report.

Ittc (2014). ITTC Symbols and Terminology List Version 2014. Technical report, International Towing Tank Conference.

Johansen, T. A., T. I. Fossen, and B. Vik (2005). Hardware-in-the-loop Testing of DP systems. *Dynamic Positioning Conference* (September), 2–16.

Journée, J. M. J. (1976). Prediction of Speed and Behaviour of a Ship in a Seaway. *ISP 23*(265), 1–24.

Jung, T. (2009). Wind Tunnel Study of Drag of Various Rope Designs. *27th AIAA Applied Aerodynamics Conference* (June), 1–16.

Kobayashi, E., H. Kagemoto, and Y. Furukawa (1995). Research on ship manoeuvrability and its application to ship design. *The 12th Marine Dynamic Symposium*, 23–90.

Kriegler, E., B. C. O'Neill, S. Hallegatte, T. Kram, R. J. Lempert, R. H. Moss, and T. Wilbanks (2012). The need for and use of socio-economic scenarios for climate change analysis: A new approach based on shared socio-economic pathways. *Global Environmental Change 22*(4), 807–822.

Kristiansen, E., A. Hjulstad, and O. Egeland (2005). State-space representation of radiation forces in time-domain vessel models. *Ocean Engineering 32*, 2195–2216.

Kung, S. Y. (1978). A New Identification and Model Reduction Algorithm via Singular Value Decompositions. In *Twelfth Asilomar Conference on Circuits, Systems and Computers*, pp. 705–714.

Lee, M.-L. (1989). Dynamic stability of nonlinear barge-towing system. *Applied Mathematical Modelling 13*(12), 693–701.

Leeuwen, G. V. and J. M. J. Journée (2001). Prediction of Ship Manoeuvrability Making Use of Model Tests. (April 1970).

Leloup, R. (2014). *Modelling approach and numerical tool developments for kite performance assessment and mechanical design; application to vessels auxiliary propulsion*. Ph. D. thesis, Université de Bretagne Occidentale.

Leloup, R., K. Roncin, M. Behrel, G. Bles, J.-B. Leroux, C. Jochum, and Y. Parlier (2016). A continuous and analytical modeling for kites as auxiliary propulsion devoted to merchant ships, including fuel saving estimation. *Renewable Energy 86*, 483–496.

Leloup, R., K. Roncin, G. Bles, J. B. Leroux, C. Jochum, and Y. Parlier (2014). Kite and classical rig sailing performance comparison on a one design keel boat. *Ocean Engineering 90*, 39–48.

Lewis, R. W., P. Bettess, and E. Hinton (1984). *Numerical methods in coupled systems*. John Wiley & Sons Inc.

Loyd, M. (1980). Crosswind Kite Power (for large-scale wind power production). *Journal of Energy 4*(3), 106–111.

Markert, B. (2010). *Weak or strong - On coupled problems in continuum mechanics*. Ph. D. thesis, University of Stuttgart.

Martin, H. R., R. W. Kimball, A. M. Viselli, and A. J. Goupee (2014). Methodology for Wind/Wave Basin Testing of Floating Offshore Wind Turbines. *Journal of Offshore Mechanics and Arctic Engineering 136*(2), 021902.

Meyer, J., R. Stahlbock, and S. Voß (2012). Slow steaming in container shipping. *Proceedings of the Annual Hawaii International Conference on System Sciences*, 1306–1314.

Minorsky, N. (1922). Directional stability of automatically steered bodies. *Naval Engineers Journal 32*(2).

Mofidi, A. and P. M. Carrica (2014). Computers & Fluids Simulations of zigzag maneuvers for a container ship with direct moving rudder and propeller. *COMPUTERS AND FLUIDS 96*, 191–203.

Molin, B. (2002). *Hydrodynamique des structures offshore*. Editions Technip.

Moss, R., M. Babiker, S. Brinkman, E. Calvo, T. Carter, J. Edmonds, I. Elgizouli, S. Emori, L. Erda, K. Hibbard, R. Jones, M. Kainuma, J. Kelleher, J. F. Lamarque, M. Manning, B. Matthews, J. Meehl, L. Meyer, J. Mitchell, N. Nakicenovic, B. O'Neill, R. Pichs, K. Riahi, S. Rose, P. Runci, R. Stouffer, D. van Vuuren, J. Weyant, T. Wilbanks, J. P. van Ypersele, and M. Zurek (2008). *Towards New Scenarios for Analysis of Emissions, Climate Change, Impacts and Response Strategies*.

Naaijen, P. and V. Koster (2010). Performance of auxiliary wind propulsion for merchant ships using a kite. *2nd International Conference on Marine Research and Transportation*, 45–53.

Naaijen, P., V. Koster, and R. Dallinga (2006). On the power savings by an auxiliary kite propulsion system. *International shipbuilding progress 53*, 255–279.

Newman, J. N. (1977). *Marine Hydrodynamics*. MIT Press.

Ogilvie, F. T. (1964). Recent Progress Towards the Understanding and Prediction of Ship.

Ottoson, P. and L. Bystrom (1991). Simulation of the dynamics of a ship manoeuvring in waves. *Transaction SNAME 99*(V), 281–298.

Perez, T. (2006). *Ship Motion Control: Course Keeping and Roll Stabilisation Using Rudder and Fins* (2005 ed.). Springer Science & Business Media.

Pérez, T. and T. I. Fossen (2008). Time-vs. frequency-domain Identification of parametric radiation force models for marine structures at zero speed. *Modeling, Identification and Control 29*(1), 1–19.

Peterson, E. W. and J. P. Hennessey (1978). On the Use of Power Laws for Estimates of Wind Power Potential.

Pocock, G. (1827). *The Aeropleustic Art Or Navigation in the Air, by the Use of Kites Or Buoyant Sails*. Sherwood & Company.

Podeur, V., D. Merdrignac, M. Behrel, K. Roncin, C. Jochum, Y. Parlier, and P. Renaud (2016). Simulation de voyage au long cours pour le calcul d ' économies de carburant : application à la propulsion par cerf-volant. *15e Journées de l'Hydrodynamique*, 1–12.

Ran, H., C.-E. Janson, and B. Allenström (2013). AUXILIARY KITE PROPULSION CONTRIBUTION TO SHIP THRUST. In *32nd International Conference on Ocean, Offshore and Arctic Engineering*, Nantes, France, pp. 1–9.

Ronen, D. (2011). The effect of oil price on containership speed and fleet size. *Journal of the Operational Research Society 62*(1), 211–216.

Salvesen, N., E. Tuck, and O. Faltinsen (1970). Ship motions and sea loads. *Trans. SNAME 78*, 250–287.

Sarpkaya, T. (2004). A critical review of the intrinsic nature of vortex-induced vibrations. *Journal of Fluids and Structures 19*(4), 389–447.

Schutt, R. R. and C. H. K. Williamson (2017). Unsteady Aerodynamics of Downwind S-Turns in Small Boat Sailing. *Fourth International Conference on Innovation in High Performance Sailing Yachts (INNOV'SAIL)*.

Shen, Z., D. Wan, and P. M. Carrica (2015). Dynamic overset grids in OpenFOAM with application to KCS self-propulsion and maneuvering. *Ocean Engineering 108*, 287–306.

Shin, Y., V. Belenky, and J. Paulling (2004). Criteria for parametric roll of large containerships in longitudinal seas. Discussion. *American Bureau of Shipping Technical papers*, 117–147.

Sinibaldi, M. and G. Bulian (2014). Towing simulation in wind through a nonlinear 4-DOF model: Bifurcation analysis and occurrence of fishtailing. *Ocean Engineering 88*, 366–392.

Skejic, R. (2013). Ships Maneuvering Simulations in a Seaway - How close are we to reality ? In *International Workshop on Next Generation Nautical Traffic Models*, pp. 91–101.

Skejic, R. and O. M. Faltinsen (2008). A unified seakeeping and maneuvering analysis of ships in regular waves. *Journal of Marine Science and Technology 13*(4), 371–394.

Smith, T. W. P., J. P. Jalkanen, B. A. Anderson, J. J. Corbett, J. Faber, S. Hanayama, E. O'Keeffe, S. Parker, L. Johansson, L. Aldous, C. Raucci, M. Traut, S. Ettinger, D. Nelissen, D. S. Lee, S. Ng, A. Agrawal, J. J. Winebrake, and A. Hoen, M. (2014). Third IMO Greenhouse Gas Study 2014. *International Maritime Organization (IMO)*, 327.

Sontag, E. D. (2013). *Mathematical Control Theory - Deterministic Finite Dimensional Systems*. Springer Science & Business Media.

Stern, F., K. Agdrup, S. Y. Kim, A. C. Hochbaum, K. P. Rhee, F. H. H. A. Quadvlieg, P. Perdon, T. Hino, R. Broglia, and J. Gorski (2011). Experience from SIMMAN 2008 - the first workshop on verification and validation of ship maneuvering simulation methods. *Journal of Ship Research 55*, 135–147.

Strandhagen, A. G. (1950). The dynamic stability on course of towed ships. *Trans of SNAME*, 32–56.

Sutulo, S. and C. Guedes Soares (2006). A uinified nonlinear mathematical model for simulating ship manoeuvring and seakeeping in regular waves. In *MARSIM 2006*.

Sutulo, S. and C. G. Soares (2005). An object-oriented manoeuvring simulation code for surface displacement ships. In *Maritime Transportation and Exploitation of Ocean and Coastal Resources: Proceedings of the 11th International Congress of the International Maritime Association of the Mediterranean*, Lisbon, Portugal.

Terink, E. J. (2009). Kiteplane flight dynamics. (December).

Terink, E. J., J. Breukels, R. Schmehl, and W. J. Ockels (2011). Flight dynamics and stability of a tethered inflatable kiteplane. *Journal of Aircraft*, 1–39.

The University of Iowa (2013). EFD Data.

Toxopeus, S. (2011). *Practical application of viscous-flow calculations for the simulation of manoeuvring ships*.

Toxopeus, S. and S. W. Lee (2008). Comparison of manoeuvring simulation programs for SIMMAN test cases. *Workshop on Verification and Validation of Ship Manoeuvring Simulation Methods SIMMAN 2008 5415*, 1–6.

Traut, M., P. Gilbert, C. Walsh, A. Bows, A. Filippone, P. Stansby, and R. Wood (2014). Propulsive power contribution of a kite and a Flettner rotor on selected shipping routes. *Applied Energy 113*, 362–372.

Varma, S. K. and J. S. Goela (1982). Effect of wind loading on the design of a kite tether. *Journal of Energy 6*(5), 342–343.

Wellicome, J. (1985). Some comments on the relative merits of various wind propulsion devices. *Journal of Wind Engineering and Industrial Aerodynamics 20*(1-3), 111–142.

Wellicome, J. and S. Wilkinson (1984). Ship propulsive kites: an initial study.

Williams, P., B. Lansdorp, and W. Ockels (2007). Modeling and control of a kite on a variable length flexible inelastic tether. *AIAA Guidance, navigation and ...*.

Williams, P., B. Lansdorp, R. Ruiterkamp, and W. Ockels (2008). Modeling, simulation, and testing of surf kites for power generation. *No. AIAA*.

Woodward, M. D. (2014). Evaluation of inter-facility uncertainty for ship manoeuvring performance prediction. *Ocean Engineering 88*, 598–606.

Yasukawa, H. (2007). Maneuvering simulations of tow and towed ships in still water. In *International Conference on Towing & Salvage of Disabled Tankers*, pp. 73–82.

Yoshimura, Y. and Y. Masumoto (2012). Hydrodynamic Database and Manoeuvring Prediction Method With Medium High-Speed Merchant Ships and Fishing Vessels. *Proceedings of International MARSIM Conference*.

Yun Li, Kiam Heong Ang, and G. Chong (2006). PID control system analysis and design. *IEEE Control Systems Magazine 26*(1), 32–41.

Investigation of the dynamic motions and operability of a ship towed by kite

Keywords: Kite, Kiteboat, Maneuvering, Seakeeping, Tether, Catenary, Coupling, Time-domain, Lock-in.

In order to reduce greenhouse gas emissions and shipping costs, the use of kites as an auxiliary propulsion device for ships is promising. In order to estimate the performance and the operability of a kite-towed vessel, a dynamic modeling of the system is implemented. A classical kite modeling is used. This model neglects the mass of the kite and assumes straight and inelastic tethers. These assumptions lead to a kinematic model depending on the lift coefficient and the aerodynamic lift to drag ration angle. A linear evolution of these aerodynamic coefficients as a function of the curvature of the flight path is proposed. In addition, by developing a quasi-analytical line model, it is shown that from 2 $m.s^{-1}$ of relative wind the straight tether assumption is reasonable. Based on the tether model, an analytical criterion assessing the minimum wind speed to enable a quasi-static kite flight is developed. To solve all the interaction terms between the kite and the ship, a time domain seakeeping model based on the linearized ship equation of motion assuming a potential flow is developed. The convolution product of the impulse response of the ship is computed with state-space systems. However, since horizontal ship motions are not well represented by such theories, a coupling with a maneuvering model is presented. Comparisons to experimental data tests show good agreements. To study the interactions between the kite and the ship, a monolithic coupling and a dissociated coupling are compared. The dissociated coupling neglects the influence of ship motions on the kite flight. In a calm water case, results obtained by the two types of coupling are very close. In regular waves, ship motions are dominated by the wave influence. Thus, with the monolithic coupling, a network of low frequency subharmonic appears in the kite excitation spectrum. The fundamental frequency of the subharmonic is given by the difference between the wave frequency and the frequency of the nearest kite excitation harmonic. When this difference is small enough, a lock-in phenomenon appears. This phenomenon is a benefit for the kite and the ship when the shift of the excitation harmonics corresponds to an increase. Furthermore, a course keeping stability study shows that the rudder needs to be actively controlled.

Evaluation des limites d'utilisation des navires tractés par kite par l'étude des mouvements de tenue à la mer et de manœuvrabilité

Mots-clefs : Kite, Kiteboat, Manœuvrabilité, Tenue à la mer, Ligne, Chainette, Couplage, simulation temporelle, accrochage de mode.

Afin de réduire les émissions de gaz à effet de serre et le coût du transport maritime, l'utilisation des cerfs-volants comme système de propulsion auxiliaire des navires est prometteuse. Pour estimer les performances et l'opérabilité d'un navire tracté par cerf-volant, une modélisation dynamique du système est alors mise en œuvre. Une modélisation analytique de cerf-volant est utilisée. Ce modèle néglige la masse du cerf-volant et suppose que les lignes sont droites et indéformables. Ces hypothèses conduisent à un modèle cinématique dépendant du coefficient de portance et de la finesse aérodynamique. Une évolution linéaire des coefficients aérodynamiques en fonction de la courbure de la trajectoire de vol est proposée. Par ailleurs, en développant un modèle quasi-analytique de ligne, il est montré qu'à partir de 2 $m.s^{-1}$de vent relatif que l'hypothèse de ligne droite est raisonnable. En se basant sur un modèle de ligne, un critère analytique de vitesse de vent minimum permettant un vol quasi-statique est présenté. Dans le but de résoudre l'ensemble des termes d'interaction entre le cerf-volant et le navire, un modèle linéarisé de tenue à la mer temporelle est développé. Le produit de convolution de la réponse impulsionnelle du navire est calculé avec des systèmes d'états. Cependant comme celle-ci représente mal les mouvements horizontaux des navires, le modèle développé est alors couplé à un modèle de manœuvrabilité. Pour étudier les interactions entre le cerf-volant et le navire un couplage monolithique et un couplage dissocié sont comparés. Le couplage dissocié néglige l'influence des mouvements du navire sur le vol du cerf-volant. En cas de mer calme, les résultats obtenus par les deux types de couplage sont très proches. En cas de houle régulière les mouvements du navire sont principalement causés par la houle. Le couplage monolithique montre qu'un réseau de sous-harmoniques basse fréquence apparait alors dans le spectre d'excitation du navire. La fréquence fondamentale des sous-harmoniques est donnée par la différence entre la fréquence de vague et la fréquence de l'harmonique la plus proche de l'excitation du kite. Quand cette différence est suffisamment petite, un phénomène d'accrochage apparait. Ce phénomène est bénéfique pour le cerf-volant et le navire quand le décalage des harmoniques d'excitation correspond à une augmentation. Par ailleurs, une étude de la stabilité de route montre qu'il est nécessaire de contrôler activement le safran.